

**GEOLOGICA ULTRAIECTINA**

Mededelingen van de  
Faculteit Aardwetenschappen  
der Universiteit Utrecht

No. 133

**MICROMECHANICS OF  
SAND GRAIN FAILURE AND  
SAND COMPACTION**

**ROLF BRZESOWSKY**

**GEOLOGICA ULTRAIECTINA**

Mededelingen van de  
Faculteit Aardwetenschappen  
der Universiteit Utrecht

No. 133

**MICROMECHANICS OF  
SAND GRAIN FAILURE AND  
SAND COMPACTION**

**ROLF BRZESOWSKY**

27 - 002

CIP-GEGEVENS KONINKLIJKE BIBLIOTHEEK, DEN HAAG

Brzesowsky, Rudolf Heinrich

Micromechanics of sand grain failure and sand compaction /  
Rudolf Heinrich Brzesowsky. - Utrecht : Faculteit Aardwetenschappen,  
Universiteit Utrecht. - (Geologica Ultraiectina, ISSN 0072-1026 ; no. 133)  
Proefschrift Universiteit Utrecht. - Met lit opg. - Met  
samenvatting in het Nederlands.  
ISBN 90-71577-87-2  
Trefw.: zand ; breuken (mechanica) / zand ; compactheid.

# **MICROMECHANICS OF SAND GRAIN FAILURE AND SAND COMPACTION**

Micromechanica van het breukgedrag van zandkorrels  
en van het compactie gedrag van zand  
(met een samenvatting in het Nederlands)

PROEFSCHRIFT

TER VERKRIJGING VAN DE GRAAD VAN DOCTOR AAN DE  
UNIVERSITEIT UTRECHT, OP GEZAG VAN DE  
RECTOR MAGNIFICUS, PROF. DR. J.A. VAN GINKEL,  
INGEVOLGE HET BESLUIT VAN HET COLLEGE VAN DECANEN  
IN HET OPENBAAR TE VERDEDIGEN OP MAANDAG  
23 OKTOBER 1995 DES NAMIDDAGS TE 12.45 UUR

DOOR

**RUDOLF HEINRICH BRZESOWSKY**

GEBOREN OP 5 OKTOBER 1963 TE EDE



PROMOTOR: PROF. DR. C.J. SPIERS  
FACULTEIT AARDWETENSCHAPPEN  
UNIVERSITEIT UTRECHT

COPROMOTOR: DR. F.K. LEHNER  
SHELL RESEARCH RIJSWIJK  
KONINKLIJKE/SHELL EXPLORATIE EN  
PRODUKTIE LABORATORIUM

The research described in this thesis has been funded by Shell Research Rijswijk, Royal Dutch Shell Exploration and Production Laboratory, The Netherlands. It has been carried out in the High Pressure/Temperature (HPT) Laboratory, Faculty of Earth Sciences, University of Utrecht, The Netherlands.

This is Geodynamics Research Institute (University of Utrecht) contribution 95047.

voor Nienke  
en  
mijn Ouders

# **CONTENTS OF THIS THESIS**

<b>ABSTRACT / SUMMARY</b>	<b>1</b>
 <b>CHAPTER 1 INTRODUCTION: Definition of Problems and Aims</b>	
1.1 SCOPE	5
1.2 BACKGROUND AND PREVIOUS WORK	5
1.3 REMAINING PROBLEMS	7
1.4 PRESENT AIMS	8
 <b>CHAPTER 2 RESPONSE OF SPHERICAL GRAINS TO SURFACE LOADING IN THE ELASTIC-BRITTLE FIELD</b>	
2.1 INTRODUCTION	9
2.2 NEAR- AND FAR-FIELD STRESS DISTRIBUTIONS : Analytical Results	11
2.2.1 Reference frames for torsionless contact loading	11
2.2.2 The Boussinesq stress field: point loading of a half-space	13
2.2.3 Uniform distributed loading of a half-space	15
2.2.4 The Hertz stress analysis	17
2.2.5 Hertzian analysis for solids of revolution (The "Hertz-Huber" Analysis)	18
2.2.6 Diametric loading of a sphere by point loads	24
2.2.7 Diametric uniformly distributed loading of a sphere	30
2.3 STRESS DISTRIBUTIONS OBTAINED USING THE FINITE ELEMENT METHOD	38

2.4	EXPERIMENTAL OBSERVATIONS AND COMPARISON WITH THEORY	
2.4.1	Experimental observations	39
2.4.2	Comparison with theory	40
2.5	RECAPITULATION OF SITES OF TENSILE AND SHEAR STRESSES IN A DIAMETRICALLY LOADED SPHERE	42
2.6	GRAIN FAILURE CRITERION FOR QUARTZ	44
2.7	CONCLUSIONS	45

### **CHAPTER 3 FAILURE BEHAVIOUR OF SINGLE SAND GRAINS: THEORY VS. EXPERIMENT**

3.1	INTRODUCTION	47
3.2	MICROMECHANICAL MODELS FOR GRAIN CRUSHING	
3.2.1	Hertzian/LEFM model	49
3.2.2.	Weibull weakest link model	51
3.3	EXPERIMENTS	
3.3.1	Starting material	54
3.3.2	Apparatus and general method	54
3.3.3	Calibration of apparatus	55
3.3.4	Detailed procedural aspects	56
3.4	MECHANICAL RESULTS	
3.4.1	Selected grain data	57
3.4.2	Batch data	58



3.5	DISCUSSION	
3.5.1	Interpretation of results for selected grains	60
3.5.2	Interpretation of batch results	63
3.6	CONCLUSIONS	74

## **CHAPTER 4 TIME-INDEPENDENT COMPACTION BEHAVIOUR OF SANDS**

4.1	INTRODUCTION	75
4.2	MICROSTRUCTURAL FACTORS AND MECHANISMS CONTROLLING COMPACTION	77
4.3	EXPERIMENTAL TECHNIQUES	
4.3.1	Starting material and sample preparation	79
4.3.2	Compaction apparatus and calibration	82
4.3.3	Acoustic emission system	85
4.3.4	Data acquisition / logging	87
4.3.5	Sample handling and testing procedure	88
4.3.6	Data processing and error analysis	91
4.4	EXPERIMENTAL RESULTS	
4.4.1	Mechanical data	91
4.4.2	Microstructural observations	94
4.4.3	Acoustic emission data	94
4.5	INTERPRETATION OF EXPERIMENTAL RESULTS	94

<b>4.6</b>	<b>MICROPHYSICAL MODEL FOR SAND COMPACTION BY HERTZIAN DISTORTION AND GRAIN CRUSHING</b>	
4.6.1	Starting point and principal assumptions	98
4.6.2	Grain contact force and properties of an ordered pack	98
4.6.3	Contact force enhancement during compaction	99
4.6.4	Grain failure criterion	100
4.6.5	Brittle strain	101
4.6.6	Elastic strain	102
4.6.7	Final model	102
<b>4.7</b>	<b>COMPARISON OF EXPERIMENTAL RESULTS WITH MICROPHYSICAL MODEL SIMULATIONS</b>	
4.7.1	Choice of numerical values	103
4.7.2	Simulation results	104
<b>4.8</b>	<b>CONCLUSIONS</b>	108

## **CHAPTER 5 COMPACTION CREEP BEHAVIOUR OF SANDS**

<b>5.1</b>	<b>INTRODUCTION</b>	109
<b>5.2</b>	<b>EXPERIMENTAL TECHNIQUES</b>	
5.2.1	Starting material and sample preparation	110
5.2.2	Compaction apparatus	111
5.2.3	Acoustic emission system	111
5.2.4	Data acquisition / logging	113
5.2.5	Sample handling and testing procedure	114
5.2.6	Data processing and error analysis	115

5.3	MECHANICAL RESULTS	
5.3.1	Two stage creep data	118
5.3.2	Single stage creep data	125
5.3.3	Complete loading paths	128
5.4	MICROSTRUCTURAL OBSERVATIONS	129
5.5	ACOUSTIC EMISSION DATA	133
5.5.1	Two stage creep tests	135
5.5.2	Single stage creep tests	137
5.6	DISCUSSION OF EXPERIMENTAL RESULTS	139
5.7	MICROPHYSICAL MODELLING CONSIDERATIONS	143
5.8	CONCLUSIONS	144

#### APPENDIX: MICROPHYSICAL MODEL FOR COMPACTION CREEP OF SANDS BY STRESS CORROSION CRACKING

A.1	Starting point and principal assumptions	145
A.2	Grain contact force and properties of an ordered pack	145
A.3	Contact force enhancement during compaction	146
A.4	Subcritical crack growth by stress corrosion	146
A.5	Grain failure criterion and grain life time	147
A.6	Brittle strain	149
A.7	Final model	151

## **CHAPTER 6 GENERAL CONCLUSIONS AND SUGGESTIONS FOR FURTHER RESEARCH**

6.1	FAILURE BEHAVIOUR OF SINGLE SAND GRAINS	152
6.2	COMPACTION AND CREEP BEHAVIOUR OF SAND AGGREGATES	153
6.3	IMPLICATIONS OF RESULTS	154
6.4	REMAINING PROBLEMS AND SUGGESTIONS FOR FURTHER RESEARCH	
6.4.1	Grain contact stress fields / grain failure criteria	155
6.4.2	Instantaneous failure behaviour of single sand grains	157
6.4.3	Time-dependent failure behaviour of single sand grains	157
6.4.4	Experimental aspects	158
6.4.5	Geotechnical applications	158
	<b>REFERENCES</b>	160
	<b>NEDERLANDSE SAMENVATTING</b>	174
	<b>NAWOORD</b>	179
	<b>CURRICULUM VITAE</b>	180



## ABSTRACT / SUMMARY

While there exists a considerable body of theoretical and experimental work regarding the time-independent compaction and compaction creep behaviour of sands under near-surface and upper-crustal conditions where brittle processes are important, a number of important questions remain unanswered. In particular, the brittle failure behaviour of single sand grains is poorly understood at the microphysical level, and previous experimental studies performed on sand aggregates have not systematically investigated the effect of applied stress, grain size and chemical environment on either time-independent compaction or compaction creep behaviour. In addition, theoretical models for compaction of sands by time-independent grain scale cracking lack a true micromechanistic basis and no microphysical models have been developed for compaction of sands by time-dependent grain scale cracking.

The present study is concerned with the development of a fundamental understanding of the micromechanical processes controlling the compaction behaviour of sands under conditions favouring brittle and elastic phenomena. The approach adopted involves theoretical and experimental investigations into the failure behaviour of single sand grains and into the compaction behaviour of sand aggregates, and addresses both time-dependent and time-independent processes. The results help provide the understanding of the fundamental processes operating during sand grain failure and sand compaction needed for on-going progress towards micromechanically based constitutive relations suitable for modelling natural and man-induced deformations of both sands and sandstones.

**Chapter 1** of the thesis introduces the problems to be investigated and defines the aims of the study.

**Chapter 2** reviews and synthesizes all of the available theoretical solutions to the stress distribution at the loaded surface and within the volume of a spherical grain subjected to diametric surface loading. A comparison between microstructural observations on the mode of failure of compressed spheres and the results of the synthesis confirms that in a spherical quartz grain, under realistic loading conditions, grain failure is expected to initiate at surface flaws which develop into ring cracks at the edge of the loaded contact area. These cracks develop under the action of the Hertzian radial tensile stress acting at the contact margin (the maximum tensile stress occurring anywhere within or on the surface of the grain) and propagate as (transgranular) convergent cone cracks leading to whole-grain failure. Combining these results with fracture mechanics considerations, a failure criterion for a brittle quartz grain is obtained.

**Chapter 3** reports constant displacement rate crushing tests carried out on

selected well-rounded single sand grains and on grains sampled from different grain size ( $d$ ) batches of a pure quartz sand. The distributed critical load at failure ( $F_c$ ) data obtained for the different batch samples show that  $F_c$  can be considered proportional to  $d^f$  where  $f \approx 1.3$ . Making use of the whole-grain failure criterion specified in Chapter 2, micromechanical models for crushing of individual grains compressed between flat platens are developed. Applying a Hertzian/fracture mechanics model for grain crushing, the  $F_c$  data obtained for the selected grains are translated into an accurate estimate of the size of flaws associated with failure ( $c_f$ ). Similarly, the distributed  $F_c$  data obtained from the different batch samples are translated into distributions of grain failure stress ( $\sigma_f$  = Hertzian radial tensile stress acting at the contact margin). A review of Weibull weakest link theory yields a statistical model for grain crushing; however, this is unable to account for the observed grain size dependence of  $\sigma_f$ . On the other hand, the Hertzian/fracture mechanics model enables the translation of the distributed  $F_c$  data, for the batch samples, into distributions of  $c_f$ , assuming spherical grains, or of "effective" radius of curvature ( $r_g$ ), characterising contact surface asperities in the case of non-spherical grains. The data imply  $c_f$  or  $r_g$  to be proportional to the grain size ( $d$ ) as  $d^g$  where  $g \approx 0.5-0.7$ . Since there is no clear physical basis for a grain size dependence of  $c_f$  and since roundness data for dune sands exhibit a similar relation between  $r_g$  and  $d$ , it is inferred that the Hertzian/fracture mechanics model assuming non-spherical grains with a distributed  $r_g$  is the most physically reasonable model for grain failure.

**Chapter 4** is concerned with experimental and theoretical aspects of the short-term compaction behaviour of quartz sands. Uniaxial compaction experiments are reported, performed on sands, at room temperature, stresses up to 30 MPa, using grain sizes of  $196 \pm 16$ ,  $275 \pm 25$  and  $378 \pm 22$   $\mu\text{m}$ , under dry and fluid-flooded conditions (using an aqueous or inert pore fluid), and applying constant loading rates in the range 3.90 to 5495 MPa/hour. The results typically show quasi-elastic loading behaviour plus permanent deformation caused by grain failure and rearrangement processes. In particular, the results show that with increasing grain size more permanent deformation is achieved. On the basis of the inferred microscale mechanisms, a microphysical model for the time-independent compaction of sands is developed, considering aggregate densification to be the sum of "elastic" strain due to grain contact distortion plus "brittle" strain due to crushing and rearrangement of individual grains. Extending the Hertzian/fracture mechanics model for grain failure formulated in chapter 3, two extreme cases of the model are formulated: (i) spherical grains with distributed flaw size at failure ( $c_f$ ), and (ii) non-spherical grains with distributed "effective" contact surface radius of curvature ( $r_g$ ). In accordance with the conclusions drawn in Chapter 3, numerical simulations produced using case (ii) of the model satisfactorily account for the grain size effect observed in the compaction tests on sands.

In **Chapter 5**, the compaction creep behaviour of sand is systematically investigated, focusing on the effect of chemical environment, applied stress and grain size. Uniaxial creep tests are reported, performed on the sands, at room temperature, (constant) applied stresses in the range 14.5 to 30 MPa and under dry and fluid-flooded conditions (using an aqueous or inert pore fluid). The results obtained show time-dependent deformation behaviour predominated by subcritical transgranular cracking leading to grain failure. Acoustic emission (AE) data monitored during creep of the sands exhibit a near-linear relation between cumulative AE event counts and strain, suggesting a direct relation between progressive grain failure and strain. The creep process is clearly promoted by a chemically active pore fluid and higher pore fluid salinity, and is strongly accelerated towards larger grain sizes and higher applied stresses. The detailed grain crushing mechanism is inferred to be growth of grain surface flaws by stress corrosion at grain-to-grain contacts. The development of a microphysical model for compaction creep of sands by this mechanism is attempted but cannot be meaningfully compared with the experimental results due to excessive sensitivity to poorly constrained input parameter values.

**Chapter 6** consists of a summary and an attempt to generalize the principal conclusions drawn in the preceding chapters. This consideration of the principal findings is followed by a discussion of their implications for the compaction and creep behaviour of fault gouge materials in seismically active upper-crustal faults, and for the creep effects expected in hydrocarbon-bearing clastic reservoir rocks in the post-production phase. The thesis is closed with a consideration of unsolved problems remaining and resulting suggestions for further research.

## CHAPTER 1 INTRODUCTION: Definition of Problems and Aims

### 1.1 SCOPE

The research reported in this thesis is concerned with the development of a fundamental understanding of the micromechanical processes controlling the compaction behaviour of sands under conditions favouring brittle and elastic phenomena, i.e. under conditions comparable to the surface and upper crust of the Earth. The approach adopted involves theoretical and experimental investigations into the failure behaviour of single sand grains and into the compaction behaviour of sand aggregates, and addresses both time-dependent and time-independent processes. The results help provide the understanding of the processes operating, during sand grain failure and sand compaction, which is needed for further progress towards a quantitative description of the material behaviour suitable for numerical modelling of natural and man-induced deformations of sands and sandstones.

### 1.2 BACKGROUND AND PREVIOUS WORK

Sand and sandstones are major constituents of clastic sedimentary rocks in the Earth's upper crust and can accordingly be expected to play a major role in controlling upper-crustal mechanics and deformation phenomena. On the basis of microstructural observations, the essentially time-independent (or short-term) mechanical compaction behaviour of porous, clastic sediments under upper-crustal conditions is believed to be controlled by grain fracture plus rearrangement (Groshong, 1988; Knipe, 1989). On the other hand, recognizing that pore fluids are known to enhance the kinetics of subcritical grain cracking mechanisms, time-dependent grain-fracture-controlled compaction creep effects may also be important in porous sediments, perhaps even alongside processes such as pressure solution (Costin, 1989; Atkinson & Meredith, 1989a; Zhang *et al.*, 1990a,b; Schutjens, 1991a,b; Elias & Hajash, 1992; Milliken, 1994; Dewers & Hajash, 1994). Thus both time-dependent and time-independent, grain failure related compaction processes are likely to play an important role in controlling the porosity and permeability evolution of clastic sedimentary rocks, for example in rapidly subsiding basin settings (Donaldson *et al.*, 1995a,b). They may also be of importance in controlling production-related compaction of hydrocarbon-bearing clastic reservoir rocks, leading to surface subsidence and to any associated small scale upper-crustal seismicity (Zoback & Byerlee, 1976; Segall, 1992; Donaldson *et al.*, 1995a,b). In addition, they could conceivably induce creep effects in such formations, after hydrocarbon extraction has ceased, giving rise to continued surface subsidence (Schutjens *et al.*, 1994, 1995). Moreover, similar cataclastic compaction and creep effects can be expected to be of importance in controlling the behaviour of fault gouge materials produced in seismically active faults (Morrow & Byerlee, 1989; Rice, 1992; King & Sammis, 1992; Sleep & Blanpied, 1992).



Aside from the above, data on the mechanical compaction behaviour of sands have become essential input for modelling the response of hydrocarbon reservoir rocks to downhole stimulation methods used for permeability enhancement, i.e. techniques designed to improve hydrocarbon recovery rates from such formations (Papamichos *et al.*, 1993; Wong *et al.*, 1993). Of course, the compaction of sands by brittle grain scale processes has also long received attention in civil engineering (soil mechanics) in the context of assessing the settlement and stability of deep foundations (Lee & Farhoomand, 1967; Vesić & Clough, 1968).

In view of the above-mentioned areas of interest, an evident need exists for a theoretically and experimentally based understanding of the mechanisms controlling the compaction behaviour of sands, in order to develop micromechanical models which can eventually be used in macroscale modelling of both natural and man-induced deformation phenomena in sands and sandstones. As an integral step in this direction, an understanding of single grain failure behaviour and its role in determining aggregate behaviour is essential.

A great deal of work has been reported in the literature on the mechanical compaction of granular earth materials under hydrostatic compression conditions from both experimental and theoretical points of view. Previous experimental studies on the time-independent compaction of porous sandstones and sands at room temperature have typically shown non-linear stress-strain behaviour with part of the deformation being elastic, as a result of grain contact distortion, and part being permanent, due to grain crushing and particle rearrangement. Beyond a specific critical effective pressure ( $P_{cr}$ ), the irrecoverable porosity reduction during loading increases significantly. The amount of compaction obtained at a given  $P_{cr}$  generally increases with increasing (initial) porosity ( $\phi$ ) and grain size ( $d$ ) (Roberts & de Souza, 1958; Ko & Scott, 1967; Borg *et al.*, 1960; Lee & Farhoomand, 1967; Vesić & Clough, 1968; Dunn *et al.*, 1973; Zoback & Byerlee, 1976; Lambe & Whitman, 1979; Wissler & Simmons, 1985; Zhang *et al.*, 1990a). At the same time, crushing tests conducted on single sand grains have shown their load at failure to increase with increasing  $d$  (Gallagher, 1976). Previous experimental studies on the time-dependent compaction (i.e. creep) of sands at room temperature have exhibited significant creep effects, associated with particle breakage, which were notably accelerated by the addition of water (Roberts & de Souza, 1958; Lee & Farhoomand, 1967; Lambe & Whitman, 1979). Microstructurally, the experimentally deformed materials have revealed that the dominant grain failure mechanism leading to aggregate time-independent compaction and compaction creep, and to single grain crushing is the development of transgranular cracks at grain-to-grain contacts due to point loading (Maxwell, 1960; Borg *et al.*, 1960; Gallagher, 1976, 1987; Gallagher *et al.*, 1974; Zhang *et al.*, 1990a; Wong, 1990; Bernabe & Brace, 1990; Gill *et al.*, 1990; Myer *et al.*, 1992). In addition, detailed microstructural observations have been reported on the modes of failure of compressed spherical grains and show that cracks causing grain failure initiate as

ring cracks at the edge of the contact area and propagate as transgranular cone cracks (Rumpf *et al.*, 1967; Arbiter *et al.*, 1969; Rumpf & Schönert, 1972; Stieß, 1976; Gallagher, 1976, 1987; Shipway & Hutchings, 1993b).

Previous theoretical studies have involved micromechanical modelling of the time-independent compaction of porous rock by grain crushing, employing Hertzian contact theory (Hertz, 1896) to describe the critical (tensile) state of stress at loaded grain contacts, and linear elastic fracture mechanics (Lawn, 1993) to formulate a grain failure criterion (Zhang *et al.*, 1990a; Wong, 1990). In addition, there is a considerable body of analytical and numerical work on the state of stress inside spherical grains loaded diametrically (Lurje, 1963; Sternberg & Rosenthal, 1952; Hiramatsu & Oka, 1966; Kienzler & Schmitt, 1990).

### 1.3 REMAINING PROBLEMS

From the above point of departure, the major problems remaining with regard to obtaining a theoretically and experimentally based understanding of the failure mode of single sand grains, and the compaction behaviour of sand aggregates, are summarized below.

First, no complete synthesis exists of available solutions to the stress distribution inside and on the surface of spherical grains subjected to diametric surface loading, and there has been little attempt to apply these to predict the full range of possible grain failure modes.

Second, the detailed failure behaviour of single sand grains is not fully understood. In particular, the failure mode and the nature and size of the flaws initiating grain breakage have not been characterized. Consequently, a grain failure criterion has not been rigorously defined. Moreover, the influence of subcritical crack growth on the strength and the failure behaviour of single sand grains has not been assessed.

Third, no physically justifiable explanation has been offered for the grain size dependence of the grain failure load observed in compaction experiments and single grain crushing tests.

Fourth, previous experimental studies suffer from the disadvantage that the effects of applied stress, grain size and chemical environment on both the time-independent and the time-dependent compaction behaviour of sands, while known to be important, have not been systematically investigated. Moreover, the detailed role of microcracking has not been evaluated using acoustic emission (AE) techniques or microstructural analysis.

Fifth, no micromechanical models for compaction of sands by time-dependent and time-independent grain scale cracking have been developed.

## 1.4 PRESENT AIMS

The aims of this thesis can now be specified as follows:

1. To review and synthesize all of the available near field (i.e grain contact) and far-field (grain volume) models describing stress distributions within individual spherical grains under diametric loading (Chapter 2).
2. To formulate a grain failure criterion based on a comparison between stress distribution models (point 1) and microstructural observations of cracking phenomena in spheres loaded to failure (Chapter 2).
3. To develop micromechanical models for grain failure incorporating the above-mentioned grain failure criterion and to test the validity of these models against diametric compression experiments performed on single sand grains, with special attention for grain size effects and the size of flaws associated with grain failure (Chapter 3).
4. To systematically investigate the short-term behaviour of sand aggregates in uniaxial compaction experiments and to develop a micromechanical model based on single sand grain behaviour, suitable for comparison with the experimental results (Chapter 4).
5. To systematically investigate the effect of chemical environment, applied stress and grain size on the compaction creep behaviour of sands (Chapter 5).
6. To gain insight into the microphysical mechanisms operative during compaction of sands, with the aid of acoustic emission (AE) and microstructural methods (Chapters 4 and 5).
7. To develop micromechanical models for compaction creep of sands by time-dependent, fluid-assisted, grain scale cracking or "stress corrosion cracking" (Chapter 5).

## CHAPTER 2 RESPONSE OF SPHERICAL GRAINS TO SURFACE LOADING IN THE ELASTIC-BRITTLE FIELD

### 2.1. INTRODUCTION

It is well established from microstructural analysis of naturally compacted or faulted, high porosity, upper-crustal rocks that, under sufficiently high effective stresses, such materials compact or deform by grain scale brittle fracture plus grain rearrangement by frictional intergranular sliding and rotation (e.g. recent reviews by Groshong, 1988; Knipe, 1989 and Lloyd & Knipe, 1992). These mechanisms are thus presumed to play an important role in controlling the essentially time-independent compaction behaviour of high porosity sandstones and sands (Pittman, 1981; Burley, 1986; Owen, 1987; Houseknecht, 1987; Wilson & McBride, 1988; Wu & Groshong, 1991; Pittman & Larese, 1991; McBride *et al.*, 1991; Hippler, 1993; Antonellini *et al.*, 1994). In particular, they are believed to be of major importance in controlling the porosity and permeability evolution of sedimentary rocks both in rapidly subsiding basin settings and in tectonic deformation of sediments (e.g. in active and passive plate margin environments) under low grade metamorphic conditions predominated by faulting and cataclasis (Donaldson *et al.*, 1995a,b). They may also be of importance in controlling production-related compaction of hydrocarbon reservoir rocks, leading to surface subsidence and to any associated small scale upper-crustal seismicity (Segall, 1989, 1992; Grasso, 1992; Segall *et al.*, 1994; Schutjens *et al.*, 1994).

Clearly, a theoretically and experimentally based understanding of these mechanisms is needed in order to develop micromechanical models which can eventually be used in macroscale modelling of both upper-crustal deformation and compaction of hydrocarbon reservoirs in the (post-) production phase. Previous experimental studies on time-independent compaction of porous sandstones and sands at room temperature have shown irrecoverable porosity reduction during loading, this increasing significantly beyond a specific critical effective pressure ( $P_{cr}$ ). The amount of compaction is generally dependent on porosity ( $\phi$ ) and grain size ( $d$ ): the larger  $\phi$  and  $d$ , the greater the compaction and the lower  $P_{cr}$ ; i.e. the weaker the material (Borg *et al.*, 1960; Lee & Farhoomand, 1967; Dunn *et al.*, 1973; Zoback & Byerlee, 1976; Lambe & Whitman, 1979; Wissler & Simmons, 1985; Zhang *et al.*, 1990a). Petrographic observations of the experimentally deformed materials have revealed that the dominant grain failure mechanism leading to compaction is the development of tensile intra- and transgranular cracks at grain-to-grain contacts due to point loading (Gallagher, 1976, 1987; Gallagher *et al.*, 1974; Zhang *et al.*, 1990a; Wong, 1990; Bernabe & Brace, 1990; Gill *et al.*, 1990; Myer *et al.*, 1992).

Micromechanical modelling of the compaction of porous rock by grain crushing under hydrostatic states of stress has been recognized as requiring the description of the critical (tensile) state of stress at grain contacts, e.g. using Hertzian contact theory (Hertz, 1882a,b, 1896) which allows the stress and deformation fields at loaded



contacts between elastic bodies to be computed (see recent reviews by Kemeny & Cook, 1991 and Myer *et al.*, 1992). Stress concentrators (flaws) at the grain contact surface are believed to be sites of ring crack nucleation and subsequent unstable growth leading to grain failure, a process which can be described using linear elastic fracture mechanics (LEFM) (Lawn, 1993). Recently, this approach was used to describe the hydrostatic compaction behaviour of cemented porous rock (e.g. sandstone) by deriving an expression for the critical effective pressure for the onset of major grain crushing ( $P_{cr}$ ) as a function of porosity and flaw size (Wong, 1990; Zhang *et al.*, 1990a). However, it is questionable in how far Hertzian contact theory applies to a cemented grain contact region (Dvorkin *et al.*, 1991, 1994; Zang & Wong, 1995). More importantly, the model derived by Wong *et al.* adopts Hertzian contact theory, to determine the grain contact stress distribution, plus an assumed rather than rigorously defined grain failure criterion. A criterion should be based on an analysis of (i) the actual (tensile) state of stress inside, on the free surface and at the loaded contact of the grain, (ii) the nature of the flaws (e.g. their size and spatial distribution) and (iii) the crack propagation mode and path of growth. As a first step in this direction, a need exists for interpreting single grain failure behaviour on the basis of theoretical analyses of the stress distribution in a sphere compressed between two rigid plates and on microstructural observations of crushed spheres.

There is a considerable body of theoretical work, both analytic and numerical, on the state of stress inside spherical grains subjected to diametric surface loading (Lurje, 1963; Sternberg & Rosenthal, 1952; Hiramatsu & Oka, 1966, Kienzler & Schmitt, 1990). In addition, detailed microstructural observations have been reported on the modes of failure of compressed spherical grains (Rumpf *et al.*, 1967; Arbiter *et al.*, 1969; Rumpf & Schönert, 1972; Gallagher, 1976, 1987; Shipway & Hutchings, 1993b). However, no complete synthesis exists of all stress solutions in combination with the identification of all possible failure modes. Firstly, inadequate computation methods and interpretation of simulation results have lead to substantial numerical errors in the suggested magnitude of (local) tensile stress components (Wijk, 1978; Shipway & Hutchings, 1993a). Secondly, inconsistency exists in the literature between microstructural observations of crack phenomena in crushed spheres and the models applied to interpret these.

This chapter reviews and synthesizes all of the available near-field (i.e. grain contact) and far-field (grain volume) stress distribution models in detail. On the basis of a comparison between microstructural observations of crack phenomena in crushed spheres and these models, crack initiation site and path predictions will be given. Moreover, the stress distribution models will serve to compare sites and magnitudes of (local) maximum tensile stresses. It will be shown that in a spherical quartz grain under realistic loading conditions the Hertzian radial contact stress is the maximum tensile stress occurring and is held responsible for ring crack initiation. This will lead to the specification of a grain failure criterion for quartz.

## 2.2 NEAR- AND FAR-FIELD STRESS DISTRIBUTIONS : Analytical Results

A closed-form, analytical solution to the problem of the complete stress distribution within a sphere subjected to surface loading, for example diametric loading, is not available (Kienzler & Schmitt, 1990). Local (near-field) contact stresses can be described using the classical Hertz analysis (Hertz, 1882a,b, 1896; Huber, 1904) for the normal stress distribution over a circular contact area. In the limiting case, when the contact area approaches a point, the Hertz solution passes into Boussinesq's solution (Boussinesq, 1885) for a stress field due to a point load applied to the surface of an elastic half-space (Stieß, 1976). However, neither analysis accounts for the far-field shape of the body or the way in which the load is applied. A solution to the stress distribution problem of a sphere under diametric compression, for example, can therefore only be approximated (e.g. using the finite element method) by superposition of the near-field Hertzian local contact stresses onto the far-field stresses obtained for diametric loading of a sphere either by concentrated (point) forces or by uniform normal stresses distributed over spherical end caps (Stieß, 1976; Kienzler & Schmitt, 1990). This superposition approach is supported by Saint-Venant's principle (Timoshenko & Goodier, 1970) which states that a system of forces applied to a small element of the surface of the body will result in localized stresses and strains only. The principle thus implies that the far-field stress distribution will be similar, independently of the loading condition at the contact (concentrated or distributed); see Stieß & Schönert (1974).

In the following, the Boussinesq solutions are reviewed for both a concentrated (point) load and a uniform normal stress distribution over a circular area of an elastic half-space. Also considered are the Hertz analysis and stress solutions obtained for diametric loading of a sphere both by point loads and by uniform normal stresses distributed over spherical end caps. In all cases, the analytical results are used to generate graphical representations of the corresponding stress distributions.

### 2.2.1 Reference frames for torsionless contact loading

Before reviewing the above-mentioned analyses it is first necessary to define a set of coordinate reference frames suitable for the treatment of the torsionless and frictionless contact loading problems in question. The four reference frames chosen are depicted in Figure 2.1. In the case of single contact problems the origin is located at the (central) contact point and Z is taken normal to the contact tangent plane. In the case of diametric loading the origin is located at the centre of the sphere and Z is taken parallel to the sphere diameter which connects the (central) loading points or poles  $P_1$ ,  $P_2$  having cartesian coordinates  $(0, 0, \pm R)$  where  $R$  is the radius of the sphere. Throughout, tensile stresses are taken as positive and shear stresses denoted  $\tau_{pq}$  are defined as acting in the direction of  $p$  on a plane normal to  $q$ . In the case of problems concerned with axi-symmetric loading about the  $z$ -axis, and using cylindrical

coordinates, the principal stresses ( $\sigma$ ) represent roots of the determinant written (e.g. Timoshenko & Goodier, 1970, art. 10, page 22; Jaeger & Cook, 1984)

$$\begin{vmatrix} \sigma_{rr}-\sigma & 0 & \tau_{rz} \\ 0 & \sigma_{\theta\theta}-\sigma & 0 \\ \tau_{rz} & 0 & \sigma_{zz}-\sigma \end{vmatrix} = 0 \Leftrightarrow \sigma = \sigma_{\theta\theta} \text{ or } \sigma = \frac{\sigma_{rr}+\sigma_{zz}}{2} \pm \sqrt{\left(\frac{\sigma_{rr}-\sigma_{zz}}{2}\right)^2 + \tau_{rz}^2} \quad (1)$$

Following Lawn (1968) and Mouginit & Maugis (1985) the principal stresses are labelled  $\sigma_1$ ,  $\sigma_2$  and  $\sigma_3$  such that in general  $\sigma_1 \geq \sigma_2 \geq \sigma_3$  and  $\sigma_2$  equals  $\sigma_{\theta\theta}$ , while  $\sigma_1$  and  $\sigma_3$  are contained in the symmetry (RZ) planes through the loading (Z) axis. Accordingly, the maximum shear stress  $\tau_{\max}$  is in general equal to the principal shear stress  $(\sigma_1 - \sigma_3)/2$ .

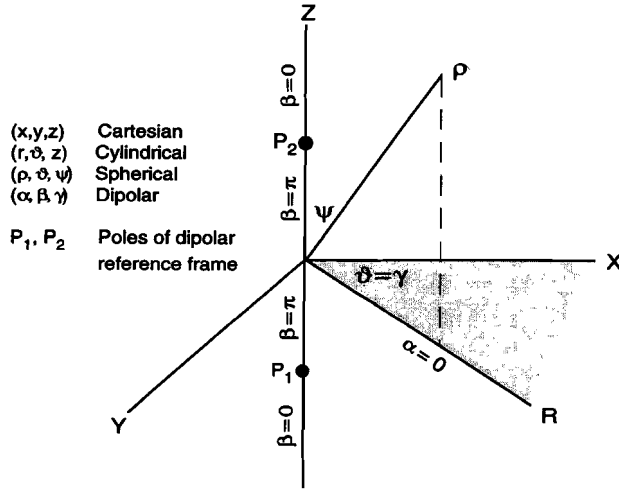


**Figure 2.1.** Coordinate reference frames for contact loading problems employed in the present chapter. In the case of single contact problems the origin is located at the (central) loading point and Z is taken normal to the contact tangent plane. In the case of diametric loading the origin is located at the centre of the sphere and Z is taken parallel to the sphere diameter connecting the (central) loading points or poles  $P_1$ ,  $P_2$ . These have cartesian coordinates  $(0, 0, \pm R)$  where  $R$  is the radius of the sphere. In the dipolar reference frame  $(\alpha, \beta, \gamma)$ , in the XZ plane ( $\gamma = 0$ ), lines of constant  $\alpha$  represent circles of radius  $1/\sinh \alpha$  centred on Z at  $z = -\cosh \alpha / \sinh \alpha$  while lines of constant  $\beta$  represent circles of radius  $1/\sin \beta$  centred on X at  $x = \cot \beta$  (see Sternberg & Sadowsky, 1952).

## 2.2.2 The Boussinesq stress field: point loading of a half-space

With reference to Figure 2.1, the solution for the torsionless axi-symmetric stress field due to a frictionless point load  $F$  acting at the origin perpendicular to the flat surface of an elastic half-space bounded by the  $XY$  plane has been given by Boussinesq (1885) (Timoshenko & Goodier, 1970, art. 138, page 398; Johnson, 1987, § 3.2). The stress components within the solid, using cylindrical coordinates  $(r, \vartheta, z)$ , are (Johnson, 1987, eqn. 3.20)

$$\sigma_{rr} = \frac{F}{2\pi} \left[ (1-2\nu) \left( \frac{1}{r^2} - \frac{z}{\rho r^2} \right) - \frac{3zr^2}{\rho^5} \right] \quad (2)$$

$$\sigma_{\vartheta\vartheta} = -\frac{F}{2\pi} (1-2\nu) \left( \frac{1}{r^2} - \frac{z}{\rho r^2} - \frac{z}{\rho^3} \right) \quad (3)$$

$$\sigma_{zz} = -\frac{3F}{2\pi} \frac{z^3}{\rho^5} \quad (4)$$

$$\tau_{rz} = -\frac{3F}{2\pi} \frac{rz^2}{\rho^5} \quad \tau_{r\vartheta} = \tau_{z\vartheta} = 0 \quad (5)$$

where  $\rho^2 = (r^2 + z^2)$  and  $\nu$  is Poisson's ratio (for equivalents in spherical coordinates see Yoffe (1982)). From these relations it is clear that a stress singularity occurs at the origin ( $\tau_{rz} \equiv 0$ , frictionless). There,  $\sigma_{zz}$  and  $\sigma_{rr}$  tend to  $\pm\infty$  respectively. Further,  $\sigma_{\vartheta\vartheta}$  approaches  $+\infty$  along the  $z$ -axis and  $-\infty$  at the solid half-space surface. At the surface and outside the origin,  $\tau_{rz} = 0$ ,  $\sigma_{zz} = 0$  and  $\sigma_{rr} = -\sigma_{\vartheta\vartheta} = (1-2\nu)F/2\pi r^2$ . In addition, along the  $z$ -axis  $\tau_{rz} = 0$ ,  $\sigma_{zz} = -3F/2\pi z^2$  and  $\sigma_{rr} = \sigma_{\vartheta\vartheta} = (1-2\nu)F/4\pi z^2$ . Inside the elastic half-space the principal stresses  $\sigma_1$  and  $\sigma_3$  remain respectively tensile and compressive, and the surface  $\sigma_2 = 0$  corresponds to the locus  $\psi \approx 51.8^\circ$  independently of  $\nu$  (Stieβ, 1976).

To illustrate the nature of the stress distributions, stress components have been computed from the above Boussinesq solutions for concentrated loading of an elastic half-space and are presented in Figures 2.2a&b. These figures show the principal stresses at the solid surface outside the origin, and along the  $z$ -axis, for different values of  $\nu$ . All stresses are scaled with respect to  $F/2\pi$ . Both figures illustrate that towards the origin  $\sigma_{zz}$  and  $\sigma_{rr}$  tend to  $-\infty$  respectively  $+\infty$ ;  $\sigma_{\vartheta\vartheta}$  approaches  $+\infty$  along the  $z$ -axis and  $-\infty$  at the boundary. This singular behaviour is intensified with increasing  $\nu$ . Note that the Poisson's ratio for quartz is generally taken as equal to 0.077 (Simmons & Wang, 1971; Sumino & Anderson, 1984).

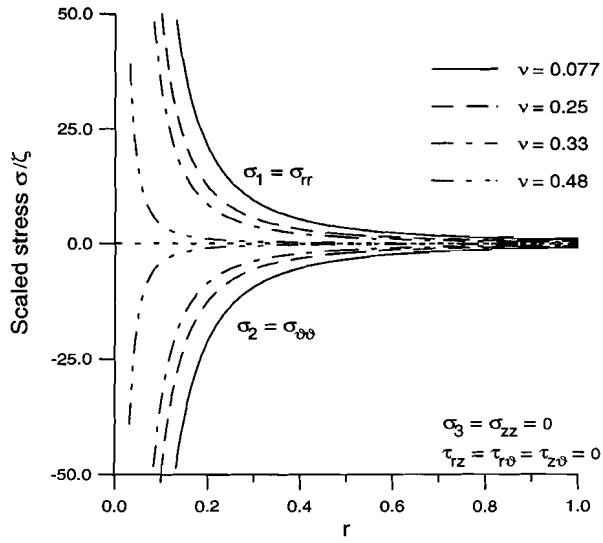


Figure 2.2a

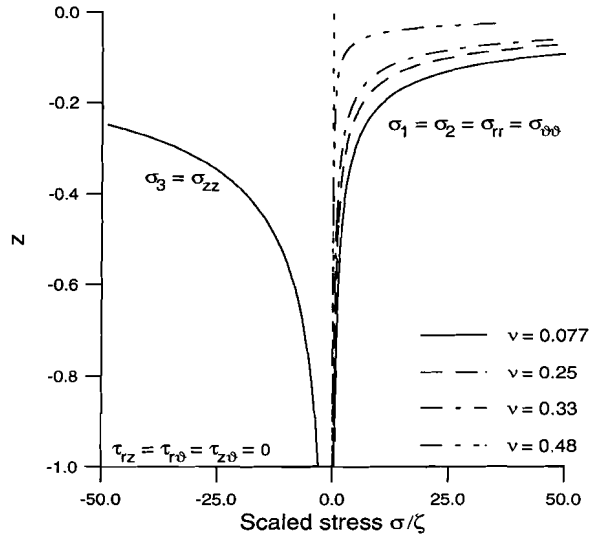


Figure 2.2b

**Figure 2.2.** Principal stresses at the solid surface, outside the origin (a), and along the  $z$ -axis (b), computed from the Boussinesq solution for point loading of an elastic half-space at the origin. Calculations performed for different values of the Poisson's ratio  $\nu$  and scaled with respect to  $\zeta = F/2\pi$ . The principal stresses  $\sigma_1$  and  $\sigma_2$  show intensified singular behaviour with increasing  $\nu$ .

### 2.2.3 Uniform distributed loading of a half-space

The solution for the torsionless axi-symmetric stress field in an elastic half-space bounded by the XY plane, due to a (frictionless) uniform pressure  $p$  applied over a circular element of the solid surface, having radius  $a$  and centre at the origin (see Figure 2.1), has also been given by Boussinesq (1885) (Love, 1929, chapter 3; Timoshenko & Goodier, 1970, art. 139, page 403; Johnson, 1987, § 3.4a). Employing the Boussinesq solutions given in section 2.2.2, the stress components along the  $z$ -axis are obtained by considering the pressure  $p$  to be produced by a point load  $F$  acting uniformly distributed over a ring area of radius  $r$  and width  $dr$  (perpendicular to the  $z$ -axis); i.e. using the equality  $F = p \, 2\pi r \, dr$ . Substituting for  $F$  in eqn. 2-5 and integrating over the entire circular element with radius  $a$  leads to the stress components *along the  $z$ -axis*, in the form (Johnson, 1987, eqn. 3.33)

$$\sigma_{rr} = \sigma_{\theta\theta} = \frac{p}{2} \left[ -(1+2\nu) + \frac{2z(1+\nu)}{\sqrt{a^2+z^2}} - \left( \frac{z}{\sqrt{a^2+z^2}} \right)^3 \right] \quad (6)$$

$$\sigma_{zz} = p \left[ -1 + \left( \frac{z}{\sqrt{a^2+z^2}} \right)^3 \right] \quad \tau_{rz} = \tau_{r\theta} = \tau_{z\theta} = 0 \quad (7)$$

At the solid surface *inside the loaded circle*,  $\sigma_{rr} = \sigma_{\theta\theta} = -(1+2\nu)p/2$ ,  $\sigma_{zz} = -p$  and  $\tau_{rz} = \tau_{r\theta} = \tau_{z\theta} = 0$  (Johnson, 1987, eqn. 3.32). Following the Boussinesq solutions for a point load given in section 2.2.2, the stress components at the solid surface *outside the loaded circle* are  $\sigma_{rr} = -\sigma_{\theta\theta} = (1-2\nu)F / (2\pi r^2)$ ,  $\sigma_{zz} = 0$  and  $\tau_{rz} = \tau_{r\theta} = \tau_{z\theta} = 0$ . Accordingly,  $\sigma_{rr}$  reaches a tensile maximum at the periphery of the loaded circle (approaching in the direction of the origin), reaching a value there of  $(1-2\nu)p/2$  (Wijk, 1978).

Again, to illustrate the nature of the stress distribution, the stress components have been computed from the Boussinesq solution for uniform distributed loading of an elastic half-space. Figures 2.3a&b show the principal stresses at the solid surface, and along the  $z$ -axis, for different values of  $\nu$ . All stresses are normalised with respect to  $p$ . At the periphery of the loaded circle, within the solid surface,  $\sigma_{rr}$  exhibits a tensile maximum which increases with decreasing  $\nu$ . Along the  $z$ -axis  $\sigma_{rr} = \sigma_{\theta\theta}$  exhibits a tensile maximum which is located at decreasing depth  $z$  and which intensifies with decreasing  $\nu$ , before going asymptotically approaching zero.

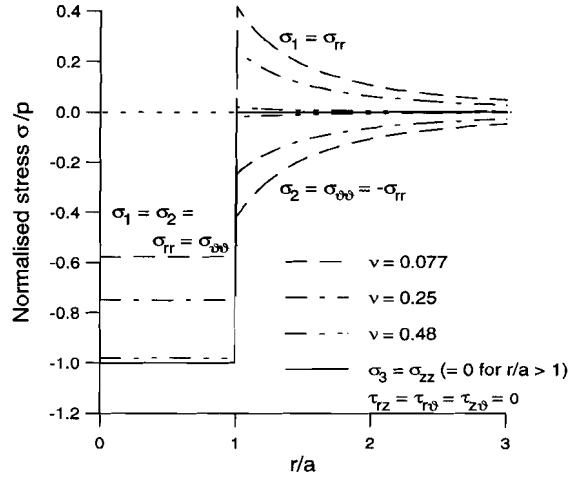


Figure 2.3a

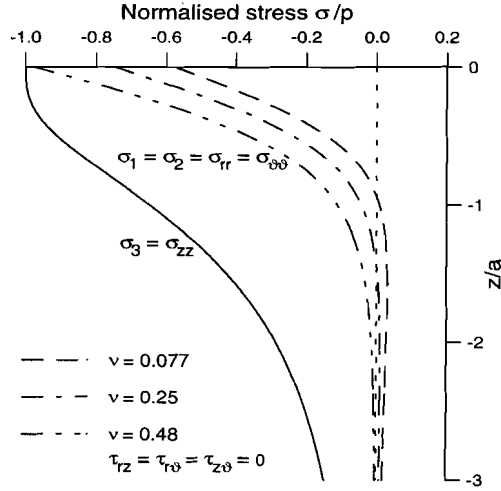


Figure 2.3b

**Figure 2.3.** Principal stresses at the solid surface (a) and along the z-axis (b), computed from the Boussinesq solution for uniform distributed loading of an elastic half-space due to a pressure  $p$  applied over a circular element of the solid surface, having radius  $a$  and centre at the origin. Calculations performed for different values of the Poisson's ratio  $\nu$  and normalised with respect to  $p$ . At the periphery of the loaded circle ( $r/a = 1$ ) (a),  $\sigma_1$  exhibits a tensile maximum which increases with decreasing  $\nu$ . Along the z-axis (b), the principal stress  $\sigma_1 = \sigma_2$  exhibits a tensile maximum which is located at decreasing depth  $z$  and which intensifies with decreasing  $\nu$ , before asymptotically approaching zero.

#### 2.2.4 The Hertz analysis

Hertz (1882a,b, 1896) obtained a complete analytic solution to the problem of the stress distribution generated at the contact of two non-conforming, isotropic, homogeneous, linear elastic bodies having continuous surfaces. Two bodies are said to be non-conforming if they possess dissimilar profiles when brought into point contact without deformation (Johnson, 1987, § 1.1). The Hertz analysis constitutes a classical result in the field of contact mechanics and is widely referred to as Hertzian contact theory. In its general form, the theory assumes torsionless loading over a frictionless, elliptical planar contact area normal to the z-axis, with centre at the origin. In addition, the following assumptions are made: (i) the shapes, profiles or separation of the bodies close to the contact can be described by appropriate 2nd order polynomials, and (ii) the size of the contact area is small compared with the smallest radius of surface curvature near the contact area. The latter ensures that the surfaces outside the contact area are approximately planar, so that the internal stress field can be calculated on the basis of a semi-infinite half-space without being seriously influenced by the proximity of the boundaries. It is also consistent with the notion that strains are sufficiently small to lie within the scope of the linear theory of elasticity (Johnson, 1987, § 4.1 & 4.2; Borodich, 1993). From this starting point, and using the cartesian reference frame of Figure 2.1, the solution which follows for a semi-ellipsoidal normal stress distribution within the contact surface is (Hertz, 1882a,b, 1896; Johnson, 1987, eqn. 3.58)

$$[\sigma_{zz}(x,y)]_{z=0} = -\frac{3F}{2\pi ab} \sqrt{1 - x^2/a^2 - y^2/b^2} = -\sigma_0 \sqrt{1 - x^2/a^2 - y^2/b^2} \quad (8)$$

where  $\sigma_0$  denotes the normal stress at the centre of the contact, and a and b are the semi-axes of the elliptical contact area ( $a > b$ ) (Johnson, 1987, eqn. 3.58). The stress distribution satisfies the principle established by Boussinesq (1885) that for two elastic bodies in contact, with continuous profiles through the edge of the contact area, the stress distribution falls to zero at the edge (Johnson, 1987, § 5.1). In the absence of adhesion or surface roughness of the contact between the two solids, this "Hertzian normal stress distribution" forms a unique solution to the contact problem (Johnson, 1987, § 4.2).

Last in the context of the general theory, it is important to note that the assumed ellipsoidal surface of each body ( $i = 1, 2$ ) at the (undeformed) contact point is characterised by the principal (respectively maximum and minimum) radii of curvature  $R'_i$  and  $R''_i$  (convex positive). Principal *relative* radii of curvature  $R'$  and  $R''$  can be defined respectively as  $1/R' = (1/R'_1) + (1/R'_2)$  and  $1/R'' = (1/R''_1) + (1/R''_2)$ . An equivalent radius (of curvature) can further be defined as  $R_e = \sqrt{(R'R'')}$  and an equivalent contact radius as  $c^* = \sqrt{(ab)}$ . Non-conforming can now be redefined as  $1/R'$  and  $1/R''$  being sufficiently large to justify the neglect of higher order terms ( $>2$ ) in the polynomial description of the separation of the two bodies (Johnson, 1987, § 4.1).



## 2.2.5 Hertzian analysis for solids of revolution (The "Hertz-Huber" Analysis)

Two elastic bodies ( $i = 1, 2$ ) in contact are solids of revolution if  $R'_1 = R''_1 = R_1$  and  $R'_2 = R''_2 = R_2$  where  $R_i$  are the significant radii of curvature. The relative radius of curvature  $R_r$  is defined as  $1/R_r = (1/R_1) + (1/R_2)$  (Johnson, 1987, § 4.1 & 4.2a). The two bodies therefore possess spherical surfaces of radii  $R_1$  and  $R_2$  in the unloaded condition. The loaded contact area is consequently circular with radius  $a$  given

$$a^3 = \frac{3FR_r}{4E^*} = \frac{3FR_1R_2}{4(R_1+R_2)} \left[ \frac{(1-\nu_1^2)}{E_1} + \frac{(1-\nu_2^2)}{E_2} \right] \quad (9)$$

where  $E_i$  are Young's moduli of the bodies (Hertz, 1882a,b, 1896; Huber, 1904; Johnson, 1987, eqn. 4.22). Due to the axi-symmetric nature of the analysis, the contact surface normal stress distribution can be rewritten using cylindrical coordinates ( $r, \vartheta, z$ ) as (Johnson, 1987, eqn. 3.39; cf. eqn. 8 above)

$$[\sigma_{zz}(r)]_{z=0} = -\frac{3F}{2\pi a^2} \sqrt{1-r^2/a^2} = -\sigma_0 \sqrt{1-r^2/a^2} \quad (10)$$

Moreover, the stress components in the RZ plane excluding the z-axis and the contact surface ( $r \neq 0, z \neq 0$ , refer Figure 2.1) are written following Huber<sup>1</sup> (1904, eqn. 10,13,15,16) and Fuchs (1913, eqn. I-VI) as (see also Love, 1929, § 5.5; Lundberg & Sjövall<sup>2</sup>, 1958; Rumpf & Schönert, 1972; Zeng *et al.*, 1992; Hills *et al.*, 1993, § 7.2; Warren *et al.*, 1994)

$$\begin{aligned} \frac{\sigma_{rr}}{\sigma_0} &= \frac{1-2\nu}{3} \frac{a^2}{r^2} \left[ 1 - \left( \frac{z}{\sqrt{u}} \right)^3 \right] + \left( \frac{z}{\sqrt{u}} \right)^3 \frac{a^2 u}{u^2 + a^2 z^2} + \frac{z}{\sqrt{u}} \left[ \frac{(1-\nu)u}{a^2 + u} + (1+\nu) \frac{\sqrt{u}}{a} \arctan \left( \frac{a}{\sqrt{u}} \right) - 2 \right] \\ \frac{\sigma_{\vartheta\vartheta}}{\sigma_0} &= -\frac{1-2\nu}{3} \frac{a^2}{r^2} \left[ 1 - \left( \frac{z}{\sqrt{u}} \right)^3 \right] - \frac{z}{\sqrt{u}} \left[ 2\nu + \frac{(1-\nu)u}{a^2 + u} - (1+\nu) \frac{\sqrt{u}}{a} \arctan \left( \frac{a}{\sqrt{u}} \right) \right] \end{aligned} \quad (12)$$

<sup>1</sup> N.B. eqn. 10 of Huber (1904) and eqn. I of Fuchs (1913) for  $\sigma_{xx}$  in the YZ plane (equivalent to  $\sigma_{\vartheta\vartheta}$  in the RZ plane) contains an error in the second term, where  $(1+\nu)$  should be replaced by  $(1-\nu)$  (see also Love, 1929, § 5.5).

<sup>2</sup> N.B. although in different algebraic form the expression for  $\sigma_{rr}$  in the RZ plane given by Lundberg & Sjövall (1958) and, later, by Zeng *et al.* (1992) is equivalent to eqn. 10 of Huber (1904) for  $\sigma_{yy}$  in the YZ plane.

$$\frac{\sigma_{zz}}{\sigma_0} = - \left( \frac{z}{\sqrt{u}} \right)^3 \frac{a^2 u}{u^2 + a^2 z^2} \quad (13)$$

$$\frac{\tau_{rz}}{\sigma_0} = \frac{r z^2}{u^2 + a^2 z^2} \frac{a^2 \sqrt{u}}{a^2 + u} \quad \tau_{r\theta} = \tau_{z\theta} = 0 \quad (14)$$

where  $u$  is given (Huber, 1904, eqn. 2)

$$2u = r^2 + z^2 - a^2 + \sqrt{(r^2 + z^2 - a^2)^2 + 4a^2 z^2} \quad (15)$$

Along the  $z$ -axis ( $r = 0$ )  $u = z^2$ . At the contact surface, inside and on the periphery of the loaded circle ( $z = 0$ ,  $r \leq a$ )  $u = 0$ , while outside the loaded circle ( $z = 0$ ,  $r > a$ )  $u = (r^2 - a^2)$ . Therefore, along the  $z$ -axis, and at the contact surface, direct substitution for  $r$ ,  $z$  and  $u$  into eqn. 11-14 leads to indeterminate solutions. Consequently, the stress components along the  $z$ -axis and at the contact surface are obtained following Huber (1904) by taking limits employing Taylor expansion series. Accordingly, along the  $z$ -axis excluding the origin ( $r = 0$ ,  $z \neq 0$ ) the stress components are written following Huber (1904, eqn. 17) as

$$\frac{\sigma_{rr}}{\sigma_0} = \frac{\sigma_{\theta\theta}}{\sigma_0} = - (1+\nu) \left[ 1 - \frac{z}{a} \arctan \left( \frac{a}{z} \right) \right] + \frac{a^2}{2(a^2 + z^2)} \quad (16)$$

$$\frac{\sigma_{zz}}{\sigma_0} = - \frac{a^2}{a^2 + z^2} \quad \tau_{rz} = \tau_{r\theta} = \tau_{z\theta} = 0 \quad (17)$$

Similarly, the stress components at the contact surface, inside and on the periphery of the loaded circle, excluding the origin ( $0 < r \leq a$ ,  $z = 0$ ) are written (Huber, 1904, eqn. 18) as

$$\frac{\sigma_{rr}}{\sigma_0} = \frac{1-2\nu}{3} \frac{a^2}{r^2} \left( 1 - \left( \frac{\sqrt{a^2 - r^2}}{a} \right)^3 \right) - \frac{\sqrt{a^2 - r^2}}{a} \quad (18)$$

$$\frac{\sigma_{\theta\theta}}{\sigma_0} = - \frac{1-2\nu}{3} \frac{a^2}{r^2} \left( 1 - \left( \frac{\sqrt{a^2 - r^2}}{a} \right)^3 \right) - \frac{2\nu \sqrt{a^2 - r^2}}{a} \quad (19)$$

$$\frac{\sigma_{zz}}{\sigma_0} = -\frac{\sqrt{a^2 - r^2}}{a} \quad \tau_{rz} = \tau_{r\theta} = \tau_{z\theta} = 0 \quad (20)$$

Also, the stress components, at the plane-projected contact surface outside the loaded circle ( $r > a$ ,  $z = 0$ ) are written (Huber, 1904, eqn. 19) as

$$\frac{\sigma_{rr}}{\sigma_0} = -\frac{\sigma_{\theta\theta}}{\sigma_0} = \frac{1-2\nu}{3} \frac{a^2}{r^2} \quad \sigma_{zz} = 0 \quad \tau_{rz} = \tau_{r\theta} = \tau_{z\theta} = 0 \quad (21)$$

Finally, the stress components at the origin are written following Huber (1904, eqn. III) as

$$\frac{\sigma_{rr}}{\sigma_0} = \frac{\sigma_{\theta\theta}}{\sigma_0} = -\frac{1+2\nu}{2} \quad \frac{\sigma_{zz}}{\sigma_0} = -1 \quad \tau_{rz} = \tau_{r\theta} = \tau_{z\theta} = 0 \quad (22)$$

The radial stress  $\sigma_{rr}$  attains a maximum tensile value at the edge of the contact circle ( $r = a$ ,  $z = 0$ ), reaching a magnitude of  $(1-2\nu)\sigma_0/3$ . At the contact surface, inside and on the periphery of the loaded circle ( $r \leq a$ )  $\tau_{rz} \equiv 0$  (frictionless) while outside the loaded circle and along the  $z$ -axis  $\tau_{rz}$  vanishes implying  $\sigma_{rr}$ ,  $\sigma_{\theta\theta}$  and  $\sigma_{zz}$  to be principal stresses at those locations. The stress components along the  $z$ -axis and at the contact surface presented above are identical to those given in Johnson (1987, eqn. 3.43-3.45) and Hills *et al.* (1993, eqn. 7.71-7.79). The Hertzian stress analysis can be reliably applied if contact strains are small (i.e. if  $a \ll R_r$  or  $a/R_r < 0.2$ ) (Yoffe, 1984).

The above equations for stress components are now applied to plot the Hertzian stress distribution at the contact of two solids of revolution. The stress components have been translated into principal stresses and maximum shear stress ( $\tau_{\max}$ ) using the relations given in section 2.2.1. Contour plots of the principal stresses and  $\tau_{\max}$  are shown in Figures 2.4a-d calculated for the elastic parameters of quartz ( $\nu = 0.077$ ) and normalised with respect to  $\sigma_0 = 3F/2\pi a^2$ . The contour plots have been constructed using a uniformly spaced 51x51 data grid. Figure 2.4a illustrates the single tensile maximum of  $\sigma_1$  at the edge of the contact circle while Figure 2.4c demonstrates that  $\sigma_3$  remains compressive. Note that  $\sigma_3$  does exceed  $\sigma_2$  in a shallow region below the free surface. The contour plot of  $\tau_{\max}$  (Figure 2.4d) exhibits a single maximum along the  $z$ -axis just beneath the contact.

**Figure 2.4a-d (next two pages).** Contourplots of the principal stresses and the maximum shear stress ( $\tau_{\max}$ ) computed from the Hertzian analysis for the stress distribution at the contact of two solids of revolution. Calculations performed for the Poisson's ratio of quartz ( $\nu = 0.077$ ) and normalised with respect to  $\sigma_0 = 3F / (2\pi a^2)$ . At the edge of the contact circle ( $r/a = 1$ ),  $\sigma_1$  attains a single tensile maximum (a). Along the  $z$ -axis,  $\tau_{\max}$  exhibits a single maximum just beneath the contact (d). The data grid of the contourplot of  $\tau_{\max}$  (d) has been interpolated on to a 80x80 contour grid with 25 equispaced levels and further smoothed adopting a cubic spline function.

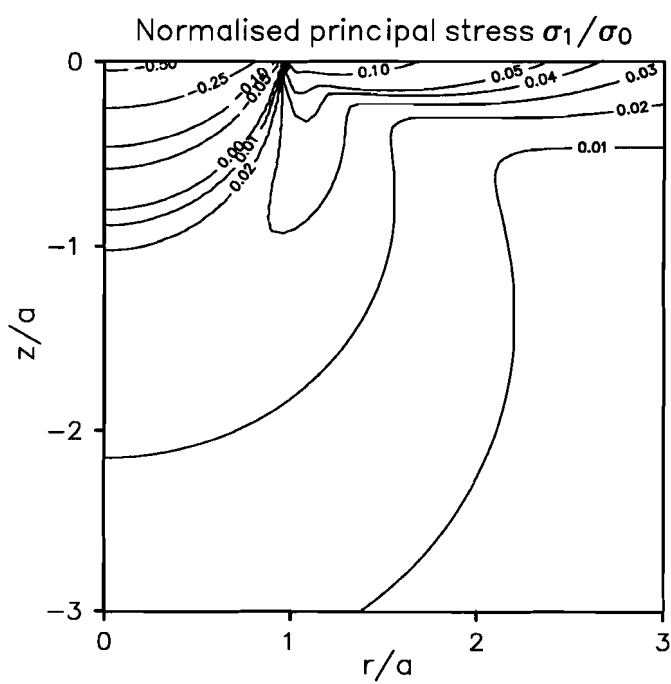


Figure 2.4a

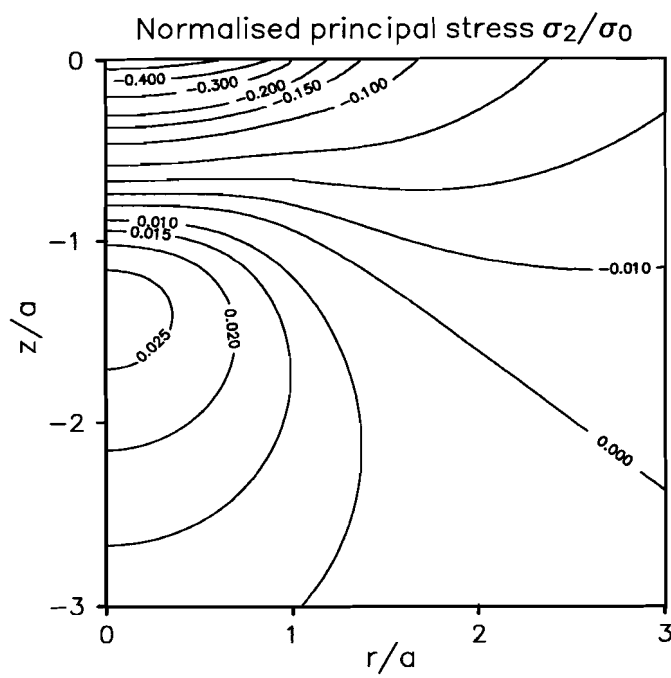


Figure 2.4b

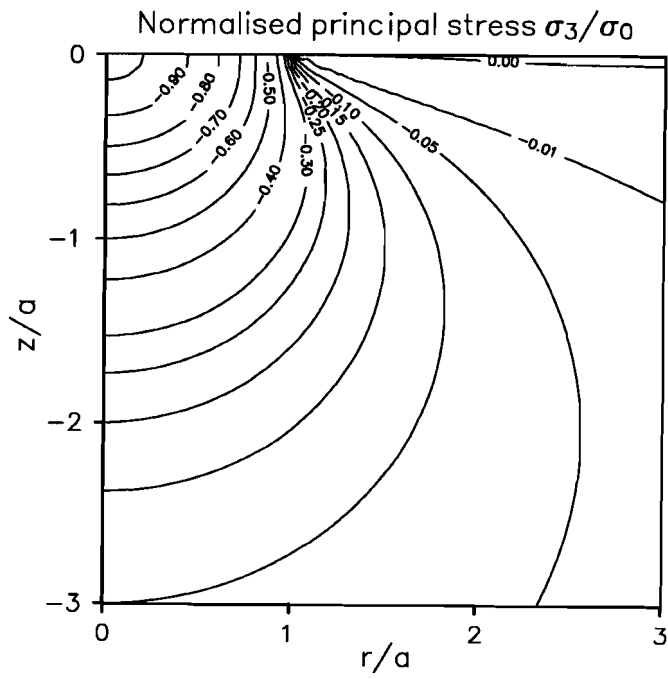


Figure 2.4c

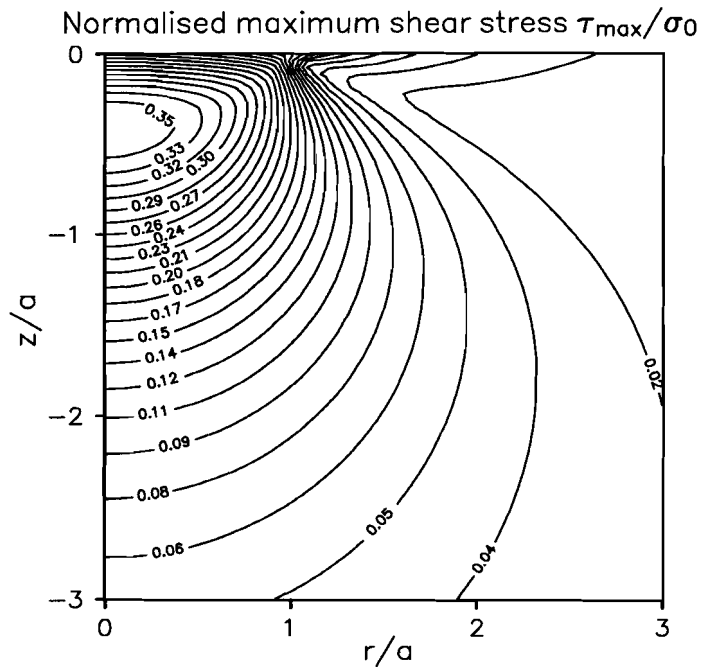


Figure 2.4d

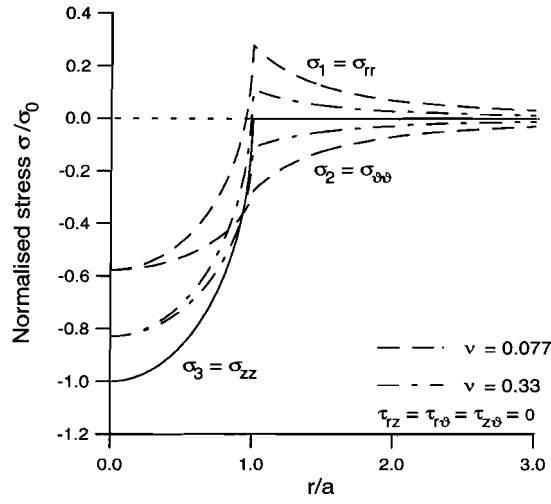


Figure 2.5a

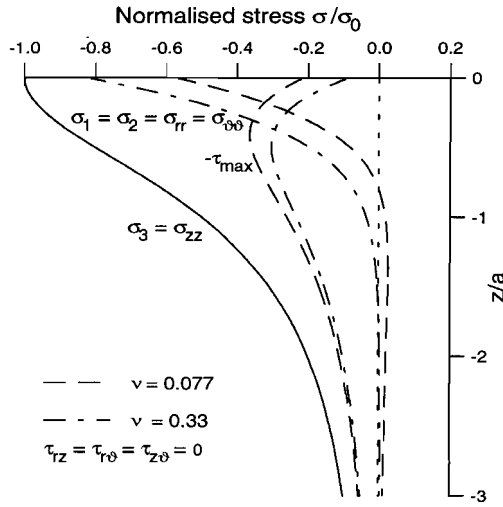


Figure 2.5b

**Figure 2.5.** Principal stresses at the contact surface (a) and along the  $z$ -axis (b), computed from the Hertzian analysis for the stress distribution at the contact of two solids of revolution. Calculations performed for different values of the Poisson's ratio  $\nu$  and normalised with respect to  $\sigma_0 = 3F / (2\pi a^2)$ . At the edge of the contact circle ( $r/a = 1$ ) (a),  $\sigma_1$  exhibits a larger tensile maximum with decreasing  $\nu$ . Along the  $z$ -axis (b), the principal stress  $\sigma_1 = \sigma_2$  exhibits a tensile maximum which is located at decreasing depth  $z$  and which intensifies with decreasing  $\nu$ , before asymptotically approaching zero. Just beneath the contact, the maximum shear stress ( $\tau_{\max}$ ) attains a single maximum which is intensified with decreasing  $\nu$ .

The contour plots of the principal stresses compare closely with those obtained by Lawn (1968), Gildemeister (1976), Mouginot & Maugis (1985) and Zeng *et al.* (1992).

Figures 2.5a&b show similarly normalised principal stresses and  $\tau_{\max}$  for different values of  $v$  at the contact surface and along the  $z$ -axis. At the edge of the contact circle,  $\sigma_{rr}$  exhibits a larger tensile maximum with decreasing  $v$ . Along the  $z$ -axis,  $\sigma_{rr} = \sigma_{\theta\theta}$  exhibits a tensile maximum which is located at decreasing depth  $z$  and which intensifies with decreasing  $v$ , before asymptotically approaching zero (see also Morton & Close, 1922). Comparing Figures 2.5a&b, it should be noted that for constant  $v$  the maximum value of  $\tau_{\max}$  along the  $z$ -axis is larger than the maximum (tensile) value of  $\sigma_{rr}$  at the edge of the contact circle.

The Hertzian stress components at the contact surface outside the loaded circle are identical to the stress components at the boundary outside the origin obtained for the Boussinesq problem for a concentrated load acting on an elastic half-space. Moreover, in the limiting case when  $a$  approaches zero, the Hertz solution passes entirely into the Boussinesq solution, implying the Hertz-Huber solution to be a valid near-field and the Boussinesq solution to be a valid far-field stress description (Gildemeister, 1976; Stieβ, 1976; Baudendistel, 1981).

Trajectories of the principal stresses within the solid are shown by e.g. Fuchs (1913), Lawn (1968), Rumpf & Schönert (1972) and Gildemeister (1976). They strongly resemble the trajectories of the Boussinesq stress field due a concentrated load shown by e.g. Lawn (1993).

## 2.2.6 Diametric loading of a sphere by point loads

Sternberg & Rosenthal (1952) and later, independently, Lurje (1963) (see Stieβ, 1976) obtained an analytic solution in polynomial form for the stress distribution in an elastic sphere with radius  $R$  under two equal oppositely directed concentrated loads  $F$  applied at the end-points of a diameter aligned parallel to the  $z$ -axis. Body forces were assumed negligible. In this section, attention will be restricted to the solution by Sternberg & Rosenthal (1952). That by Lurje (1963) yields a closely similar stress distribution (see Stieβ, 1976).

The solution by Sternberg & Rosenthal (1952) is based on the torsionless axisymmetric Boussinesq stress function approach for a frictionless concentrated load acting normal to the solid surface of an elastic half-space (see section 2.2.2). The final solution  $[S]$  gives the stress tensor field (the stress components) inside and on the surface of the sphere in spherical coordinates. Note that the spherical reference system  $(r, \gamma, \vartheta)$  used by Sternberg & Rosenthal (1952) has been redefined in this study as  $(\rho, \vartheta, \psi)$  (see Figure 2.1). The final solution  $[S]$  consists of the sum of two solutions denoted by  $[\bar{S}_2]$  and  $[R_2]$  as explained below.

The solution  $[\bar{S}_2]$  essentially represents the superposition of two Boussinesq solutions with oppositely directed concentrated (point) loads. Sternberg & Rosenthal (1952) give expressions in closed form for the stress components arising from the

solution  $[\bar{S}_2]$  using "dipolar" coordinates  $(\alpha, \beta, \gamma)$  (see Figure 2.1). [This coordinate system is described in detail by Sternberg & Sadowsky (1952).] The stress components given by Sternberg & Rosenthal (1952) for the  $[\bar{S}_2]$  solution are expressed in terms of trigonometric and hyperbolic functions of  $\psi$ ,  $\alpha$  and  $\beta$ . Of particular importance is that, along the z-axis (where  $\beta = \pi$  and  $\alpha = \pm \infty$ ), Sternberg & Rosenthal's function  $\bar{q} = \sinh \alpha$  can be written as  $-2Rp/(R^2 - \rho^2)$ ; moreover, the function  $p = \cos \beta = -1$  and the function  $\bar{p} = \sin \beta = 0$ . Due to the latter two conditions the stress components  $\sigma_\beta$ ,  $\sigma_\gamma$  and  $\tau_{\alpha\beta}$  given by the solution  $[\bar{S}_2]$  form singularities along the z-axis. The solution  $[R_2]$  is a superposed stress field which removes surface tractions artificially introduced due to  $[\bar{S}_2]$  and is presented by Sternberg & Rosenthal (1952) as a series solution containing Legendre polynomial functions  $P_n$  of negative degree (see Sternberg *et al.*, 1952; Abramowitz & Stegun, 1972, eqn. 8.21).

To illustrate the nature of the stress distribution in a sphere loaded diametrically by two oppositely directed point loads, stress components have been computed in the meridional XZ plane adopting the final solution  $[S]$  from Sternberg & Rosenthal (1952). Spherical coordinates are used (see Figure 2.1). Stress components and principal stresses at the surface of the sphere, along the unloaded x-axis (in the equatorial plane) and along a conical section (constant  $\psi$ ) are depicted in Figures 2.6-2.7 normalised with respect to  $\sigma_m = F/\pi R^2$ . Stress components are presented as symbolled lines; principal stresses as plain or dashed lines.

At the surface of the sphere ( $\rho = R$ ) (Figure 2.6), both the radial stress  $\sigma_{\rho\rho}$  and the shear stress  $\tau_{\rho\psi}$  vanish satisfying the free boundary condition; the other (normal) components are therefore principal stresses. Figure 2.6 illustrates that  $\sigma_{\theta\theta}$  reaches a (local) tensile maximum of  $\xi_s \sigma_m$  at the surface of the sphere. The location of the maximum in terms of the angle  $\psi$  depends on  $\nu$ :  $\xi_s \sim 0.79$  at  $\psi \sim 17^\circ$  for  $\nu = 0.48$ , and  $\xi_s \sim 0.33$  at  $\psi = 90^\circ$  for  $\nu = 0.077$  (quartz). Towards the loading point ( $\psi = 0^\circ$ ),  $\sigma_{\theta\theta}$  approaches  $-\infty$ . At the surface of the sphere,  $\sigma_{\psi\psi}$  becomes tensile at an increasing angle  $\psi$  with decreasing values of  $\nu$ , approaching  $+\infty$  towards the loading point ( $\psi = 0^\circ$ ). The singular behaviour of  $\sigma_{\theta\theta}$  and  $\sigma_{\psi\psi}$  corresponds to that demonstrated at the solid surface of an elastic half-space (towards the origin) by the Boussinesq solution for a concentrated load (see Figure 2.2a). The tensile singularity in  $\sigma_{\psi\psi}$  corresponds, when loading occurs over a finite area, to the maximum tensile stress  $\sigma_{rr}$  at the edge of the contact circle obtained with the Hertz-Huber analysis (Stieβ, 1976; see also Figure 2.5a). The stress components depicted in Figure 2.6 are identical to the results obtained by Stieβ (1976) using the solution due to Lurje (1963).

The stresses close to the z-axis become increasingly affected by the above-mentioned z-axis singularities in  $\sigma_\beta$ ,  $\sigma_\gamma$  and  $\tau_{\alpha\beta}$ , with increasing  $\nu$ . The computed stresses remain only regular and continuous beyond a considerable distance from the z-axis ( $x/R \approx 0.01 - 0.04$  dependent on  $\nu$ ).



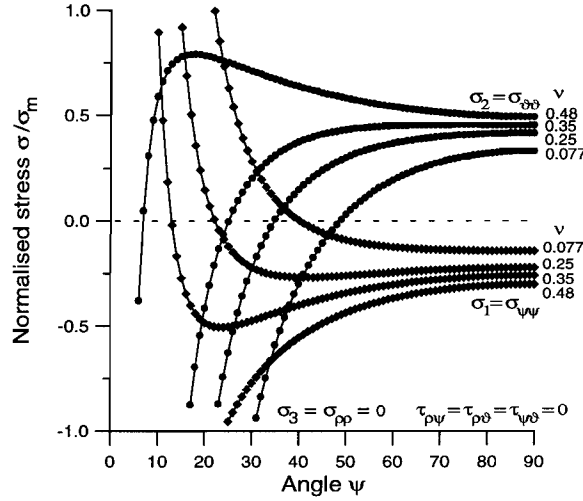


**Figure 2.6.** Principal stresses at the surface of a sphere loaded diametrically by two oppositely directed point loads. The stresses have been computed adopting the solution by Sternberg & Rosenthal (1952), for different values of the Poisson's ratio  $\nu$  and normalised with respect to  $\sigma_m = F / \pi R^2$ . The principal stress  $\sigma_2 = \sigma_{\theta\theta}$  reaches a larger tensile maximum with increasing  $\nu$ . Towards the loading point ( $\psi = 0^\circ$ ),  $\sigma_1$  and  $\sigma_2$  exhibit intensified singular behaviour with increasing  $\nu$ .

For this reason, stresses in the equatorial plane ( $\psi = \pi/2$ ) computed for  $x/R \geq 0.04$  are depicted in Figure 2.7a. Towards the centre of the sphere  $\sigma_{\rho\rho}$  and  $\sigma_{\theta\theta}$  become equal (a requirement for axi-symmetry) and reach an extrapolated (local) tensile maximum of  $\xi_e \sigma_m$  at the centre of the sphere. Replotting for different values of  $\nu$  shows that  $\xi_e$  increases slightly with decreasing  $\nu$ :  $\xi_e \sim 0.56$  for  $\nu = 0.48$  and  $\xi_e \sim 0.71$  for  $\nu = 0.077$ .

Similarly, stresses along a conical section ( $\psi = 6^\circ$ ) computed for  $\rho/R \geq 0.1$  ( $x/R \geq 0.01$ ) are shown in Figure 2.7b. Towards the free surface of the sphere (i.e. close to the contact point),  $\sigma_{\psi\psi}$  rises steeply from a large compressive to a finite tensile value, just before reaching the surface of the sphere. Plots drawn for different values of  $\nu \leq 0.4$  show that the sudden rise of  $\sigma_{\psi\psi}$  becomes more pronounced with decreasing  $\nu$ , and that its finite tensile value at the surface of the sphere increases towards a singularity at the contact point ( $\psi = 0^\circ$ ) (Stieß, 1976; see also Figure 2.6). Moreover, close to the free surface of the sphere,  $\sigma_1$  remains tensile and becomes equal to  $\sigma_{\psi\psi}$ , while  $\sigma_2 = \sigma_{\theta\theta}$  sets off to compressive values. The stresses  $\sigma_3$  and  $\sigma_{\rho\rho}$  tend to a large compressive maximum value but become zero at the free surface of the sphere.

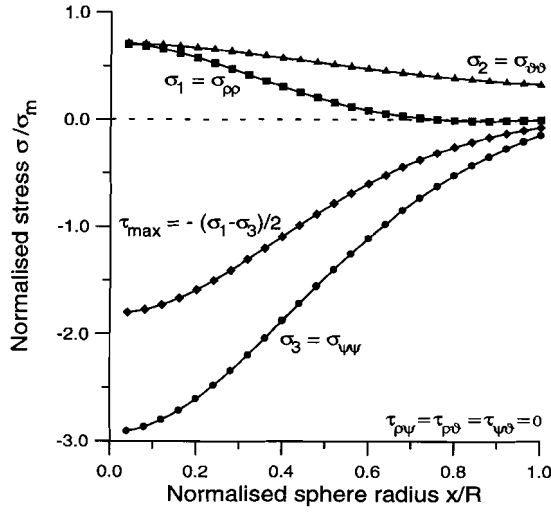


Figure 2.7a

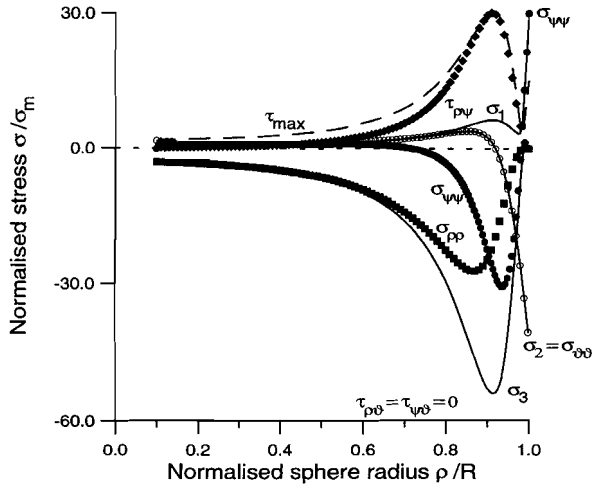


Figure 2.7b

**Figure 2.7.** Stresses along the unloaded  $x$ -axis (equatorial plane,  $x/R \geq 0.04$ ) (a) and along a conical section ( $\psi = 6^\circ$ ,  $\rho/R \geq 0.1$ ) (b) of a sphere loaded diametrically by two oppositely directed point loads. The stresses have been computed adopting the solution by Sternberg & Rosenthal (1952), for the Poisson's ratio of quartz ( $\nu = 0.077$ ) and normalised with respect to  $\sigma_m = F / \pi R^2$ . Along the  $x$ -axis (a), towards the centre of the sphere, the principal stresses  $\sigma_1$  and  $\sigma_2$  become equal and reach a tensile maximum. Along the conical section (b), towards the free surface of the sphere,  $\sigma_{\psi\psi}$  rises steeply from a large compressive to a finite tensile value, just before reaching the surface of the sphere.

Contour plots of the principal stresses and the maximum shear stress ( $\tau_{\max}$ ) within and at the free surface of the sphere constructed employing the methods outlined in section 2.2.5 are depicted in Figures 2.8a-d. They can be favourably compared with results obtained by Stieß (1976) using the solution due to Lurje (1963).

The behaviour of the normal stress components and the principal stresses in Figures 2.6, 2.7b and 2.8, within and at the free surface of the sphere towards the loading point, is comparable to that demonstrated along the z-axis and at the solid surface towards the origin by the Boussinesq solution for concentrated loading of an elastic half-space (see Figures 2.2a&b). Note that in the immediate neighbourhood of the contact point within and at the free surface of the solid the solution for the stress field offered by Sternberg & Rosenthal (1952) and by the Boussinesq solution are physically unrealistic.

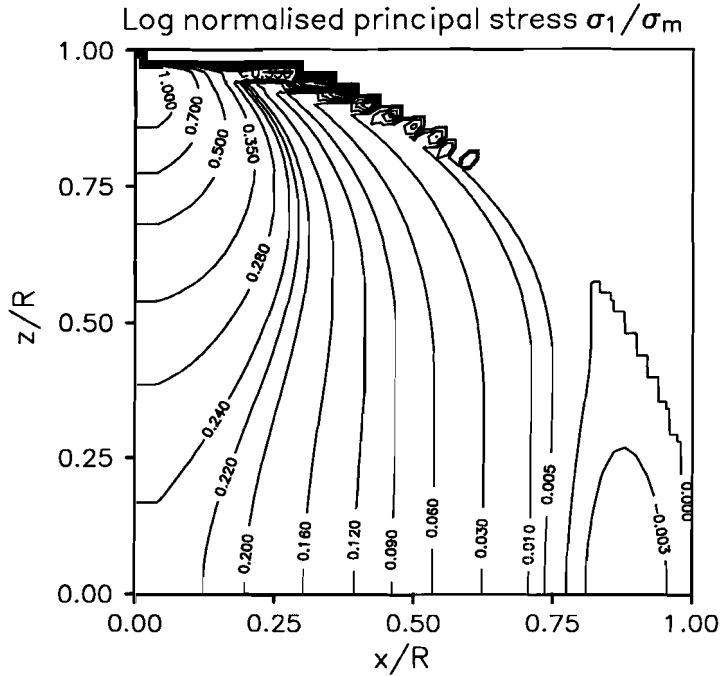


Figure 2.8a

**Figure 2.8a-d (cf. next two pages).** Contourplots of the principal stresses and the maximum shear stress ( $\tau_{\max}$ ) within and at the free surface of a sphere loaded diametrically by two oppositely directed point loads. The stresses have been computed adopting the solution by Sternberg & Rosenthal (1952), for  $x/R \geq 0.04$ , for the Poisson's ratio of quartz ( $\nu = 0.077$ ), normalised with respect to  $\sigma_m = F / \pi R^2$ , and transformed to  $\pm \log_{10}(\pm \sigma / \sigma_m + 1)$  dependent on the sign of  $\sigma$ .

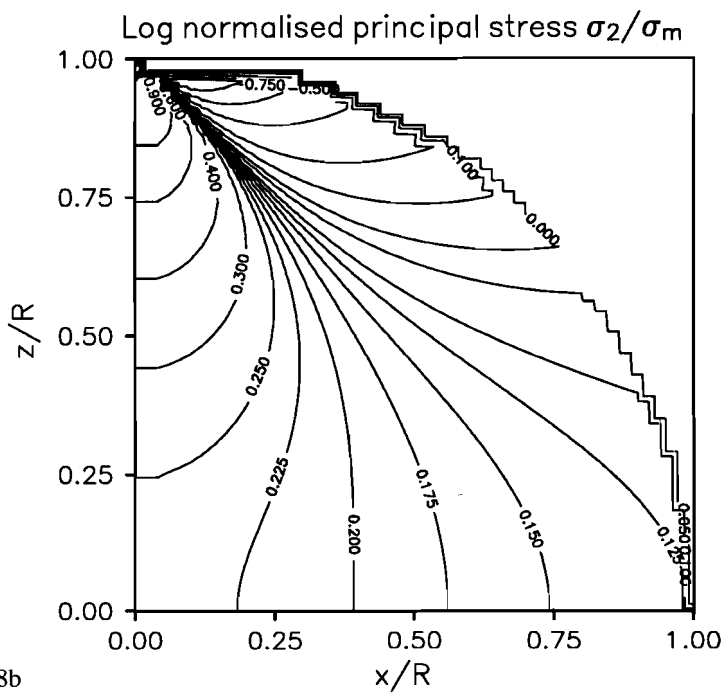


Figure 2.8b

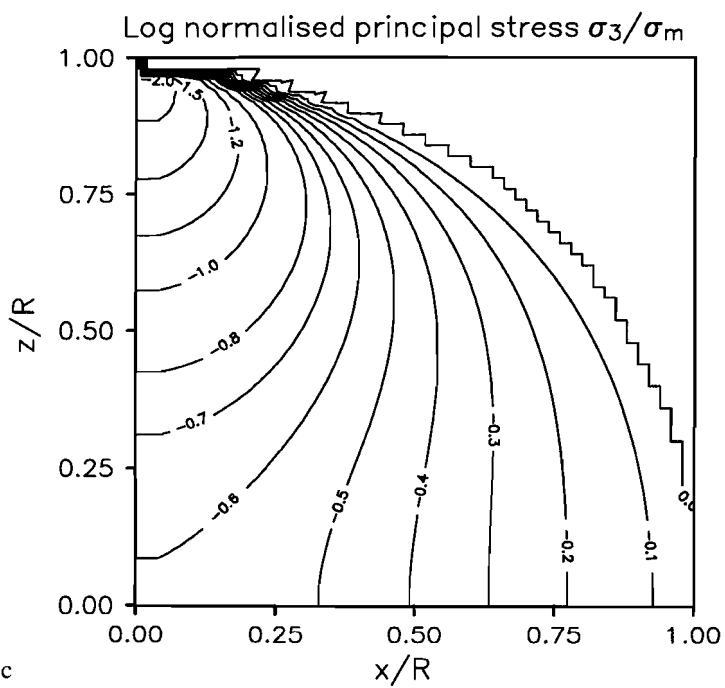


Figure 2.8c

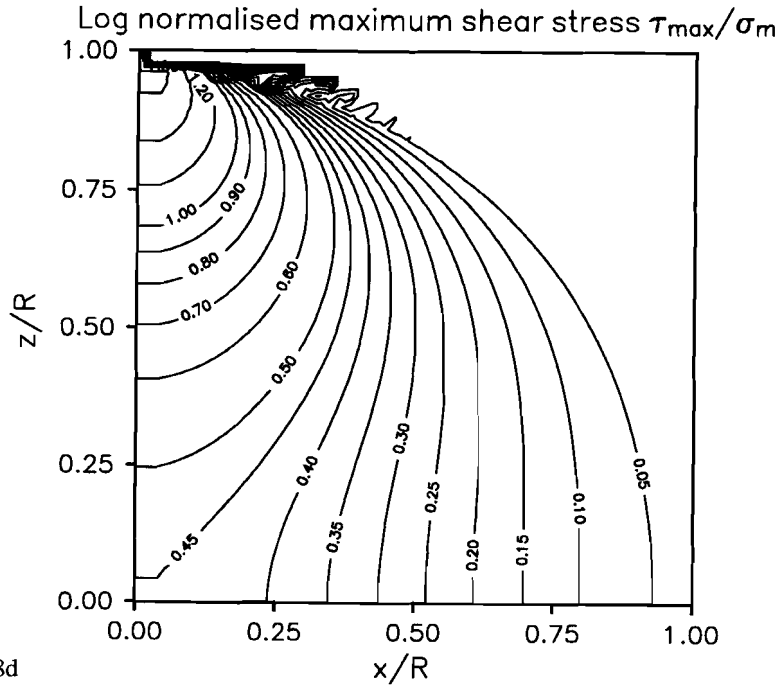


Figure 2.8d

### 2.2.7 Diametric uniformly distributed loading of a sphere

Hiramatsu & Oka (1966) have obtained a solution for the torsionless axi-symmetric stress distribution in an elastic sphere with radius  $R$  subjected to a radially directed frictionless normal pressure ( $p$ ) uniformly distributed over two diametrically opposite spherical caps of angular width  $\psi_0$ . The pressure  $p$  acts on a spherical cap of area  $A = 2\pi R^2(1 - \cos\psi_0)$ . However, if the height of the cap is assumed negligibly small the pressure can be considered to act on a small circle with radius  $a$  and plane area  $A \approx \pi a^2 = \pi R^2 \sin^2\psi_0$ . Note that the spherical reference system  $(r, \phi, \vartheta)$  used by Hiramatsu & Oka (1966) has been redefined in this study as  $(\rho, \vartheta, \psi)$  (refer Figure 2.1). The stress components are given by Hiramatsu & Oka (1966) in terms of summation series containing Legendre polynomial functions  $P_n$  (see also Oka & Majima, 1970; Wijk, 1978; Shipway & Hutchings, 1993a).

Here, stress components have been computed in the meridional  $XZ$  plane for a Poisson's ratio  $\nu$  equal to 0.25 and for different values of  $\psi_0$ , employing the above-mentioned equations of Hiramatsu & Oka (1966) and making the minor corrections and simplifications identified by Shipway & Hutchings (1993a). Stress components at the surface of the sphere, along the unloaded  $x$ -axis (the equatorial plane) and along the loaded  $z$ -axis are depicted in Figures 2.9-2.11 normalised with respect to either  $p$  or  $\sigma_m = F/\pi R^2$  ( $F = pA$ ).

Stress components at the surface of the sphere ( $\rho = R$ ) are shown in Figures 2.9a&b computed for  $\psi_0 = 5.7^\circ$  ( $a/R \approx 0.1$ ). The shear stress  $\tau_{\rho\psi}$  vanishes satisfying the free boundary condition; the other (normal) stress components are therefore principal stresses. The radial stress  $\sigma_{\rho\rho}$  remains zero from the equator ( $\psi = 90^\circ$ ) to the edge of the loading cap where it exhibits intensified Gibbs vibration (see Figure 2.9a and Shipway & Hutchings, 1993a) and jumps discontinuously to  $-p$  (see Figure 2.9b). Figure 2.9a illustrates that  $\sigma_{\theta\theta}$  reaches a (local) tensile maximum at the surface of the sphere in the equatorial plane ( $\psi = 90^\circ$ ); at the edge of the loading cap  $\sigma_{\theta\theta}$  attains a finite compressive value (see Figure 2.9b). Plots redrawn for smaller  $\psi_0$  demonstrate that the magnitude of the (local) tensile maximum of  $\sigma_{\theta\theta}$  increases with decreasing  $\psi_0$  (see also Shipway & Hutchings, 1993a, their Figures 5&6). Figures 2.9a&b show that at the surface of the sphere, moving from the equator ( $\psi = 90^\circ$ ),  $\sigma_{\psi\psi}$  attains a finite tensile value close to the edge of the loading cap, before jumping discontinuously to a finite compressive value at the edge of the cap. The stress components depicted in Figure 2.9a coincide with those computed for  $\nu = 0.25$  at the surface of the sphere adopting the solution after Sternberg & Rosenthal (1952) (see Figure 2.6). The behaviour of the normal stress components demonstrated in Figure 2.9b corresponds to that of  $\sigma_{rr}$ ,  $\sigma_{\theta\theta}$  and  $\sigma_{zz}$  at the solid surface of an elastic half-space loaded by a uniform pressure over a circular area (see Figure 2.3a).

In the equatorial plane ( $\psi = \pi/2$ ) (Figure 2.10a&b),  $\sigma_{\rho\rho}$  and  $\sigma_{\theta\theta}$  become equal towards the centre of the sphere (a requirement for axi-symmetry) and reach an extrapolated (local) tensile maximum at the centre of the sphere whose magnitude, if normalised with respect to  $p$ , increases with larger  $\psi_0$  and, if normalised with respect to  $\sigma_m$ , decreases with larger  $\psi_0$ . The stress components depicted in Figure 2.10a for the smallest  $\psi_0 = 2^\circ$  more or less coincide with those computed for  $\nu = 0.25$  at the equatorial plane adopting the solution after Sternberg & Rosenthal (1952) (see Figure 2.7a).

Along the z-axis ( $\psi = 0$ ) (Figures 2.11a&b),  $\sigma_{\theta\theta}$  and  $\sigma_{\psi\psi}$  are equal (a requirement for axi-symmetry) and reach a tensile maximum which increases and is located closer to the loading cap with smaller  $\psi_0$ . Further plotting for smaller values of  $\nu$  shows that the tensile maximum of  $\sigma_{\theta\theta} = \sigma_{\psi\psi}$  increases strongly (see also Shipway & Hutchings, 1993a, their Figures 2.3&2.4). Figure 2.11b illustrates that towards the centre of the loading cap all stress components tend to  $-p$ . This behaviour is comparable with that of stress components along the z-axis in an elastic half-space obtained with the Boussinesq solution for uniform distributed loading (see Figure 2.3b).

In order to further demonstrate the similarity between the solutions after Sternberg & Rosenthal (1952) and Hiramatsu & Oka (1966), principal stresses and maximum shear stress ( $\tau_{\max}$ ) within and at the free surface of the sphere, normalised with respect to  $\sigma_m$ , have been computed for  $\nu = 0.077$  and setting  $\psi_0$  to  $1^\circ$ . The resulting contour maps constructed employing the methods outlined in section 2.2.5 are shown in Figures 2.12a-d. The contour lines of  $\tau_{\max}$  closely follow the trends of isochromatics observed in diametrically compressed photoelastic spheres or disks (Hiramatsu & Oka, 1966; Gallagher, 1987).

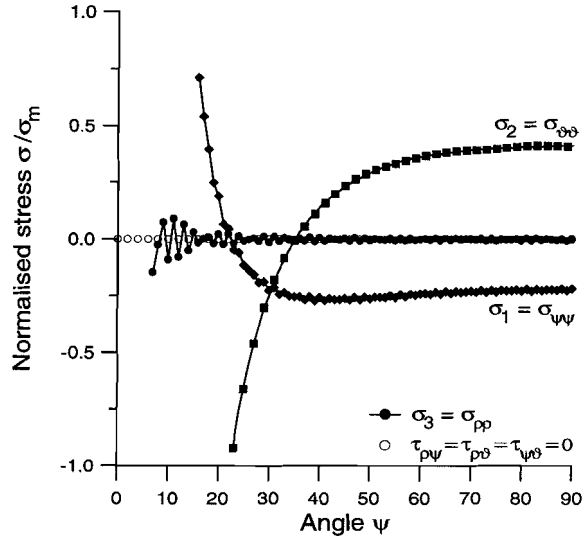


Figure 2.9a

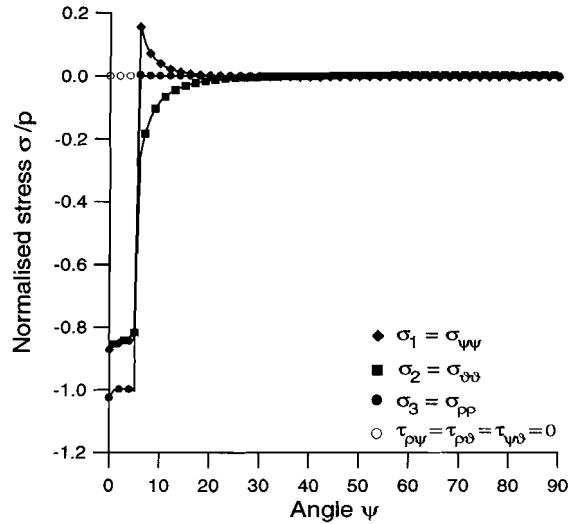


Figure 2.9b

**Figure 2.9a&b.** Principal stresses at the surface of a sphere loaded diametrically by a uniform pressure  $p$  distributed over spherical end caps. The stresses have been computed adopting the solution by Hiramatsu & Oka (1966), for a Poisson's ratio equal to 0.25, for a cap angular width  $\psi_0$  equal to  $5.7^\circ$  ( $a/R = 0.1$ ), and normalised with respect to either  $p$  or  $\sigma_m = F / \pi R^2$ . At the equator ( $\psi = 90^\circ$ ),  $\sigma_2 = \sigma_{\theta\theta}$  attains a maximum tensile value. Just before the edge of the loading cap,  $\sigma_1 = \sigma_{\psi\psi}$  reaches a tensile maximum before jumping discontinuously to a finite compressive value at the edge of the cap.

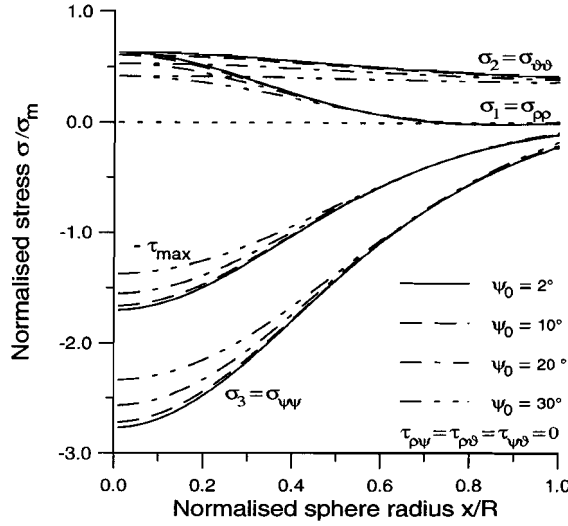


Figure 2.10a

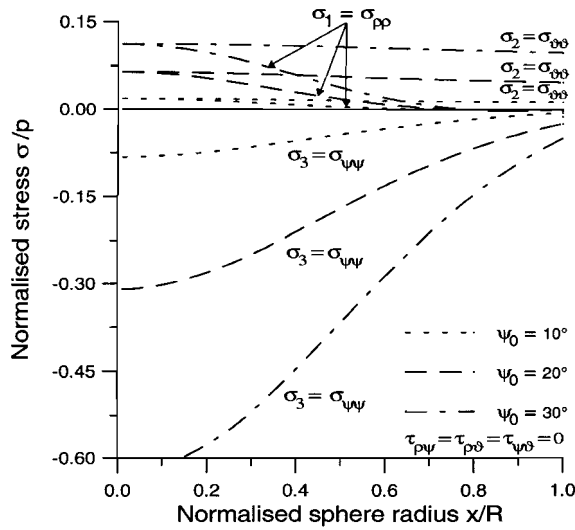


Figure 2.10b

**Figure 2.10a&b.** Principal stresses along the unloaded  $x$ -axis (equatorial plane) of a sphere loaded diametrically by a uniform pressure  $p$  distributed over spherical end caps. The stresses have been computed adopting the solution by Hiramatsu & Oka (1966), for a Poisson's ratio equal to 0.25, for different values of the cap angular width  $\psi_0$  and normalised with respect to either  $p$  or  $\sigma_m = F / \pi R^2$ . Towards the centre of the sphere,  $\sigma_1$  and  $\sigma_2$  become equal and reach a tensile maximum whose magnitude, if normalised with respect to  $p$ , increases with larger  $\psi_0$  and, if normalised with respect to  $\sigma_m$ , decreases with larger  $\psi_0$ .



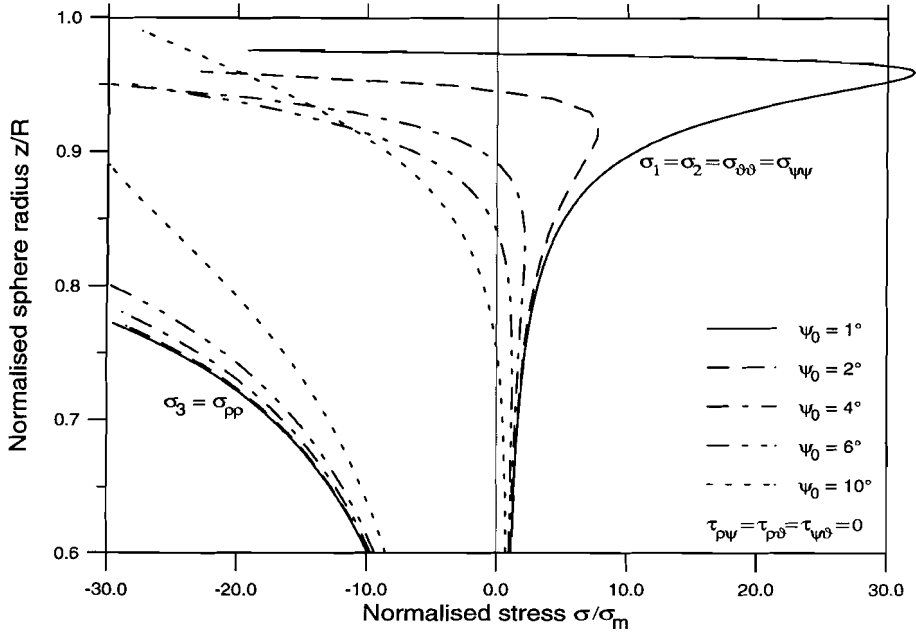


Figure 2.11a

**Figure 2.11a&b.** Principal stresses along the  $z$ -axis of a sphere loaded diametrically by a uniform pressure  $p$  distributed over spherical end caps. The stresses have been computed adopting the solution by Hiramatsu & Oka (1966), for a Poisson's ratio equal to 0.25, for different values of the cap angular width  $\psi_0$ , for  $z/R \geq 0.6$ , and normalised with respect to either  $p$  or  $\sigma_m = F / \pi R^2$ . The principal stress  $\sigma_1 = \sigma_2$  exhibits a tensile maximum which increases and is located closer to the loading cap with smaller  $\psi_0$ . Towards the centre of the loading cap all stresses tend to  $-p$ .

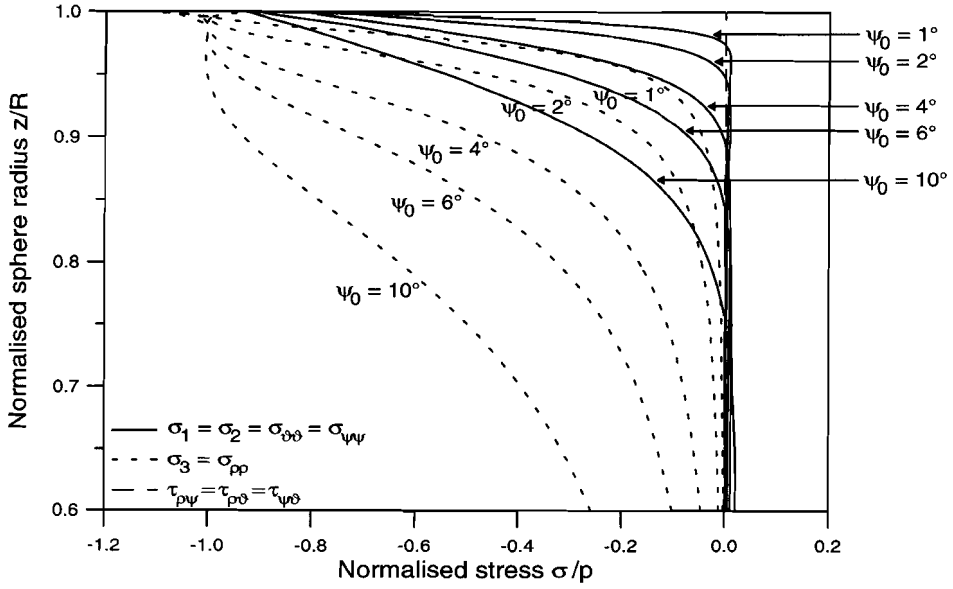


Figure 2.11b

**Figure 2.12a-d** (see next two pages). Contourplots of the principal stresses and the maximum shear stress ( $\tau_{max}$ ) within and at the free surface of a sphere loaded diametrically by a uniform pressure  $p$  distributed over spherical end caps. The stresses ( $\sigma$ ) have been computed adopting the solution by Hiramatsu & Oka (1966), for the Poisson's ratio of quartz ( $\nu = 0.077$ ), for a cap angular width  $\psi_0$  equal to  $1^\circ$ , normalised with respect to  $\sigma_m = F / \pi R^2$ , and transformed to  $\pm \log_{10}(\pm \sigma / \sigma_m + 1)$  dependent on the sign of  $\sigma$ .

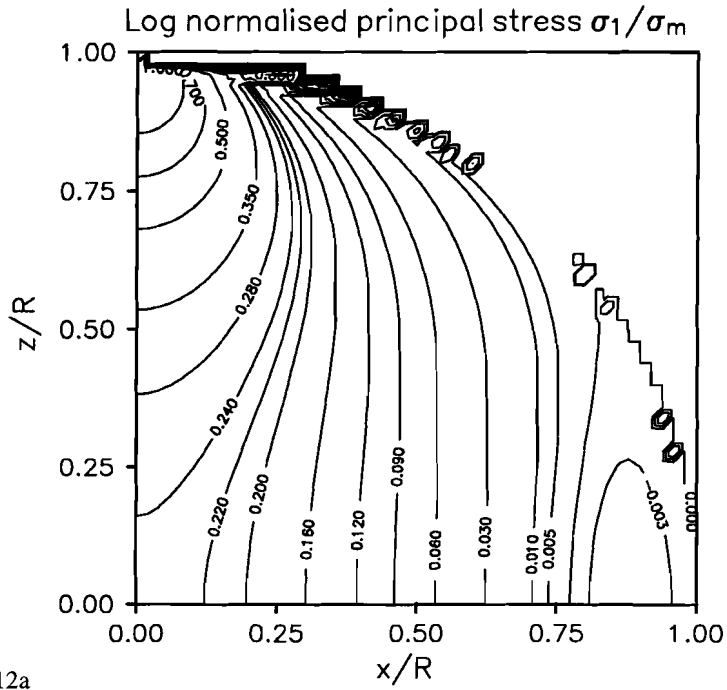


Figure 2.12a

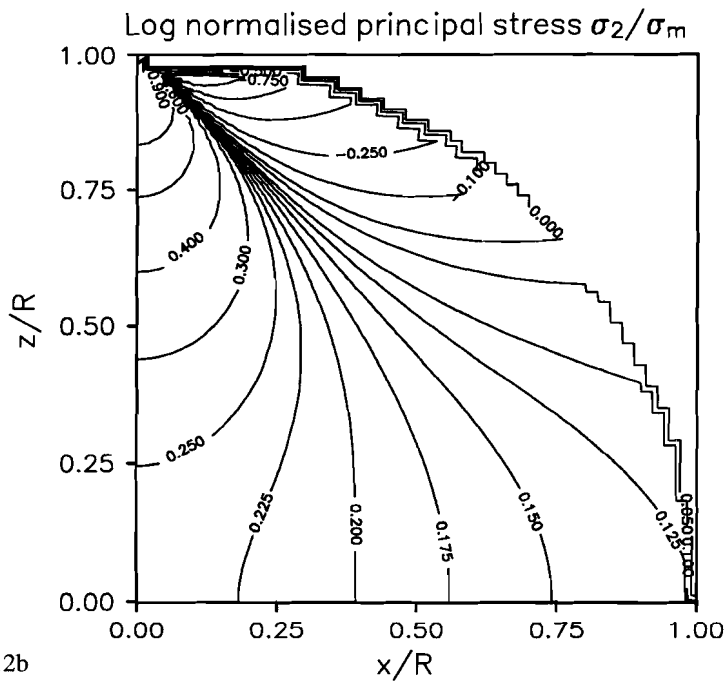


Figure 2.12b

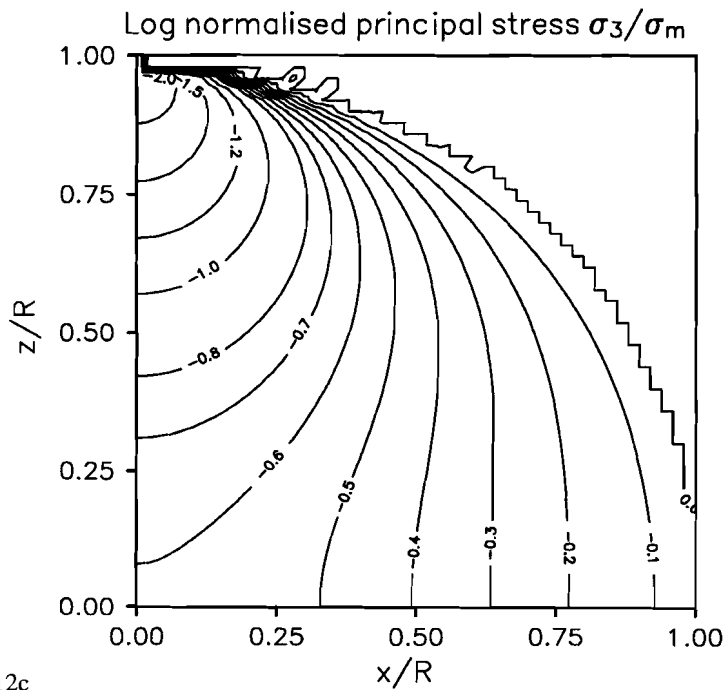


Figure 2.12c

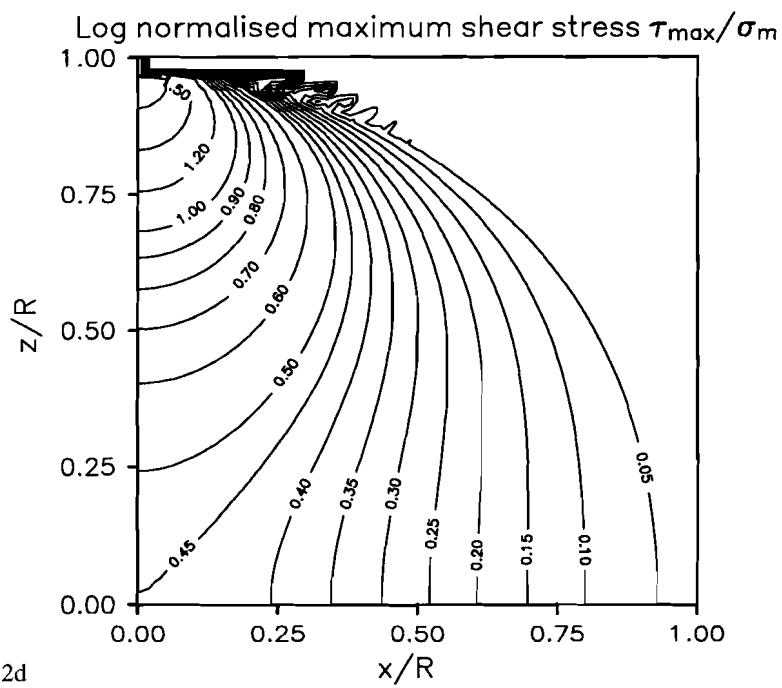


Figure 2.12d

On the basis of a similar plot as Figure 2.11a Hiramatsu & Oka (1966) and Oka & Majima (1970) suggest sphere failure to initiate along the z-axis at the tensile maximum of  $\sigma_{\vartheta\vartheta} = \sigma_{\psi\psi}$  and define the failure stress to be constant and equal to  $\xi_z \sigma_m$  where  $\xi_z \sim 0.7-0.9$  for  $\nu = 0.14-0.33$  and  $\psi_0 = 10-20^\circ$ . However, as demonstrated in Figure 2.11a, the magnitude of the maximum tensile stress ( $\xi_z \sigma_m$ ) is clearly not a constant but strongly dependent on  $\psi_0$ . Usage of this definition thus leads to a gross underestimate of the failure stress for  $\psi_0 < 10^\circ$  (Wijk, 1978; Shipway & Hutchings, 1993a).

## 2.3 STRESS DISTRIBUTIONS OBTAINED USING THE FINITE ELEMENT METHOD

Kienzler & Schmitt (1990) (see also Baudendistel, 1981 and Kienzler & Baudendistel, 1985) have performed a 2D finite element (FE) analysis of the stress distribution in a sphere compressed between two rigid plates by superposition of near-field Hertzian contact stresses and far-field stresses due to diametrically applied point forces. The latter stress field is obtained using the analysis by Lurje (1963) and is similar to that given by Sternberg & Rosenthal (1952). The FE analysis has been performed using spherical coordinates  $(r, \phi, \vartheta)$  redefined in this study as  $(\rho, \vartheta, \psi)$ . In the analysis (see Baudendistel, 1981) it has been verified that the stress components obtained from FE calculations for an elastic material show a smooth transition between the Hertz and the Lurje solution: e.g. along the z-axis,  $\sigma_{zz}$  obtained by FE method agrees closely with both analytical solutions for  $0.15 \leq z/a \leq 0.5$ . However, further along the z-axis with increasing  $z/a$  (depth) the computed  $\sigma_{xx}$  and  $\sigma_{yy}$  show a growing discrepancy compared with the Hertz solution, and can only be accurately described by the far-field Lurje solution. It has been further verified that even for large  $a/R$  ratio the contact area remains approximately planar so that the Hertz solution can be considered valid in the near-field.

Kienzler & Baudendistel (1985) (see also Kienzler & Schmitt, 1990) show contourmaps in the meridional XZ plane and 2D-plots along the z-axis of the principal stresses  $\sigma_1$  and  $\sigma_2 = \sigma_{\vartheta\vartheta}$ , and of the differential stress  $(\sigma_1 - \sigma_3)$ . The stresses have been obtained from FE calculations for elastic, non-linear elastic, viscoelastic, non-linear viscoelastic-plastic and elastic-plastic materials when flattening of the sphere is small ( $\delta/R = 0.0325$ , where  $\delta$  is the Hertzian elastic distortion). Focusing on the results for an elastic material, Kienzler & Baudendistel (1985) show that the circumferential stress  $\sigma_{\vartheta\vartheta}$  at the free surface of the sphere remains tensile from the equator to just outside the contact circle where  $\sigma_{\vartheta\vartheta}$  becomes compressive. The meridional stress  $\sigma_{\psi\psi}$  at the free surface becomes maximum tensile just outside the contact circle and subsequently compressive under the area of contact. With increasing  $a/R$  ratio, the magnitude of the maximum tensile meridional stress  $\sigma_{\psi\psi}$  at the contact edge decreases (Baudendistel, 1981). The radial stress  $\sigma_{\rho\rho}$  at the free surface vanishes satisfying the corresponding boundary condition. The described trend of the stress components at the free surface

of the sphere, for an elastic material, is closely similar to that demonstrated by the stress components at the contact of spherical surfaces as prescribed by the Hertzian analysis for solids of revolution (refer section 2.2.5 and Figure 2.5a). The trend is also similar to that demonstrated by the stress components at the free surface of a sphere subjected either to diametric point loading (refer section 2.2.6 and Figure 2.6) or to diametric uniformly distributed loading (refer section 2.2.7 and Figure 2.9).

## 2.4 EXPERIMENTAL OBSERVATIONS AND COMPARISON WITH THEORY

### 2.4.1 Experimental observations

Numerous investigators have performed compression tests on spheres or grains of different material (glass, perspex, single-crystal quartz sand or sapphire) loaded diametrically until failure between either platens of different material (steel, alloy, glass, ceramic) or glass spheres and at various temperatures in the range  $-196$  to  $22\text{ }^{\circ}\text{C}$  (e.g. Rumpf *et al.*, 1967; Rumpf & Schönert, 1972; Stieß, 1976; Gallagher, 1976, 1987; Shipway & Hutchings, 1993b). The configuration and the nomenclature of the cracks typically observed are illustrated in Figure 2.13.

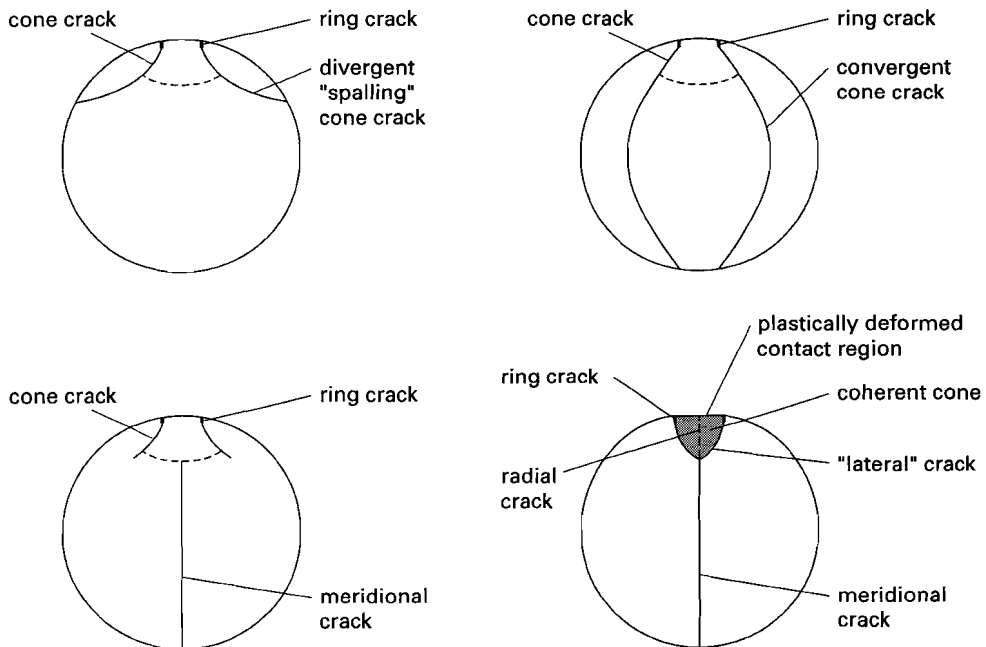


**Figure 2.13.** Nomenclature and configuration of the cracks typically observed in compression tests on spheres.

First, the Karlsruhe-Freiburg group (Rumpf *et al.*, 1967; Rumpf & Schönert, 1972; Stieß, 1976; see also Kienzler & Baudendistel, 1985; Kienzler, 1985; Kienzler & Schmitt, 1990) have shown that glass spheres with a diameter  $\geq 80 \mu\text{m}$  compressed at  $22^\circ\text{C}$  exhibited shallow ring cracks near the contact circle passing into cone cracks. At low compression rates ( $\leq 0.1 \text{ mm/min}$ ) the cone cracks evolved into divergent ("spalling") cone cracks running to the free surface. At high compression rates ( $\geq 0.5 \text{ mm/min}$ ) the cone cracks either proceeded as convergent cone cracks (onion peels) or gave rise to subsequent meridional cracks splitting the spheres in orange segment shaped fragments. Glass spheres with a diameter  $\leq 25 \mu\text{m}$  compressed at  $22^\circ\text{C}$  showed in addition to ring cracks plastically deformed contact regions, "lateral" cracks giving rise to coherent cones, and radial cracks evolving into meridional cracks. Failed perspex spheres generally exhibited meridional cracks; at  $-196^\circ\text{C}$  in addition to coherent cones below the contact points.

Second, Shipway & Hutchings (1993b) observed that (as-received) glass and sapphire spheres compressed between ceramic platens fractured mainly into two hemispherical fragments commonly with coherent cones below the contact points, associated with flattened contact areas and separated from the rest of the sphere by ring cracks. Glass and sapphire spheres subjected to surface abrasion and compressed between elastically and plastically deforming platens failed at significantly lower loads and exhibited no coherent cones.

Third, Gallagher (1976, 1987) found failed sand grains to exhibit crushing near contact points and fracture surfaces which possessed hourglass-like cross-sectional shapes, forming lenses or columns parallel to the loading axis. Specifically, sand grain fracture surfaces showed Wallner lines (Wallner, 1939) and crack branching related patterns such as hackles, periodic undulations and conchoidal regions.

#### 2.4.2 Comparison with theory

The above experimental observations have been compared, by the various authors, with theoretical studies of stress distributions in spheres subjected to diametric loading. On this basis, predictions have been made about type, path and time-order of the cracks developed. These comparisons are reconsidered, in the following, in the light of the computations presented in section 2.2.

Kienzler & Schmitt (1990) (see also Kienzler & Baudendistel, 1985; Kienzler, 1985) inferred that in an elastic brittle sphere (e.g. a glass or perspex sphere compressed at respectively  $22^\circ\text{C}$  and  $-196^\circ\text{C}$ ) above a critical load a tensile (mode I; Lawn, 1993) ring crack develops first at the edge of the contact circle under the action of the maximum tensile stress component  $\sigma_{\psi\psi}$ . No meridional crack forms since  $\sigma_{\theta\theta}$  is compressive at the edge of the contact circle. Note that for the purpose of comprehension and assuming the stress field to be undisturbed by the presence of the crack, the stress components driving the crack can be considered along a conical section (e.g. at  $\psi = 6^\circ$ ) as depicted in Figure 2.7b. Under low (kinetic) energy

conditions, the ring crack is thought to be halted directly beneath the surface since  $\sigma_{\psi\psi}$  becomes compressive. If sufficient energy is available the ring crack may proceed by two mechanisms dependent on the crack propagation mode. Firstly, the ring crack is envisaged to retain its direction and to follow trajectories of  $\tau_{\max}$  giving rise to a convergent cone crack. Accordingly, the ring crack is inferred to become driven by the (increasing) shear stress field; i.e. to change its propagation mode to shear (mode II). However, if the resulting cone bounded by the cone crack remains coherent and is further pressed into the sphere it acts as a wedge increasing the tensile magnitude of  $\sigma_{\theta\theta}$  inside the sphere and giving rise to (subsequent) tensile meridional cracks initiating from the mantle of the cone. Only at extreme energy levels the convergent cone crack remains propagating through the entire sphere forming "onion peel" fracture surfaces. Secondly, the ring crack is supposed to proceed in mode I and to arrive deeply enough into the sphere in order to get into the range of the tensile principal stress  $\sigma_1$  in the meridional plane. Consequently, the crack is inferred to deviate from its original orientation and to follow trajectories of  $\sigma_3$  giving rise to a divergent cone crack. Subsequently, the crack may either be halted due to a diminishing  $\sigma_1$  or be deviated even more by local inhomogeneities, running towards the free surface and evolving into a "spalling crack" splitting fragments off the sphere. Kienzler (1985) has included the presence of cracks in the FE analysis described in section 2.3. He shows that in an elastic brittle sphere with small flattening ( $\delta/R = 0.03$ ) a ring crack can only proceed while retaining his direction due to shear load which is in support of the mode II crack mechanism. Kienzler & Schmitt (1990) (see also Kienzler & Baudendistel, 1985; Kienzler, 1985) inferred that in an elastic-plastic sphere (e.g. perspex spheres compressed at 22 °C) the peak of  $\sigma_{\psi\psi}$  at the edge of the contact circle diminishes due to plastic flow and that  $\sigma_{\theta\theta}$  becomes tensile all along the free surface giving rise to a predominance of throughgoing meridional cracks.

Employing the stress solution for diametric uniformly distributed loading of a sphere (refer section 2.2.7), Shipway & Hutchings (1993b) have translated the mean critical force at failure of compressed glass and sapphire spheres, for each platen material used, into maximum values of surface tensile circumferential ( $\sigma_{\theta\theta}$ ), axial tensile ( $\sigma_{\psi\psi} = \sigma_{\theta\theta}$ ) and axial maximum shear stress ( $\tau_{\max}$ ). In case of glass spheres, the computed maximum values of axial tensile stress varied considerably between platens of different material while both the maximum values of the surface tensile and the axial maximum shear stress showed rather less variability. For sapphire spheres compressed between elastically deforming platens effectively constant maximum values of axial maximum shear stress were obtained. In addition, maximum values of the surface tensile stress calculated for abraded glass spheres were practically constant for different platen material. On this basis and considering microstructural observations Shipway & Hutchings (1993b) inferred failure of glass and sapphire spheres to initiate respectively at the surface in tensile mode (due to the maximum value of  $\sigma_{\theta\theta}$ ) and along the z-axis in shear mode (due to the maximum value of  $\tau_{\max}$ ). Moreover, the authors discussed the discrepancy, for as-received glass spheres compressed between elastically



deforming platens, between the mentioned tensile failure criterion and the observed coherent cones, inferred to be associated with shear failure. Therefore, Shipway & Hutchings (1993b) suggested initial failure in the glass spheres to be associated with local shear failure below the contact points (due to the maximum value of  $\tau_{\max}$  along the z-axis) and to be followed by further crack propagation in tensile mode. In addition, Shipway & Hutchings (1993a,b) did not consider the maximum value of the surface tensile tangential stress ( $\sigma_{\psi\psi}$ ) just outside the contact area (see section 2.2.7) since it was inferred to only initiate the development of divergent cone cracks leading to spalling near the contact area and not to catastrophic sphere failure.

Gallagher (1987) interpreted the hourglass-like cross-sectional shape of fracture surfaces of failed sand grains to be reminiscent of contour patterns of  $\tau_{\max}$  in a diametrically compressed sphere (refer Figures 2.4 or 2.12). In addition, he suggested the specific fractographic features on the fracture surfaces to point at failure initiation sites predominantly in a lenticular region, near the loading axis and below the contact points. On this basis and employing the Hertz-Huber stress analysis (refer section 2.2.5) Gallagher (1987) suggested grain failure to initiate either along the z-axis beneath the contact points due to the maximum value of  $\tau_{\max}$  (refer Figure 2.5b) or in the centre of the grain, erroneously adopting equation 16, due to a supposedly maximum tensile  $\sigma_r$ . However, as shown in Figure 2.5b,  $\sigma_r$  tends to zero along the z-axis with increasing depth (i.e. towards the grain centre). Moreover, according to Kienzler & Schmitt (1990), the Hertz stress analysis is no longer valid for  $z/a > 0.5$  in a diametrically loaded sphere.

In summary, the results presented by Gallagher (1987) and Shipway & Hutchings (1993b) do not provide convincing arguments for the definition of an initiation site for sphere failure. Therefore, giving preference to the work of Kienzler *et al.*, it is inferred that cracks causing failure of brittle spheres in diametric compression initiate as tensile ring cracks at the edge of the contact area due to the maximum tensile value of  $\sigma_{\psi\psi}$  and propagate as shear-driven convergent cone cracks along trajectories of  $\tau_{\max}$ , with possible subsequent meridional cracks developing at the mantle of the cone under the action of  $\sigma_{\phi\phi}$ .

## 2.5. RECAPITULATION OF SITES OF TENSILE AND SHEAR STRESSES IN A DIAMETRICALLY LOADED SPHERE

In the following, the various sites and magnitudes of (local) tensile and shear stress maxima in a diametrically loaded sphere will be considered on the basis of the analytical results presented in section 2.2. The sites can be identified as (see also Shipway & Hutchings, 1993a): (i) the maximum tensile radial stress  $\sigma_r$  at the edge of the contact area (Hertz-Huber analysis, Figure 2.5a), (ii) the maximum of the maximum shear stress  $\tau_{\max}$  on the z-axis (Hertz-Huber analysis, Figure 2.5b), (iii) the maximum tensile circumferential stress  $\sigma_{\phi\phi}$  on the free surface of the sphere (for  $\nu \leq 0.4$  at the equator) (solution after Sternberg & Rosenthal, 1952, Figure 2.6), (iv) the maximum

tensile stress  $\sigma_{\psi\psi} = \sigma_{\vartheta\vartheta}$  in the centre of the sphere (solution after Sternberg & Rosenthal, 1952, Figure 2.7a) and (v) the maximum tensile stress  $\sigma_{\psi\psi} = \sigma_{\vartheta\vartheta}$  on the z-axis beneath the loading cap, which is strongly dependent on  $\psi_0$  (solution after Hiramatsu & Oka, 1966, Figure 2.11a).

Assuming that failure is associated with the propagation of mode I cracks under the action of a tensile stress (Hertz, 1896), attention is now restricted to sphere failure initiated through the development of such cracks; site (ii) (maximum  $\tau_{\max}$ , suggested to be responsible for mode II shear cracks) is hence excluded from the comparison. Maximum tensile stresses occurring at sites (iii) and (iv) obtained adopting the solution after Hiramatsu & Oka (1966) are also excluded since it has been shown in section 2.2.7 that (a) they coincide with stresses computed using the solution after Sternberg & Rosenthal (1952) and (b) their magnitude increases with smaller  $\psi_0$ . Therefore, the stresses considered at sites (iii) and (iv) should be envisaged as "worst case" values if  $\psi_0$  tends to zero. It should be noted that, as reported in section 2.2, the maximum tensile stresses at sites (i), (iv) and (v) increase and at site (iii) decrease with smaller values of Poisson's ratio  $\nu$ . The stresses computed for  $\nu = 0.077$  (quartz) at sites (i), (iv) and (v) should for this reason likewise be considered as "worst case" values.

The tensile stresses listed are depicted in Figure 2.14 as a function of load applied to a spherical quartz grain.

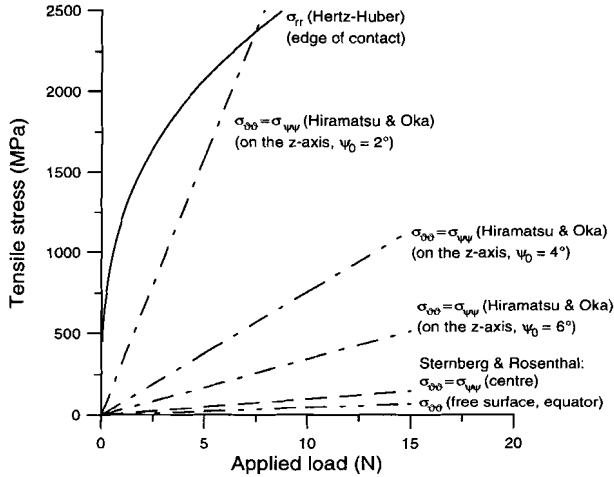


**Figure 2.14.** Maximum tensile stresses in a diametrically loaded spherical quartz grain, at the edge of the contact circle, in the centre and at the free surface, and along the z-axis. The stresses have been computed adopting the Hertz-Huber analysis and the solutions due to Sternberg & Rosenthal (1952) and Hiramatsu & Oka (1966) respectively, for a sphere radius  $R$  equal to  $150 \mu\text{m}$ , and for different values of the cap angular width  $\psi_0$ . For representative loads at failure of the grains considered the Hertzian radial stress  $\sigma_{rr}$  at the edge of the contact circle is the maximum tensile stress occurring.

The maximum tensile stress at site (i) is calculated considering two spherical quartz grains in contact while at site (v) it is plotted for different values of  $\psi_0$  ( $2^\circ$ ,  $4^\circ$  and  $6^\circ$ ). Note that the Young's modulus of quartz is equal to 95.68 GPa (Simmons & Wang, 1971; Sumino & Anderson, 1984). Natural quartz sand grains of the size considered have a critical load at failure in the range 1-15 N (this study, chapter 3 and Gallagher, 1987). At these loads, approximate values of  $\psi_0$  fall in the range  $4^\circ$  to  $11^\circ$  if calculated assuming a planar contact area (see section 2.2.7). Figure 2.14 demonstrates clearly that for representative loads the Hertzian radial stress  $\sigma_r$  at the edge of the contact circle is the maximum tensile stress occurring anywhere within or on the surface of the grain.

## 2.6 GRAIN FAILURE CRITERION FOR QUARTZ

Since it has been demonstrated above that the maximum tensile stress in a quartz sphere loaded diametrically occurs at the edge of the contact circle and since the main flaws to be expected are surface flaws, and since cracks initiating at the contact circle edge have been inferred to lead to whole-grain failure, a whole-grain failure criterion for a brittle quartz sphere in diametric compression can be formulated by combining the expression for the maximum tensile stress with LEFM considerations. Accordingly, assuming the sphere to contain surface flaws of initial dimension  $c_0 \ll R$ , a tangentially aligned flaw at the edge of the contact can be viewed as a straight single-ended (edge) crack in an elastic half-space subjected to a locally uniform and constant tensile stress equal to the maximum Hertzian radial stress  $\sigma_T = (1-2\nu)\sigma_0/3$  where  $\sigma_0$  denotes the normal stress at the centre of the contact. The crack tip stress will then be characterised by the mode I stress intensity factor  $K_I = 1.12 \sigma_T \sqrt{\pi c_0}$  where  $c_0$  is the initial flaw dimension (Lawn, 1993). Specifically, grain failure will initiate if the flaw develops into a ring crack at the edge of the contact and if  $\sigma_T$  exceeds the local material cohesive strength, or in terms of LEFM, if  $K_I$  attains a value equal to the fracture toughness  $K_{Ic}$ . Thus for quartz, the grain failure criterion can be written

$$K_{Ic} = 1.12 \sigma_T \sqrt{\pi c_f} \quad (23)$$

where  $K_{Ic}$  is equal to 1 MPa  $\sqrt{m}$  (Atkinson, 1979; Atkinson & Meredith, 1989b) and  $c_f$  is the flaw dimension at failure. This criterion is the same as developed by Wong *et al.*, but has the advantage that it has been shown a) to represent the failure condition for the point of maximum tensile stress within and on the surface of the grain and b) to lead to whole grain failure, rather than simply assuming these points.

Fully exhaustive theoretical verification of this criterion requires numerical computations of the crack tip stress field at all points along its advancement path in order to verify that the propagating crack remains unstable at all points (i.e. that the instability criterion  $dK_I/dc > 0$  is satisfied) (cf. Mai & Lawn, 1986).

## 2.7 CONCLUSIONS

A review and synthesis has been presented of all available theoretical solutions to the elastic stress distribution in a sphere loaded diametrically. It has been shown that near-field (contact) stresses can be satisfactorily described with the classical Hertz-Huber solution and far-field (internal) stresses adopting the solution after Sternberg & Rosenthal (1952) for a sphere under concentrated loads. Furthermore, on the basis of a comparison between microstructural observations of crack phenomena in crushed spheres, reported in the literature, and the theoretical solutions, predictions of crack initiation site and propagation path leading to sphere failure have been given. In addition, the stress distribution models have served to identify the sites and magnitudes of (local) maximum tensile stresses. On this basis a failure criterion for a brittle quartz grain has been formulated.

## CHAPTER 3      FAILURE BEHAVIOUR OF SINGLE SAND GRAINS: THEORY VS. EXPERIMENT

### 3.1 INTRODUCTION

It is widely accepted from microstructural studies that grain scale brittle fracture plus grain rearrangement play an important role in controlling the time-independent compaction behaviour of high porosity sandstones and sands under upper-crustal conditions (Burley, 1986; Wilson & McBride, 1988; Groshong, 1988; Wu & Groshong, 1991; Antonellini *et al.*, 1994; cf. chapter 2). In particular, grain scale fracture and rearrangement are believed to be mechanisms of major importance in controlling the porosity and permeability evolution of sedimentary rocks in rapidly subsiding basin settings (Donaldson *et al.*, 1995b). They may also be of importance in controlling production-related compaction of hydrocarbon reservoir rocks, leading to surface subsidence (Zoback & Byerlee, 1976; Schutjens *et al.*, 1994).

Clearly, a theoretically and experimentally based understanding of these mechanisms is needed in order to develop micromechanical models which can eventually be used in macroscale modelling of both upper-crustal deformation and the compaction of clastic hydrocarbon reservoirs in the (post-)production phase. As an integral step in this direction, an understanding of single grain failure behaviour is essential.

Previous experimental studies on time-independent compaction of porous sandstones and sands at room temperature have shown irrecoverable porosity reduction during loading, this increasing significantly beyond a specific critical effective pressure ( $P_{cr}$ ). The amount of compaction obtained at a given effective pressure generally increases with increasing porosity ( $\phi$ ) and grain size ( $d$ ). Indeed, the larger  $\phi$  and  $d$ , the greater the compaction and the lower  $P_{cr}$ , i.e. the weaker the material (Borg *et al.*, 1960; Lee & Farhoomand, 1967; Vesić & Clough, 1968; Dunn *et al.*, 1973; Zoback & Byerlee, 1976; Lambe & Whitman, 1979; Wissler & Simmons, 1985; Zhang *et al.*, 1990a). At the same time, crushing tests conducted on single sand grains have shown their load at failure to increase with larger  $d$  (Gallagher, 1976). With regard to microscale failure mode, petrographic observations of experimentally deformed materials have revealed that the dominant grain failure mechanism leading to aggregate compaction and single grain crushing is the development of tensile intra- and transgranular cracks at grain contacts due to point loading (Gallagher, 1976, 1987; Gallagher *et al.*, 1974; Zhang *et al.*, 1990a; Wong, 1990; Bernabe & Brace, 1990; Gill *et al.*, 1990; Myer *et al.*, 1992; cf. chapter 2).

On the basis of the above-mentioned work, micromechanical modelling of the compaction of porous rock by grain crushing under hydrostatic states of stress has been recognized as requiring the description of the critical (tensile) state of stress at grain contacts, e.g. using Hertzian contact theory (Hertz, 1896; cf. chapter 2) which

allows the stress and deformation fields at loaded contacts between elastic bodies to be computed (see recent reviews by Kemeny & Cook, 1991 and Myer *et al.*, 1992). Stress concentrators (flaws) at the grain contact surface are believed to be sites of ring crack nucleation and subsequent unstable growth leading to grain failure, a process which can be described using linear elastic fracture mechanics (LEFM) (Lawn, 1993). Recently, this approach was used to describe the hydrostatic compaction behaviour of cemented porous rock (e.g. sandstone) by deriving an expression for the critical effective pressure for the onset of major grain crushing ( $P_{cr}$ ) as a function of porosity and flaw size (Wong, 1990; Zhang *et al.*, 1990a). However, while the model derived by Wong *et al.* adopts Hertzian contact theory and LEFM to determine the grain contact stress distribution and a ring crack extension criterion, it does not in itself lead to a strictly defined whole-grain failure criterion. More importantly, the  $\phi$  and  $d$  dependence of  $P_{cr}$  observed in compaction experiments is not an intrinsic property of their model but is introduced by relating the grain failure load to  $P_{cr}$  on the basis of a random packing model and by assuming (with no independent justification) that the flaw dimension (at failure) scales linearly with  $d$ .

In chapter 2, a criterion similar to that of Wong *et al.* was formulated, but treating flaw dimension to be independent of grain size, and based on a review and synthesis of all available theoretical solutions to the elastic stress distribution in a sphere loaded diametrically. Making use of a comparison between microstructural observations of crack phenomena in crushed spheres and the theoretical solutions, predictions of crack initiation site and propagation path leading to sphere failure were given. It was demonstrated that, in a spherical quartz grain, the Hertzian radial contact stress is the maximum tensile stress ( $\sigma_T$ ) occurring and that it is this stress ( $\sigma_T$ ) which can be held responsible for ring crack initiation leading to whole-grain failure. This whole-grain failure criterion, however, does not directly offer an explanation for the grain size dependence of the grain failure load obtained from compaction experiments and single grain crushing tests. In addition, to apply the whole-grain failure criterion to sand grains in practise, data are needed on the dimension of flaws associated with failure ( $c_f$ ).

In this chapter, the whole-grain failure criterion of chapter 2 is applied to a sphere-platen contact with circular or elliptical area. A Hertzian/LEFM micro-mechanical model for grain crushing is thus developed predicting the critical force at failure ( $F_c$ ) to be a function of grain size (or contact surface curvature) and flaw size. A review of Weibull weakest link theory enables the formulation of an alternative statistical model for grain crushing. This demonstrates that a purely statistical grain size effect upon grain failure probability can influence the grain size dependence of the failure stress. The applicability of both models is tested by comparison with diametric compression experiments performed on single sand grains. Results are reported of crushing tests carried out a) on selected, well-rounded grains, and b) on grains sampled from four different grain size batches.

Applying the Hertzian/LEFM model, the  $F_c$  data obtained for the selected well-rounded grains lead to an estimate for mean  $c_f$ . However, neither the Hertzian/LEFM model applied for spherical grains, nor the Weibull statistical model, successfully explain the observed dependence of the force at grain failure on grain size. It is argued that the Hertzian/LEFM model assuming non-spherical grains with distributed effective radius of curvature offers the most physically reasonable explanation for the behaviour of the grains tested.

### 3.2 MICROMECHANICAL MODELS FOR GRAIN CRUSHING

The following section deals with the development of micromechanical models for single grain failure under conditions of diametric compression between flat platens. First, Hertzian contact theory will be applied for this loading state in combination with an LEFM approach, following the derivation developed in Chapter 2. This results in a deterministic grain failure criterion. A second, statistical model for single grain failure will then be developed after reviewing basic aspects of the Weibull weakest link theory.

#### 3.2.1 Hertzian/LEFM model

This model describes the failure of a grain loaded diametrically between two flat platens making use of an equilibrium or Griffith-type crack extension law (Griffith, 1920; Lawn, 1993). Both solids are assumed to be elastic and to make idealized Hertzian contact (cf. chapter 2, section 2.2.4 and 2.2.5).

According to Hertzian contact theory for solids of revolution (chapter 2, section 2.2.5) the radius ( $a$ ) of the contact circle between a grain ( $g$ ), with spherical pre-contact surface, and a flat plate ( $p$ ), with infinite radius of curvature  $R_p$ , is given by the relation (Johnson, 1987, eqn. 3.39)

$$a^3 = \frac{3FR_r}{4E^*} = \frac{3FR_g}{4} \left[ \frac{(1-\nu_g^2)}{E_g} + \frac{(1-\nu_p^2)}{E_p} \right] \quad (1)$$

where  $R_r$  is the relative radius of curvature defined  $1/R_r = (1/R_g) + (1/R_p)$ ,  $R_g$  is the grain contact radius of curvature,  $\nu_i$  ( $i = g, p$ ) are the Poisson's ratios of the two solid materials,  $E_i$  are the Young's moduli, and  $F$  is the total normal load transmitted between grain and platen. Further, the Hertzian radial stress  $\sigma_{rr}$  within the contact (cylindrical coordinates) reaches a maximum tensile value  $\sigma_T = (1-2\nu_g)\sigma_0/3$  at the edge of the circular contact area, where  $\sigma_0 = 3F/2\pi a^2$  is the normal stress at the centre of the contact. In a grain with an ellipsoidal contact surface,  $\sigma_{rr}$  reaches a maximum tensile value  $\sigma_T$  at the edge of the elliptical contact area (semi-axes  $a > b$ ) in the direction of the long axis  $a$  and equal to (Johnson, 1987, eqn. 4.35)

$$\sigma_T = \frac{(1-2\nu)ab}{a^2-b^2} \sigma_0 \left( \frac{a}{\sqrt{a^2-b^2}} \tanh^{-1} \left[ \frac{\sqrt{a^2-b^2}}{a} \right] - 1 \right) \quad (2)$$

In this case,  $\sigma_0 = 3F/2\pi ab$ , which for  $a/b < 3$  modifies to (Johnson, 1987, eqn. 4.32)

$$\sigma_0 \approx \sqrt[3]{\frac{6F(E^*)^2}{\pi^3 R_e^2}} \quad (3)$$

where  $R_e$  is the equivalent radius of curvature defined, for a grain - flat platen contact,  $R_e = \sqrt{(R'_g R''_g)}$ ;  $R'_g$  and  $R''_g$  being the principal (respectively maximum and minimum) radii of curvature (cf. chapter 2, section 2.2.4). In addition, for a grain - flat platen contact,  $a/b \approx (R'_g/R''_g)^{2/3}$  (Johnson, 1987, eqn. 4.33).

It is now assumed that the grain contains prepresent, Griffith-type, surface flaws of initial dimension  $c_0$ . In accordance with Hertzian and LEFM theory, if  $a \ll R_g$  and  $c_0 \ll R_g$ , a tangentially aligned flaw at the edge of the contact can be considered as a straight single-ended (edge) crack (in a semi-infinite half-space) subjected to a locally uniform and constant tensile stress equal to  $\sigma_T$ . The crack tip stress will then be characterised by the mode I stress intensity factor (Lawn, 1993, eqn. 2.20)

$$K_I = \sigma_T m^* \sqrt{\pi c_0} \quad (4)$$

where  $m^* \approx 1.12$  is an edge correction factor. Employing the concepts formulated in chapter 2, the flaw will develop into an tensile ring crack at the edge of the contact and will initiate grain failure if  $\sigma_T$  exceeds the local material cohesive strength, or in terms of LEFM, if  $K_I$  attains a value equal to the fracture toughness  $K_{Ic}$ , i.e. if

$$K_I = K_{Ic} = \sigma_T m^* \sqrt{\pi c_f} \quad (5)$$

where  $c_f$  is the ("critical") crack dimension at failure. In line with the arguments given in chapter 2, it is assumed here that the crack will remain unstable along its advancement path, causing instantaneous / catastrophic grain failure.

Combining the above relations for  $\sigma_T$ ,  $\sigma_0$ ,  $a$  and  $K_I = K_{Ic}$ , the critical force at failure ( $F_c$ ), for a grain with an initially spherical contact surface, is now given by the criterion

$$F_c = \frac{9\pi\sqrt{\pi} K_{Ic}^3 R_g^2}{2c_f\sqrt{c_f} (m^*)^3 (1-2\nu_g)^3 (E^*)^2} \quad (6)$$

For a grain with an initially ellipsoidal surface, the analogous relation, taking into account the given expression for  $R_e$  and the approximation for  $a/b$ , is



$$F_c \approx \frac{\pi\sqrt{\pi} K_{Ic}^3 (R'_g)^3}{6c_f\sqrt{c_f} (m^*)^3 (1-2\nu_g)^3 (E^*)^2 (R''_g)} \frac{q_e^3\sqrt{q_e}}{\tanh^{-1}[\sqrt{q_e}] - \sqrt{q_e}} \quad (7)$$

where  $q_e$  is denoted  $q_e = 1 - (R''_g/R'_g)^{4/3}$ . Focusing now on the model developed for spherical grain contact surfaces (i.e. eqn. 6), it is clear that in the case of spherical grains with a grain size  $d = 2R_g$  and a fixed or narrowly distributed value of  $c_f$ , the grain failure load  $F_c$  is predicted to be proportional to  $R_g^2$ , i.e.  $F_c \propto d^2$ . On the other hand, for a given population of grains with distributed values of  $c_f$  or  $R_g$  (including variable asperity radius),  $F_c$  will also be a distributed quantity.

### 3.2.2. Weibull weakest link model

#### *General aspects*

In materials science, it has long been recognized that the failure stress (i.e. the strength) of brittle materials tested under nominally identical sample and loading conditions is a statistically distributed quantity, and it is common practice to describe the strength and flaw size characteristics using Weibull statistics (Weibull, 1951; Jayatilaka & Trustrum, 1977a,b; Kittl & Diaz, 1988; Lamon, 1988; Lawn, 1993). The Weibull theory idealizes the failure process adopting the *weakest link concept*. Within the theory, a solid component with total volume  $V_{tot}$  or surface area  $A_{tot}$  subjected to an applied stress field is envisaged to be composed of solid elements with unit or representative elementary volume  $V_0$  or surface area  $A_0$ . In the original Weibull theory, the solid component is assumed to be an isotropic homogeneous linear elastic continuum. The elements are considered to contain several planar flaws and to be analogous to the links of a chain, with the weakest link determining the strength of the chain (Weibull, 1951; Batdorf & Heinisch, 1978; Lamon, 1988; Bazant *et al.*, 1991; Curtin & Sher, 1992). Depending upon the location of the failure-causing flaws, either the solid volume  $V_{tot}$  or the solid surface area  $A_{tot}$  is considered; for this reason, general measures  $Z_{tot}$  and  $Z_0$  are introduced in the following theoretical analysis to represent  $V_{tot}$  or  $A_{tot}$  and  $V_0$  or  $A_0$  respectively. Being dependent on the weakest (= biggest) flaw, the bulk material strength is determined by the extreme tail of the flaw size distribution. This aspect of "extreme value statistics" implies the strength to be an extrinsic quantity: the larger the solid component, the more likely a weaker flaw will be encountered, hence the lower the strength will be, statistically speaking (Curtin & Sher, 1992). It is referred to as the *statistical size effect* of the Weibull theory (Weibull, 1952; Kittl & Diaz, 1988; Bazant *et al.*, 1991).

The Weibull theory considers the flaws within the solid elements to be shear insensitive (only a tensile failure mechanism is thought to be operative), to be randomly oriented, to be uniformly distributed with respect to both their spatial location and orientation, and their population to be invariant in time. Moreover, the weakest link formulation envisages the solid elements to be stochastically independent and mutually exclusive (i.e. purely random and non-overlapping). Finally, elemental failure is assumed to occur independently (i.e. without mechanical interaction between elements) and with equal probability. Material failure is thus identified with unstable catastrophic flaw propagation throughout the bulk of the solid, independently of the strength of the other elements encountered on the crack path (Batdorf & Crose, 1974; Matthews *et al.*, 1976; Batdorf & Heinisch, 1978; Lamon, 1988; Chao & Shetty, 1990; Quinn & Morrell, 1991; Bazant *et al.*, 1991; Scholten, 1993). These assumptions are referred to as the *Poisson postulates* and enable the survival probability  $P_s$  of the solid component to be expressed as the joint probability of survival of all its  $N$  elements according to (Bazant *et al.*, 1991)

$$P_s = \prod_i^N (P_s)_i = \exp[N \ln(P_s)_i] \equiv \exp[-R_{rup}] \quad (8)$$

where  $(P_s)_i$  is the elemental survival probability and  $R_{rup}$  is known as the "risk of rupture". Since  $N$  is equal to  $Z_{tot}/Z_0$ ,  $R_{rup}$  can be written explicitly (Bazant *et al.*, 1991) as

$$R_{rup} = -N \ln(P_s)_i = \left( -\frac{1}{Z_0} \ln(P_s)_i \right) Z_{tot} \Leftrightarrow R_{rup} = \frac{1}{Z_0} \int_0^{Z_{tot}} -\ln(P_s)_i dZ \quad (9)$$

Weibull (1939, 1951) recognized the term  $-\ln(P_s)_i$  to be a function  $\psi$  of an equivalent stress  $\sigma_{eq}$ , defined as a scalar representation of the elemental stress tensor  $(\sigma_{kl})_i$ , such as the mean stress  $(\bar{\sigma}_n)$  acting normal to the crack plane ( $\sigma_{eq} = \bar{\sigma}_n$ ) (Thiemeier *et al.*, 1991). Weibull suggested an empirical power relation for  $\psi(\sigma_{eq})$ , known as the *Weibull or specific risk function*, and given by

$$\psi(\sigma_{eq}) = \left( \frac{\sigma_{eq} - \sigma_{lim}}{\sigma_{ch}} \right)^m \quad (\sigma_{eq} > \sigma_{lim}, m > 0) \quad (10)$$

where  $\sigma_{lim}$  is the lower limit or threshold strength,  $\sigma_{ch}$  is the characteristic strength and  $m$  is the Weibull modulus. Moreover, the *elemental failure probability*, denoted by  $(P_f)_i$  and equal to  $1 - (P_s)_i$ , represents the probability that the elemental failure stress  $(\sigma_f)_i$  is less than or equal to  $\sigma_{eq}$  (i.e.  $\Pr[(\sigma_f)_i \leq \sigma_{eq}]$ ). Accordingly, substitution of equations 9 and 10 into 8 yields an expression for the *failure probability of the solid component*  $(P_f)$  given by

$$P_f = 1 - P_s = 1 - \exp[-R_{rup}] = 1 - \exp\left[-\frac{1}{Z_0} \int_0^{Z_{tot}} \left(\frac{\sigma_{eq} - \sigma_{lim}}{\sigma_{ch}}\right)^m dZ\right] \quad (11)$$

Alternatively viewed,  $m$ ,  $\sigma_{lim}$  and  $\sigma_{ch}$  here represent the shape, datum and scale parameters of the distribution function  $P_f$  respectively.

### *Uniaxial stress model*

In the case of a *uniaxial tensile stress* field with magnitude  $\sigma_a$ , applied to an assembly of elements containing flaws oriented normal to  $\sigma_a$ ,  $\bar{\sigma}_n$  can be taken as equal to  $\sigma_a$ , so that  $\sigma_{eq}$  is equal to  $\sigma_a$ . Consequently, making the usual assumption for brittle materials that  $\sigma_{lim} = 0$  (Jayatilaka & Trustrum, 1977), eqn. 11 reduces to

$$P_f = 1 - \exp\left[-\frac{Z_{tot}}{Z_0} \left(\frac{\sigma_a}{\sigma_{ch}}\right)^m\right] \quad (12)$$

In accordance with the weakest link concept, the (global) strength of a material ( $\sigma_f$ ) is thus equal to  $\sigma_a$  at failure.

### *Weibull model for grain failure*

Application of the Weibull weakest link model to single grain failure is now attempted, broadly following Kschinka *et al.* (1986), assuming that individual grains are spherical and can hence be represented by their grain volume  $V_{tot} = 4\pi R_g^3/3$  or surface area  $A_{tot} = 4\pi R_g^2$ . Now, considering grain failure to initiate at either volume or surface flaws, located within the effective grain volume  $V_{eff} = \gamma_V V_{tot}$  or surface area  $A_{eff} = \gamma_A A_{tot}$  (where  $\gamma_V$  and  $\gamma_A$  are scaling factors) and subjected to a locally uniform and constant tensile stress field, the Weibull model for uniaxial stress can be applied. Accordingly, the failure stress ( $\sigma_f$ ) of an individual grain exhibits a clear grain size dependence if eqn. 12 is written, taking  $\sigma_a = \sigma_f$  and replacing  $Z_{tot}$  by  $Z_{eff}$ , in the form

$$\sigma_f = \sigma_{ch} \left( -\frac{hZ_0 \ln(1 - P_f)}{4\pi\gamma_Z} \right)^{1/m} R_g^{-j/m} \quad (13)$$

where  $h = 1$  and  $j = 2$  for surface flaws and  $h = j = 3$  for volume flaws. Only in case of surface flaws causing failure, the failure criterion formulated in section 3.2.1 can be directly employed by substituting the relation  $\sigma_T = (1 - 2\nu_g)\sigma_0/3$  for  $\sigma_f$  in eqn. 13.

### 3.3 EXPERIMENTS

We now report a series of diametric compression experiments performed on single sand grains, the aim being to test the applicability of the above Hertzian/-LEFM and Weibull models for single grain failure.

#### 3.3.1 Starting material

The sand used was obtained by taking fresh samples of the Heksenberg Formation (Middle Miocene age) from the "Beaujean" quarry near Heerlen, The Netherlands. The sand has been characterized as a beach or dune deposit (Kuyl, 1975) and shows a grain size of  $251 \pm 46 \mu\text{m}$ . ICP-ES measurements indicate a quartz content of at least 99 wt % with zircon and NaAl-rich feldspar present as trace minerals. The feldspar trace material was successfully removed from each batch by washing in water using a gravitational separation method. Imaged using SEM, most sand grains appear subrounded and show a pitted and grooved, but otherwise smooth surface. Some grains ( $< 0.5 \%$ ) possess a thin surface layer of iron oxide / hydroxide.

#### 3.3.2 Apparatus and general method

One-dimensional brittle crushing tests have been performed on single sand grains loaded between flat, ceramic-composite ( $\text{TiC} + 30 \text{ wt}\% \text{ Al}_2\text{O}_3$ ) anvils at room temperature and using a constant anvil displacement rate of  $\sim 0.01 \text{ cm/min}$ . Loading was achieved using a conventional, motor-driven testing rig. The anvils measured 12.65 mm diameter by 8 mm thickness, and have a Young's modulus of 400 GPa and a Poisson's ratio of 0.23 (approximated using tables 143 and 176 from the Ceramic Source 1991•1992).

The crushing tests were performed on single sand grains from four sieved batches with grain sizes of  $115 \pm 9$ ,  $196 \pm 16$ ,  $275 \pm 25$  and  $378 \pm 22 \mu\text{m}$ . The grains were placed on a 50-60  $\mu\text{m}$  foil of different "soft" materials (brass, aluminium or teflon) either under "lab dry" conditions or immersed in a drop of distilled water (see Figure 3.1). The soft substrate was used to eliminate tensile stresses arising from grain surface irregularities, in order to prevent cracks from initiating at the grain bottom.

Anvil position was measured using a Hewlett Packard linear variable differential transformer (LVDT) with a 1.27 mm stroke mounted directly across the sand grain sample. Load was measured with a Transducer Inc. 100 lbs load cell. For each grain, the initial diameter ( $x$ ) (i.e. grain height measured parallel to the loading axis) and the critical force at failure ( $F_c$ ) were accurately determined from a 2-channel flatbed recorder displaying the load and position signals as a function of time.

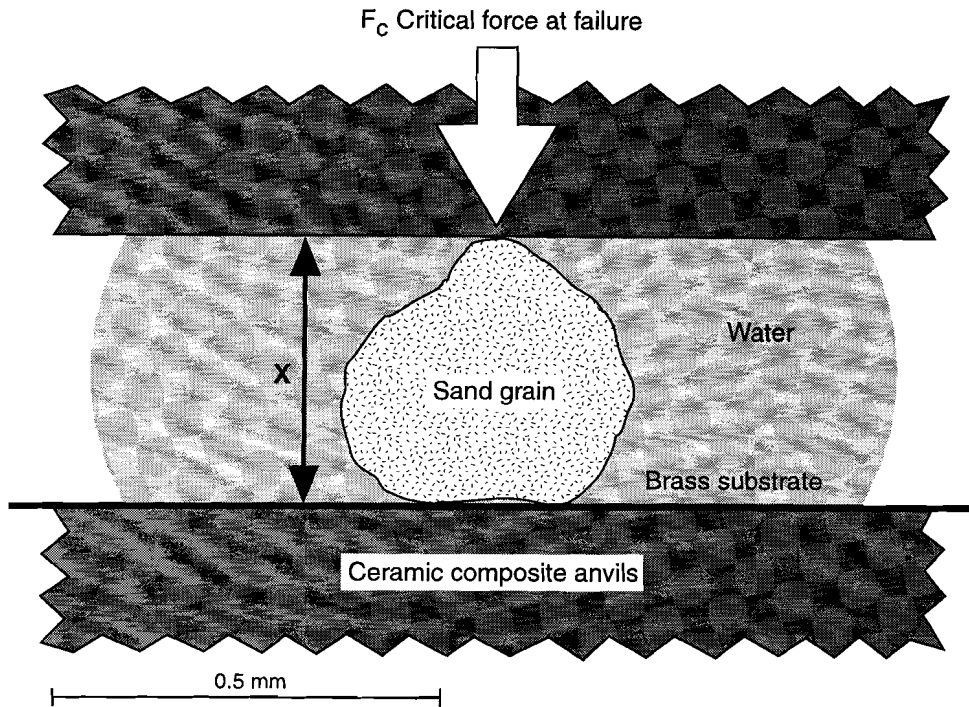


**Figure 3.1.** Semi-schematic diagram illustrating the anvil loading configuration used in the present one-dimensional crushing tests on single sand grains.

### 3.3.3 Calibration of apparatus

The anvil displacement rate was checked against a 0.01 mm resolution dial gauge and a digital stopwatch, resolving  $0.009606 \pm (9.73 \times 10^{-5})$  cm/min. The LVDT was calibrated in the range  $\pm 1$  mm using this dial gauge and a digital voltmeter (DVM) with a  $\pm 0.05$  % accuracy. The load cell was calibrated in the range 0-35 N with respect to an Entran 150 lbs load cell (model ELH-401) using similar DVM's. The Entran load cell specifications were themselves checked in the range 0-25 N against known weights. Conventional error analysis has shown the standard errors in  $x$  and  $F_c$  to be less than 0.77% and 1.16% respectively. For this reason, no attempt has been made to plot error bars for individual  $F_c$ - $x$  data pairs.

### 3.3.4 Detailed procedural aspects

Two types of test were performed, namely tests on selected grains and tests on randomly sampled grain size batches. The selected grain tests were carried out on well rounded grains with measurable radius of curvature chosen from the  $378 \pm 22$   $\mu\text{m}$  sieved fraction. The batch tests (see Table 3.1) were carried out on samples of 200 grains taken from each of the four grain size fractions separated, with no attempt to measure grain surface radii of curvature directly.

In preparing grains for the selected grain tests, a single layer of sand grains sampled from the  $378 \pm 22$   $\mu\text{m}$  batch was first immersed in an epoxy resin film deposited on a glass slide. After hardening of the resin, a quarter to a third of the average grain height was removed by gentle polishing, after which the epoxy resin was dissolved in ethanol. From this sample of grains, individual grains were selected using light microscopy, on the basis of a visibly spherical or ellipsoidal smooth surface opposite to the polished flat. The selected grains were subsequently photographed in perpendicular directions corresponding to maximum and minimum radii of curvature. These radii were determined, with an estimated 10% relative error, from photographic prints by fitting circles to the grain surface profile. The crushing tests were performed on the selected grains with the polished flat placed downwards on a 50  $\mu\text{m}$  brass foil and with the grains immersed in a drop of distilled water.

**Table 3.1.** *Overview of batch crushing tests performed on single sand grains, showing test conditions and types of substrate material used.  
Each box in the table represents a single batch sample of 200 grains tested under the conditions shown.*

Test condition	Grain size d ( $\mu\text{m}$ )			
	$115 \pm 9$	$196 \pm 16$	$275 \pm 25$	$378 \pm 22$
wet	brass	brass	brass	brass
"lab dry"	teflon		teflon	teflon
"lab dry"			none	
"lab dry"			brass	
"lab dry"			aluminium	

### 3.4 MECHANICAL RESULTS

#### 3.4.1 Selected grain data

The critical force at failure ( $F_c$ ) data obtained from the crushing tests performed on the selected grains are shown in Figure 3.2 as a function of the equivalent radius of curvature defined  $R_e = \sqrt{(R'_g R''_g)}$  where  $R'_g$  and  $R''_g$  are the two perpendicular radii determined from photo prints (cf. section 3.2.1). The data show a broad scatter with no visible trend.

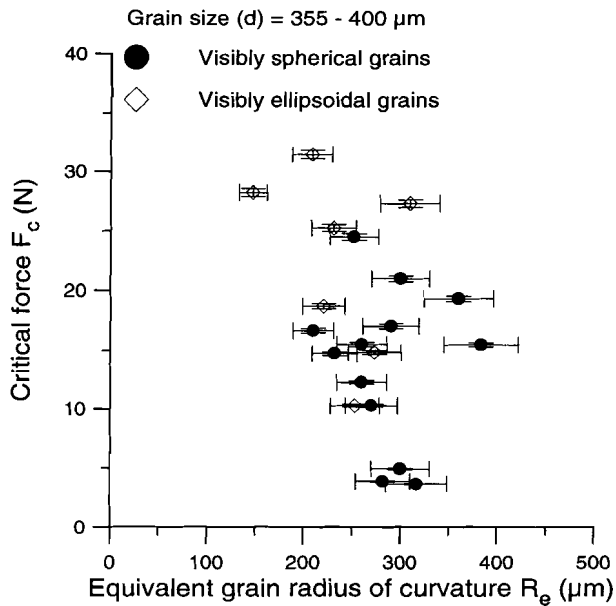


**Figure 3.2.** Critical force at failure data obtained from crushing tests on single sand grains with visibly spherical or ellipsoidal contact surfaces and different equivalent radius of curvature using a brass substrate (50  $\mu\text{m}$  foil) and with grains immersed in a drop of distilled water (selected grain tests).

### 3.4.2 Batch data

A typical histogram of  $F_c$  data obtained from the crushing tests on the four grain size batches is depicted in Figure 3.3. This particular histogram was obtained from tests using a brass substrate and with grains immersed in a drop of distilled water. For all batches tested, however, the  $F_c$  data approximately follow a log-normal distribution and the initial grain diameter ( $x$ ) data a normal distribution. This enables arithmetic averages (means) and sample standard deviations of  $\ln F_c$  and  $x$  to be calculated employing the log-normal and normal distribution models respectively.

The means of the  $F_c$  distributions obtained from crushing experiments on the various batches tested are shown as a function of grain size in Figure 3.4 (brass substrate and with grains immersed in a drop of distilled water) and in Figure 3.5 (teflon substrate, "lab dry"). Grain size is plotted either in terms of the mean measured initial grain diameter ( $x$ ), or as the equivalent-sphere mean grain size. The latter is obtained by fitting a sphere to the mean grain volume of the sand grains sampled from each grain size batch, the mean grain volume being calculated from the sample mass, the number of constituent grains and the density of quartz. The error bars in Figures 3.4 and 3.5 represent standard errors approximated by  $s/\sqrt{n}$ , where  $s$  is the sample standard deviation and  $n$  is the number of sample elements (Rice, 1988). The data show that  $F_c$  can be considered proportional to  $d^f$  where  $f \approx 1.3$ .

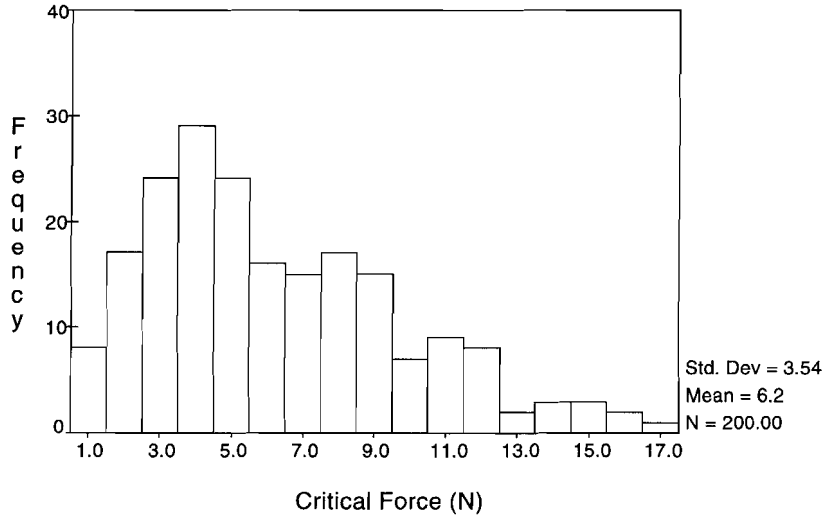


**Figure 3.3.** Typical histogram of critical force at failure data obtained from crushing tests on single sand grains of the 250-300  $\mu\text{m}$  size batch using a brass substrate (50  $\mu\text{m}$  foil) and with grains immersed in a drop of distilled water.



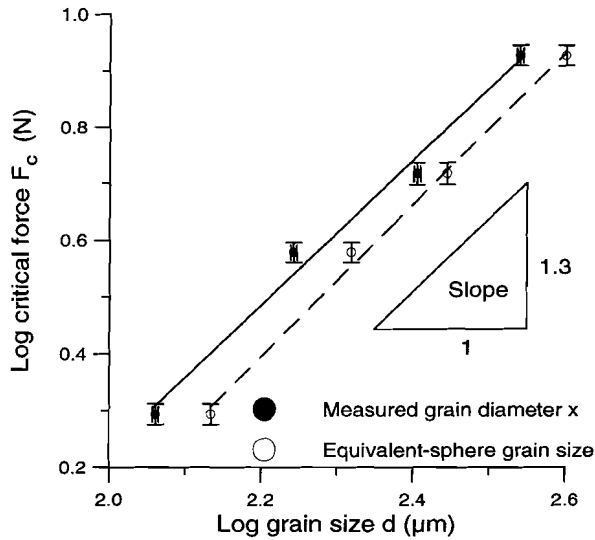


**Figure 3.4.** Log-log plot of mean critical force at failure ( $F_c$ ) vs. mean grain size ( $d$ ) obtained from crushing tests on the four sand grain size batches performed using a brass substrate ( $50 \mu\text{m}$  foil) and with grains immersed in a drop of distilled water. The data show that  $F_c$  can be considered proportional to  $d^f$  where  $f \approx 1.3$ .

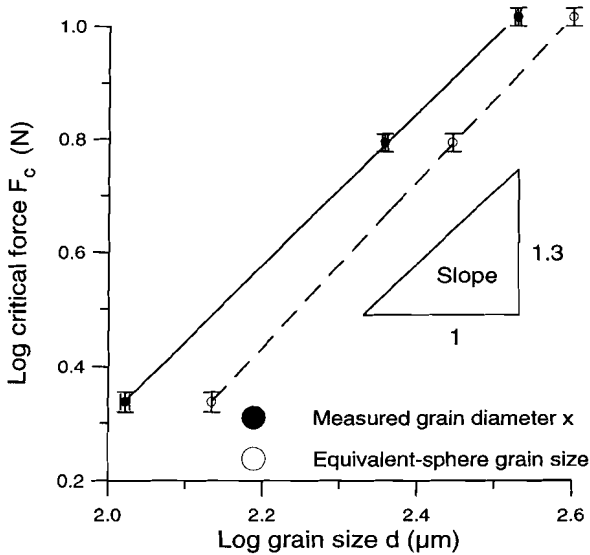


**Figure 3.5.** Log-log plot of mean critical force at failure ( $F_c$ ) vs. mean grain size ( $d$ ) obtained from crushing tests on the four sand grain size batches performed using a teflon substrate ( $50 \mu\text{m}$  foil) under "lab dry" condition. The data show that  $F_c$  can be considered proportional to  $d^f$  where  $f \approx 1.3$ .

Figure 3.6 displays the means of the  $F_c$  distributions obtained from crushing tests performed on  $275 \pm 25 \mu\text{m}$  grain batches using various substrates and under dry and wet conditions. The means do not differ significantly, in comparison to those obtained for different grain size. On this basis, it is inferred that humidity and type of substrate material do not significantly influence  $F_c$ .

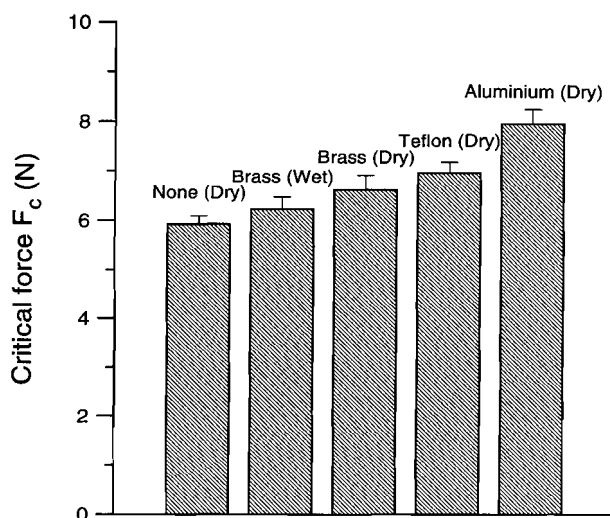


**Figure 3.6.** Mean critical force at failure ( $F_c$ ) data obtained from crushing tests on sand grains of the 250-300  $\mu\text{m}$  size batch using none or different substrate (50  $\mu\text{m}$  foil, aluminium 60  $\mu\text{m}$ ) and under "lab dry" or wet condition (grains immersed in a drop of distilled water). Note that the  $F_c$  data do not differ significantly, in comparison to those obtained for different grain size.

### 3.5 DISCUSSION

#### 3.5.1 Interpretation of results for selected grains

The highly scattered  $F_c$  vs.  $R_e$  data for the selected grains depicted in Figure 3.2 are plotted in log-log space in Figure 3.7, without displaying error bars for  $R_e$ . Linear regression of the data employing the method of least squares yields a best fit power law equation of the form  $F_c \propto R_e^f$  where  $f \approx -1.1$ . However, the data exhibit extremely poor correlation; the sample and range of  $R_e$  investigated are obviously too small in comparison with the variability in  $F_c$  and error in measuring  $R_e$ .

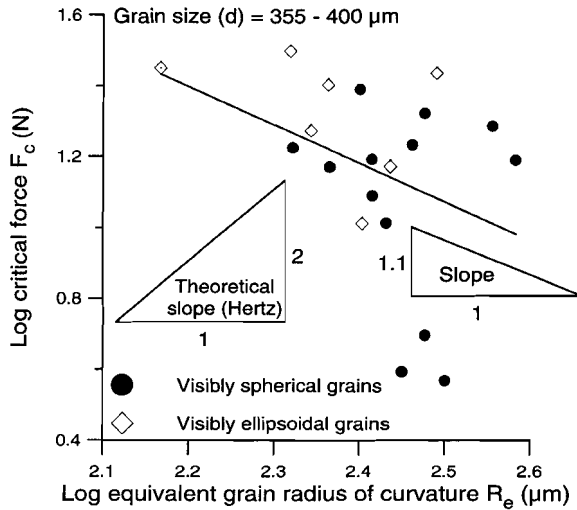


**Figure 3.7.** Log-log plot of critical force at failure ( $F_c$ ) vs. equivalent grain radius of curvature ( $R_e$ ) constructed from the  $F_c$  data of selected sand grains with visibly spherical or ellipsoidal contact surfaces. The crushing tests were carried out using a brass substrate (50  $\mu\text{m}$  foil) and with grains immersed in a drop of distilled water. Linear regression of the data yields a best fit power relation of the form  $F_c \propto R_e^f$  where  $f \approx -1.1$ . However, the data exhibit extremely low correlation (coefficient of determination = 0.139, residual mean square = 0.067,  $n = 20$ ).

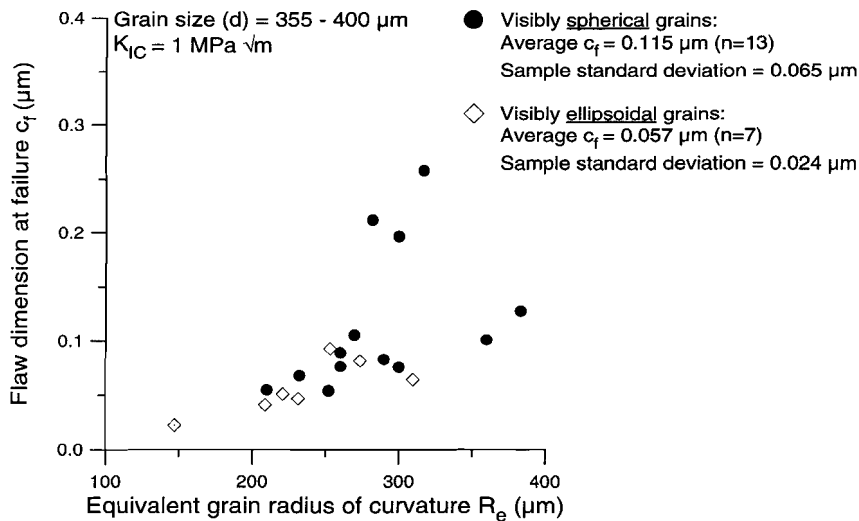


**Figure 3.8.** Values of flaw dimension at failure obtained by translating critical force at failure data of selected sand grains with visibly spherical or ellipsoidal contact surface, using the Hertzian/LEFM model (cf. Figure 3.7).

Since the selected grains possessed smooth spherical or ellipsoidal contact surfaces, it is reasonable to suppose that the Hertzian/LEFM model can be applied to estimate the size of the flaws causing failure of individual grains. To this end, the  $F_c$  data for the selected grains have been translated into a flaw dimension at failure ( $c_f$ ) adopting either equation 6 or its equivalent for grains with ellipsoidal surface (eqn. 7) taking the Young's modulus and Poisson's ratio of quartz equal to 95.68 GPa and 0.077 respectively (Simmons & Wang, 1971; Sumino & Anderson, 1984). The fracture toughness ( $K_{Ic}$ ) of quartz is considered equal to 1 MPa  $\sqrt{m}$ , a representative value based on double torsion tests performed on synthetic quartz single crystals at room temperature and under ambient or water immersed conditions (Atkinson, 1979; Atkinson & Meredith, 1989b). The  $c_f$  values obtained are depicted in Figure 3.8 as a function of the equivalent radius of curvature  $R_e$ . Once again, the data show a large scatter so that no systematic relation between  $c_f$  and  $R_e$  can be inferred. Nonetheless, for the grains with spherical surface the data do show an average  $c_f$  of 0.115  $\mu m$  (sample standard deviation 0.065  $\mu m$ ). For the ellipsoidal grains,  $c_f$  (mean) = 0.057  $\mu m$  (sample standard deviation 0.024).

In the literature, various estimates of the "Griffith" flaw dimension have been reported. In highly brittle covalent-ionic solids, like mono-crystalline quartz, theory and observations suggest that the characteristic dimension should range from 1 nm for pristine surfaces to 1  $\mu m$  for aged material, the flaws occurring at the surface and being initiated due to particle impingement (Suresh, 1992; Lawn, 1993). In addition, Zhang *et al.* (1990a) have compiled critical effective pressure ( $P_{cr}$ ) data for compaction of porous quartzitic rocks and granular quartz sands of varying grain size ( $d$ ) and porosity. At the critical pressure, accelerated porosity decrease was observed during loading. Assuming the compaction behaviour to be time-independent, this point is believed to represent the onset of major grain crushing. On the basis of an aggregate compaction model adopting the same failure criterion as presented in this chapter (eqn. 6), Zhang *et al.* (1990a) used the  $P_{cr}$  data to evaluate the flaw sizes at failure ( $c_f$ ). For Ottawa sand ( $d = 75\text{-}1000 \mu m$ ), Zhang *et al.* (1990a) calculate  $c_f$  values in the range  $0.0135 \pm 0.0015 \mu m$  using a  $K_{Ic}$  equal to 0.307 MPa  $\sqrt{m}$  (cf. Atkinson & Avdis, 1980). However, Ferguson *et al.* (1987) report this  $K_{Ic}$  value to be miscalculated; instead they propose a value of 1.3 MPa  $\sqrt{m}$ . Reinterpreting the  $P_{cr}$  data for Ottawa sand using  $K_{Ic} = 1 \text{ MPa } \sqrt{m}$  yields flaw sizes at failure in the range  $0.14 \pm 0.02 \mu m$ . Thus, the estimate of the flaw dimension at failure ( $c_f$ ) presented in this chapter ( $0.115 \pm 0.065 \mu m$ ) is within the range suggested by previous workers (Lawn, 1993; Zhang *et al.*, 1990a). It is important to note, however, that the flaw dimension associated with failure is not necessarily equal to the initial flaw dimension ( $c_0$ ). During continued loading, an initial flaw may extend either, at a stress intensity  $K_I < K_{Ic}$ , by subcritical crack growth or, at the critical point  $K_I = K_{Ic}$ , in a stable or equilibrium manner if  $dK_I/dc \leq 0$ . Only if the instability criterion  $dK_I/dc > 0$  is satisfied at the critical point, unstable flaw propagation will occur leading to catastrophic failure (Mai & Lawn, 1986).

### 3.5.2 Interpretation of batch results

#### *Applicability of the Weibull weakest link model*

A similar grain size dependence of the critical load at failure as demonstrated for the batch samples in Figures 3.4 and 3.5 can be deduced from the failure stress data for crushed glass spheres presented by Kschinka *et al.* (1986). These authors performed diametric compression experiments on soda-lime-silica glass spheres of ten size classes with average diameters in the range 510-3680  $\mu\text{m}$ . Individual spheres, hand sorted into groups of nearly perfect spheres, were loaded between hardened steel platens using an Instron testing machine at a crosshead speed of 12.7 mm/min. Kschinka *et al.* (1986) succeeded in explaining the observed sphere size dependence of the failure stress using a Weibull weakest link model.

Following Kschinka *et al.* (1986), an attempt is made to explain the grain size dependence of the failure stress ( $\sigma_f$ ), as determined from the present batch experiments, in terms of the Weibull weakest link model. Applying the Hertzian failure criterion defined in section 3.2.1 (i.e. taking  $\sigma_f$  equal to  $\sigma_T = (1-2\nu_g)\sigma_0/3$ ), assuming spherical grains (i.e. taking  $R_g$  equal to  $x/2$  in eqn. 1) and using the elastic parameters for quartz given in section 3.5.1, the critical load at failure ( $F_c$ ) data obtained from the crushing tests on the different batches have been translated into values of  $\sigma_T$ . Figure 3.9 shows a typical histogram of  $\sigma_T$  data, obtained from translating the  $F_c$  data depicted in Figure 3.3.

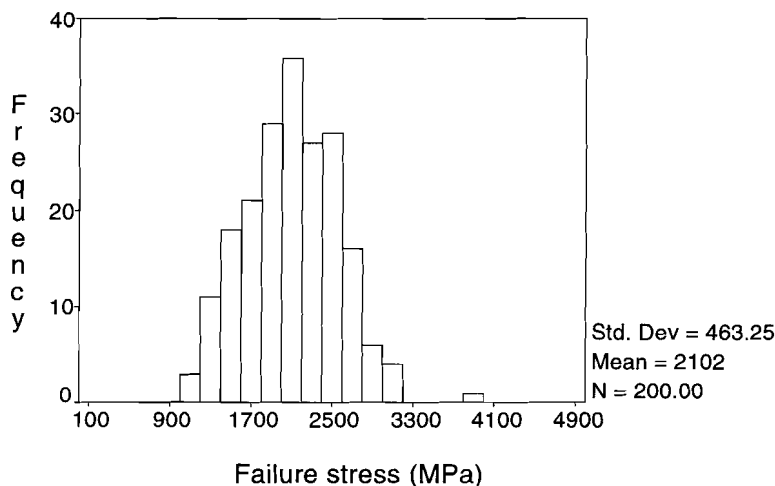


**Figure 3.9.** Typical histogram of failure stress data determined by translating critical force at failure ( $F_c$ ) data adopting the Hertzian failure criterion. The  $F_c$  data have been obtained from crushing tests on sand grains of the 250-300  $\mu\text{m}$  size batch using a brass substrate (50  $\mu\text{m}$  foil) and with grains immersed in a drop of distilled water.

Several methods are in use for fitting either a Weibull density or distribution function to strength ( $\sigma_f$  histogram) data (Trustrum & Jayatilaka, 1979; Dortmans & de With, 1991). One method is based on rewriting the Weibull formula for uniaxial stress (eqn. 12), taking  $\sigma_f = \sigma_{eq} = \sigma_a$  equal to  $\sigma_T$ , in the so-called two-parameter form

$$\ln(\ln(1 - P_f)^{-1}) = -m \ln k + m \ln \sigma_T \quad (14)$$

where  $k$  is an alternative Weibull scale parameter defined  $k = \sigma_{ch}(Z_0/Z_{tot})^{1/m}$ . Using the Weibull formula for uniaxial stress, Dortmans & de With (1991) have performed a Monte Carlo simulation generating random sets of failure probability  $(P_f)_j$  and strength  $(\sigma_f)_j$  for (arbitrary) samples with normally distributed experimental error and for given values of  $m$  and  $k$ . They have shown that an estimator for  $(P_f)_j$  denoted  $(P_f)_j = (j-0.5)/n$ , where  $n$  is the total number of samples tested and  $j$  is the rank of the sample in order of increasing  $(\sigma_f)_j$ , leads, if employing a linear least-squares fit procedure to the computed  $(P_f)_j - (\sigma_f)_j$  data given in a form suitable for comparison with eqn. 14, to the least biased estimates for  $m$  and  $k$ . Figure 3.10 shows translated  $\sigma_T$  data obtained from the crushing tests performed using a brass substrate (and with grains immersed in a drop of distilled water) plotted in a form suitable for comparison with and fitting of eqn. 14. Linear regression of the  $\sigma_T$  data from each separate batch, employing the method of least squares, yields the Weibull parameters  $m$  (the slope) and  $k$  (from the intercept) listed in Table 3.2. The high correlation coefficients of these fits suggest the Weibull formula to be a satisfactory representation of the  $\sigma_T$  distribution for each batch. Note that the Weibull modulus  $m$  and its confidence interval do not exhibit a systematic trend with respect to the (average) grain size ( $d$ ) of each batch. In addition, the scale parameter  $k$ , corresponding to the mean of the  $\sigma_T$  distribution for each batch, decreases with larger  $d$ .

A second method involves maximum likelihood estimation of the Weibull density function parameters  $m$  and  $k$ , satisfying the equations (Johnson & Kotz, 1970)

$$\frac{1}{m} - \frac{\sum_{j=1}^n (\sigma_T)_j^m \ln(\sigma_T)_j}{\sum_{j=1}^n (\sigma_T)_j^m} - \frac{\sum_{j=1}^n \ln(\sigma_T)_j}{n} = 0 \quad \text{and} \quad k = \left( \frac{\sum_{j=1}^n (\sigma_T)_j^m}{n} \right)^{1/m} \quad (15)$$

Estimates for  $m$  and  $k$  are calculated using the iterative bisection method for root location (e.g. Press *et al.*, 1988). The results for the wet crushing tests with brass substrate are listed in Table 3.3. A 95% confidence interval for the parameter  $m$  is given obtained with a statistical test method developed by Thoman *et al.* (1969).

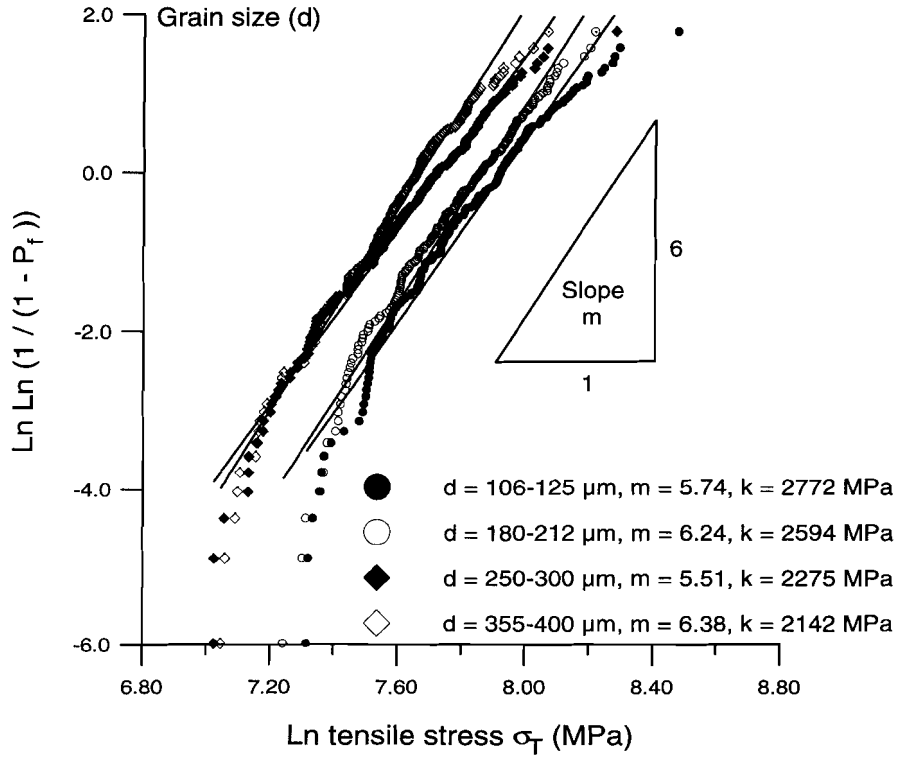


**Figure 3.10.** Standard Weibull plot of failure stress data versus cumulative failure probability ( $P_f$ ) determined by translating critical force at failure ( $F_c$ ) data adopting the Hertzian failure criterion assuming spherical grains. The  $F_c$  data have been obtained from crushing tests on the four sand grain size batches performed using a brass substrate (50  $\mu\text{m}$  foil) and with grains immersed in a drop of distilled water. Linear least squares fits of the data yield Weibull moduli ( $m$ ) of  $\sim 6$  for each size batch.

**Table 3.2.** Weibull parameters of strength distributions obtained by linear least squares regression of strength data presented in Figure 3.10.  
Data for grain size batches tested wet and using brass substrate.

Grain size d ( $\mu\text{m}$ )	115 $\pm$ 9	196 $\pm$ 16	275 $\pm$ 25	378 $\pm$ 22
m	5.74	6.24	5.51	6.38
$s_{\bar{x}}$ of m	0.1	0.09	0.07	0.08
95 % ci of m	0.20	0.18	0.14	0.16
k (MPa)	2772	2594	2276	2143
upper k (MPa)	3025	2799	2414	2278
lower k (MPa)	2548	2409	2149	2019
cc	0.94	0.96	0.97	0.97

$s_{\bar{x}}$  estimated standard error  
ci confidence interval  
cc correlation coefficient

The confidence interval (ci) of the Weibull modulus m is determined performing a Student's t-test. Following Rice (1988) a  $100(1-\alpha')\%$  ci is defined equal to  $t_{n-df}(\alpha'/2) * s_{\bar{x}}$  where df are the degrees of freedom,  $\alpha'$  is the level of significance and  $s_{\bar{x}}$  is the standard error of the parameter. In the present context,  $df=2$  and  $n=200$  yielding for  $\alpha'=5\%$  (i.e. a 95% ci)  $t_{198} \approx 1.98$ .

**Table 3.3.** Weibull parameters of strength distributions obtained by maximum likelihood estimation.  
Data for grain size batches tested wet and using brass substrate.

Grain size d ( $\mu\text{m}$ )	115 $\pm$ 9	196 $\pm$ 16	275 $\pm$ 25	378 $\pm$ 22
m	4.75	5.60	4.80	5.60
95 % ci of m	0.55	0.66	0.55	0.64
k (MPa)	2582	2440	2119	2016

ci confidence interval (Thoman *et al.*, 1969)



Taking into account the corresponding confidence intervals, it can be seen that the Weibull parameters  $m$  and  $k$  in Tables 3.2 and 3.3, determined using the two different fitting methods, agree well.

In order to test the applicability of the Weibull weakest link model for grain failure developed in section 3.2.2, the grain size dependence of the  $\sigma_T$  data for each batch will be considered, employing eqn. 13 for  $\sigma_f = \sigma_T$  and at constant  $P_f$ . If the flaws causing grain failure in the different batches originate from a single population, the Weibull moduli  $m$  obtained for each batch would have to be similar to the modulus obtained for the entire sample of grains. Surface flaws of sand grains are known to be generated due to grain collision and abrasion during sedimentary transport. Therefore, a single surface flaw population is believed to be a reasonable assumption for sand grains sampled from the same sedimentary environment with an identical transport history.

The median ( $P_f = 0.5$ ) of a Weibull distribution described by a two-parameter formula is given by  $k(\ln 2)^{1/m}$  (Johnson & Kotz, 1970). Figure 3.11 focuses on median strength values as a function of grain radius  $R$  (i.e. taking  $2R$  equal to the measured grain diameter  $x$ ), calculated for the wet crushing tests with brass substrate, using this relation and the  $m$  and  $k$  parameters listed in Tables 3.2 and 3.3. In addition, lower and upper median strength data are determined from Table 3.2 using the standard errors in  $m$  and  $m \ln k$ . In case of surface flaws causing failure, the slope of lines fitting the median strength data should be equal to  $-2/m$  according to eqn. 13 (with  $R_g = R$ ), yielding  $m = 8$  for the entire sample of grains. Since this value is well outside the 95% confidence intervals given for the moduli  $m$  listed in Tables 3.2 and 3.3, it is inferred that the Weibull weakest link model developed in this chapter is not able to account for the observed grain size dependence of the grain failure stress. The case of volume flaws causing failure is not considered since the Hertzian failure criterion employed in the calculation of the strength applies only to failure arising from surface flaws.

#### *Applicability of the Hertzian/LEFM model*

The grain size ( $d$ ) dependence of the critical load at failure ( $F_c$ ) as deduced from Figures 3.4 and 3.5 differs from that predicted by the Hertzian/LEFM model which predicts  $F_c \propto d^2$ . If the basic Hertzian/LEFM assumptions of the model are correct, this implies that either the flaw dimension at failure or the effective grain contact or asperity radius must be functionally related to grain size  $d = 2R_g$ . To examine this possibility, the  $F_c$  data (i.e. distributions) represented in Figures 3.4 and 3.5 have been translated into distributions of 1) flaw size at failure ( $c_f$ ) assuming a perfectly spherical grain geometry and using eqn. 6 with  $x = d = 2R_g$ , and 2) into distributions of "effective" grain radii of curvature ( $r_g$ ) characterising asperity amplitude. In the latter case the model is applied dropping the assumption of spherical grains, using the relation  $R_g = r_g$  in eqn. 6 and assuming constant  $c_f$  (taken equal to the mean or lower bound value obtained from the selected grain tests).

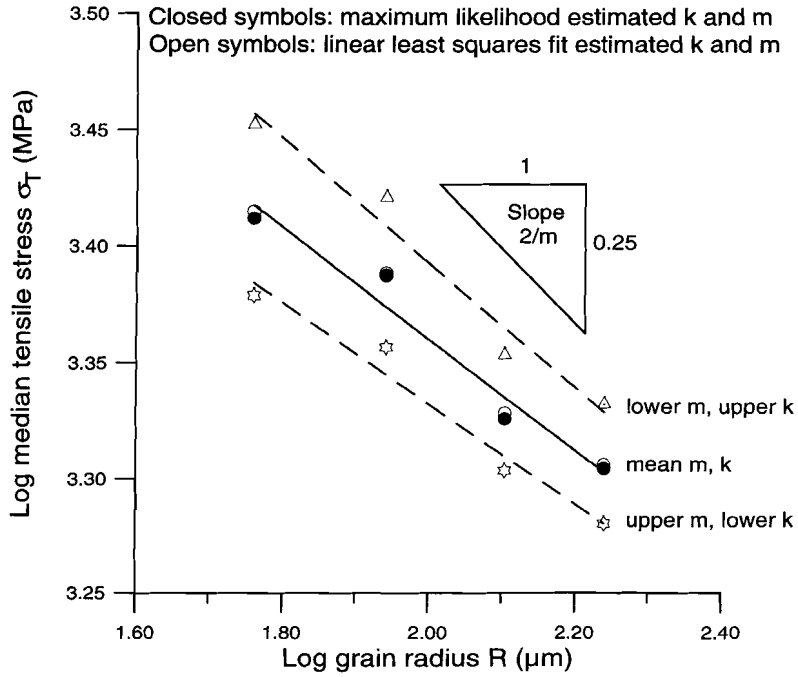


**Figure 3.11.** Log-log plot of median failure stress ( $\sigma_f = \sigma_T$ ) vs. mean grain radius constructed for the wet crushing tests on sand grain batches performed using brass substrate ( $50 \mu\text{m}$  foil) and with grains immersed in a drop of distilled water. The Weibull model for grain failure is adopted assuming spherical grains and using the Weibull parameters  $k$  and  $m$  listed in Tables 3.2 and 3.3. Upper and lower  $k$  and  $m$  values represent  $k$  and  $m$  values  $\pm$  standard error. Linear least squares fitting of the data yields a slope of  $\sim -0.25$ . In case of surface flaws causing failure this resembles a Weibull modulus  $m \approx 8$  for the entire sample of grains, notably unequal to the moduli obtained for each size batch.

Typical histograms of translated  $c_f$  and  $r_g$  values obtained in the above manner from the  $F_c$ -data depicted in Figure 3.3 are shown in Figures 3.12 and 3.13 (using mean  $c_f$ ).

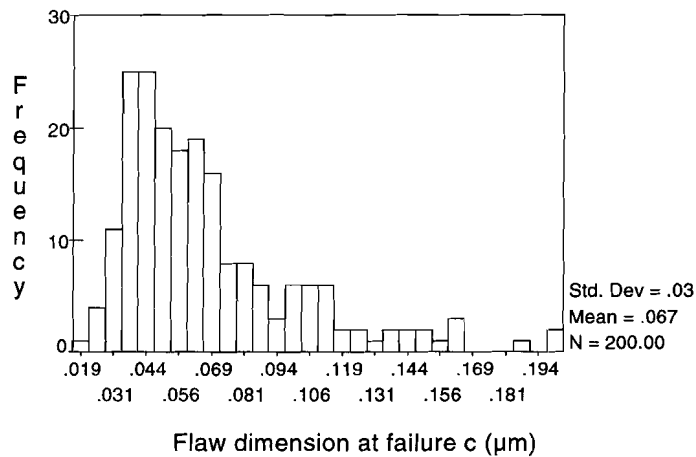


**Figure 3.12.** Typical histogram of flaw dimension at failure constructed by translating the critical force at failure data of Figure 3.3 (250-300  $\mu\text{m}$  grain size batch) using the Hertzian/LEFM model applied assuming spherical grains with radius of curvature equal to half the measured initial grain diameter.

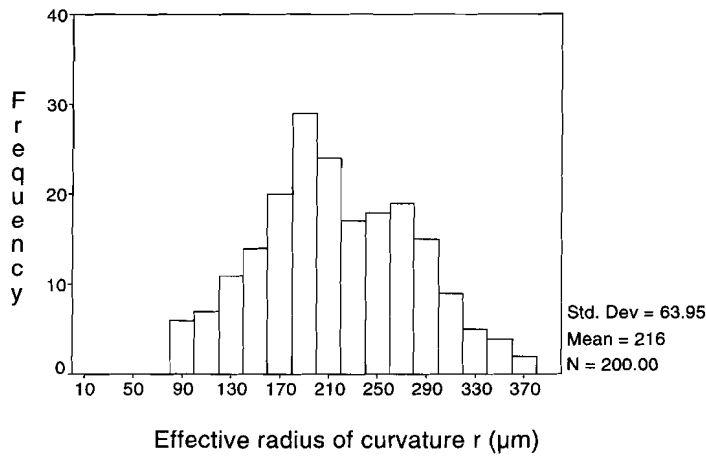


**Figure 3.13.** Typical histogram of effective radius of curvature constructed by translating the critical force at failure data of Figure 3.3 (250-300  $\mu\text{m}$  grain size batch) using the Hertzian/LEFM model applied assuming non-spherical grains and a constant flaw dimension at failure equal to 0.115  $\mu\text{m}$ .

For all batches tested, however, the distributed  $c_f$  values approximately follow a log-normal distribution and the  $r_g$  values a normal distribution. This enables arithmetic averages (means) and sample standard deviations of  $\ln c_f$  and  $r_g$  to be calculated employing the appropriate distribution models. The means of the  $c_f$  and  $r_g$  distributions obtained from the  $F_c$  data of the size fractions represented in Figure 3.4 are plotted as a function of grain size ( $d$ ) in Figures 3.14 and 3.15. The grain size plotted is either the mean measured initial grain diameter ( $x$ ) or the equivalent-sphere grain size calculated from the average grain mass; error bars represent standard errors (see section 3.4.2). These plots show that both  $c_f$  and  $r_g$  can be described proportional to  $d^f$  where  $f \approx 0.5$ -0.7. A similar relation is obtained if the lower bound estimate for  $c_f$  is used. If the  $F_c$  data depicted in Figure 3.5 (obtained from crushing tests using teflon substrate under "lab dry" condition) are likewise treated, similar results are obtained with  $f \approx 0.45$ -0.7. To compliment the (log-)normal distribution statistics obtained for  $c_f$  and  $r_g$ , fitting a Weibull density function to histograms of the translated  $c_f$  and  $r_g$  values for each batch tested in wet condition using brass substrate, and employing the previously treated method of maximum likelihood estimation, yields estimates for the Weibull parameters  $m$  and  $k$  listed in Table 3.4.

**Table 3.4.** Weibull parameters of distributions of flaw dimension at failure ( $c_f$ ) and effective radius of curvature ( $r_g$ ) obtained by maximum likelihood estimation.  
Data for grain size batches tested wet and using brass substrate.

Distribution	Weibull parameter	Grain size $d$ ( $\mu\text{m}$ )			
		$115 \pm 9$	$196 \pm 16$	$275 \pm 25$	$378 \pm 22$
$c_f$	$m$	2.35	2.47	2.10	2.37
	$k$ ( $\mu\text{m}$ )	0.050	0.056	0.076	0.081
$r_g$ ( $c_f = 0.115 \mu\text{m}$ )	$m$	3.54	3.92	3.73	3.90
	$k$ ( $\mu\text{m}$ )	146	202	239	302
$r_g$ ( $c_f = 0.05 \mu\text{m}$ )	$m$	3.54	3.92	3.73	3.90
	$k$ ( $\mu\text{m}$ )	78	108	128	162

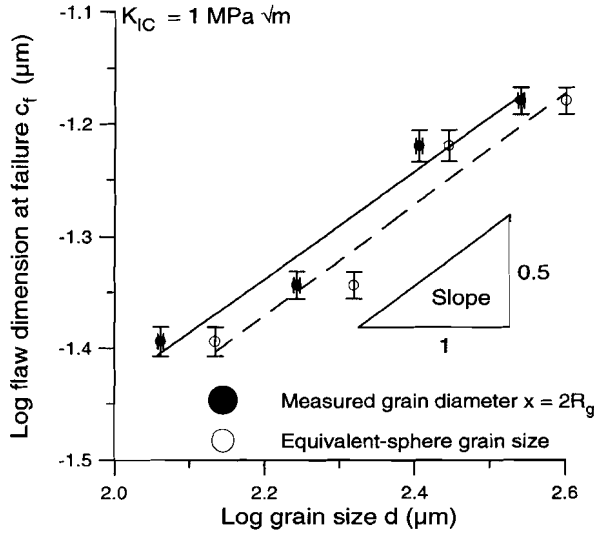


**Figure 3.14.** Log-log plot of mean flaw dimension at failure ( $c_f$ ) vs. mean grain size ( $d$ ) constructed by translating the critical force at failure data of Figure 3.4 using the Hertzian/LEFM model applied assuming spherical grains with radius of curvature  $R_g$  equal to half the measured initial grain diameter. Note that  $c_f$  can be considered proportional to  $d^f$  where  $f \approx 0.5$ .

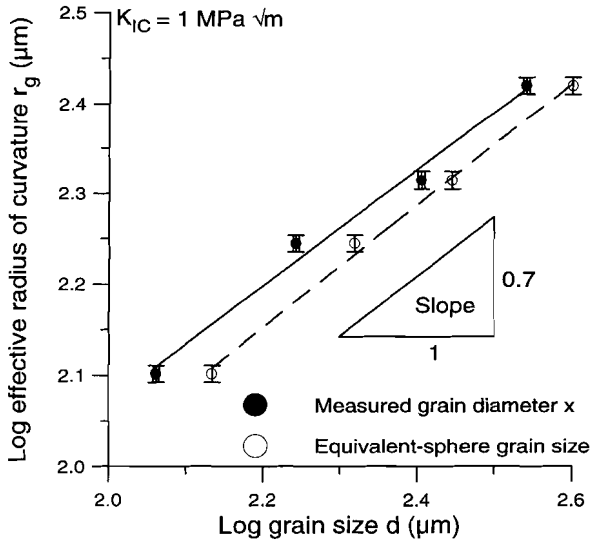


**Figure 3.15.** Log-log plot of mean effective radius of curvature ( $r_g$ ) vs. mean grain size ( $d$ ) constructed by translating the critical force at failure data of Figure 3.4 using the Hertzian/LEFM model applied assuming non-spherical grains and a constant flaw dimension at failure equal to  $0.115 \mu\text{m}$ . Note that  $r_g$  can be considered proportional to  $d^f$  where  $f \approx 0.7$ .

In order to decide if there is any physical basis for expecting  $c_f$  or  $r_g$  to be related to  $d$  in the manner documented above, grain microstructural constraints will now be examined. Firstly, the sand grains used in this study are not spherical whereas a perfectly spherical grain geometry is assumed for computing  $c_f$  from  $F_c$ . Moreover, if the flaws at the surface of the sand grains are assumed to be generated due to grain collision and abrasion during sedimentary transport, there is no physical basis to argue that their initial dimension ( $c_0$ ) (or the mean of their size distribution) should be grain size dependent. In addition, the selected grains with visibly spherical or ellipsoidal contact surfaces do not show a systematic relation between flaw size at failure ( $c_f$ ) and grain size (see section 3.5.1). These arguments (coupled with the assumption that  $c_f = c_0$ , cf. section 3.5.1) suggest that the observed grain failure behaviour cannot be explained by a Hertzian/LEFM model in combination with a grain size dependent flaw size ( $c_f$ ).

Secondly, it is important to consider that in sedimentary petrology the shape or external morphology of quartz sand grains is characterised by independent properties of form, roundness and surface texture distinguishable by their different scales with respect to grain size (Barrett, 1980). *Form* can be estimated by elongation parameters based on ratios involving orthogonal principal axes ( $a_e > b_e > c_e$ ) of assumed ellipsoidal grains. It may also be quantified in terms of *sphericity*, defined as  $d/a_e$  (Wadell, 1932, 1935),  $(b_e c_e / a_e^2)^{1/3}$  (Krumbein, 1941),  $(c_e^2 / a_e b_e)^{1/3}$  (Folk, 1955; Sneed & Folk, 1958) or  $\sqrt[3]{(R_{ins}/R_{ci})}$  (Riley, 1941) where  $R_{ins}$  is the radius of the largest inscribed sphere and  $R_{ci}$  is the radius of the smallest circumscribed sphere. *Roundness* reflects grain angularity or surface roughness caused by variations in radii of curvature of edges, corners and faces. It may be quantified as  $(\sum(r_i/R_{in}))/n$  (Wadell, 1932) or  $r_s/R_{in}$  (Dobkins & Folk, 1970; Folk, 1978) where  $r_i$  is the radius of curvature of the  $i$ -th grain corner (of a total  $n$ ) and  $r_s$  is the radius of curvature of the sharpest corner (Barrett, 1980). Sphericity and roundness defined as above can be quantified in the context of the present investigation using a simple geometric model implying the following relations

$$r_g \approx R_{ci} - R_{ins} \approx \frac{\sum_{i=1}^n r_i}{n} \approx r_s \quad (16)$$

$$a_e \approx 2R_{ci} \quad \text{and} \quad c_e \approx b_e \approx 2R_{ins}$$

$$d \approx 2R_{ins}$$

Figure 3.16 shows sphericity and roundness data compiled from morphology studies on dune sands of various grain size ( $d$ ) translated into  $r_g$  vs  $d$  plots. Furthermore, roundness ( $r_s/R_{in}$ ) has been determined in thin section of a random sample of grains from three out of four grain size fractions used in this study. The average roundness values obtained for each fraction are likewise translated into  $r_g$  vs  $d$  data using the

relations given in eqn. 16 and added to Figure 3.16. The data depicted in this graph show  $r_g$  to be approximately proportional to  $d^f$  where  $f \approx 0.65 - 1.3$ . This kind of relationship is well known in sedimentary petrology and has been attributed to more effective abrasion of larger sized particles (Donaldson *et al.*, 1995a). Notably, this relation is in reasonable agreement with the  $r_g$  vs  $d$  plot of Figure 3.15. On this basis, it is inferred that the observed grain failure behaviour (batch tests, wet condition, brass or teflon substrate) is best explained by a Hertzian/LEFM model in combination with grain size dependent sphericity / roundness as expressed by the effective radius of curvature ( $r_g$ ).

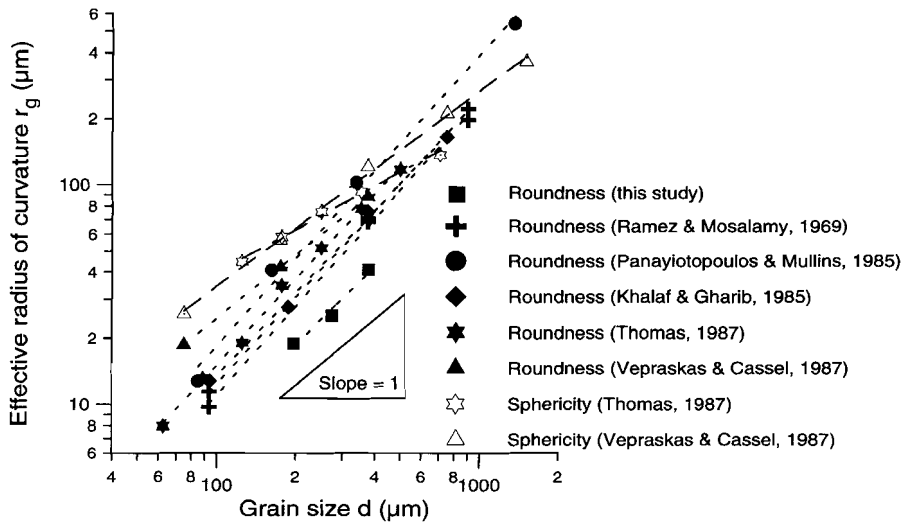


**Figure 3.16.** Log-log plot of effective radius of curvature ( $r_g$ ) vs. grain size ( $d$ ) constructed by translating sphericity and roundness data compiled from morphology studies on dune (aeolian) sands. The figure includes roundness data determined from grain size fractions used in this study. The data show that  $r_g$  can be considered proportional to  $d^f$  where  $f \approx 0.65-1.3$ , which is in reasonable agreement with the grain size dependence of  $r_g$  expressed in Figure 3.15.

### 3.6 CONCLUSIONS

Crushing tests have been carried out on selected, well-rounded single sand grains and on grains sampled from different grain size batches. Applying a Hertzian/LEFM model, the grain failure load ( $F_c$ ) data obtained for the selected grains have been translated into an accurate estimate of the size of surface flaws at failure ( $c_f$ ). Likewise, the distributed  $F_c$  data obtained for the different batches have been translated into distributions of failure stress ( $\sigma_f$ ). Assuming a single flaw population causing grain failure and spherical grains, a Weibull weakest link model is unable to account for an observed grain size dependence of  $\sigma_f$ . The Hertzian/LEFM model enables the translation of the distributed  $F_c$  data into distributions of  $c_f$  or effective radius of curvature ( $r_g$ ). The data imply  $c_c$  or  $r_g$  to be proportional to the grain size ( $d$ ) as  $d^f$  where  $f \approx 0.5-0.7$ . Since there is no clear physical basis for a grain size dependence of  $c_f$  and since sphericity and roundness data for dune sands exhibit a similar relation between  $r_g$  and  $d$ , it is inferred that the Hertzian/LEFM model assuming non-spherical grains with a distributed  $r_g$ , caused by surface asperities, is the most physically reasonable model for grain failure. In other words, grain failure is inferred to be controlled by propagation of surface cracks at loaded asperities under the action of the Hertzian contact stresses which take a maximum value at the contact periphery. This work provides insight into grain failure and could, therefore, shed light on the micromechanics of sand compaction used in modelling studies of both upper-crustal deformation and the compaction of clastic hydrocarbon reservoirs in the (post-)production phase.



## CHAPTER 4 TIME-INDEPENDENT COMPACTION BEHAVIOUR OF SANDS

### 4.1 INTRODUCTION

The time-independent volumetric compaction behaviour of sands, that is instantaneous compaction for which creep effects are negligible, forms a subject of major relevance in a number of areas of the Earth sciences and geomechanics. For example, time-independent compaction processes, such as grain breakage and rearrangement, operative in clastic porous sediments are believed to play an important role in determining porosity and permeability reduction during burial, alongside time-dependent processes such as pressure solution (Groshong, 1988; Schutjens, 1991a,b; Milliken, 1994; Onasch, 1994). Similar time-independent compaction effects can be expected to occur in fault gouge materials produced in seismically active faults and may play an important role in controlling changes in the fluid transport properties of such faults as a result of changes of the in-situ stress state (Marone & Scholz, 1989; Rice, 1992; King & Sammis, 1992).

In addition, considerable attention has been focused in the last decades on the time-independent compaction behaviour of water- and hydrocarbon-bearing clastic reservoirs with a view to predicting production-related subsidence effects (Zoback & Byerlee, 1976; Segall, 1992). Recently, data on the instantaneous compaction behaviour of sands and sandstones has also become essential input for modelling the effects of downhole methods used for the enhancement of reservoir permeability and hydrocarbon recovery rates, e.g. the shaped-charge jet perforation method (Papamichos *et al.*, 1993). Furthermore, the compaction behaviour of sands is highly relevant to modelling the response of oil sands during cyclic steam stimulation (Wong *et al.*, 1993), a technique which is expected to significantly improve recovery rates from such formations.

Of course, in civil engineering (soil mechanics) the time-independent compaction behaviour of sands has long received attention in the context of assessing the settlement and stability of deep foundations (Lee & Farhoomand, 1967; Vesić & Clough, 1968). Finally, aside from Earth sciences and geo-engineering, the compaction behaviour of granular materials is of great interest in materials science (powder technology), notably with respect to the cold pressing of ceramic powders as a first stage in the preparation of advanced materials (Swinkels *et al.*, 1983; Helle *et al.*, 1985; Jagota *et al.*, 1988).

Because of the above mentioned areas of interest, a great deal of work has been done on sand and granular materials compaction from both experimental and theoretical points of view. Experimental studies have been carried out into the time-independent compaction behaviour of sands under both one-dimensional and hydrostatic compression conditions (e.g. Lambe & Whitmann, 1979). These have typically shown non-linear stress-strain behaviour with part of the deformation

being elastic, presumably as a result of grain contact distortion, and part being permanent, inferred to be due to rolling- or sliding-induced grain rearrangement (Roberts & de Souza, 1958; Ko & Scott, 1967; Lambe & Whitmann, 1979). At higher stresses ( $> 7$  MPa), grain crushing enhances further compaction, as revealed by major grain size reduction and sometimes audible cracking sounds (Roberts & de Souza, 1958; Lambe & Whitmann, 1979; Gill *et al.*, 1990); microstructurally, sands deformed at high stresses exhibit transgranular cracks radiating from the points of contact of neighbouring grains (Maxwell, 1960; Borg *et al.*, 1960). In general, the overall compressibility of the sands (including elastic and permanent effects) is known to be favoured by higher initial porosity, increasing grain angularity, increasing grain size and size uniformity, and decreasing intrinsic grain strength (Borg *et al.*, 1960; Zoback & Byerlee, 1976; Lambe & Whitmann, 1979; Lee & Farhoomand, 1967; Vesić & Clough, 1968). However, many of these effects have not been investigated systematically and are not well understood at the level of a quantitative mechanism-based description. In particular, there have been few systematic investigations into the somewhat enigmatic effect of grain size on the compaction behaviour of sands (an exception is the pioneering work by Borg *et al.* and Lee & Farhoomand), or into the detailed role of microcracking using acoustic emission (AE) techniques or microstructural analysis.

Theoretical and numerical modelling studies of the compaction of granular media have been largely based on the consideration of the elastic contact distortion of a 2-D or 3-D array of spherical grains, in most cases allowing for intergranular frictional sliding rearrangements and considering non-hydrostatic states of stress (for overview see Shen *et al.*, 1991; Thornton, 1993; Mehta, 1994). Few attempts have been made to incorporate the effects of brittle grain crushing via an appropriate fracture mechanics approach, though the papers by Issa & Nelson (1989), Ouwerkerk (1991), Papamichos *et al.* (1993) and Liu *et al.* (1993) do to some extent allow for particle failure. In these papers, however, grain failure is not related to a microphysical mechanism but is described only in threshold strength terms.

In summary of previous work then, the majority of experimental data for sand compaction suffer from the disadvantage that the operative microcracking mechanisms and effects of grain size have not been thoroughly investigated. In the case of theoretical and numerical studies, microphysical aspects of grain failure have not been incorporated and the effects of grain size observed in compaction experiments cannot be explained (cf. Zhang *et al.*, 1990a,b, for sandstones).

This chapter is concerned with both experimental and theoretical aspects of the compaction behaviour of sands. It begins with a brief review of the mechanisms capable of producing sand compaction. It proceeds to report one-dimensional compaction experiments designed to systematically investigate the effect of initial porosity, loading history, loading rate, chemical environment and grain size on the compaction behaviour of sands at room temperature. Acoustic emission (AE) detection and microstructural methods are used to gain insight into the microphysical mechanisms operative. Results are compared with a simple micro-

physical model for the compaction of sands based on the Hertzian / LEFM model developed in chapter 3, allowing for grain contact crushing plus elastic contact distortion. In accordance with the conclusions drawn from the single grain crushing experiments reported in chapter 3, the model satisfactorily accounts for the grain size effect observed in the compaction tests on sands in terms of a grain size dependence of grain strength reflecting a grain size dependent departure from sphericity.

## 4.2 MICROSTRUCTURAL FACTORS AND MECHANISMS CONTROLLING COMPACTION

Before describing the present sand experiments, it is useful to review briefly the background concerning the microstructural factors and mechanisms controlling the time-independent compaction behaviour of dry sands and granular materials in general.

The mechanical response of non-cohesive granular materials exhibits complex behaviour such as dual discrete / continuum characteristics (so called "double identity" - Barker, 1994), and is affected by numerous *microstructural factors and reorganization processes* (for overview see Bideau & Hansen, 1993 and Mehta, 1994). These include geometrical disorder (Guyon *et al.*, 1990; Roux *et al.*, 1993; Barker, 1994), contact disorder (i.e. heterogeneity of particle interaction - Roux *et al.*, 1993; Troadec & Dodds, 1993; Adams & Briscoe, 1994), heterogeneity of grain strength properties (Myer *et al.*, 1992; Liu *et al.*, 1993; Adams & Briscoe, 1994), grain shape statistics (Liu *et al.*, 1993, Troadec & Dodds, 1993; Barker, 1994; Behringer & Baxter, 1994; Adams & Briscoe, 1994), non-sequential reorganisation (i.e. interactive or collective restructuring of grain arrays - Barker, 1994) and the development of load supporting grain networks (chains, bonds). The last are manifested by arches of stress-conducting grains surrounding unstressed, free grains (Behringer & Baxter, 1994; Adams & Briscoe, 1994). Beyond the elastic range, such chains are irreversibly broken and continuously remade and in such an assembly a non-uniform strain distribution is characteristic (Behringer & Baxter, 1994; Adams & Briscoe, 1994).

Bearing in mind these microstructural factors and reorganization processes, it is well established from the fields of rock, soil and granular mechanics, and from materials science (powder technology), that a granular aggregate of non-cohesive particles subjected to hydrostatic or uniaxial compactional loading can deform by a variety of basic *mechanisms* (e.g. Wong *et al.*, 1993). The essentials are outlined below:

- a. Firstly, spherical particles, if rigid and strong, will rearrange by rolling or sliding until the aggregate "locks up" (a meta-stable equilibrium) (Rowe, 1962; Horne, 1965; cf. Wong *et al.*, 1993, Behringer & Baxter, 1994; Adams & Briscoe, 1994).

- b. In the case of real materials with non-spherical particles, the same type of locking behaviour occurs; rearrangement and compaction after the "interlocking" stage is only possible if deformation of contact asperities or edges occurs (Gallagher *et al.*, 1974; Lambe & Whitman, 1979; Fischmeister & Arzt, 1983; Behringer & Baxter, 1994; Adams & Briscoe, 1994).
- c. If the particles behave elastically, post-locking compaction can occur by contact distortion due to normal loading (as described by classical Hertzian theory) combined with localized frictional sliding due to tangential loading. In this case, the physical integrity of the particles is maintained. Compaction (aggregate compressibility) by this mechanism has been modelled analytically for *regular lattices* of spheres by Mindlin (1954), Duffy & Mindlin (1957) and by Deresiewicz (1958). Ko & Scott (1967) have developed similar expressions for a *random* arrangement of clusters of regular arrays of spheres under normal loading, considering grain angularity and distributed intergranular gap width. Micromechanical models for the mechanical response of a granular material under quasi-static and non-hydrostatic loading conditions, in which the material is modelled as a random assembly of elastic disk-shaped or spherical particles interacting through frictional sliding and normal contact forces, have been developed by Jenkins *et al.* (1989), Bathurst & Rothenburg (1990), Subhash *et al.*, (1991), Chang *et al.*, (1992a,b), Mehrabadi *et al.* (1992, 1993), Rothenburg & Bathurst (1993), Chang (1993) and Kruyt (1994). These models have been used as a basis for numerical simulations employing the discrete element method (DEM) following Cundall & Strack (1979).
- d. Beyond the elastic range, further compaction of real granular materials can only occur by brittle or internal deformation of the particles and/or grain contacts, permitting accommodation by rolling or sliding. At low temperatures, i.e. for clastic rock materials under upper-crustal conditions, grain or asperity crushing will occur if stress concentrations at grain contacts exceed the material strength (Zhang *et al.*, 1990a,b). At elevated temperatures, particles or asperities may deform by intracrystalline or diffusive processes (Arzt *et al.*, 1983; Spiers & Brzesowsky, 1993). Recently, micromechanical models have been developed for the compaction of granular materials employing the DEM as cited above, allowing not only for elastic distortion and frictional rearrangement, but also for grain failure by introducing a distribution of grain and/or intergranular bond strengths (Issa & Nelson, 1989; Ouwerkerk, 1991; Papamichos *et al.*, 1993; Liu *et al.*, 1993).

### 4.3 EXPERIMENTAL TECHNIQUES

The present experiments consisted of a series of load-cycling, uniaxial compaction experiments performed on sands, focusing on the effect of initial porosity, loading history, loading rate, chemical environment (dry versus drained conditions, aqueous versus inert pore fluid) and grain size.

#### 4.3.1 Starting material and sample preparation

Sand for use in the present experiments was obtained by taking fresh samples of the Heksenberg Formation (Middle Miocene age) from the "Beaujean" quarry near Heerlen, The Netherlands. The sand has been characterised as a beach or dune deposit by Kuyl (1975) and shows a grain size of  $251 \pm 46 \mu\text{m}$ . X-ray diffraction (XRD) analysis and inductively coupled plasma emission spectroscopy (ICP-ES) measurements indicate a quartz content of at least 99 wt % with zircon and Na-rich feldspar present as principal trace minerals. In reflected light, some sand grains ( $< 0.5 \%$ ) show a thin surface layer of iron oxide / hydroxide; this observation is supported by a 0.02 wt % Fe ICP-ES measurement. Imaged using scanning electron microscopy (SEM) (see Figure 4.1a), most sand grains appear as subrounded and show a generally smooth surface with patches (dimension  $50 \mu\text{m}$ ) of rounded and triangular pits (dimension  $5\text{-}15 \mu\text{m}$ ), with grooves (dimension  $5 \times 50 \mu\text{m}$ ) and depressions (dimension  $50 \mu\text{m}$ ) created by broken out fragments. In thin section (see Figure 4.1b), they are seen to be mostly intact (no loss of cohesion of the grains is observed). About 97-98 % of the total population of grains are monocrystalline and subrounded (ranging subangular to rounded). The majority of these grains ( $\sim 60 \%$  of the total) contain intersecting patterns of inclusion trails (inferred to originate from healed intragranular cracks), while only a few ( $\sim 10 \%$  of the total) exhibit "closed" (non-healed) intragranular cracks subparallel to the inclusion trails. Some of the monocrystalline grains ( $\sim 15 \%$ ) exhibit undulatory extinction, while only a few ( $< 5 \%$ ) contain inclusion trails following the grain profile (i.e. "dust rims") and/or "open" intragranular cracks (visible since filled with epoxy resin coloured with blue dye). Fewer than 2-3 % of the total population of grains are polycrystalline and subangular to subrounded. These grains contain subgrains, (randomly oriented) inclusion trails and (short) intragranular cracks.

Fractions of the sand, with grain sizes of  $196 \pm 16$ ,  $275 \pm 25$  and  $378 \pm 22 \mu\text{m}$ , were prepared using a Retsch Ltd. sieving machine and thread-woven sieves (DIN 4188 or ASTM mesh size). From the sieved fractions, the feldspar trace material was successfully removed using two gravitational separation methods; i.e. applying a heavy liquid (bromoform) separation technique ( $196 \pm 16 \mu\text{m}$  and  $378 \pm 22 \mu\text{m}$  fractions) or by washing in water ( $275 \pm 25 \mu\text{m}$  fraction). The present compaction tests were carried out using constant mass (7.5 gram) samples taken from the three sieved fractions.

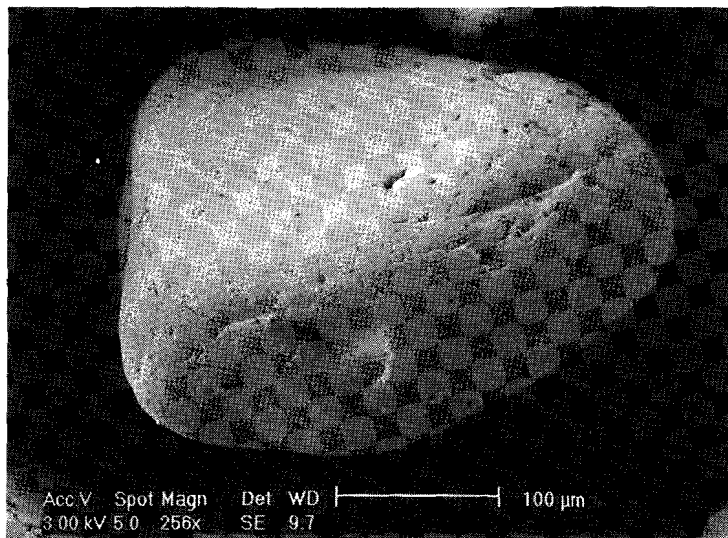
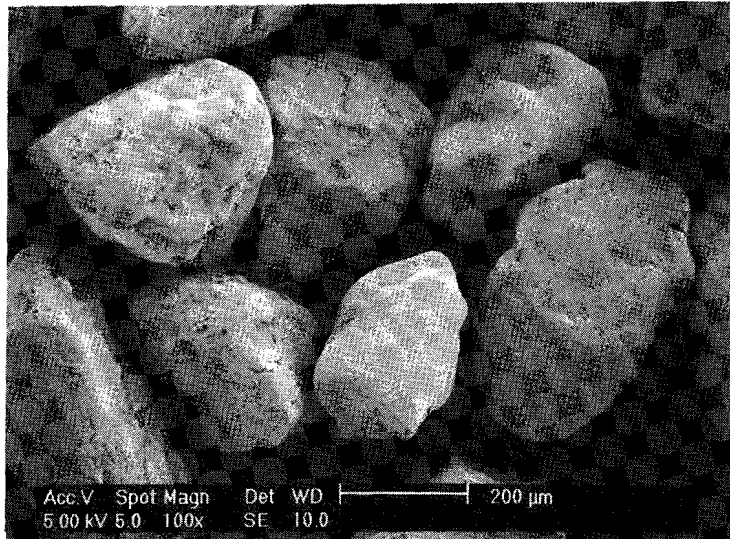
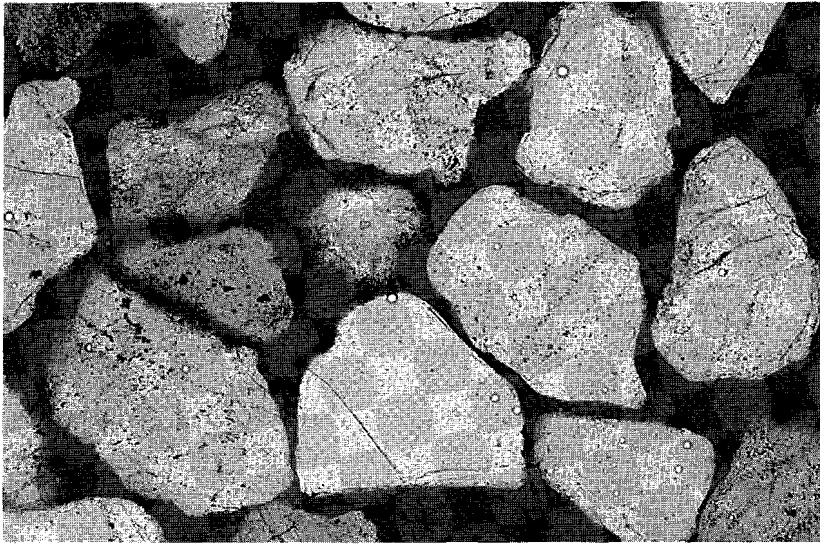
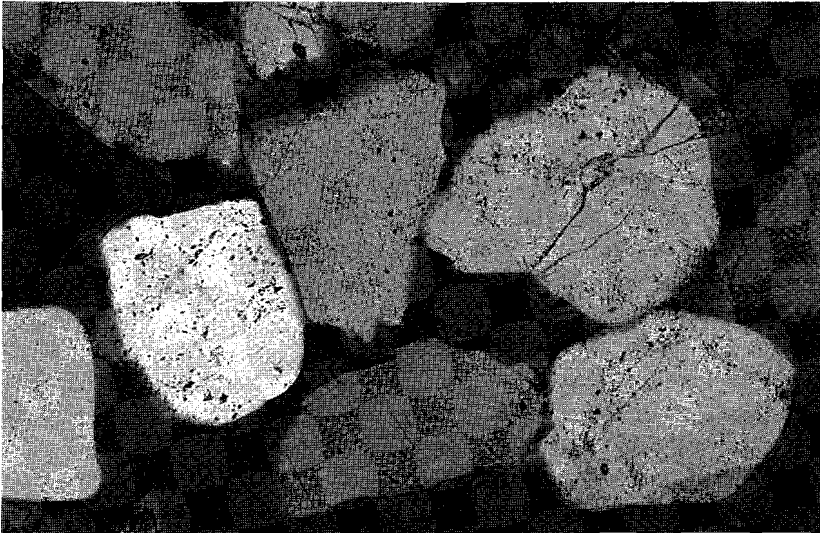


**Figure 4.1a.** SEM micrographs of the Heksenberg sand used in the present compaction experiments (starting material, sieved grain size fraction  $275 \pm 25 \mu\text{m}$ , washed) illustrating that most sand grains appear as sub-rounded and show a generally smooth surface with patches of pits (dimension  $5\text{-}15 \mu\text{m}$ ), with grooves / scratches (dimension  $5 \times 50 \mu\text{m}$ ) and depressions (dimension  $50 \mu\text{m}$ ) created by broken out fragments.



150  $\mu\text{m}$



150  $\mu\text{m}$

**Figure 4.1b.** Optical micrographs of the Heksenberg sand used in the present compaction experiments (starting material, sieved grain size fraction  $275 \pm 25 \mu\text{m}$ , washed) showing that grains are mostly intact with only a few grains (about 10 % of the total) exhibiting "closed" intragranular microcracks. About 60 % of the grains contain intersecting patterns of subparallel fluid inclusion trails.

#### 4.3.2 Compaction apparatus and calibration

The compaction experiments were performed on individual sand samples, at room temperature, under both dry (lab or "vacuum dry") and drained (fluid-flooded) conditions, using the one-dimensional or uniaxial apparatus depicted in Figure 4.2a. This apparatus is a modified version of that described by Schutjens (1991a,b). As described by Schutjens, the compaction vessel and pistons are constructed from Monel K-500, a corrosion resistant Ni-Cu-Al-Fe alloy (DIN NiCu30Al). The main modifications made to the apparatus are as follows.

Firstly, the bottom piston has been divided into two segments, A and B (see Figure 4.2a). The top segment (A) consists of a Monel tip-piece pressed into a hardened stainless steel lower member (DIN X35CrMo17, Werkstoffnr. 1.4122). A piezoelectric ceramic transducer for acoustic emission (AE) detection has been emplaced within the Monel tip and spring-loaded against the flat end of the bore, using greased Teflon foil to ensure good acoustic coupling (see Figure 4.2b).

The disk-shaped AE sensor (thickness 2 mm, diameter 5 mm) is of the lead zirconate titanate type (PZT-6, Fuji Ceramics Co.) and possesses a calibrated resonant frequency of  $\sim 940$  kHz when vibrating in thickness mode. The bore of the lower segment of the bottom piston contains a K-type (chromel-alumel alloy) sheathed thermocouple (resolution  $0.05$  °C) electrically isolated with respect to the piston bore wall by a thin layer of Teflon.

Secondly, a modified Monel 400 porous plate (DIN  $\sim$ NiCu30Fe, sintered plate, initial filtration grade  $40\text{ }\mu\text{m}$ , Mott Metallurgical Co.) has been added to the tip of the top piston, to prevent sand grains from entering the piston bore. A Teflon ring behind this porous plate prevents sand grains from passing between vessel wall and piston. The filter plate was preloaded (i.e. work hardened) at  $60\text{ kN}$  to ensure no deformation would occur during testing. The plate was pressed into the top piston at  $20\text{ kN}$ , this force being maintained for 1 hour to eliminate any time-dependent displacement effects.

Minor changes were also made to the piston seals in that both the top and bottom pistons were equipped with Viton rubber "O"-rings (Shore A hardness  $70^\circ$ ), lubricated using Molykote 111 Compound silicon grease (® Dow Corning Co., vapour pressure  $< 0.7\text{ kPa}$  at  $20^\circ\text{C}$ ).

As described by Schutjens (1991a,b), load was applied to the apparatus via the moveable top piston using an Instron 1362 servo-controlled testing machine. For the present tests, this was operated with a  $10\text{ kN}$  load cell in "load control" mode. Displacement of the loading ram was measured using the linear variable differential transducer (LVDT,  $\pm 50\text{ mm}$  stroke) located in the drive unit of the testing machine. Displacement of the top piston relative to the vessel was measured using a Sangamo precision LVDT, with a  $\pm 5\text{ mm}$  stroke, mounted on the top piston (see Figure 4.2a).



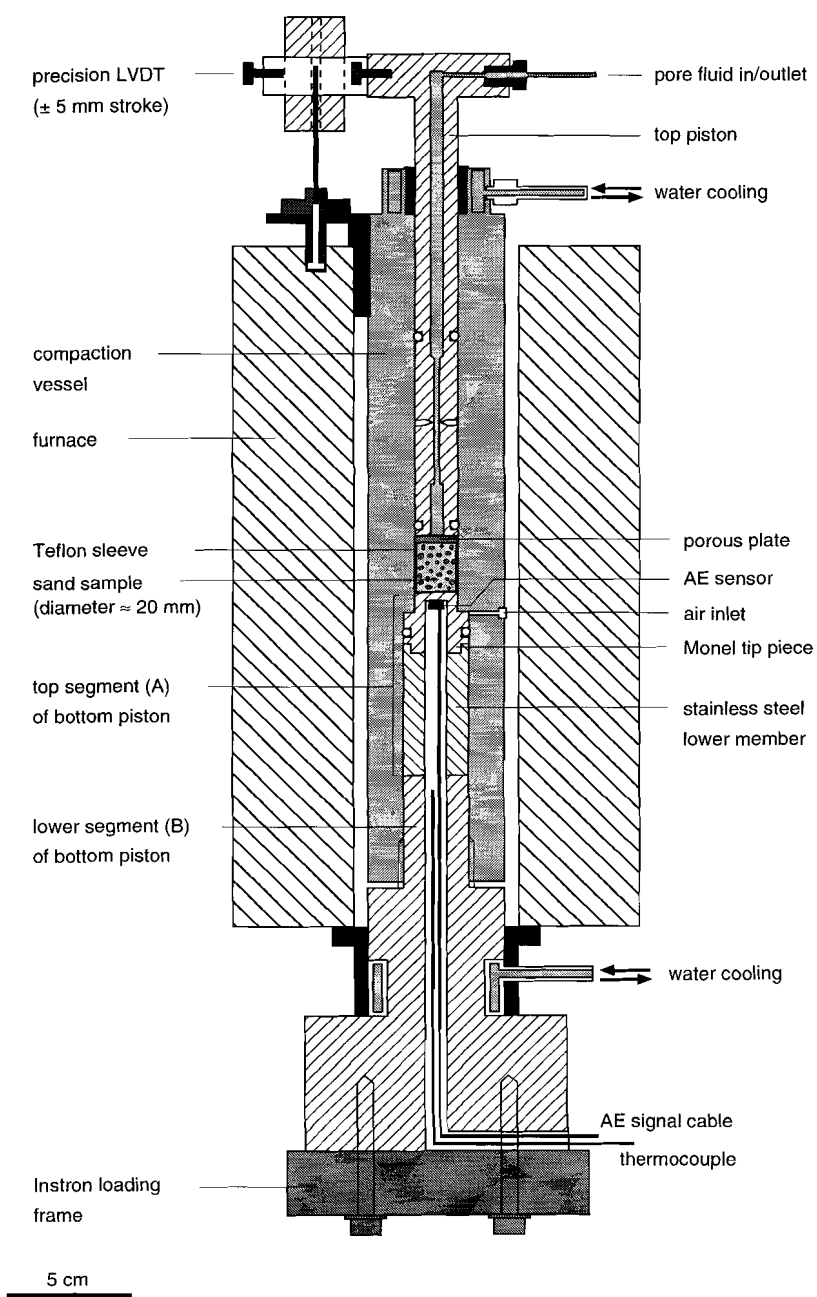


**Figure 4.2a.** *Semi-schematic diagram showing the one-dimensional or uniaxial deformation apparatus used in the present compaction experiments on sands.*

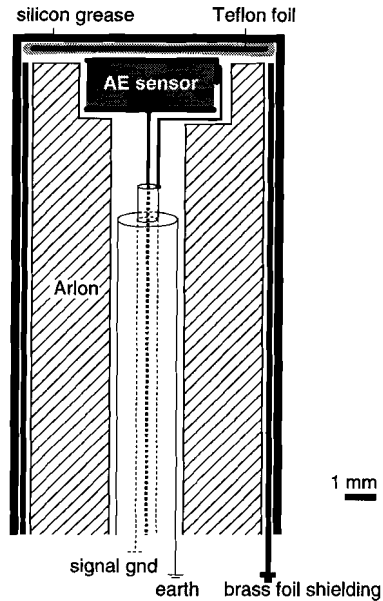


**Figure 4.2b.** Detailed section of the bore of the Monel tip piece, situated in the top segment of the bottom piston, showing the transducer for acoustic emission (AE) detection, spring loaded against the flat end of the bore by the hollow Arlon rod. The greased Teflon foil ensures good acoustic coupling.

The Sangamo LVDT was directly calibrated, in the range  $\pm 5$  mm, using a 0.01 mm resolution Mitutoyo micrometer screw gauge (range 75-100 mm) and a digital Volt meter with a  $\pm 0.05$  % recorded value accuracy resulting in an overall resolution of 0.1  $\mu$ m. The accuracies of the Instron load cell and LVDT have been assumed equal to the manufacturer's specifications (max. error  $\pm 0.1$  % of full scale range). Calibration of the stiffness characteristics of the apparatus, as measured by both LVDT's, was carried out using a Monel K-500 cylindrical dummy with a length similar to the sand sample ( $\sim 15$  mm) and a diameter equal to 18 mm, cycling the applied load in the range 0 - 9.8 kN and employing a constant loading rate in the range 341-472 MPa/hour. Between consecutive loading cycles, the apparatus was taken apart in order to take into account the effect of piston repositioning relative to the loading frame. Since the elastic distortion of the pistons was found to be non-linear, tenth-order polynomials were fitted to the force-displacement data obtained for both LVDT's. This behaviour is thought to be due to the presence of the porous plate. During the calibration loading tests, no AE activity was detected.

### 4.3.3 Acoustic emission system

The acoustic emission (AE) activity monitoring system used in this study was specially designed and built in the HPT laboratory at Utrecht. Like all such systems, it enabled sensing, amplification, frequency filtering, discrimination and counting of wave packets emanating from microseismic events within the sand sample. The low level AE signals required amplification of around 1000x (60 dB gain) before discrimination from background noise on the basis of amplitude. Subsequent counting was limited to whole wave packets (single events) by blocking the digital counters for a controlled period, of the order of typical packet durations, immediately after each packet arrival. The maximum effective AE event rate countable by the system was ~ 500 events per second. The details of the system are described below (see Figure 4.3a).

The output of the AE sensor, located in upper segment of the bottom piston (see section 4.3.2), was directly fed, via coaxial cable, into a nearby precision pre-amplifier (36 dB gain) and then further into a remote multistage signal conditioning system. In this system, the signal passed serially through the following elements: i) a variable gain (-8 to 4 dB) buffer, ii) a 100 kHz, fourth-order, high-pass active filter (Butterworth type, with -24 dB/octave roll off and 8 dB gain), and iii) a 1 MHz, sixth-order, low-pass active filter (Butterworth type, with -36 dB/octave rolloff and 12 dB gain). This sequence restricted the amplified signal to a frequency band of 100 kHz - 1 MHz, eliminating low frequency interference and sensor resonance effects. At this stage, the frequency-limited signals had typically experienced 54 dB amplification with a typical noise level of 10 mV peak-to-peak (p-p). The maximum output values of typical AE waveforms were in the range 1 - 10 V p-p. Such signal-to-noise ratios of 40 - 60 dB allowed easy discrimination on amplitude. This was achieved by passing the conditioned AE signal through a parallel pair of discrimination units (channels) each consisting of a fast comparator, to provide adjustable discrimination (threshold) levels, upon which counting of events could be initiated. Each comparator output triggered (digital) monostable ("one-shot") multivibrators sending TTL (transistor-transistor logic) pulses with a preset width or "stretching time" (PST) to a digital counter. These counters were situated on a daughter board in the personal computer (PC) used for logging (see section 4.3.4), each counter having 16 bit capacity and a maximum count rate of 4 MHz. Retriggering of the multivibrator (i.e. starting a further delay cycle) occurs at each rising edge of the AE waveform crossing the comparator threshold during the active duration of the pulse. After the last retriggering, the monostable endures for one further PST which, together with any earlier retriggered delay, is counted as one AE "event" (for details on the electronic components see Tompkins & Webster, 1988; Horowitz & Hill, 1989).

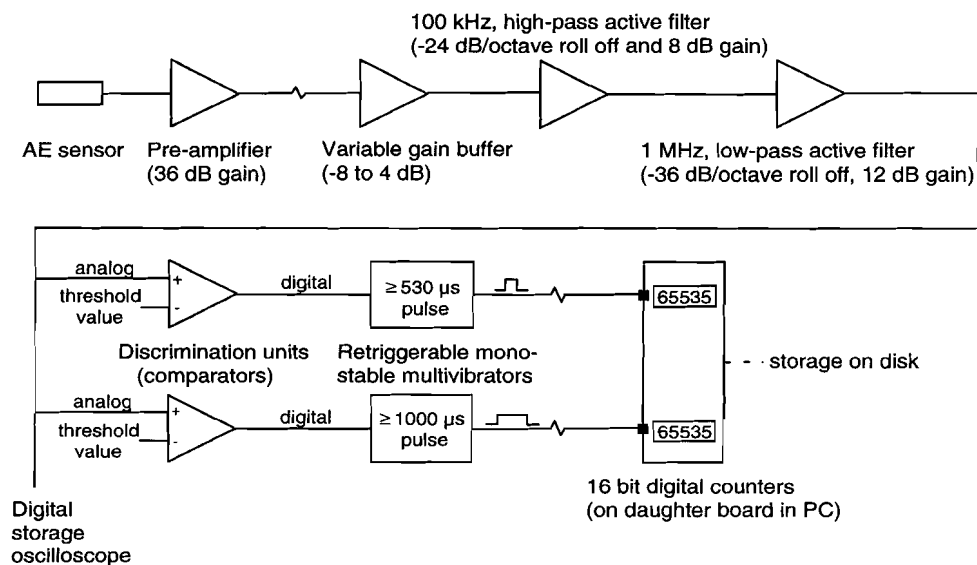


**Figure 4.3a.** Semi-schematic diagram of the acoustic emission (AE) activity monitoring system illustrating the various stages of the signal conditioning system.

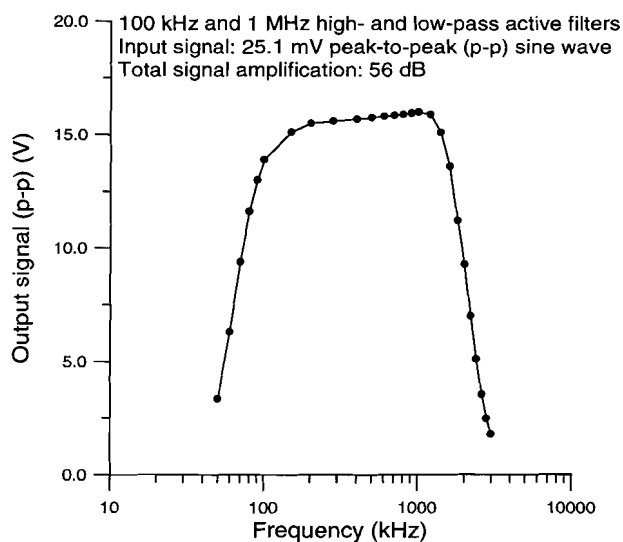


**Figure 4.3b.** Filter output characteristics of the AE signal conditioning system.

For setting up and calibration purposes, the conditioned AE waveform was displayed on a Gould 4072 digital storage oscilloscope (100 MHz bandwidth; maximum sample rate 400 MHz on a 250 ns/division timebase). Using a RS232 serial interface with an Olivetti M24 PC, the waveforms could also be stored on floppy disk with a resolution of 1008 data points per 10 divisions of timebase range. The filter output characteristics of the AE signal conditioning system have been determined using a digitally synthesized function generator (model AFG, Rohde & Schwarz GmbH, with 20 MHz range). A 25.1 mV p-p sine wave input signal, with a frequency in the range 50 kHz - 3 MHz was applied using a total signal amplification of 56 dB. The characteristics are depicted in Figure 4.3b.

During use, a constant discrimination trigger-threshold of 125 mV was set for both counter channels. Triggering of the counting system by random noise was found not to occur for threshold levels set above 15 mV. Total applied signal amplification factors ranged from 48 to 68 dB. Pulse stretching times (PST) of the two counter channels were set to 530 and 1000  $\mu$ s respectively. This served as a check for wave packet arrival-bunching effects; namely, for well spaced events the count rates obtained with the two separate channels should be identical. AE waveforms observed during dry sand compaction typically endure for 1-1.5 ms before the last retriggering. Consequently, the maximum AE event rate countable is estimated to be 500 events per second. The minimum sound velocity (shear waves) in dry sand is 400 m/s and in water-saturated sand 1 km/s (37 % porosity, 35 MPa effective pressure; see Fjaer *et al.*, 1992, page 140 and appendix A.4). Therefore, the first reflected AE signal arrives at the sensor after a maximum of 75  $\mu$ s in dry tests and after 30  $\mu$ s in wet tests; i.e. well within the minimum chosen PST, so that erroneous multiple counting of reflected events was avoided.

#### 4.3.4 Data acquisition / logging

After signal conditioning, the voltage output of the Instron load cell, the Instron LVDT, the Sangamo LVDT and the thermocouple (TC) were recorded on a 6-channel chart recorder (maximum error / non-linearity  $\pm$  0.3 % of full scale range). To obtain maximum accuracy and resolution, the pen-position monitor voltage for each channel was amplified (12 dB linear amplifier unit), digitized using a 16 bit resolution ADC76KG-converter ( $\text{\textcircled{R}}$  Burr Brown Co., maximum non-linearity  $\pm$  0.003 % of full scale range), and logged using a Laser Turbo XT/2 personal computer (PC) equipped with a programmable peripheral interface (PPI) card. The total maximum error of the amplification and the analog-to-digital conversion process was negligible compared with the chart recorder stage.

The continuous logging of the AE counters and the digitized transducer signals by the Laser PC (via the PPI card) was supervised using a specifically developed computer program, DASA EHPT. This program reduces the transducer signals to the (uncorrected) physical quantities which they respectively represent; namely, the load

cell output to force (kN), the output of the Instron and Sangamo LVDT's to displacement (mm) and the TC output to temperature (°C). The program writes these data and the cumulative AE event count to disk at regular time intervals (5, 10 or 300 s, depending on the applied loading rate).

#### 4.3.5 Sample handling & testing procedure

Prior to each test, the fully assembled vessel was placed on a laboratory bench, the top piston was removed, and the loose sand sample was deposited into the open vessel using an elongated glass funnel to prevent grains from sticking to the vessel wall. In all cases, the sample was surrounded by a thin-walled Teflon sleeve or pot (height 16 mm, thickness  $0.13 \pm 0.02$  mm) previously inserted into the bore of the vessel to reduce friction between the sample and the vessel wall. After introduction of the sample, the piston was reinserted into the vessel until the sample was just touched and the vessel was mounted into the Instron frame. The piston was then withdrawn by 1-2 mm and the vessel tapped to help the sample settle and thus to obtain an essentially constant sample length. The piston was then gently advanced in "position control" mode until a small "set point" load (0.075 kN; applied stress 0.24 MPa) was attained. At this stage, the system was switched into "load control" mode. The "initial" sample length was then determined using the Instron LVDT as a measure of piston position and using a pair of vernier calipers (50  $\mu$ m precision) to measure the protrusion of the top piston from the vessel. The procedure produced a well controlled "starting aggregate" with a reproducible porosity of  $42 \pm 0.3$  %. The initial agitation and minor loading of the sand was intended to produce a more or less "locked" aggregate (cf. section 4.2); i.e. to diminish the role of pure interparticulate motion in accommodating compaction during continued loading. After determining their initial length, the sand samples were compacted under dry or fluid-flooded conditions, ramping or cycling the applied stress ( $\sigma_a$ ) in the range  $0.24 \leq \sigma_a \leq 30$  MPa using constant loading rates of 3.90, 282, 390 and 5495 MPa/hour. In the majority of cases, the load ramping or cycling stages were followed by a constant load stage during which creep effects were monitored at the maximum stress applied. In all, 44 tests were performed under the conditions listed in Table 4.1.

As mentioned above, the present tests were performed under both dry and fluid-flooded conditions, i.e. with the sample porosity maintained under "lab dry" or "vacuum dry" conditions, *or* flooded with an inert liquid or water held at 1 atm by "draining" to air. The "vacuum dry" test condition was achieved by attaching a vacuum line to the pore fluid in/outlet in the top piston (see Figure 4.2a) after initial loading at 0.24 MPa. The vacuum was generated using an Edwards single stage rotary vacuum pump (ultimate vacuum, without gas ballast, measured to be  $\sim 46$  Pa).

**Table 4.1.** Overview of compaction experiments performed on sands at room temperature. Test conditions shown.

Experiment no.	Test condition	Grain size d (µm)	Loading rate (MPa/hour)	Direct loading (DL) or cycling (C)	Max. applied stress $\sigma_a$ (MPa)
BS 1 to 4	"lab dry"	275 ± 25	390	C	30
BS 7, 9	vacuum	275 ± 25	390	C	30
BS 8 <sup>a</sup>	vacuum	275 ± 25	3.90	C	30
BS 5, 6, 10 to 13, 30, 31, 44	"dry vacuum"	275 ± 25	390	C	30
BS 32	"dry vacuum"	275 ± 25	390	C	22
BS 24, 25	"dry vacuum"	196 ± 16	282	C	22
BS 14 to 23, 29, 33 to 36	"dry vacuum"	275 ± 25	282	C	22
BS 26-28	"dry vacuum"	378 ± 22	282	C	22
BS 37, 40, 41	fluid-flooded (distilled water)	275 ± 25	5495	DL	30
BS 43	fluid-flooded (distilled water)	275 ± 25	5495	DL	20
BS 42	fluid-flooded (distilled water)	275 ± 25	5495	DL	10
BS 38, 39	fluid-flooded (n-decane)	275 ± 25	5495	DL	30

The line contained a gas-washing or Drechsel bottle filled with silicon oil (Dow Corning Co. ® 200 fluid, polydimethylsiloxane, viscosity  $5 \cdot 10^{-5} \text{ m}^2 \text{ s}^{-1}$ , vapour pressure < 0.7 kPa at 20 °C) to detect any leaks in the vacuum system and, closer to the piston, two glass chambers in series filled with drying agent (activated alumina). The high vacuum (mineral) oil inside the pump has a vapour pressure of  $\leq 7 \cdot 10^{-4} \text{ Pa}$  at 20 °C and 0.045 Pa at 100 °C (working temperature ~ 70 °C). The vacuum system was sealed using Glisseal high-vacuum paraffin-based grease (® Borer GmbH) with a vapour pressure of 0.0267 Pa at 21 °C. On the basis of

<sup>a</sup> No subsequent creep.

comparing the vapour pressures mentioned, and assuming that any silicon oil vapour would be adsorbed by the drying agent, it is inferred that neither the vacuum oil, the silicon oil, nor the grease could contaminate the sample due to evaporation. The drained test condition was achieved by vacuum flooding the sample, at the initial "set point" load (0.24 MPa) with an inert fluid (*n*-decane, as-received analytical grade C<sub>10</sub>H<sub>22</sub>) or with distilled water saturated with silica. The aqueous pore fluid was prepared by dissolving a fixed mass of sodium metasilicate (Na<sub>2</sub>SiO<sub>3</sub> · 9H<sub>2</sub>O) in order to yield an equilibrium SiO<sub>2</sub> concentration (~ 6 ppm at 25 °C and 0.1 MPa fluid pressure) (Morey *et al.*, 1962; Walther & Helgeson, 1977; Robie *et al.*, 1979; Rimstidt & Barnes, 1980; Hicks, 1989; Schutjens, 1991a). Subsequently, a small quantity of 0.1 M hydrochloric acid solution was added to obtain a pH between 6 and 7. The composition of the fluid at this point should thus have been 6.3 ppm SiO<sub>2</sub> and ~ 2 · 10<sup>-4</sup> M NaCl. Before use, saturation with respect to SiO<sub>2</sub> was ensured by allowing the pore fluid to circulate in a closed polyefine container with quartz sand test material at the bottom. This whole procedure was adopted to minimize sand dissolution by any mechanism other than (tensile) stress-related solution transfer or corrosion effects.

Tests were terminated by unloading the samples to the initial "set point" load (0.24 MPa) at a constant rate in the range 282-550 MPa/hour. Fluid-flooded samples were then briefly evacuated to remove the bulk of the pore fluid phase, allowing air to enter via the air inlet in the vessel wall (see Figure 4.2a). After reducing the load fully to zero, the apparatus was taken out of the testing rig and dismantled in a vertical position, removing both the top piston and the lower segment of the bottom piston. Subsequently, pushing a glass piston (diameter = 20 mm) gently against the top of the samples, the vessel was turned upside down and the upper segment of the bottom piston was removed. Then, the samples were carefully pressed out of the vessel, in an upward direction, into a glass tube (internal diameter = 20 mm) located in the position of the upper segment of the bottom piston. This allowed the sample, including the Teflon sleeve, to be placed in a cylindrical polyefine container and to be dried for 2-3 days at ~ 70 °C in a stove, with minimum disturbance to the friable aggregate structure. Finally, the samples were impregnated using a low-viscosity epoxy resin (Epotech 301 ® Logitech Ltd., aliphatic amine, specific gravity 1.08 g/cm<sup>3</sup>, dynamic viscosity 100 cP) coloured with a blue dye (Oil Blue A ® Du Pont Co., concentration 4 % wt). Thin sections (thickness 30 µm) were made in perpendicular directions parallel to the cylindrical sample axis. A broadly similar procedure was followed for selected dry tested samples. One (BS 8) was removed dry, in disturbed condition. A second (BS 44) was flooded with *n*-decane at the set point load to enhance its cohesion. A third (BS 10), tested using a Teflon pot (i.e. sleeve closed at bottom end) was impregnated with epoxy resin before removal from the vessel.



#### 4.3.6 Data processing and error analysis

At the end of each sand compaction test, the Teflon sleeves and/or pot were found to be intact (i.e. not perforated by the sand grains) and of more or less unchanged thickness. Since the diameter of the vessel bore is 20 mm, the radius of the sample was taken as 9.9 mm when calculating the initial porosity (at the "set point" load) and the applied stress during the test. Processing of the raw Instron load and Sangamo LVDT displacement records into volumetric strain versus applied axial stress data was done using a PC, and included a correction for the elastic distortion of the pistons carried out using the tenth order polynomial calibration referred to in section 4.3.2. Conventional error analysis showed the absolute or relative errors in both logged and processed values of Sangamo LVDT displacement, Instron displacement, Instron load, volumetric strain and applied axial stress to be less than 5  $\mu\text{m}$ , 0.3%, 0.3%, 0.6% and 0.5% respectively. For this reason, no attempt has been made to plot error bars for individual points in graphical representations of the data.

### 4.4 EXPERIMENTAL RESULTS

#### 4.4.1 Mechanical data

Regardless of whether they were tested under dry or fluid-flooded conditions, all samples of the same grain size and initial porosity showed closely similar stress - strain behaviour during load ramping and cycling. On the other hand, grain size and initial porosity were found to have significant effects, as described below. The creep behaviour observed in the final stages of the tests is reported in the following chapter.

A typical applied stress versus volumetric strain plot reflecting the effect of loading history on the compaction of "lab dry" sand from the  $275 \pm 25 \mu\text{m}$  size fraction is depicted in Figure 4.4, illustrating that permanent deformation was obtained in loading cycles performed to successively higher stresses up to 30 MPa. Note that with larger initial porosity ( $\phi_i$ ) more permanent deformation was attained at 30 MPa. However, having achieved 30 MPa, repeated loading cycles at lower stresses between fixed limits produced reproducible, quasi-elastic (stable) hysteresis loops with diminishing or no further permanent deformation. In the quasi-elastic regions (deformation recoverable), the average (apparent) constrained modulus was found to be  $(2.79 \pm 1.02) \cdot 10^9 \text{ Pa}$ . It was found that samples from the  $275 \pm 25 \mu\text{m}$  fraction, with  $\phi_i \geq 42 \pm 0.3 \%$  (see also section 4.3.5), attain a constant porosity ( $37.4 \pm 0.3 \%$ ) during initial loading up to 30 MPa.

A similar plot reflecting the effect of loading rate and chemical environment is shown in Figure 4.5. These compaction experiments were conducted applying constant loading rates of 3.90, 390 and 5495 MPa/hour respectively.

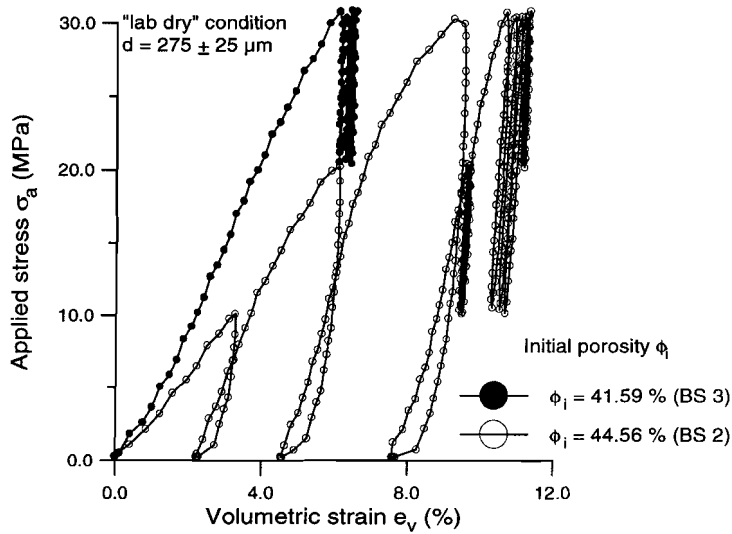


**Figure 4.4.** Typical applied stress versus volumetric strain plot obtained from compaction experiments BS 2 and 3, performed on sands of the  $275 \pm 25 \mu\text{m}$  grain size ( $d$ ) fraction under “lab dry” condition (room  $T$ , loading rate = 390 MPa/hour). The data illustrate that, with larger initial porosity, more permanent deformation is obtained in loading cycles performed to successively higher stresses up to 30 MPa. Having reached 30 MPa, loading cycles at lower stresses exhibit quasi-elastic behaviour.

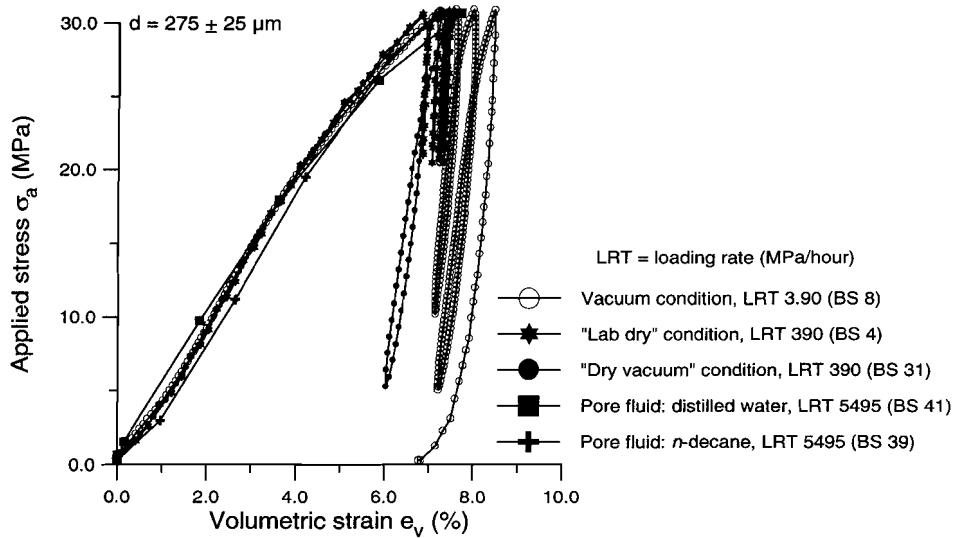


**Figure 4.5.** Typical applied stress versus volumetric strain plot obtained from compaction experiments BS 4, 8, 31, 39 and 41, performed on sands of the  $275 \pm 25 \mu\text{m}$  grain size ( $d$ ) fraction under the various conditions shown and applying different constant loading rates (room  $T$ , initial porosity  $\phi_i = 41.9 \pm 0.1 \%$ ). The data show that there is no significant effect of loading rate or chemical environment on the compaction behaviour.

The slowest loading test was carried out in vacuum condition, the tests at the intermediate loading rate were done under "lab dry" and "dry vacuum" conditions, and the fastest loading tests were performed in drained condition using *n*-decane or distilled water as pore fluid. The data presented in Figure 4.5 show no significant effect of either loading rate or chemical environment. This is evident from the fact that the stress-strain curves obtained from the tests under "dry" ("lab dry", vacuum and "dry vacuum") conditions correspond to those obtained from drained tests conducted using an inert pore fluid. Similarly, the behaviour shown by samples flooded with *n*-decane is much like that of sands tested with distilled water as pore fluid. The stress-strain data of the slowest ("vacuum dry") loading test exhibit a progressive decrease in quasi-elastic stiffness with subsequent loading cycles; the average (apparent) constrained moduli of consecutive quasi-elastic loading cycles are  $3.29$ ,  $3.01$  and  $2.48 \cdot 10^9$  Pa respectively.

With regard to the influence of grain size, Figure 4.6 demonstrates a systematic effect of grain size on the stress-strain behaviour of the sands tested in the "dry vacuum" condition. Note that with increasing grain size more permanent deformation is achieved.

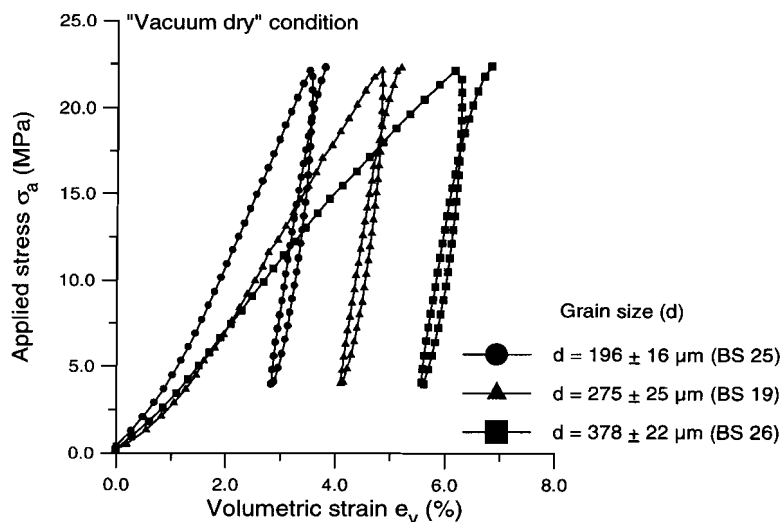


**Figure 4.6.** Typical applied stress versus volumetric strain plot obtained from compaction experiments BS 19, 25 and 26, performed on sands of the  $196 \pm 16$ ,  $275 \pm 25$  and  $378 \pm 22 \mu\text{m}$  grain size fractions, under "vacuum dry" conditions (room  $T$ , initial porosity  $\phi_i = 41.9 \pm 0.18$  %, loading rate =  $282 \text{ MPa/hour}$ ). The data demonstrate that with increasing grain size more permanent deformation is achieved.

#### 4.4.2. Microstructural observations

Microstructural analysis was performed on thin sections of the deformed sand samples, prepared as described in section 4.3.5, using optical microscopy (transmission method). Here, attention will be restricted to the microstructure developed in dry tested samples (BS 8, 10 and 44, see Table 4.1) since these showed only minor creep effects after the load cycling stage of the tests.

In contrast to the undeformed sand (microstructurally described in section 4.3.1), ~ 30 % of the sand grains, subjected to load cycling with or without subsequent creep in the "(dry) vacuum" condition (samples BS 8, 10, 44), exhibit trans- and intragranular cracks. These cracks cut the pre-existing closed cracks or inclusion trails observed in the undeformed sands and do not widen to such an extent that the grains lose cohesion. In the disturbed sample (BS 8), the sand grains (and the grain fragments) exhibit a major size reduction and a high angularity. In samples retrieved undisturbed (BS 10 and 44), these cracks fan out from crushed, grain-to-grain contacts. The brittle deformation features are homogeneously distributed through the samples: there is no proof of clustering or linkage of failed grains (failure localization is not observed). Furthermore, the trans- and intragranular cracks show no preferred orientation: the crack pattern is essentially random. The fraction of broken grains ( $F_{bg}$ ) was crudely estimated in samples BS 10 and 44, yielding  $F_{bg}$ - values of 36 and 38 %, observing 591 and 751 grains respectively.

#### 4.4.3 Acoustic emission data

A typical AE waveform obtained during loading of the sands in "dry vacuum" condition is shown in Figure 4.7. Cumulative AE event counts obtained from a typical sand loading test to 30 MPa carried out in "dry vacuum" condition are plotted as a function of applied stress in Figure 4.8. The data clearly illustrate that a larger cumulative AE event count is obtained at 30 MPa, when applying the short pulse stretching time (PST) (500  $\mu$ s) in comparison to the cumulative count acquired with the long PST (1000  $\mu$ s).

### 4.5 INTERPRETATION OF EXPERIMENTAL RESULTS

From the mechanical data presented in Figures 4.4 - 4.6 it can be concluded that after initial loading to 30 MPa, dry load-cycling behaviour at lower stresses is quasi-elastic and, therefore, presumably does not change the microstructure. The constant porosity but larger permanent deformation attained after initial loading up to 30 MPa of samples from the  $275 \pm 25 \mu$ m batch, with initial porosity larger than or equal to 41.7 %, are thought to be an effect of grain settling processes occurring before reaching a "locked" aggregate state characteristic of the maximum load of 30 MPa (see section 4.2 and 4.3.5).

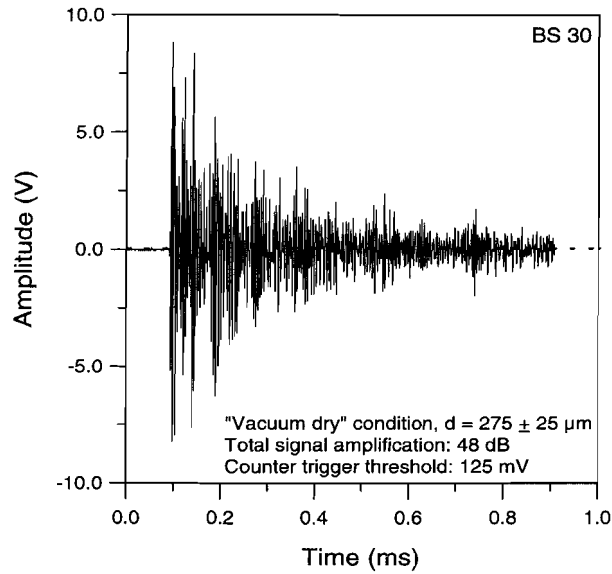


**Figure 4.7.** Typical AE wave packet detected during compaction test BS 30, performed on sands of the  $275 \pm 25 \mu\text{m}$  grain size ( $d$ ) fraction under "vacuum dry" conditions, at an applied stress ( $\sigma_a$ )  $\approx 25 \text{ MPa}$ .

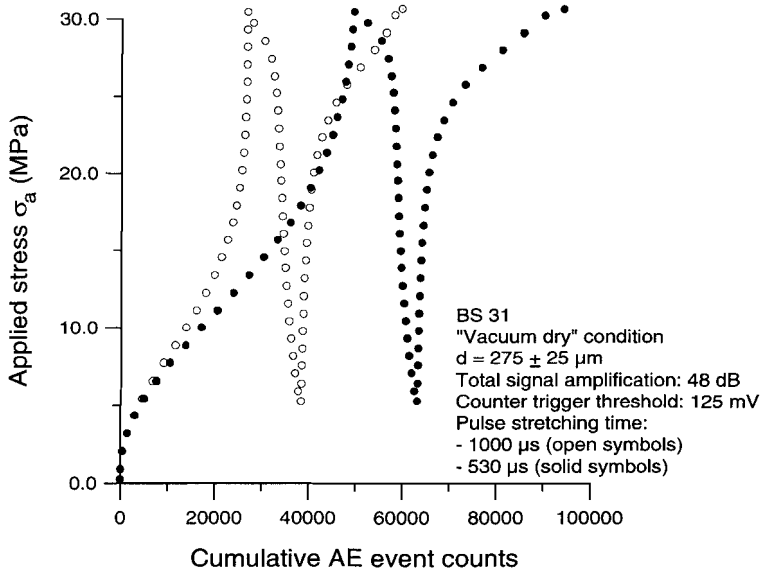


**Figure 4.8.** Cumulative AE event counts obtained during a typical compaction test performed on sands of the  $275 \pm 25 \mu\text{m}$  grain size fraction under "vacuum dry" conditions (room  $T$ , loading rate =  $390 \text{ MPa/hour}$ ). The data clearly illustrate that a larger cumulative AE count is obtained when applying the shorter pulse stretching time (test no. BS 31, mechanical data see Figure 4.5).

The absence of a clear effect of loading rate (within the range investigated) on the compaction behaviour of the sands suggests that time-dependent densification mechanisms play no significant role on the timescales of the load ramping and load cycling sequences employed in the present tests. Likewise, the insignificant effect of environment (dry versus drained condition with *n*-decane as an inert pore fluid) indicates that pure frictional compaction processes (particle sliding) play a minor role even at the fastest loading rate. Finally, an added aqueous (chemically active) fluid does not enhance compaction, implying that water does not significantly promote deformation at the time scale investigated, either via unstable crack formation plus grain failure, crack growth by stress corrosion plus grain failure, or any other mechanism.

From the microstructural observations made on sand samples subjected to initial loading (and subsequent creep) under "(dry) vacuum" conditions (BS 8, 10 and 44), compaction of all samples is inferred to have involved particle fragmentation (crushing) caused by trans- and intragranular cracking. Since the loading cycles conducted below the initially attained maximum applied stress of 30 MPa are reproducible, and presumably do not change the microstructure, and since relatively little permanent deformation occurred during the final constant load stage of tests BS 10 and 44, the fraction of broken grains ( $F_{bg}$ ) determined in thin sections of these samples is thought to represent an upper bound estimate of  $F_{bg}$  for the corresponding maximum stress level (30 MPa) and grain size of  $275 \pm 25 \mu\text{m}$ .

Since no AE activity was detected during loading of the steel dummy sample used for stiffness calibrations, the AE events observed on the oscilloscope (and counted) during sand compaction are inferred to be caused by the sample, i.e. by grain crushing involving trans- / intragranular cracking and by sliding-induced rearrangement of grains and grain fragments. The cumulative AE event counts depicted in Figure 4.8 were used to construct the plot of AE event count rate (average rate for a particular time interval) versus applied stress ( $\sigma_a$ ) displayed in Figure 4.9. Although it was observed on the oscilloscope that the AE event rate strongly increased with larger  $\sigma_a$ , the AE event count rate plotted in Figure 4.9 flattens off and even decreases with larger  $\sigma_a$ , when reaching a level of 100-400 Hz (5-10 MPa). Note also that the AE event count rates recorded by the counters with different pulse stretching time (PST) diverge above 5 MPa. The levelling off illustrates the inability of the AE signal conditioning system to "count" AE event rates above 500 Hz. The divergence and the levelling off reflect the effect of the different PST's for the two counting channels. It is widely accepted that (additional) undercounting of AE events (known as the "masking effect") will occur due to (i) the distributed nature of the occurrence (interval) time of AE events in relation to the PST applied, (ii) the amplitude distribution of AE events resulting in an underestimate of the number of small amplitude events, if these are concealed by coincident (overlapping) large amplitude (= long duration) events and (iii) attenuation of AE waveforms to levels below discrimination (Oda *et al.*, 1989; Cox

and Meredith, 1993; Lockner, 1993). In addition, the time interval between consecutive AE events (the occurrence time) is generally considered as a purely random, non-interactive (discrete) point process, following e.g. a Poisson distribution (Oda *et al.*, 1989; Nishizawa & Noro, 1990; Lockner, 1993). However, it is plausible that during the sand loading experiments, grain failure interaction effects will occur, giving rise to clustering of AE events in space and time and hence causing additional undercounting of AE events due to an enhancement of the effect described under (i). Consequently, the AE event count rate data for both PST's shown in Figure 4.9, at values of the applied stress above 5 MPa, should be regarded an underestimate of the actual AE event rate. Nonetheless, the AE data do serve to indicate that brittle events were important during the present experiments, with AE event count rates exceeding 500 per second at stresses around 10 MPa.

In conclusion, integrating the interpretation of the mechanical, microstructural and AE data discussed above, compaction of the present sand aggregates is inferred to be primarily controlled by elastic distortion and grain crushing and to be somehow favoured at larger grain sizes.

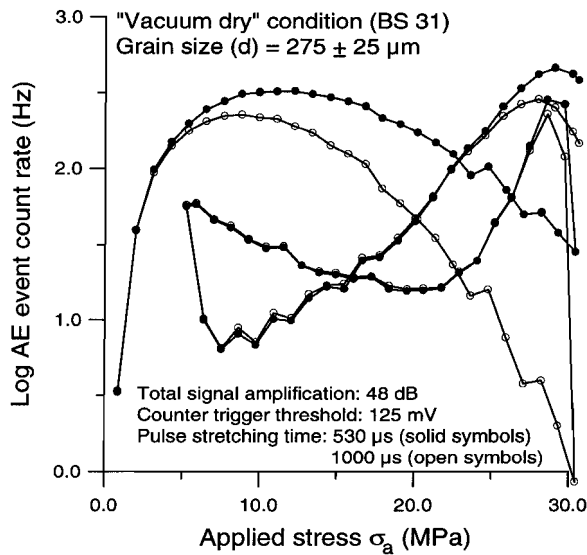


**Figure 4.9.** Plot of AE event count rate versus applied stress ( $\sigma_a$ ) constructed using the cumulative AE event count data presented in Figure 4.8 (test no. BS 31). In contrast with the strongly increasing AE event rates observed on the oscilloscope during increased loading, the AE event count rate data flatten off at values of  $\sigma_a$  above 5 MPa, at a level of 100-400 Hz. Note also that the AE event count rates recorded by the counters with different pulse stretching time (PST) diverge above 5 MPa. The levelling off illustrates the inability of the AE signal conditioning system to count AE event rates above 500 Hz while the divergence and the levelling off reflect the effect of the different PST's for the two counting channels.

## 4.6 MICROPHYSICAL MODEL FOR SAND COMPACTION BY HERTZIAN DISTORTION AND GRAIN CRUSHING

### 4.6.1 Starting point and principal assumptions

On the basis of the densification mechanisms reviewed and the experimental results presented in this chapter, a microphysical model for time-independent compaction of sands is now developed. In accordance with the conclusions drawn from the mechanical, microstructural and AE data, sand aggregate compaction during loading is modelled as the sum of "elastic" strain due to Hertzian grain contact distortion and "brittle" strain due to crushing (instantaneous failure) of individual grains, the latter contributing to an incremental volume change due to subsequent, sliding-induced rearrangement of grains and grain fragments. The sand aggregate is treated as an ordered packing of monosized grains. Major assumptions include that no interaction occurs between grain failure events and that, after grain failure and subsequent rearrangement, the aggregate spatial structure can still be approximated by the ordered packing initially imposed. Note that on the basis of percolation theory (Zallen, 1983; Stauffer & Aharony, 1992; Isichenko, 1992), global interactions are not expected below a threshold of 32 % of the grains having failed for a simple cubic pack. Furthermore, the grains and/or contact regions are considered to be Hertzian solids of revolution (cf. chapter 2, section 2.2.4 and 2.2.5), i.e. torsionless axi-symmetric loading is assumed to occur over a frictionless circular planar contact area with radius  $a$ . The remote state of applied stress ( $\sigma_a$ ) is regarded as hydrostatic and the grain contact force distribution is assumed uniform. These last two assumptions are justified as follows. First, the ratio of the axial stress to the horizontal stress ( $1/K_0$ ) for the present experiments is probably close to 1 as demonstrated in previous studies of similar materials (Lambe & Whitman, 1979; Karig & Hou, 1992; Chang *et al.*, 1992b, 1993). Thus, in accordance with the assumption of frictionless contacts, considering the applied uniaxial stress to be homogeneously transmitted through the sample is a reasonable first approximation. Second, deformation features are uniformly distributed (no localization occurs) and cracks are randomly oriented, suggesting that grain contact disorder and collective restructuring of grain arrays are not important.

### 4.6.2 Grain contact force and properties of an ordered pack

The first step in the present model is to specify the magnitude of the grain contact force in an ordered pack, as well as some basic relations defining pack volume and porosity.

According to Hertzian theory, the total normal load  $F$  exerted between two grains across a contact can be written (Johnson, 1987, eqn. 4.21)



$$F = \int_0^a [\sigma_{zz}(x)]_{z=0} 2\pi x dx = \frac{2\pi\sigma_0 a^2}{3} \quad (1)$$

where  $\sigma_0$  is the normal stress at the centre of the contact and  $[\sigma_{zz}(x)]_{z=0}$  (cartesian coordinates) is the surface normal stress distribution (cf. chapter 2, section 2.2.5). The contact radius  $a$  is described by the relation  $a^3 = 3FR_t/(4E^*)$  where  $R_t$  is the relative radius of curvature defined as  $1/R_t = (1/R_1) + (1/R_2)$  and  $1/E^* = (1-\nu_1^2)/E_1 + (1-\nu_2^2)/E_2$  with  $R_i$ ,  $\nu_i$  and  $E_i$  ( $i = 1, 2$ ) being respectively the significant radii of curvature (of the spherical unloaded grain contact surfaces), the Poisson's ratio's and the Young's moduli of the grains (cf. chapter 2, section 2.2.5.). Alternatively,  $F$  can be expressed as  $\pi a^2 \sigma_n$  where  $\sigma_n$  is the mean normal contact stress. In any ordered packing of grains with size  $d$ , the force balance condition prescribes the applied stress  $\sigma_a$  to be equal to  $\zeta_\sigma \pi a^2 \sigma_n / d^2$ . Here, the scaling factor  $\zeta_\sigma$  ranges from 1 for simple cubic (SC) packing, to  $2/\sqrt{3}$  for simple hexagonal (SH) packing, to  $2\sqrt{2}$  for face centred cubic (FCC) packing.

Turning to the initial (external) volume  $V_0$  of a sand aggregate with constant mass  $m_a$  and solid phase density  $\rho_m$ , this is given

$$V_0 = \eta N_0 d^3 = \eta \left( \frac{6m_a}{\pi \rho_m d^3} \right) d^3 = \frac{6\eta m_a}{\pi \rho_m} \quad (2)$$

where  $N_0$  is the initial number of (intact) grains. Here, the term  $\eta d^3$  represents packing unit cell volume per grain. From this it is easily shown that the aggregate initial porosity ( $\phi_0$ ) can be expressed as  $1-(\pi/6\eta)$ . The scaling factor  $\eta$  ranges from 1 for SC packing, to  $1/2\sqrt{3}$  for SH packing, to  $1/2\sqrt{2}$  for FCC packing.

#### 4.6.3 Contact force enhancement during compaction

After failure and local rearrangement, a grain in the aggregate spatial structure can be envisaged (i) to remain load supporting, (ii) to vanish leaving no empty site or (iii) to no longer support load and hence to increase the load on surrounding grains without significantly changing the packing structure (as previously assumed). For situations (i) and (ii), the grain contact normal load ( $F$ ) remains as given in eqn. 1. For situation (iii), load enhancement at a given applied stress ( $\sigma_a$ ) can be incorporated following the relation

$$F = \frac{\sigma_a d^2}{\zeta_\sigma} \frac{N_0}{N_0 - n_N} \quad (3)$$

where  $n_N$  is the cumulative number of failed grains.

#### 4.6.4 Grain failure criterion

Having considered the magnitude of the force transmitted across grain contacts in the model pack, grain crushing is now accounted for by applying the grain failure criterion formulated in chapter 2, employing the Hertzian / linear elastic fracture mechanics (LEFM) model for the crushing of individual sand grains developed in chapter 3. Following these earlier treatments, impinging grains are envisaged as elastic solids in idealised Hertzian elastic contact, with pre-present, Griffith-type, surface flaws of initial dimension  $c_0$ . Moreover, a flaw at the edge of the circular contact area is considered an edge crack subjected to the Hertzian maximum tensile radial stress  $\sigma_T = (1-2\nu)\sigma_0/3$ , so that the crack tip stress is characterised by the mode I stress intensity factor  $K_I = \sigma_T m^* \sqrt{\pi c_0}$  where  $m^* \approx 1.12$  is an edge correction factor (Lawn, 1993). The flaw is viewed to evolve into an extensional ring crack at the edge of the contact, and to initiate grain failure if  $\sigma_T$  exceeds the material cohesive tensile strength, or in terms of LEFM, if  $K_I$  attains a value equal to the fracture toughness  $K_{Ic}$ , i.e. if  $K_I = \sigma_T m^* \sqrt{\pi c_f} = K_{Ic}$  where  $c_f$  is the ("critical") crack dimension at failure. In general, the possibility of both equilibrium and subcritical extension of the initial Griffith flaw would mean  $c_f \geq c_0$ . It is assumed that a crack of dimension  $c_f$  will remain unstable along its advancement path, causing instantaneous / catastrophic grain failure.

Making use of the relations for  $\sigma_T$ ,  $\sigma_0$ ,  $a$  and  $K_I = K_{Ic}$  given above, the critical force at failure ( $F_c$ ) for an individual grain is now given by the criterion

$$F_c = \frac{9\pi\sqrt{\pi} K_{Ic}^3 R_r^2}{2c_f\sqrt{c_f} (m^*)^3 (1-2\nu)^3 (E^*)^2} \quad (4)$$

If all grains in the model pack were identical and contained identical surface flaws (or flaws at failure), the above would predict simultaneous failure of all grains at a fixed applied stress. This is clearly unrealistic. In reality,  $F_c$  will be a distributed quantity due to the distributed nature of  $c_f$  and  $R_r$  at the grain-to-grain level. Bearing this in mind, the model can be extended to a population of grains having distributed  $F_c$  by considering two extreme cases: (i) *spherical* grains with constant radius of curvature  $R$  ( $R_r = d/4$ ) plus a grain-to-grain distribution of flaw sizes at failure ( $c_f$ ) (assumed constant per grain) with the failure criterion expressible in terms of  $F$  as

$$(c_f)_c = \left( \frac{K_{Ic}}{m^* \sigma_T \sqrt{\pi}} \right)^2 = 4\pi \left( \frac{K_{Ic} a^2}{m^* (1-2\nu) F} \right)^2 = 3\pi \left( \frac{K_{Ic}}{m^* (1-2\nu)} \right)^2 \sqrt[3]{\frac{3}{4F^2} \left( \frac{R_r}{E^*} \right)^4} \quad (5)$$

or (ii) *non-spherical* grains with constant flaw size at failure  $c_f$ , plus a grain-to-grain

distribution of effective radius of curvature  $r_g$ , characterising distributed contact asperity amplitude, with the fracture criterion expressible in terms of  $F$  as

$$(r_g)_c = \frac{4RE^*a^3}{3RF - 4E^*a^3} = \left( \frac{3}{E^*} \sqrt{\frac{1}{2F} \left( \frac{K_{Ic}}{m^*(1-2\nu)} \right)^3 \frac{\pi\sqrt{\pi}}{c_f\sqrt{c_f}}} - \frac{1}{R} \right)^{-1} \quad (6)$$

Implicit in case (ii) of the model is the assumption that, despite the non-spherical nature of the grains, the aggregate spatial structure can be treated as an ordered packing with an equivalent-sphere mean grain size  $d_{eq}$ . Furthermore, an asperity with effective radius of curvature  $r_g$ , on a specific grain, is considered to be always in contact with that side of a neighbouring grain whose radius of curvature  $R$  ( $\neq r_g$ ) is described by the relation  $d_{eq} = 2R$ . Accordingly,  $R_r$  is expressed as  $r_g R / (r_g + R) = r_g d_{eq} / (2r_g + d_{eq})$ .

#### 4.6.5 Brittle strain

Grain failure is considered to contribute to an incremental volume change equal to  $\alpha d^3$  or  $\alpha d_{eq}^3$  where  $\alpha$  is a dimensionless constant ( $0 \leq \alpha \leq \pi/6$ ). At a certain applied load, a cumulative number  $n_N$  of grains will have failed contributing to a "brittle volumetric strain"  $e_{v(br)} = (n_N \alpha d_{eq}^3) / V_0 = (\alpha/\eta)(n_N/N_0)$ . Now, the ratio  $n_N/N_0$  ( $\lim N_0 \rightarrow \infty$ ) represents the cumulative probability of grain failure at a load  $F \leq F_c$  (i.e.  $\Pr[F \leq F_c]$ ) and is therefore expressible using any suitable cumulative distribution function. Furthermore, it follows from eqns. 4-6 that the probability  $\Pr[F \leq F_c]$  coincides with the probability of existence of a grain with a flaw at failure of size  $c_f \geq (c_f)_c$  or an effective radius of curvature of size  $r_g \leq (r_g)_c$ .

Assuming a Weibull distribution of  $c_f$ , the "brittle volumetric strain"  $e_{v(br)}$  for case (i) of the model can accordingly be written as

$$e_{v(br)(i)} = \frac{\alpha}{\eta} \frac{n_N[c_f \geq (c_f)_c]}{N_0} \sim \frac{\alpha}{\eta} \left( 1 - W((c_f)_c) \right) = \frac{\alpha}{\eta} \exp \left[ - \left( \frac{(c_f)_c}{k} \right)^m \right] \left( \lim_{N_0 \rightarrow \infty} \right) \quad (7)$$

where  $n_N[c_f \geq (c_f)_c]$  is the cumulative number of (failed) grains with a flaw dimension at failure  $c_f$  greater than or equal to  $(c_f)_c$  at a specific contact force  $F$ , and where  $W((c_f)_c)$  is the Weibull cumulative distribution function,  $k$  and  $m$  being the scale and shape parameters of this distribution (see chapter 3, section 3.2.2). A Weibull distribution is chosen because both the density and the probability functions are convenient analytical functions passing through the origin.

Likewise, assuming a Weibull distribution of  $r_g$ , the "brittle strain" for case (ii) of the model can be expressed as

$$e_{v(br)(ii)} = \frac{\alpha}{\eta} \frac{n_N[r_g \leq (r_g)_c]}{N_0} \approx \frac{\alpha}{\eta} W((r_g)_c) = \frac{\alpha}{\eta} \left[ 1 - \exp \left[ - \left( \frac{(r_g)_c}{k} \right)^m \right] \right] \left( \lim_{N_0 \rightarrow \infty} \right) \quad (8)$$

where  $n_N[r_g \leq (r_g)_c]$  is the cumulative number of (failed) grains with an effective radius of curvature  $r_g$  smaller than or equal to  $(r_g)_c$  at contact force  $F$ .

#### 4.6.6 Elastic strain

"Elastic strain" is described along the following lines. The mutual approach of grain centres during loading (the Hertzian contact distortion) is given by the relation  $\delta = \pi a \sigma_0 / (2E^*) = 3F / (4aE^*)$  (Johnson, 1987, eqn. 4.20). The linear "elastic strain"  $\epsilon_{(el)}$  due to contact distortion of neighbouring grains can be written as  $\delta/d$ . Moreover, for any ordered packing under a hydrostatic state of stress, the "elastic volumetric strain"  $e_{v(el)}$  equals  $1 - (1 - \epsilon_{(el)})^3$ . For case (i) of the model, the linear "elastic strain"  $\epsilon_{(el)}$  is given by

$$\epsilon_{(el)(i)} = \frac{\delta}{d} = \frac{1}{d} \sqrt[3]{\frac{1}{R_r} \left( \frac{3F}{4E^*} \right)^2} \quad (9)$$

For case (ii) of the model, the Hertzian distortion is distributed from grain contact to contact. The linear "elastic strain"  $\epsilon_{(el)}$  can therefore be described as

$$\epsilon_{(el)(ii)} = \frac{\delta_{tot}}{N_0 d_{eq}} \approx \sqrt[3]{\left( \frac{3F}{4d_{eq}^2 E^*} \right)^2} \int_0^\infty w((r_g)_c) \sqrt[3]{2 + \frac{d_{eq}}{(r_g)_c}} d((r_g)_c) \left( \lim_{N_0 \rightarrow \infty} \right) \quad (10)$$

where  $\delta_{tot}$  is the total elastic distortion considering  $N_0$  contacting grains in a row and  $w((r_g)_c)$  is the probability density function of the assumed Weibull distribution of  $r_g$ .

#### 4.6.7 Final model

The final expression for total volumetric strain  $e_{v(tot)}$  as a function of  $\sigma_a$  is obtained adopting the relation  $e_{v(tot)} = e_{v(br)} + e_{v(el)}$ .

For case (i) of the model, substitution of equation 3 and the relation  $R_r = d/4$  into equations 5 and 9 demonstrates  $(c_r)_c$  and the "elastic strain" to be grain size independent. The "brittle" strain for case (i) of the model only exhibits a grain size dependence if the Weibull parameters  $m$  and  $k$  are grain size dependent. For case (ii) of the model, substitution of equation 3 and the relation  $2R = d_{eq}$  into equations 6 and 10 illustrates  $(r_g)_c$  and the "elastic strain" to be grain size dependent, the latter only due to the definite integral involved.

In this microphysical model, Weibull statistics are adopted to describe the distributed nature of the major parameters, since both the density and the probability function of the Weibull distribution are convenient analytical functions passing through the origin. However, in chapter 3, section 3.2.2, Weibull theory has been shown to be able to directly express the failure probability of a material (e.g. an aggregate) in terms of the failure probability of its elemental volumes (e.g. grains). In that context, each grain is considered to possess a distributed failure stress or strength ( $\sigma_T$ ). In contrast, the present approach associates each grain with a specific  $\sigma_T$  which can essentially be interpreted as the mean value of an extremely narrow strength distribution per grain. Consequently, the adopted distributed nature of  $\sigma_T$  through the aggregate represents a distribution of mean grain strengths. It should be noted, however, that contrary to the Weibull weakest link concept, the present model envisages (elemental) grain failure to cause no (global) material failure.

#### 4.7 COMPARISON OF EXPERIMENTAL RESULTS WITH MICROPHYSICAL MODEL SIMULATIONS

In order to compare the experimental sand compaction data, reported in section 4.4.1, with the compaction behaviour predicted by the above microphysical model, the model has been used as a basis for numerical simulations focusing on the effect of grain size ( $d$  or  $d_{eq}$ ).

##### 4.7.1 Choice of numerical values

Applied stress ( $\sigma_a$ ) vs total volumetric strain ( $e_{v(tot)}$ ) data have been computed employing the model for both extreme cases (i and ii) and increasing the applied load in equally spaced steps of 0.01 N (or 0.05 N) to obtain  $\sigma_a$ - data up to 22 MPa. For the purpose of simulating subsequent unloading to 3.5 MPa, similar  $\sigma_a - e_{v(tot)}$  data sets were computed considering only the elastic recovery of the aggregate. Load cycling was not simulated since no allowances were made for any hysteresis effects in the model. For case (i) of the model, the grain size  $d$  was taken equal to 196, 275 or 378  $\mu\text{m}$ , corresponding to the mean grain sizes of the sieved fractions used in this study. For case (ii) of the model,  $d_{eq}$  was chosen equal to 208, 279 or 399  $\mu\text{m}$ , corresponding to values of equivalent sphere mean grain size ( $d_{eq}$ ) calculated for each grain size fraction.

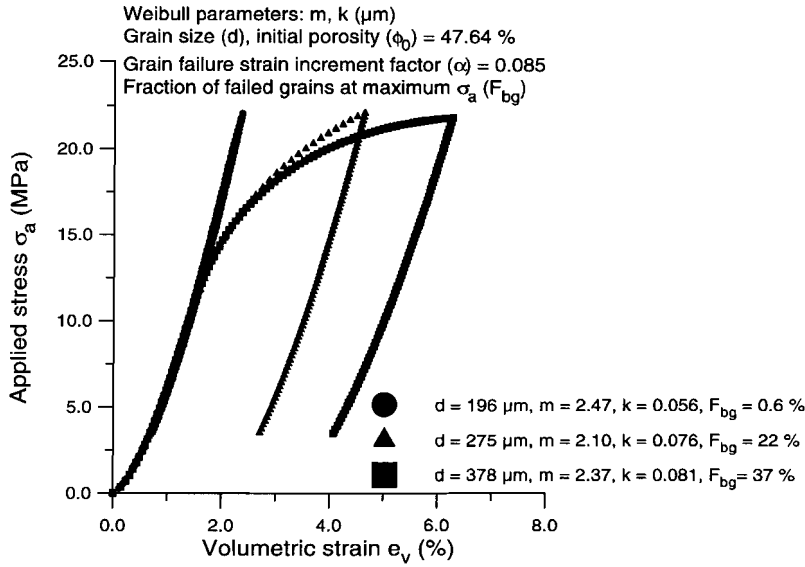
Weibull parameters  $k$  and  $m$  characterising the distribution of crack size at failure ( $c_f$ ) or effective radius of curvature ( $r_g$ ) of each grain size batch were obtained from the crushing tests on single sand grains sampled from these batches as reported in chapter 3 (Table 3.4), ignoring possible loading rate effects. For case (ii) of the model, the Weibull parameters  $k$  and  $m$  were calculated taking  $c_f$  equal to 0.115 or 0.05  $\mu\text{m}$ , the mean and respectively lower bound values obtained from the crushing tests on visibly spherical single sand grains selected from the  $378 \pm 22 \mu\text{m}$  batch, also reported in chapter 3 (section 3.3.4).

The quartz density, Young's modulus and Poisson's ratio were taken as 2.648  $\text{g/cm}^3$ , 95.68 GPa and 0.077 respectively (Simmons & Wang, 1971; Sumino & Anderson, 1984). The moduli were computed on the basis of single crystal elastic constants applying the Hill averaging method, assuming a macroscopically homogeneous, isotropic polycrystalline aggregate of zero porosity, with crystals in random orientation (Birch, 1966). This approach was used in order to take into account the random crystallographic orientation of sand grains in a stressed sample. The quartz fracture toughness ( $K_{Ic}$ ) was taken equal to 1 MPa  $\sqrt{\text{m}}$ , a representative value based on double torsion tests on synthetic quartz single crystals at room temperature and under vacuum (0.1 Pa), ambient or water-immersed conditions (Atkinson, 1979; Meredith & Atkinson, 1982; Darot & Gueguen, 1986; Atkinson & Meredith, 1989b; Reuschlé, 1989; Reuschlé *et al.*, 1989; Gueguen *et al.*, 1990).

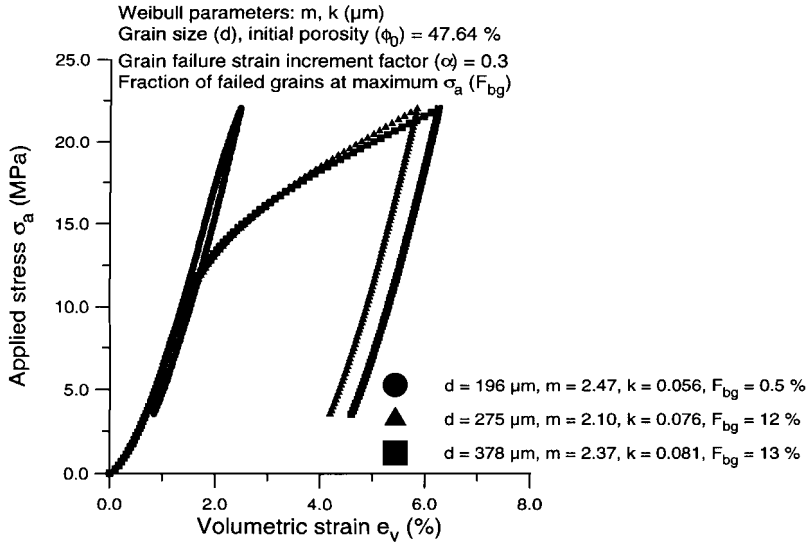
In addition, simple cubic (SC) packing was assumed during the simulation: i.e. taking  $\zeta_\sigma$  and  $\eta$  equal to 1 and the initial porosity ( $\phi_0$ ) equal to 47.64 %. As previously stated, the factor  $\alpha$  should be in the range  $0 \leq \alpha \leq \pi/6$ . In individual simulations, the factor  $\alpha$  has been chosen such that the stress and the total volumetric strain ( $e_{v(\text{tot})}$ ) at the point of load reversal exactly coincides with that point for the experimental data of the  $378 \pm 22 \mu\text{m}$  fraction compacted under "dry vacuum" conditions.

#### 4.7.2 Simulation results

The simulated  $\sigma_a - e_{v(\text{tot})}$  curves are depicted in Figures 4.10 - 4.13, at a scale similar to the experimental data plotted in Figure 4.6 for purposes of comparison. Figure 4.10 shows  $\sigma_a - e_{v(\text{tot})}$  curves produced from simulating the microphysical model for case (i), namely spherical grains with distributed crack size at failure ( $c_f$ ), and considering contact force enhancement. The factor  $\alpha$  fitted (0.085) falls well within its expected range. However, the computed fraction of broken grains ( $F_{bg} = n_N/N_0$ , eqn. 7 and 8) at 22 MPa for a grain size ( $d$ ) of 378  $\mu\text{m}$  (37 %) is too large to validate the major assumptions of the model. Therefore, similar  $\sigma_a - e_{v(\text{tot})}$  curves, depicted in Figure 4.11, were constructed for this case of the model, disregarding load enhancement (i.e. without employing equation 3), changing  $\sigma_a$  in steps of 0.22 MPa. In comparison to the results presented in Figure 4.10, the  $F_{bg}$ -values computed at 22 MPa are substantially lower; the fitted factor  $\alpha$  takes a value of 0.3 which is acceptable and the  $F_{bg}$ -value at 30 MPa for  $d = 275 \mu\text{m}$  equals 25 %, which is also reasonable.



**Figure 4.10.** Applied stress versus volumetric strain curves computed from simulating case (i) of the microphysical model for sand compaction, namely spherical grains with Weibull distributed crack size at failure, and considering contact force enhancement. The factor  $\alpha$  fitted (0.085) falls well within its expected range, the fraction of broken grains computed at 22 MPa for a grain size of 378  $\mu\text{m}$  (37 %) is too large to validate the major assumptions of the model.



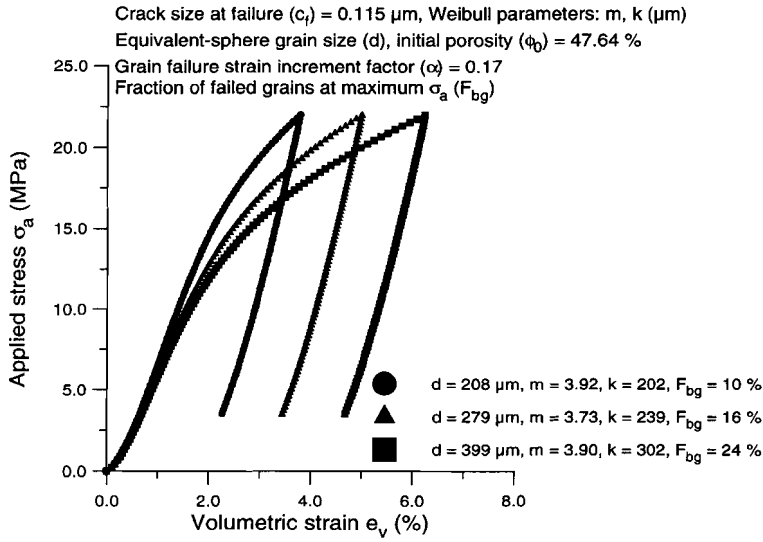
**Figure 4.11.** Applied stress versus volumetric strain curves computed from simulating case (i) of the microphysical model for sand compaction, namely spherical grains with Weibull distributed crack size at failure, and considering no contact force enhancement. In comparison with the results presented in Figure 4.10, the fraction of broken grains at 22 MPa obtained for each grain size is substantially lower; the factor  $\alpha$  fitted (0.3) is acceptable.

Figure 4.12 shows  $\sigma_a - e_{v(\text{tot})}$  curves produced from simulating the microphysical model for case (ii), namely non-spherical grains with distributed effective radius of curvature ( $r_g$ ) assuming constant (mean)  $c_f$  equal to  $0.115 \mu\text{m}$ . Taking into account load enhancement, the  $F_{bg}$ -values computed for each grain size became larger than 50 % towards 15 - 20 MPa. For this reason, the  $\sigma_a - e_{v(\text{tot})}$  curves depicted in Figure 4.12 were constructed without employing equation 3. The  $F_{bg}$ -values obtained at 22 MPa and the fitted  $\alpha$  value of 0.17 are reasonable. The  $F_{bg}$ -value computed at 30 MPa for  $d = 275 \mu\text{m}$  equals 49 %. In addition, similar  $\sigma_a - e_{v(\text{tot})}$  curves, depicted in Figure 4.13, were constructed for this case of the model assuming constant (lower bound)  $c_f$  equal to  $0.05 \mu\text{m}$ , notably taking into account load enhancement. The  $F_{bg}$ -values obtained are extremely low, therefore yielding a factor  $\alpha$  equal to 0.57 which is (slightly) too large. It should be noted, however, that the maximum  $\alpha$  stated ( $\pi/6$ ) could be in principle larger if also pore volume decrease due to grain failure is considered. The  $F_{bg}$ -value computed at 30 MPa for  $d = 275 \mu\text{m}$  equals 12 %.

Simulating the model for a simple hexagonal (SH) packing ( $\phi_0 = 39.54 \%$ ) yielded similar results in all cases. However, computed  $F_{bg}$ -values were substantially lower.

Let us now focus on a comparison of the simulations and the experimental data of Figure 4.6. Both cases of the model lead to  $\sigma_a - e_{v(\text{tot})}$  curves for individual grain size fractions which resemble the experimental data in form. Clearly, the overall behaviour (form of the  $\sigma_a - e_{v(\text{tot})}$  curves, grain size dependence and fraction of broken grains at maximum  $\sigma_a$ ) predicted by the microphysical model assuming (a) non-spherical grains with distributed effective radius of curvature, (b) constant  $c_f$  equal to  $0.05 \mu\text{m}$ , and (c) considering load enhancement, shows the best qualitative agreement with both the sand compaction test results depicted in Figure 4.6 and the fraction of broken grains estimated from thin sections of deformed material (reported in section 4.4.2.). On this basis it is inferred that the grain size effect seen in the experimental data is due to a grain size dependent departure from sphericity inherent in this case of the model. This hypothesis is supported by the argument presented in chapter 3, that there is no clear basis for a grain size dependence of  $c_f$ .





**Figure 4.12.** Applied stress versus volumetric strain curves computed from simulating case (ii) of the microphysical model for sand compaction, namely non-spherical grains with Weibull distributed effective radius of curvature and constant (mean) crack size at failure equal to 0.115  $\mu\text{m}$ , and considering no contact force enhancement. The fraction of broken grains computed at 22 MPa for each grain size and the factor  $\alpha$  fitted are reasonable.

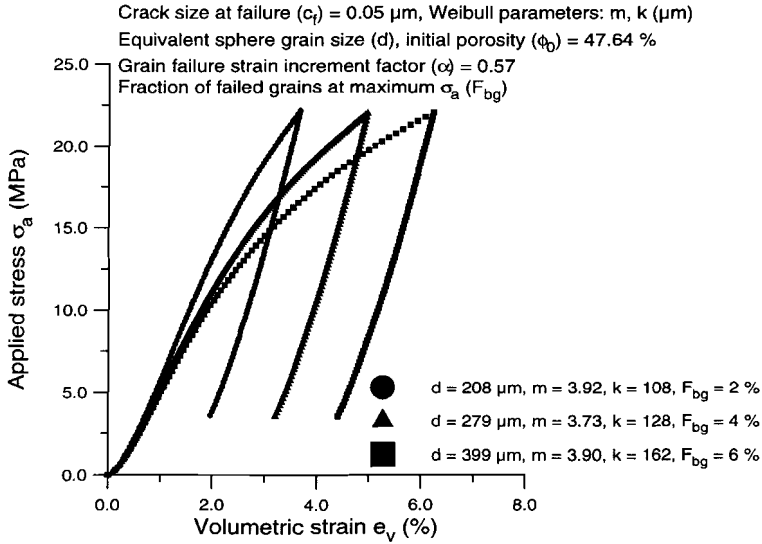


**Figure 4.13.** Applied stress versus volumetric strain curves computed from simulating case (ii) of the microphysical model for sand compaction, namely non-spherical grains with distributed effective radius of curvature and constant (mean) crack size at failure equal to 0.05  $\mu\text{m}$ , and considering contact force enhancement. The fraction of broken grains computed at 22 MPa for each grain size is extremely low, yielding a fitted factor  $\alpha$  (0.57) which is (slightly) out of its expected range.

## 4.8 CONCLUSIONS

Uniaxial compaction experiments performed on sands, at room temperature, stresses up to 30 MPa, and under dry and fluid-flooded conditions, have shown quasi-elastic loading behaviour and permanent deformation caused by grain contact distortion and grain failure. A microphysical model has been developed, based on these processes, in an attempt to explain the sand compaction behaviour. Two extreme cases of the model have been considered: (i) spherical grains with distributed flaw size at failure and (ii) non-spherical grains with distributed effective surface radius of curvature characterising contact asperity amplitude. Results produced by simulating case (ii) of the model offer the best agreement with the shapes and the grain size dependent trend of the experimental stress-strain curves, suggesting that a grain size dependent departure from sphericity of the grains is important in controlling the compaction behaviour of sands.

## CHAPTER 5      COMPACTION CREEP BEHAVIOUR OF SANDS

### 5.1 INTRODUCTION

The time-independent or short-term compaction behaviour of dry and wet sands has been extensively investigated, both in the laboratory and from a micromechanical modelling point of view, and has been shown primarily to involve grain fracture and rearrangement processes (the systematics of which are now well understood), with relatively little effect of pore fluids (Lambe & Whitmann, 1979; Liu *et al.*, 1993; this thesis, chapter 4). On the other hand, it is commonly assumed that pore fluids enhance the kinetics of subcritical grain cracking mechanisms alongside processes such as pressure solution (Costin, 1989; Atkinson & Meredith, 1989a; Zhang *et al.*, 1990a,b; Schutjens, 1991a,b; Elias & Hajash, 1992), so that time-dependent compaction creep effects may be important in sands and sandstones under natural conditions. It has been speculated, for example, that such creep effects may occur in hydrocarbon-bearing clastic reservoirs during the post-production phase, possibly leading to continued surface subsidence (Schutjens *et al.*, 1994, 1995). In addition, time-dependent compaction creep processes are believed to play a role in determining the porosity and permeability evolution of clastic sediments deposited in subsiding basin settings (Donaldson *et al.*, 1995a). Furthermore, similar creep effects can be expected to control cataclastic creep in fault gouge materials, thus influencing time-dependent aspects of seismic and aseismic fault slip behaviour (Morrow & Byerlee, 1989; Blanpied *et al.*, 1992; Sleep & Blanpied, 1992).

Limited experimental work has been carried out on the time-dependent compaction creep behaviour of sands at room temperature and under one-dimensional or hydrostatic compression conditions. For example, transient creep effects have been observed during compression tests performed on sands, over time intervals of the order of one day, following the application of consecutive stress increments (Robert & de Souza, 1958; Lee & Farhoomand, 1967; Lambe & Whitman, 1979). During these creep stages, compaction of the sands, associated with particle breakage, was accelerated by the addition of water and "cracking sounds" were noted (Lee & Farhoomand, 1967). Significant creep effects have also been observed in wet sands subjected to long-term (~ 1000 days) uniaxial compaction at constant load under drained conditions (de Waal, 1986); de Waal attributed these to pure intergranular sliding.

Despite the potentially important implications of such creep effects in understanding production-induced reservoir compaction, previous experimental studies have not systematically investigated the effect of applied stress, grain size and chemical environment on the long-term compaction creep behaviour of sands. Moreover, the detailed microphysical processes operating, particularly the role of microcracking and the effect of fluid have not been directly investigated using either acoustic emission techniques or microstructural analysis. Accordingly, no

truly microphysically based rate model has yet been put forward for the compaction creep behaviour of sands. Nonetheless, the previous experimental work does serve to indicate that creep effects may be important in controlling the long-term compaction behaviour of sands.

In this chapter, the compaction creep behaviour of sands will be systematically investigated at a basic level, focusing on the effect of chemical environment, applied stress and grain size. Acoustic emission (AE) detection and microstructural methods are used to gain insight into the microphysical mechanisms operative. Furthermore, an attempt is made to develop a simple microphysical model for the compaction creep of sands based on the Hertzian / linear elastic fracture mechanics (LEFM) model developed in chapters 3 and 4, and assuming stress corrosion cracking to be responsible for time-dependent grain failure of wet sands.

## 5.2 EXPERIMENTAL TECHNIQUES

The experiments consisted of a series of uniaxial compaction creep experiments performed on sands under both dry and fluid-flooded (drained) conditions, using aqueous pore fluids of varying salinity as well as inert pore fluids for control purposes. Applied stress and grain size were independently varied to determine these effects too. The starting material, apparatus and general experimental techniques employed were identical to those used in the short-term sand compaction experiments reported in chapter 4.

### 5.2.1 Starting material and sample preparation

The sand used was obtained from the Heksenberg Formation (Middle Miocene age) exposed in the "Beaujean" quarry near Heerlen, The Netherlands. It has been characterised as a beach or dune deposit (Kuyl, 1975), shows a grain size of  $251 \pm 46 \mu\text{m}$ , and is an almost pure quartz sand with less than 1 wt % Na-rich feldspar present as a trace mineral (cf. chapter 4, section 4.3.1). Most sand grains are sub-rounded and show a largely smooth surface with pits and grooves. About 10 % of the grains exhibit "closed" intragranular microcracks, while  $\sim 60$  % of the grains contain intersecting patterns of subparallel fluid inclusion trails (cf. chapter 4).

Fractions of the sand, with grain sizes of  $196 \pm 16$ ,  $275 \pm 25$  and  $378 \pm 22 \mu\text{m}$ , were prepared for testing using a Retsch Ltd. sieving machine and thread-woven sieves (DIN 4188 or ASTM mesh size). The feldspar trace material was subsequently removed by applying either a heavy liquid (bromoform) separation technique ( $196 \pm 16 \mu\text{m}$  and  $378 \pm 22 \mu\text{m}$  fractions) or by washing in water ( $275 \pm 25 \mu\text{m}$  fraction). The compaction creep tests were carried out using constant mass (7.5 gram) samples taken from each sieved fraction.

### 5.2.2 Compaction apparatus

The compaction creep experiments were performed on individual sand samples, at room temperature, under both dry (i.e. "vacuum dry") and drained (i.e. fluid-flooded) conditions, using the one-dimensional or uniaxial apparatus depicted in Figure 5.1a (see also chapter 4, section 4.3.2). A special feature of this apparatus is the piezoelectric ceramic transducer, for acoustic emission (AE) detection, emplaced within the top segment of the bottom piston (see Figure 5.1b). Axial load was applied to the apparatus via the moveable top piston using an Instron 1362 servo-controlled testing machine. This was operated with a 10 kN load cell in "load control" mode (max. error  $\pm 0.1$  % of full scale range). Displacement of the loading ram was measured using the linear variable differential transducer (LVDT,  $\pm 50$  mm stroke, max. position error  $\pm 0.1$  % of full scale range) located in the drive unit of the testing machine. Displacement of the top piston relative to the vessel was measured using a Sangamo precision LVDT, with a  $\pm 5$  mm stroke, mounted on the top piston. This system allowed applied stresses to be measured and controlled to within 32 kPa, and piston displacement to be measured to within  $0.1 \mu\text{m}$  (cf. chapter 4). Sample temperature was measured to within  $0.05^\circ\text{C}$  using a type K thermocouple inserted into the bore of the lower segment of the bottom piston (Figure 5.1a).

### 5.2.3 Acoustic emission system

The acoustic emission (AE) activity monitoring system used in conjunction with the present apparatus is described in detail in chapter 4, section 4.3.3. Like all such systems, it enabled sensing, amplification, frequency filtering, discrimination and counting of wave packets emanating from microseismic events within the sample. The AE signals required amplification of around 1000x (60 dB gain) before discrimination from back-ground noise on the basis of amplitude. A parallel pair of counter channels were employed each consisting of a fast comparator, with adjustable discrimination level, which triggered multivibrators sending pulses to a digital counter. Subsequent counting was limited to whole wave packets (single events) by blocking the digital counters, situated on a daughter board in the personal computer (PC) used for logging all data channels, for a controlled period of time ("the "pulse stretching time", of the order of typical packet durations) immediately after each packet arrival. The AE wave packets could be displayed on a digital storage oscilloscope (for specifications see chapter 4).

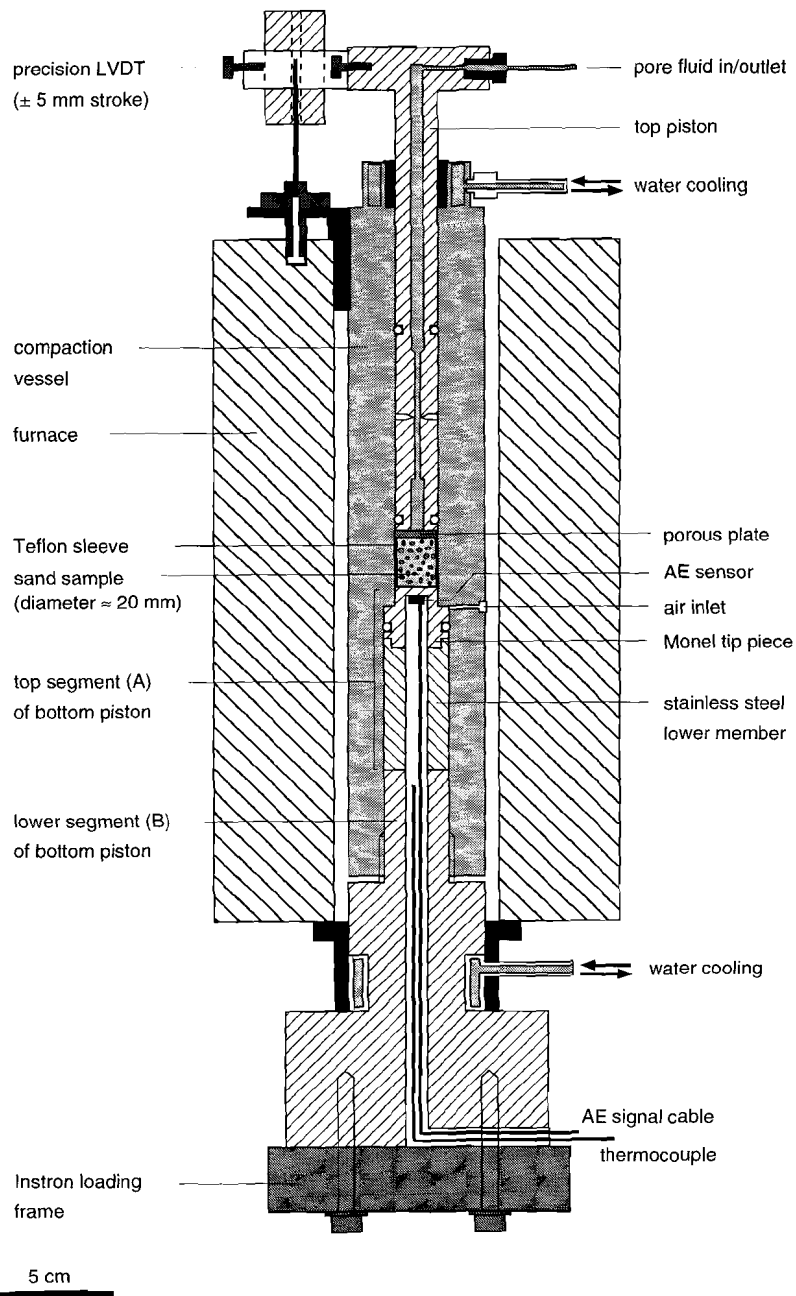


**Figure 5.1a.** Semi-schematic diagram showing the one-dimensional or uniaxial deformation apparatus used in the present compaction creep experiments on sands.

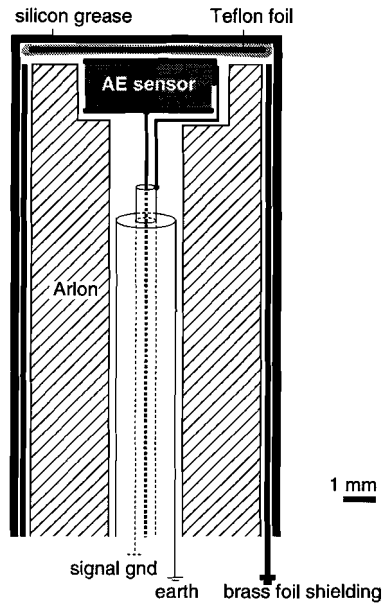


**Figure 5.1b.** Detailed section of the bore of the Monel tip piece, situated in the top segment of the bottom piston, showing the transducer for acoustic emission (AE) detection, spring-loaded against the flat end of the bore by the hollow Arlon rod. The greased Teflon foil ensures good acoustic coupling.

During use, constant discrimination trigger-thresholds in the range 125 to 700 mV were set for the two counter channels contained in the system. Triggering of the counting systems by random noise was found not to occur for threshold levels set above 15 mV. Total applied signal amplification factors ranged from 48 to 68 dB. Pulse stretching times (PST) for the two counter channels were set to 530 and 1000  $\mu$ s respectively, or to 530 and 2450  $\mu$ s respectively. AE waveforms observed during dry and "wet" compaction creep of sand typically endure for 0.75 and 0.25 ms respectively before the last retriggering. Consequently, the maximum AE event rates countable by the AE system are estimated to be 800 and 1300 Hz for dry and "wet" material.

#### 5.2.4 Data acquisition / logging

After signal conditioning, the voltage output of the Instron load cell, the Instron LVDT, the Sangamo LVDT and the thermocouple were recorded on a 6-channel chart recorder (max. error  $\pm 0.3$  % of full scale range). To obtain maximum accuracy and resolution, the pen-position monitor voltage for each channel was amplified (12 dB gain), digitized (16 bit resolution), and logged using a personal

computer (PC) equipped with a programmable peripheral interface (PPI) card. The maximum errors associated with the amplification and digitization steps were negligible compared with the chart recorder stage (cf. chapter 4).

The continuous logging of the two AE counter channels and the digitized transducer signals by the PC (via the PPI card) was supervised using a specifically developed computer program, DASA EHPT. This program reduces the transducer signals to the (uncorrected) physical quantities which they respectively represent; namely, the load cell output to force (kN), the output of the Instron and Sangamo LVDT's to displacement (mm) and the thermocouple output to temperature ( $^{\circ}\text{C}$ ). The program writes these data, and the cumulative AE event counts for the two counting channels to disk at regular time intervals (5 to 600 s, depending on creep rate).

#### 5.2.5 Sample handling & testing procedure

Individual dry sand samples were deposited into the vessel employing the funnel method described in chapter 4 (section 4.3.5). In all cases, the samples were surrounded by a thin-walled Teflon sleeve (height 16 mm, thickness  $0.13 \pm 0.02$  mm) positioned in the bore of the vessel to reduce friction between the sample and the vessel wall. After inserting the top piston, mounting the compaction apparatus into the Instron apparatus, and tapping the vessel wall to settle the sample, the sample was loaded in "position control" mode to a small "touch point" stress equal to 0.2 MPa. At this stage, the system was switched into "load control" mode, and the "initial" sample length was determined from the piston position with respect to the vessel top (cf. chapter 4). The procedure produced a well controlled "starting aggregate" with a reproducible porosity of  $42 \pm 0.3$  %.

After determining their initial length at the "touch point" stress, the sand samples were subjected to two different testing procedures:

##### 1. *two stage creep tests:*

In these tests, the samples were first subjected to load cycling under dry conditions ramping the applied stress ( $\sigma_a$ ) throughout the range  $0.2 \leq \sigma_a \leq 21.7$  or  $0.2 \leq \sigma_a \leq 30$  MPa and using constant loading rates of 282 or 390 MPa/hour. Cycling was terminated by arresting the loading ramp at a creep stage stress of 7.2, 10.9, 14.5, 18.1, 20, 21.7, or 30 MPa. After allowing compaction *creep under dry conditions* until creep rates diminished to values below  $10^{-8} \text{ s}^{-1}$  (after ~ two days), the samples were then flooded with pore fluid at the same stress, leading to a *creep stage under flooded and drained conditions*.

##### 2. *single stage creep tests:*

In this case, samples were flooded with pore fluid at the initial "touch point" stress and directly loaded (i.e. *under flooded and drained conditions*) to the desired creep stress (10, 20, or 30 MPa), using a constant loading rate of 5495 MPa/hour. The initial loading stage thus lasted for 6.7, 13.3, or 20 s.



In all, 37 successful tests were performed with the experimental variables and under the conditions listed in Table 5.1. The short-term behaviour obtained during the initial load ramping/cycling stage of the two stage creep tests, and of the single stage creep tests, have been reported in chapter 4.

As already indicated, the tests were performed under both dry and fluid-flooded/drained conditions, i.e. (i) with the sample porosity maintained under vacuum or "vacuum dry" conditions, *or* (ii) flooded with an inert liquid or aqueous solution held at 1 atm by "draining" to air. The details of the system used to evacuate samples via the pore fluid port in the top piston (see Figure 5.1a), after initial loading at 0.2 MPa, were described in chapter 4. The so-called "vacuum dry" test condition was achieved by incorporating into the vacuum line two glass chambers, connected in series and filled with drying agent (activated alumina). The drained test condition was achieved by flooding the sample, either after dry creep (two stage creep tests) or at the initial "touch point" stress (single stage creep tests), with an inert fluid (*n*-decane, analytical grade  $C_{10}H_{22}$ ), with distilled water saturated with silica, or with an NaCl solution (1 or 6.15 molar NaCl) saturated with silica (cf. chapter 4).

Tests were terminated by unloading the samples to the initial "touch point" stress (0.2 MPa) at a constant rate in the range 282-550 MPa/hour. Fluid-flooded samples were then briefly evacuated to remove the bulk of the pore fluid phase, allowing air to enter via the air inlet in the vessel wall (Figure 5.1a). After reducing the load fully to zero, the apparatus was taken out of the testing rig and dismantled in a vertical position. Samples were then carefully extracted from the vessel, dried, impregnated with coloured epoxy resin and sectioned according to methods described in chapter 4, with minimum disturbance to the friable aggregate structure. A broadly similar procedure was followed for selected dry tested samples. One (BS 10), tested using a Teflon pot (i.e. sleeve closed at bottom end) was impregnated with epoxy resin before removal from the vessel. A second (BS 44) was flooded with *n*-decane at the set point load to enhance its cohesion. No special precautions were taken to preserve the coherence of the remaining dry-tested samples (BS 2 and 7); these were simply pushed out of the vessel, after dismantling the apparatus, and collected in disturbed condition.

#### 5.2.6 Data processing and error analysis

At the end of each sand compaction creep test, the Teflon sleeves and/or pot were found to be intact (i.e. not perforated by the sand grains) and showed no measurable thickness change. Since the diameter of the vessel bore is 20 mm, the radius of the sample was taken as 9.9 mm when calculating sample porosity and applied stress during the tests. Processing of the raw load, Sangamo LVDT displacement and time records obtained during creep, into volumetric strain ( $e_v$ ) versus time data and volumetric strain rate ( $\dot{\beta}$ ) versus  $e_v$  data included a correction for elastic distortion of the pistons (cf. chapter 4).

**Table 5.1.** Overview of compaction creep experiments performed on sands at room temperature.  
Aqueous pore fluids (distilled water and NaCl solutions) saturated with silica.  
Test conditions shown.

(a) Two stage creep tests									
Experiment no.	Maximum stress (MPa) applied before creep	Applied stress $\sigma_a$ (MPa) during both creep stages	Grain size $d$ ( $\mu\text{m}$ )	Dry creep stage			Flooded creep stage		
				Starting porosity (%)	Test condition	Duration (days)	Starting porosity (%)	Type of pore fluid	Duration (days)
BS 2	30	30	$275 \pm 25$	37.5	vacuum	$\sim 4$	37.1	<i>no flooded creep</i>	-
BS 3	30	30	$275 \pm 25$	37.5	vacuum	$\sim 0.03$	37.1	distilled water	$\sim 5$
BS 4	30	30	$275 \pm 25$	37.0	vacuum	$\sim 0.03$	36.6	1 M NaCl solution	$\sim 5$
BS 5	30	30	$275 \pm 25$	37.8	"dry vacuum" <sup>a</sup>	$\sim 2$	37.1	distilled water	$\sim 10$
BS 6	30	30	$275 \pm 25$	37.6	"dry vacuum" <sup>a</sup>	$\sim 2$	36.7	1 M NaCl solution	$\sim 10$
BS 7	30	30	$275 \pm 25$	38.0	vacuum	$\sim 4$	37.0	<i>no flooded creep</i>	-
BS 9	30	30	$275 \pm 25$	37.4	vacuum	$\sim 2$	36.7	distilled water	$\sim 24$
BS 10, 44	30	30	$275 \pm 25$	37.1; 37.6	"dry vacuum"	$\sim 7; \sim 2$	36.5; 36.9	<i>no flooded creep</i>	-
BS 11, 30, 31	30	30	$275 \pm 25$	37.6; 37.5; 37.3	"dry vacuum"	$\sim 2$	37.0; 36.7; 36.2	distilled water	$\sim 16; \sim 9; \sim 10$
BS 13	30	20	$275 \pm 25$	38.2	"dry vacuum"	$\sim 2$	38.1	distilled water	$\sim 9$
BS 35, 36	21.7	21.7	$275 \pm 25$	39.1; 39.1	"dry vacuum"	$\sim 2$	38.7; 38.7	<i>n</i> -decane	$\sim 6; \sim 8$
BS 29, 32	21.7	21.7	$275 \pm 25$	39.2; 39.1	"dry vacuum"	$\sim 2$	38.7; 38.6	distilled water	$\sim 8; \sim 11$
BS 19, 20	21.7	21.7	$275 \pm 25$	39.0; 39.0	"dry vacuum"	$\sim 2$	38.6; 38.6	6.15 M NaCl solution	$\sim 13; \sim 9$

<sup>a</sup> drying agent =  $P_2O_5$  (phosphorous pentoxide)

(a) Two stage creep tests (continued)									
Experiment no.	Maximum stress (MPa) applied before creep	Applied stress $\sigma_a$ (MPa) during both creep stages	Grain size d ( $\mu\text{m}$ )	Dry creep stage			Flooded creep stage		
				Starting porosity (%)	Test condition	Duration (days)	Starting porosity (%)	Type of pore fluid	Duration (days)
BS 22, 23	21.7	18.1	275 $\pm$ 25	39.4; 39.2	"dry vacuum"	~ 2	39.2; 39.1	distilled water	~ 10; ~ 11
BS 15, 21	21.7	14.5	275 $\pm$ 25	39.3; 39.4	"dry vacuum"	~ 2	39.2; 39.3	distilled water	~ 10; ~ 7
BS 18	21.7	10.9	275 $\pm$ 25	39.7	"dry vacuum"	~ 2	39.7	distilled water	~ 2
BS 16, 17	21.7	7.2	275 $\pm$ 25	39.7; 39.6	"dry vacuum"	~ 2	39.7; 39.6	distilled water	~ 4; ~ 5
BS 24, 25	21.7	21.7	196 $\pm$ 16	39.6; 39.5	"dry vacuum"	~ 2	39.3; 39.2	distilled water	~ 9; ~ 8
BS 27, 28	21.7	21.7	378 $\pm$ 22	38.4; 38.1	"dry vacuum"	~ 2	37.7; 37.4	distilled water	~ 13; ~ 8

(b) Single stage creep tests (under flooded conditions)					
Experiment no.	Applied stress $\sigma_a$ (MPa)	Grain size d ( $\mu\text{m}$ )	Porosity (%) at start of creep stage	Type of pore fluid	Duration (days)
BS 37, 40, 41	30	275 $\pm$ 25	37.4; 37.4; 37.6	distilled water	~ 7; ~ 3; ~ 7
BS 38, 39	30	275 $\pm$ 25	37.8; 37.7	<i>n</i> -decane	~ 7; ~ 7
BS 43	20	275 $\pm$ 25	39.4	distilled water	~ 7
BS 42	10	275 $\pm$ 25	40.7	distilled water	~ 5

Except where otherwise mentioned, strain ( $e_v$ ) was calculated with respect to the length of the sample at the beginning of the dry and flooded creep stages respectively (i.e. defining a strain origin at the start of each creep or constant stress stage). Strain rates ( $\dot{\beta}$ ), defined  $\dot{\beta} = -\dot{V}/V$  where  $V$  represents instantaneous volume, were calculated by linear regression of the time - displacement records, within a displacement interval defined such that the max. error in  $\dot{\beta}$  was less than 5 %. Conventional error analysis showed the errors in both logged and processed values of Sangamo LVDT displacement, Instron displacement, Instron load, volumetric strain and applied axial stress to be less than 5  $\mu\text{m}$ , 0.3%, 0.3%, 0.6% and 0.5% respectively. For this reason, no attempt has been made to plot error bars for individual points in graphical representations of the data.

### 5.3 MECHANICAL RESULTS

#### 5.3.1 Two stage creep data

Two stage compaction creep curves illustrating the effect of chemical environment are shown in Figure 5.2a. The data were obtained from tests performed on sand from the  $275 \pm 25 \mu\text{m}$  size fraction, at a constant applied stress of 21.7 MPa, and under "dry vacuum" and subsequent flooded conditions. The volumetric strain data displayed in Figure 5.2a were calculated with respect to the length of the sample at the beginning of the "dry vacuum" creep stage. Furthermore, the discrete data were used to construct plots of volumetric strain rate ( $\dot{\beta}$ ) versus volumetric strain ( $e_v$ ) - see Figures 5.2b and 5.2c.

**Figures 5.2a-c (see next two pages).** *Two stage compaction creep curves and plots of volumetric strain rate ( $\dot{\beta}$ ) versus volumetric strain ( $e_v$ ) obtained from tests performed on sands of the  $275 \pm 25 \mu\text{m}$  grain size ( $d$ ) fraction, at room temperature, at a constant applied stress ( $\sigma_a$ ) of 21.7 MPa, and under "dry vacuum" and subsequent flooded conditions (aqueous pore fluids saturated with silica). The data show that samples maintained in the "dry vacuum" condition exhibited strongly decelerating creep after ~ two days. However, the later addition of aqueous pore fluids saturated with silica resulted in a dramatic enhancement of creep, with creep being particularly favoured by an increased NaCl content. In contrast, flooding with n-decane only slightly enhanced creep rates. The  $e_v$  data displayed in Figures 5.2a and 5.2b were calculated with respect to the length of the samples at the beginning of the "dry vacuum" creep stage, whereas those given in Figure 5.2c were computed with respect to the length of the samples at the beginning of the flooded creep stage. Since the creep data obtained from test BS 32, conducted in the "dry vacuum" condition, were found to be affected by room temperature drift, they are excluded from the plots.*

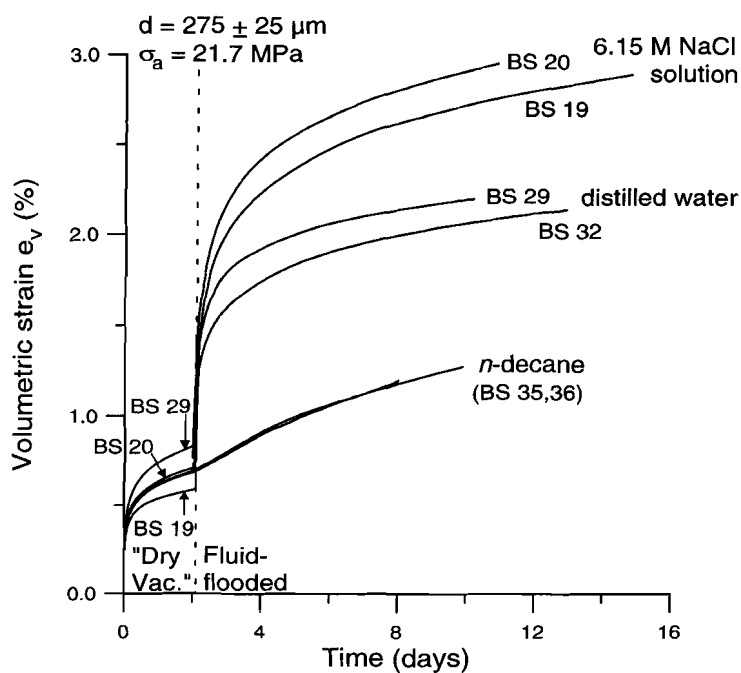


Figure 5.2a

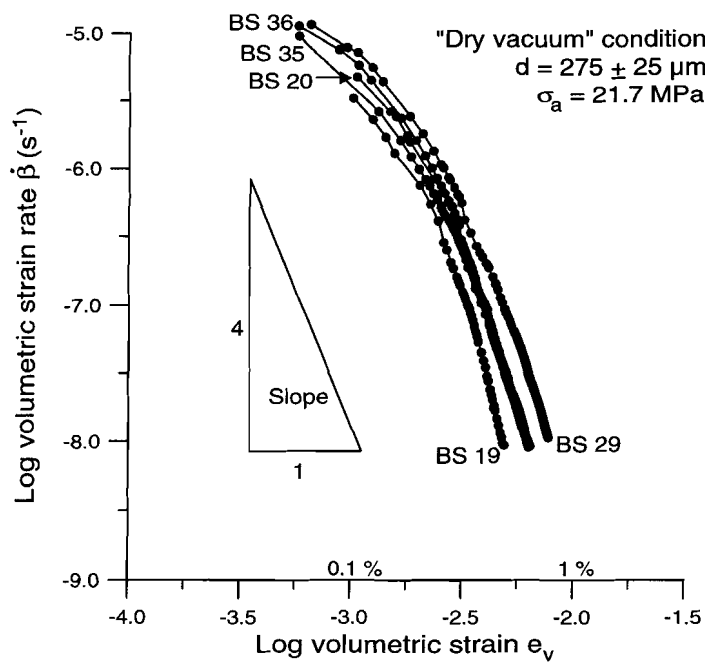


Figure 5.2b

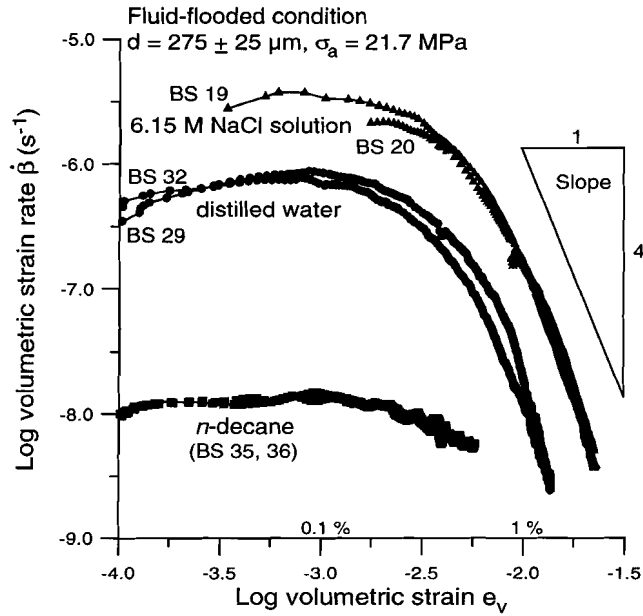


Figure 5.2c

From Figures 5.2a and 5.2b, it is evident that samples maintained in the "dry vacuum" condition exhibited strongly decelerating creep falling to rates of  $\sim 10^{-8} \text{ s}^{-1}$  after  $\sim$  two days. However, Figures 5.2a and 5.2c illustrate that the later addition of aqueous pore fluids resulted in a dramatic enhancement of creep, with creep being particularly favoured by an increased pore fluid salinity (NaCl content). In contrast, flooding with inert pore fluid (*n*-decane) only slightly enhanced creep rates. In all cases, no instantaneous deformation was observed at the point of flooding. Two stage creep tests performed on the same material at 30 MPa, and under vacuum or "dry vacuum" and subsequent flooded conditions showed closely similar effects of chemical environment. Again, the addition of aqueous pore fluids accelerated creep dramatically, with creep being enhanced by an increased pore fluid salinity. On the other hand, no systematic effect of vacuum condition (vacuum vs. "dry vacuum") was observed.

Two stage compaction creep curves and  $\dot{\epsilon}$ - $e_v$  plots obtained from two stage creep tests, reflecting the effect of applied stress ( $\sigma_a$ ) and grain size ( $d$ ) on creep under "dry vacuum" conditions are depicted in Figures 5.3a-d. Clearly, creep was favoured and compaction rates (at constant  $e_v$ ) increased with increasing  $\sigma_a$  and  $d$ . Similar plots illustrating the effect of  $\sigma_a$  and  $d$  on creep of the same sand samples after flooding with distilled water saturated with silica are shown in Figures 5.4a-d.

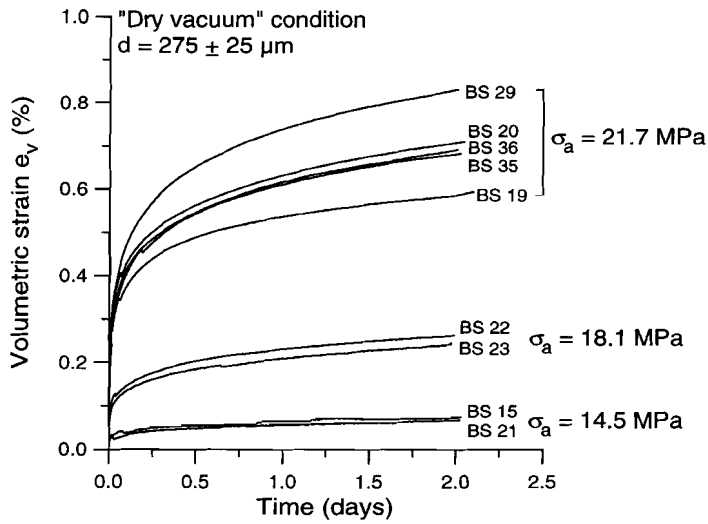


Figure 5.3a

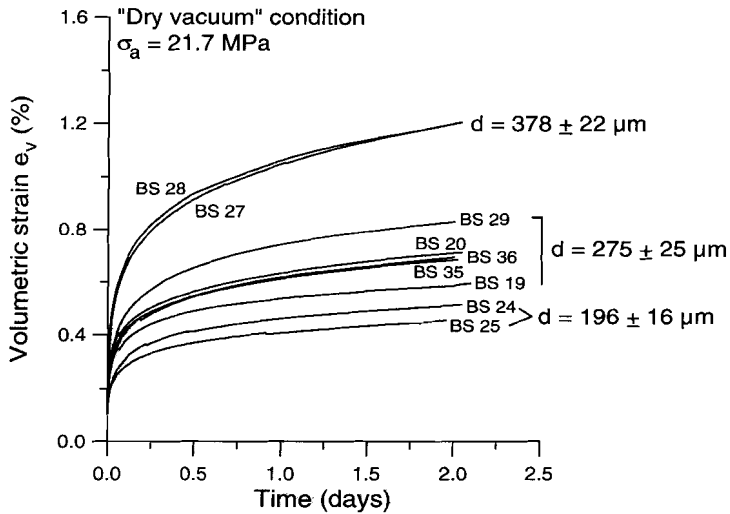


Figure 5.3b

**Figures 5.3a-d (cf. next page).** Compaction creep curves and plots of volumetric strain rate ( $\dot{\epsilon}_v$ ) versus volumetric strain ( $e_v$ ) obtained from two stage creep tests reflecting the effect of applied stress ( $\sigma_a$ ) and grain size ( $d$ ) on creep under "dry vacuum" conditions (room  $T$ ). The data demonstrate that creep was favoured with increasing  $\sigma_a$  and  $d$ . The  $e_v$  data displayed in Figures 5.3a-d were calculated with respect to the length of the samples at the beginning of the "dry vacuum" creep stage. Since the creep data obtained from test BS 32 were found to be affected by room temperature drift, they are excluded from the plots.

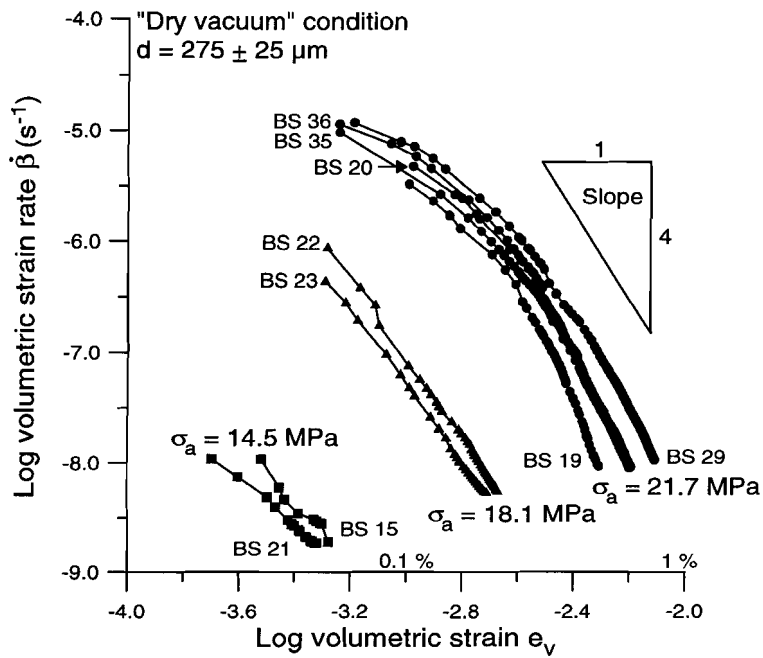


Figure 5.3c

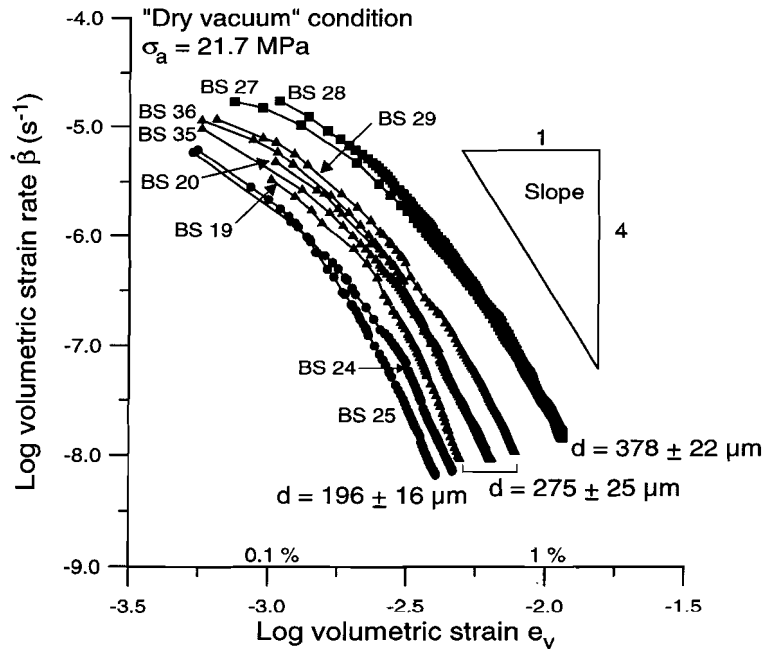


Figure 5.3d



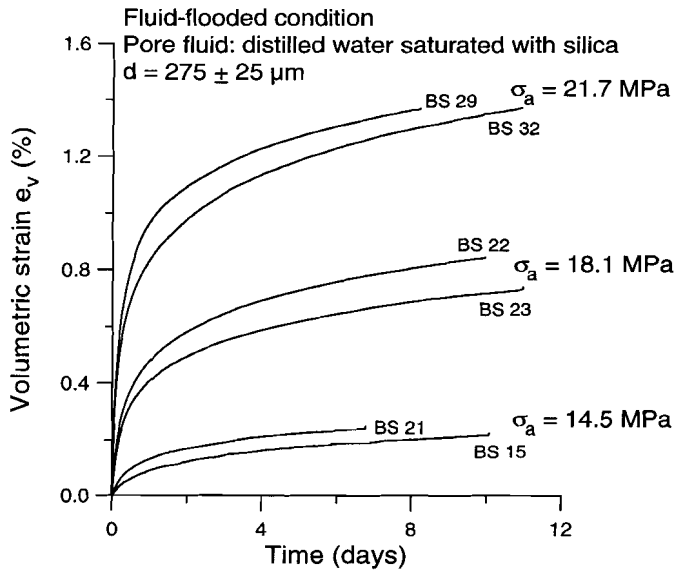


Figure 5.4a

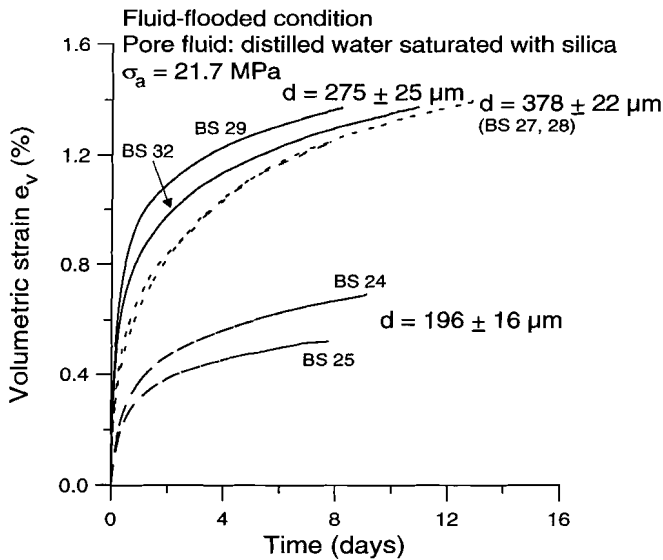


Figure 5.4b

**Figures 5.4a-d (cf. next page).** Compaction creep curves and plots of volumetric strain rate ( $\dot{\epsilon}$ ) versus volumetric strain ( $e_v$ ) obtained from two stage creep tests reflecting the effect of applied stress ( $\sigma_a$ ) and grain size ( $d$ ) on creep under flooded conditions (room  $T$ ) using distilled water saturated with silica as pore fluid. The data show that creep was favoured with increasing  $\sigma_a$ . The effect of  $d$  was less clear cut. The  $e_v$  data displayed in Figures 5.4a-d were calculated with respect to the length of the samples at the beginning of the "flooded" creep stage.

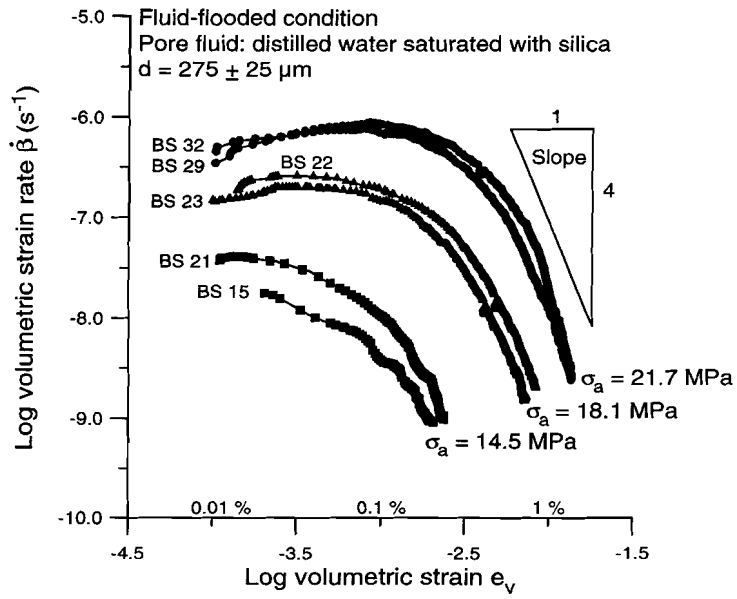


Figure 5.4c

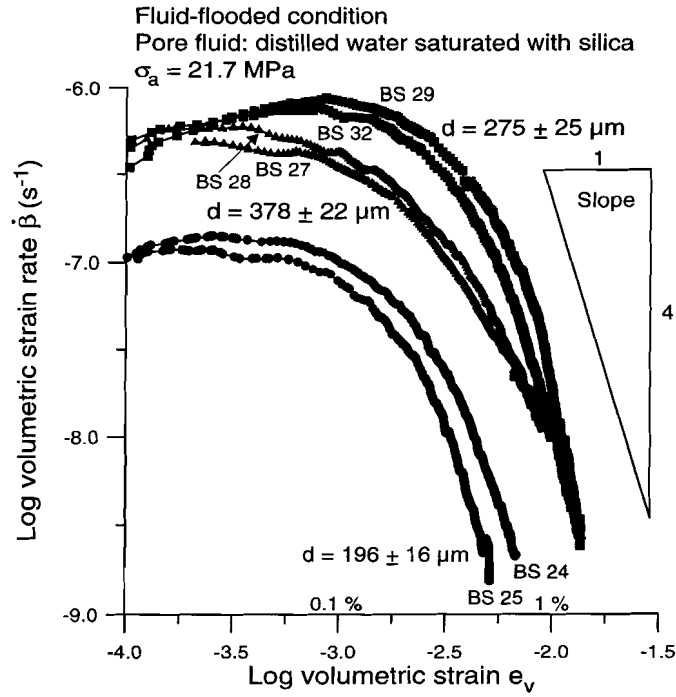


Figure 5.4d

Again, creep was favoured and compaction rates (at constant  $e_v$ ) were enhanced with increasing  $\sigma_a$ . However, the effect of  $d$  was less clear cut, with the intermediate grain size exhibiting faster creep in the first eight days than either the coarse or fine fractions. Assuming a power law relation between  $\dot{\beta}$  and  $\sigma_a$  (i.e.  $\dot{\beta} \propto \sigma_a^f$ ), the data depicted in Figures 5.3c and 5.4c imply the exponent  $f$  to be  $\sim 21$  under "dry vacuum" conditions ( $e_v = 0.05\%$ ) and  $\sim 12-17$  under wet conditions ( $e_v = 0.1-0.25\%$ ) demonstrating extreme sensitivity of  $\dot{\beta}$  to  $\sigma_a$ . With regard to the sensitivity of  $\dot{\beta}$  to  $d$  (assuming  $\dot{\beta} \propto d^g$ ), the data shown in Figures 5.3d and 5.4d yield an exponent  $g$  of  $\sim 4-8$  under "dry vacuum" conditions ( $e_v = 0.1-0.5\%$ ) and  $\sim 6-11$  under wet conditions ( $e_v = 0.01-0.5\%$ ,  $d = 196 \pm 16$  and  $275 \pm 25 \mu\text{m}$ ). The  $\dot{\beta}-e_v$  plots depicted in Figures 5.2-5.4 demonstrate compaction creep rates of sands under "dry vacuum" and flooded (aqueous pore fluids) conditions to hardly differ at similar  $e_v$  ( $> 0.5\%$ ),  $\sigma_a$  and  $d$ , and to be roughly proportional to  $e_v^{-4}$ . The creep data obtained from two stage creep tests performed at 20 and 30 MPa, using distilled water saturated with silica as pore fluid, are omitted from Figures 5.3 and 5.4 due to a different initial loading procedure, resulting in a different starting porosity (cf. Table 5.1). Moreover, at applied stresses of 7.2 and 10.9 MPa, neither the dry nor flooded samples, where the pore fluid was distilled water saturated with silica, exhibited creep. Therefore, the corresponding creep data are likewise excluded from Figures 5.3 and 5.4.

### 5.3.2 Single stage creep data

Compaction creep curves and  $\dot{\beta}-e_v$  plots illustrating the effect of chemical environment on the creep of samples tested in single stage mode are shown in Figures 5.5a&b. All data presented were obtained from tests performed on material from the  $275 \pm 25 \mu\text{m}$  size fraction, at an applied stress of 30 MPa under flooded/drained conditions. Since the reproducibility of the creep data is highly sensitive to the starting porosity, only data of tests BS 39 and 41, having similar starting porosities, are displayed (refer Table 5.1). The volumetric strain ( $e_v$ ) data displayed in Figure 5.5 were calculated with respect to the length of the sample at the point when load ramping was stopped, i.e.  $e_v$  does not include ramping strain. At strains  $> 1.6\%$ , more creep and faster creep rates were obtained in the sample flooded with distilled water saturated with silica, in comparison to the sample flooded with *n*-decane. Similar creep curves and  $\dot{\beta}-e_v$  plots showing the effect of applied stress ( $\sigma_a$ ) on creep under conditions where the pore fluid was distilled water saturated with silica are depicted in Figures 5.6a&b. Evidently, initial compaction (creep) and creep rates (at constant  $e_v$ ) were strongly enhanced with increasing  $\sigma_a$ . Assuming a power law relation between  $\dot{\beta}$  and  $\sigma_a$  (i.e.  $\dot{\beta} \propto \sigma_a^h$ ), the data displayed in Figure 5.6b imply the exponent  $h$  to be  $\sim 15$  under wet conditions ( $e_v = 0.8\%$ ). At  $e_v > 1.6\%$ , Figures 5.5b and 6b show that compaction rates in the single stage creep tests (at constant strain) are roughly proportional to  $e_v^{-7.5}$ , in case of samples flooded with distilled water saturated with silica, and to  $e_v^{-12.5}$ , in case of samples flooded with *n*-decane.

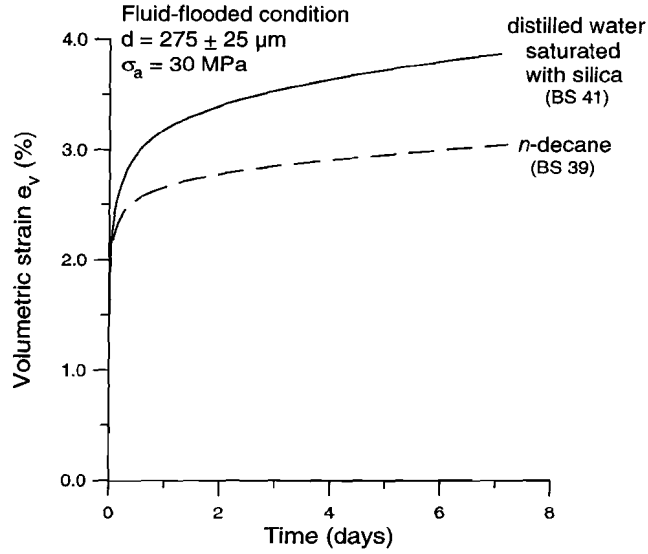


Figure 5.5a

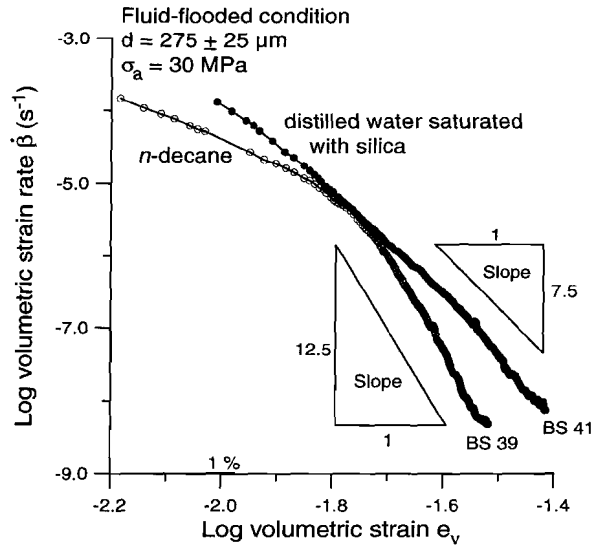


Figure 5.5b

**Figures 5.5a&b.** Compaction creep curves and plots of volumetric strain rate ( $\dot{\epsilon}$ ) versus volumetric strain ( $e_v$ ) obtained from single stage creep tests performed on sands of the  $275 \pm 25 \mu\text{m}$  grain size ( $d$ ) fraction, at a constant applied stress ( $\sigma_a$ ) of 30 MPa, and under flooded conditions (room T). Note that at strains  $> 1.6\%$ , creep was enhanced in the sample flooded with distilled water saturated with silica, in comparison to the sample flooded with *n*-decane. The  $e_v$  data displayed in Figures 5.5a&b were calculated with respect to the length of the samples at the point when load ramping was stopped.

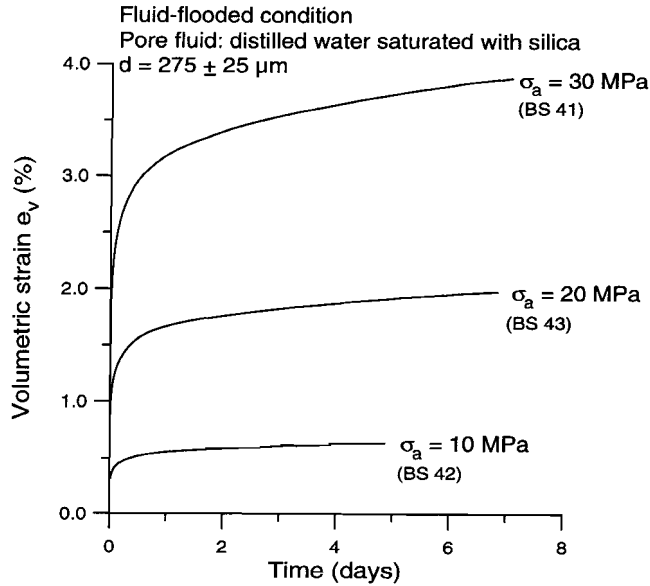


Figure 5.6a

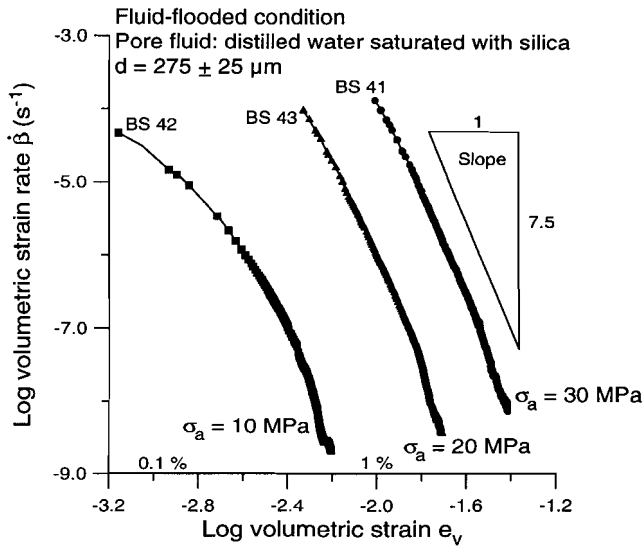
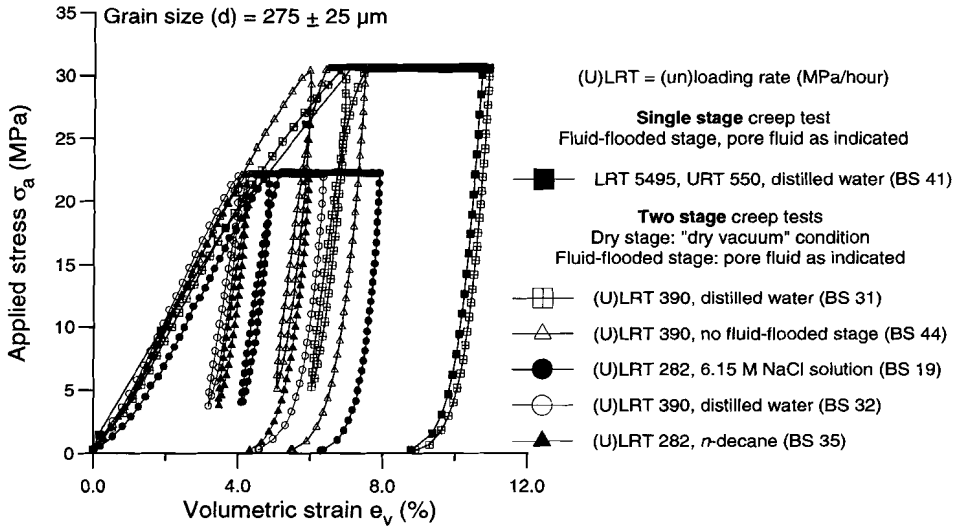


Figure 5.6b

**Figures 5.6a&b.** Compaction creep curves and plots of volumetric strain rate ( $\dot{\epsilon}$ ) versus volumetric strain ( $e_v$ ) obtained from single stage creep tests performed on sands of the  $275 \pm 25 \mu\text{m}$  grain size ( $d$ ) fraction, at room temperature, reflecting the effect of applied stress ( $\sigma_a$ ), and using distilled water saturated with silica as pore fluid. The data show that creep was favoured with increasing  $\sigma_a$ . The  $e_v$  data displayed in Figures 5.6a&b were calculated with respect to the length of the samples at the point when load ramping was stopped.

### 5.3.3 Complete loading paths

Typical, complete loading paths of single and two stage creep tests (aqueous pore fluids saturated with silica) employing creep stresses of 30 and 21.7 MPa respectively, are presented in the applied stress versus volumetric strain plot shown in Figure 5.7 (cf. chapter 4, section 4.4.1 and Figure 4.5 therein). The final unloading stress-strain data for each test plotted clearly illustrate how much permanent deformation was achieved after compaction creep both under "dry vacuum" (BS 44) and under flooded (BS 19, 31, 32, 35 and 41) conditions. Moreover, these unloading data exhibit an apparent stiffness which closely matches the quasi-elastic stiffness exhibited in the pre-creep loading cycles of the two stage creep tests considered (BS 19, 31, 32, 35 and 44).



**Figure 5.7.** Typical applied stress versus volumetric strain ( $e_v$ ) plot illustrating the complete loading paths of single and two stage creep tests performed using aqueous pore fluids saturated with silica (initial porosity  $\phi_i = 41.9 \pm 0.2 \%$ ). The  $e_v$  data were calculated with respect to the "initial" sample length at the "touch point" stress (0.2 MPa).

## 5.4 MICROSTRUCTURAL OBSERVATIONS

Microstructural analysis was performed on thin sections of the deformed sand samples using optical microscopy (transmission method). In the following, the general deformation microstructure of sands from the  $275 \pm 25 \mu\text{m}$  fraction, subjected to creep under "dry vacuum" conditions at an applied stress of 30 MPa, will first be described in order to characterise the microstructural damage introduced into samples during the pre-flooding stages of the two stage creep tests. The microstructures observed in sands from the  $275 \pm 25 \mu\text{m}$  fraction, subjected to subsequent creep under flooded conditions at an applied stress of 21.7 or 30 MPa, will then be described, focusing on the effects of pore fluid composition, (initial) grain size and applied stress. Finally, the microstructure of sands from the  $275 \pm 25 \mu\text{m}$  fraction, subjected to single stage creep tests under flooded conditions at an applied stress of 30 MPa, will be characterised. Attention is concentrated upon the deformation microstructures obtained under the extreme conditions (i.e. "dry vacuum" versus flooded at an applied stress of 21.7 or 30 MPa) since these represent end-member microstructure signatures. Moreover, the microstructures observed in sands from the  $275 \pm 25 \mu\text{m}$  fraction, subjected to single or two stage creep under flooded conditions at applied stresses lower than 21.7 MPa, were found to contain similar features as samples subjected to creep under flooded conditions at an applied stress of 21.7 MPa, although the amount of microstructural damage accumulated was lower.

In contrast to the undeformed sand,  $\sim 30\%$  of the sand grains in samples subjected to creep under "dry vacuum" conditions during the first phase of a *two stage* creep test, at an applied stress of 30 MPa (BS 10 and 44), exhibit transgranular and divergent cone ("spalling") cracks fanning out from crushed, grain-to-grain contacts (see Figure 5.8a).

**Figure 5.8 (see next two pages).** *Optical micrographs of sand samples subjected to creep under different conditions at room temperature. (a-I, a-II) Sample BS 44 subjected to creep under "dry vacuum" conditions during the first phase of a two stage creep test performed at an applied stress of 30 MPa. Note the transgranular (t) and divergent cone (c) cracks fanning out from grain-to-grain contacts. (b) Sample BS 32 subjected to second stage creep under flooded conditions, at an applied stress of 21.7 MPa (distilled water saturated with silica as pore fluid). The microstructure exhibits grains fragmented due to multiple, transgranular (t) and divergent cone (c) cracks fanning out from inferred grain-to-grain contacts. (c) Sample BS 35 subjected to second stage creep under flooded conditions, at an applied stress of 21.7 MPa (n-decane as pore fluid). The deformation microstructure is closely similar to that seen in Figure 5.8a, except that a smaller fraction of grains are broken. (d-I, d-II, e) Sample BS 31 subjected to second stage creep under flooded conditions, at an applied stress of 30 MPa (distilled water saturated with silica as pore fluid). The microstructure exhibits intense grain fragmentation, with clusters of  $\sim 10$ -25 cracks per grain radiating from grain-to-grain contacts.*



**Figure 5.8a-I**

150  $\mu$ m



**Figure 5.8a-II**

75  $\mu$ m



**Figure 5.8b**

75  $\mu$ m

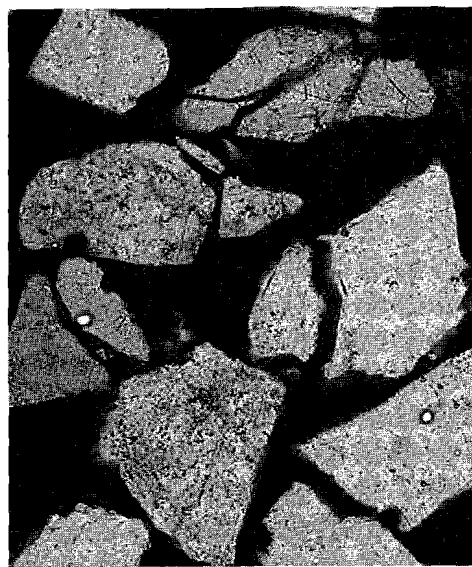


**Figure 5.8c**

150  $\mu$ m



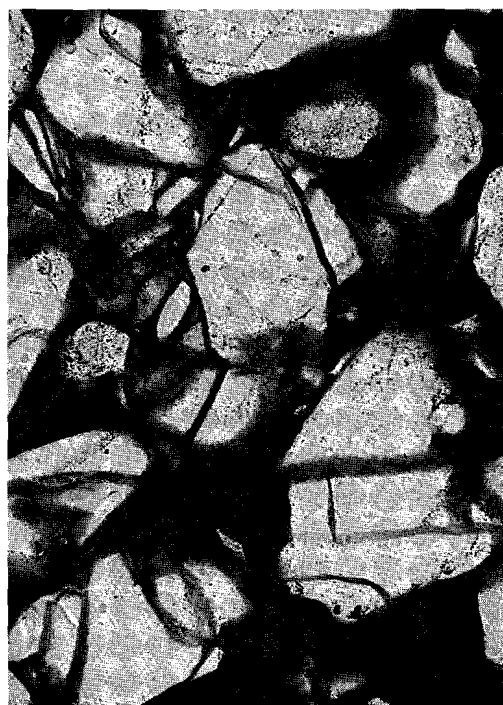


**Figure 5.8d-I**

150  $\mu$ m

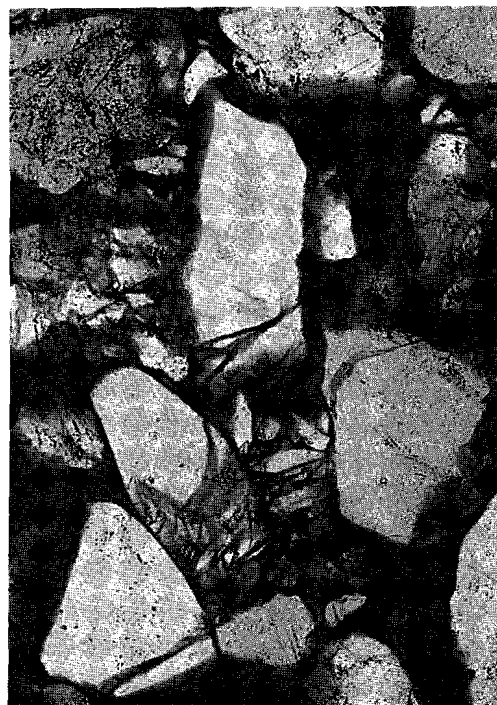


**Figure 5.8d-II**

150  $\mu$ m

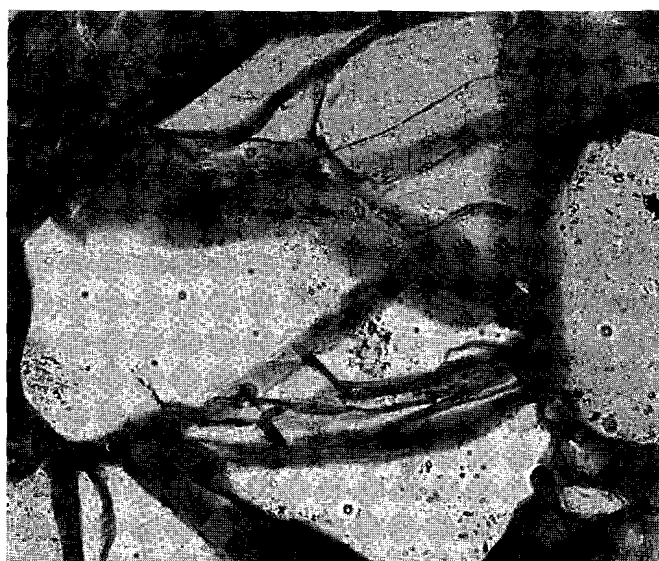


**Figure 5.8e**

75  $\mu$ m

These cracks (~ 1-3 per grain) are generally straight, cut the pre-existing closed cracks or inclusion trails observed in the undeformed sands, and do not widen to such an extent that the grains lose cohesion.

Compared with the dry-deformed material, samples subjected to *second stage* creep under flooded conditions, using an aqueous pore fluid, exhibit far more transgranular and divergent cone ("spalling") cracks fanning out from grain-to-grain contacts. The grains are fragmented due to multiple, generally curved cracks, they show high angularity and are often surrounded by broken-off grain fragments. In a typical sample (BS 32 - applied stress = 21.7 MPa,  $e_v = 4.6\%$ , distilled water saturated with silica as pore fluid), ~ 50 % of the grains have failed exhibiting ~ 2-5 cracks per grain (see Figure 5.8b). Sands taken from the three different grain size fractions, subjected to creep at an applied stress of 21.7 MPa and flooded with distilled water (BS 24, 32 and 28), typically show a closely similar deformation microstructure: however, the microstructural damage accumulated (the number of failed grains) does increase slightly with larger grain size. In material loaded to the same stress but flooded with a 6.15 M NaCl solution saturated with silica (BS 19), ~ 60 % of the grains have failed and exhibit ~ 3-8 cracks per grain. On the other hand, the deformation microstructure observed in material loaded at 21.7 MPa and flooded with *n*-decane (BS 35), is closely similar to the microstructure of the dry deformed material, except that ~ 20 % of the grains have failed (see Figure 5.8c). In sand loaded at an applied stress of 30 MPa and flooded with distilled water saturated with silica (BS 31,  $e_v = 8.9\%$ ), ~ 90 % of the grains have failed and show intense grain fragmentation, with clusters of ~ 10-25 cracks per grain radiating from grain-to-grain contacts (see Figures 5.8d&e).

Finally, a representative sand sample subjected to *single stage* creep at an applied stress of 30 MPa and using distilled water saturated with silica as pore fluid (BS 41), shows deformation features broadly corresponding to the microstructural damage of sands subjected to two stage creep at 30 MPa using similar pore fluid: ~ 80 % of the grains have failed with 5-15 cracks per grain. On the other hand, a sand subjected to single stage creep at 30 MPa using *n*-decane as pore fluid (BS 39) shows a ~ 40 % grain failure frequency with 1-4 cracks per failed grain.

The microstructural trends observed can be summarized as follows, focusing on the effect of (i) chemical environment (dry or flooded condition with *n*-decane as pore fluid *versus* "wet" condition with aqueous pore fluid saturated with silica, at similar applied stress), (ii) salinity of the aqueous pore fluid (at similar applied stress) (iii) grain size (with distilled water saturated with silica as pore fluid and at similar applied stress), and (iv) applied stress (with distilled water saturated with silica as pore fluid). First, with regard to the effect of chemical environment, sand samples subjected to two stage creep and flooded with an aqueous (chemically active) pore fluid show a substantially larger fraction of failed grains and far more cracks per grain in comparison with material subjected to only the first "dry vacuum" phase of the test or to single stage creep and flooded with an inert fluid

(*n*-decane). Second, sand samples subjected to two stage creep and flooded with an aqueous pore fluid exhibit a slightly larger fraction of broken grains and a major increase in cracks per grain, with a higher NaCl concentration. Third, sands from different size fractions and subjected to two stage creep with distilled water saturated with silica as pore fluid demonstrate a slight increase in the number of broken grains with larger grain size. Finally, sand samples subjected to either two stage or single stage creep with distilled water saturated with silica as pore fluid feature a major increase in the fraction of broken grains and the number of cracks per grain with higher applied stress.

In general, the brittle deformation features, observed in all samples are homogeneously distributed and there is no evidence of clustering or linkage of failed grains (failure localization is not observed). Furthermore, the transgranular and "spalling" cracks show no preferred orientation; the crack pattern is essentially random.

## 5.5 ACOUSTIC EMISSION DATA

Acoustic emission (AE) data were obtained during compaction creep experiments BS 27-44 (Table 5.1). Typical AE waveforms obtained are shown in Figures 5.9a&b. Throughout this section, the volumetric strain ( $\epsilon_v$ ) data presented have been calculated with respect to the length of the sample at the point when load ramping/cycling was stopped.

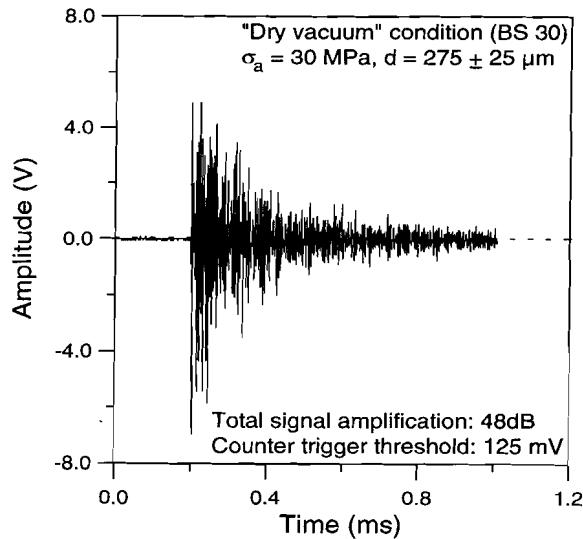


**Figure 5.9a.** Typical AE wave packet detected during the "dry vacuum" phase of the two stage creep test BS 30 (room *T*, grain size *d*, applied stress  $\sigma_a$ ).

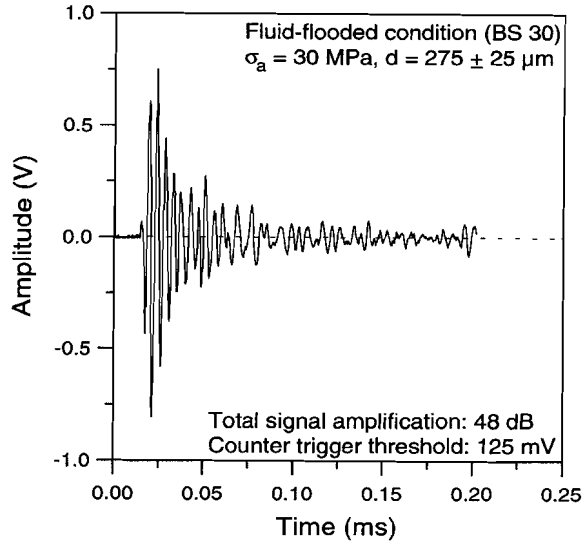


**Figure 5.9b.** Typical AE wave packet detected during the flooded phase of the two stage creep test BS 30 (room T, grain size  $d$ , applied stress  $\sigma_a$ , pore fluid: distilled water saturated with Si).

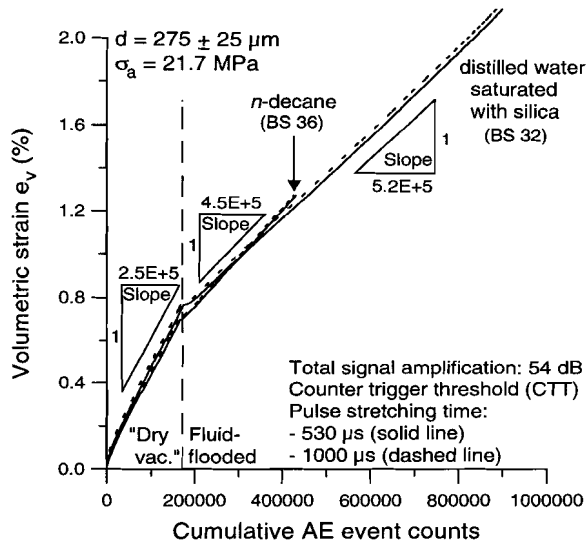


**Figure 5.10a.** Cumulative AE event count versus volumetric strain ( $e_v$ ) data obtained during typical two stage creep tests (BS 32, 36) performed on sands of the  $275 \pm 25 \mu\text{m}$  grain size fraction, at a constant applied stress ( $\sigma_a$ ) of 21.7 MPa, and at room temperature. The data, which are almost unaffected by pulse stretching time, exhibit a near-linear relation between cumulative AE counts and  $e_v$  as well as a clear effect of chemical environment. Individual data points are indistinguishable in the curves presented. The  $e_v$  data were calculated with respect to the length of the samples at the beginning of the "dry vacuum" creep stage.

### 5.5.1 Two stage creep tests

Cumulative AE event count versus  $e_v$  data representative of two stage creep tests (BS 32 and 36) performed on  $275 \pm 25 \mu\text{m}$  sand samples, at an applied stress of 21.7 MPa are shown in Figure 5.10a. These data, which are almost unaffected by pulse stretching time (PST), show a near-linear relation between cumulative AE event counts and  $e_v$  as well as a clear effect of chemical environment on AE activity. After the addition of pore fluid, the number of AE event counts, obtained per unit  $e_v$ , show a significant increase in comparison with the "dry vacuum" stage. Further, the samples flooded with distilled water saturated with silica yielded slightly more AE event counts per  $e_v$  than material flooded with *n*-decane. Since different settings of the AE system (and a different initial loading procedure) were employed during creep tests at 30 MPa, the effect of applied stress on AE activity could not be assessed.

The cumulative AE event counts depicted in Figure 5.10a, obtained with a PST of 530  $\mu\text{s}$ , have been used to construct the plot of AE event count rate (average rate for current logging interval) versus  $e_v$  displayed in Figure 5.10b. This clearly illustrates that the addition of pore fluid resulted in a large increase in the time rate of AE event counts, and that count rates at constant  $e_v$  were higher in samples flooded with aqueous solution than with *n*-decane.

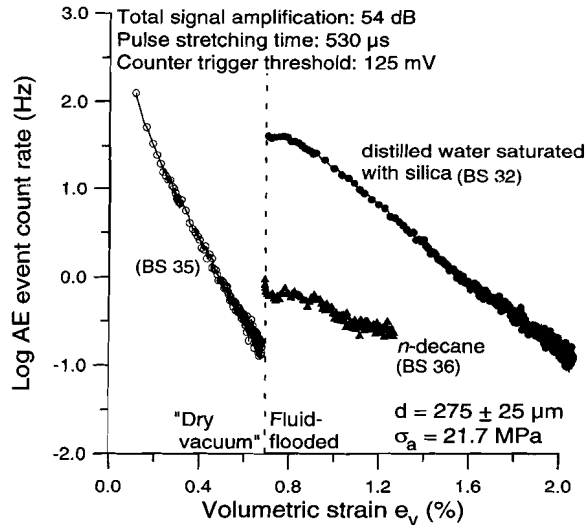


**Figure 5.10b.** Plot of AE event count rate versus volumetric strain ( $e_v$ ) constructed using the cumulative AE event count data presented in Figure 5.10a, obtained with a pulse stretching time of 530  $\mu\text{s}$ . The data illustrate that the addition of pore fluid resulted in a large increase of event count rate, and that count rates were higher in samples flooded with distilled water than with *n*-decane.

Similar plots illustrating the effect of grain size ( $d$ ) on AE characteristics in two stage creep tests (performed at 21.7 MPa) are depicted in Figures 5.11a&b. The data again show a near-linear relation between cumulative AE event counts and  $e_v$ , and little or no significant effect of PST. Moreover, the data demonstrate that, during both the "dry vacuum" and the flooded creep stages, the coarser grained samples yielded fewer AE event counts per unit  $e_v$  than the finer ones. At constant  $e_v$ , however, the data displayed in Figure 5.11b (PST of 530  $\mu$ s) show a trend towards higher AE event count rates with increasing  $d$ .

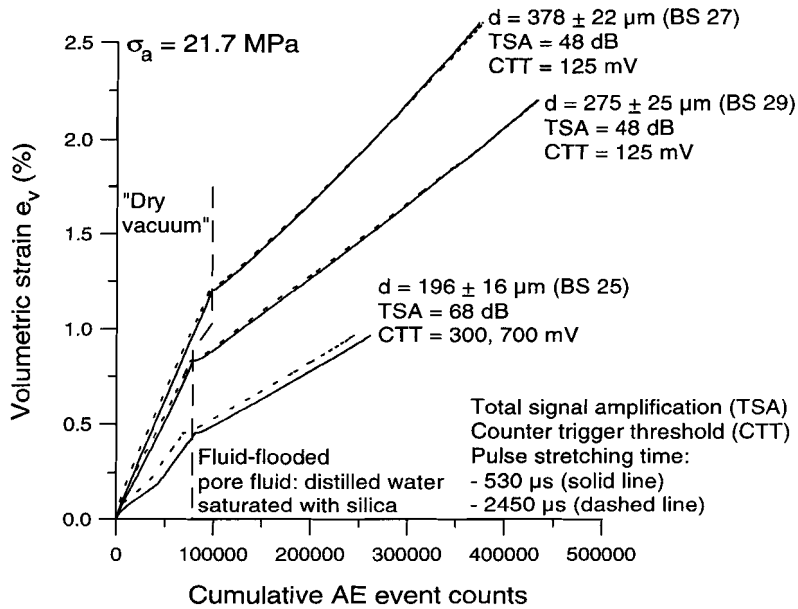


Figure 5.11a

**Figures 5.11a&b.** Plots of cumulative AE event count and AE event count rate versus volumetric strain ( $e_v$ ) obtained during typical two stage creep tests (BS 25, 27, 29) showing the effect of grain size ( $d$ ), at an applied stress of 21.7 MPa and room T. Note the near-linear relation between cumulative AE counts and  $e_v$ . The  $e_v$  data displayed in Figures 5.11a&b were calculated with respect to the length of the samples at the beginning of the "dry vacuum" creep stage. Individual data points are indistinguishable in the curves presented in Figure 5.11a. The vertical dotted lines in Figure 5.11b show the point of addition of pore fluid.

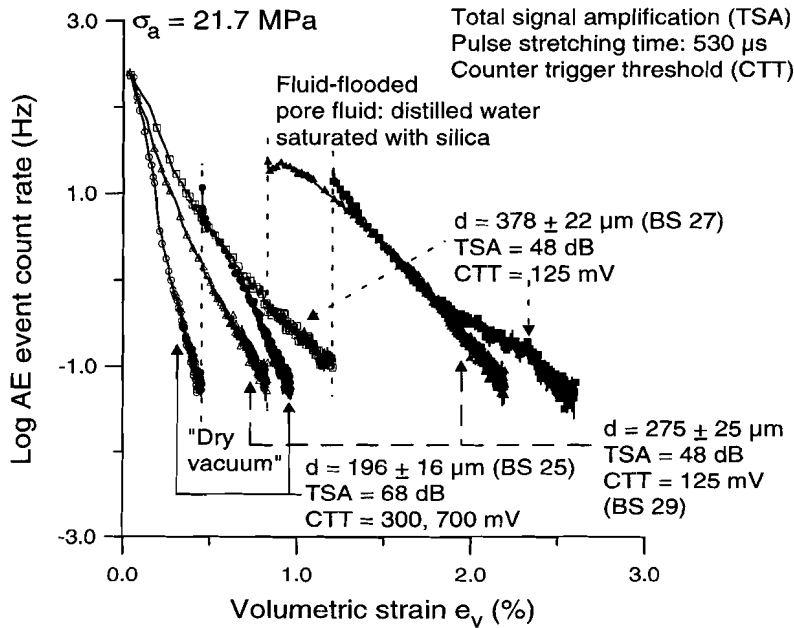


Figure 5.11b

### 5.5.2 Single stage creep tests

Representative cumulative AE event count and AE event count rate data obtained from the single stage creep tests ( $275 \pm 25 \mu\text{m}$  size fraction, applied stresses of 10, 20 and 30 MPa) are shown in Figures 5.12a&b. During initial stages of creep, the data depicted in Figure 5.12a exhibit a highly non-linear relation between cumulative AE event counts and  $e_v$  which intensifies with increasing applied stress ( $\sigma_a$ ). At strains  $> 1.5 \%$ , the data show a near-linear relation between cumulative AE event counts and  $e_v$  as well as clear effects of  $\sigma_a$ , chemical environment and PST. With increasing  $\sigma_a$ , a larger number of AE event counts is obtained both per unit  $e_v$  and, at constant  $e_v$ , with a PST of 530  $\mu\text{s}$ . Furthermore, the samples tested at 30 MPa and flooded with distilled water saturated with silica yielded more AE event counts at constant  $e_v$  than material flooded with *n*-decane. At constant  $e_v$ , the data presented in Figure 5.12b (PST of 530  $\mu\text{s}$ ) show that AE event count rates were significantly higher with increasing  $\sigma_a$  and higher in sands tested at 30 MPa and flooded with distilled water saturated with silica, in comparison to material drained in *n*-decane.

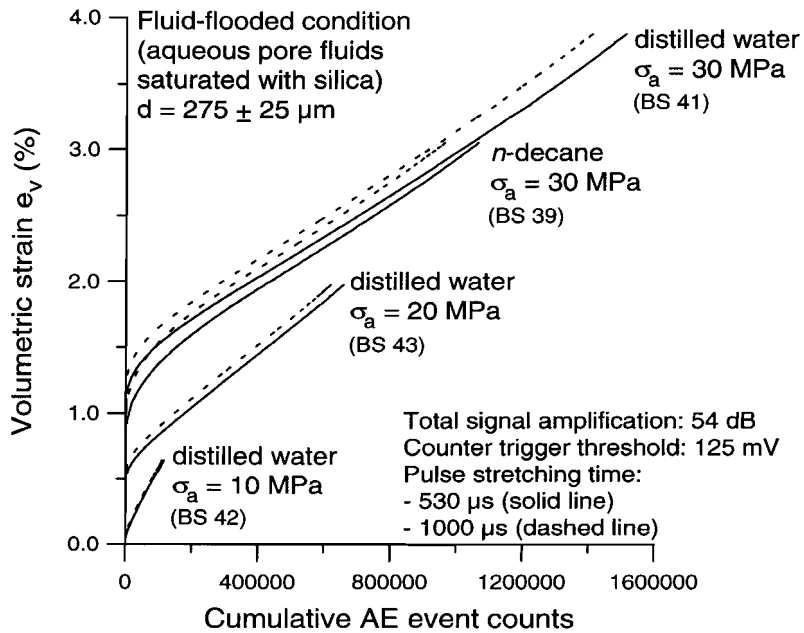


Figure 5.12a

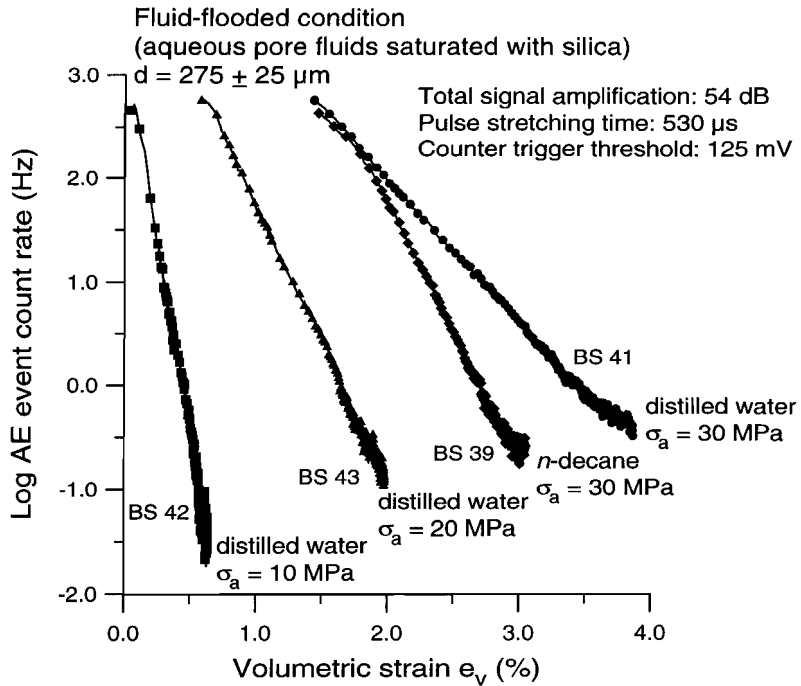


Figure 5.12b



**Figures 5.12a&b (facing page).** *Plots of cumulative AE event count and AE event count rate versus volumetric strain ( $e_v$ ) obtained during typical single stage creep tests (BS 39, 41-43) performed on sands of the  $275 \pm 25 \mu\text{m}$  grain size (d) fraction under flooded conditions (room T). The data show a clear effect of applied stress ( $\sigma_a$ ) and demonstrate that the sample flooded with distilled water saturated with silica yielded higher AE event count rates in comparison to the sample flooded with *n*-decane. The  $e_v$  data displayed in Figures 5.12a&b were calculated with respect to the length of the samples at the point when load ramping was stopped, i.e.  $e_v$  does not include ramping strain. Individual data points are indistinguishable in the curves presented in Figure 5.12a.*

The non-linear relation between cumulative AE event count and  $e_v$  obtained during initial stages of creep illustrates the inability of the AE signal conditioning system to "count" AE event rates above 1300 Hz. In general, during all creep tests, minor undercounting of AE events, due to e.g. clustering of AE events in time, can not be ruled out, so that AE event count (rate) data should be regarded a lower bound of the actual AE event rate (cf. chapter 4, section 4.5).

## 5.6 DISCUSSION OF EXPERIMENTAL RESULTS

The mechanical data presented above firmly demonstrate that the compaction behaviour of the present dry and flooded sand aggregates is time-dependent. Moreover, the relatively insignificant effect of flooding dry samples with *n*-decane suggests that pure frictional compaction processes (particle sliding with no chemical effects) played a minor role during the "dry vacuum" and "flooded" phases of the two stage creep tests, implying that the samples reached a "locked" aggregate state during the initial load ramping/cycling stage. From the microstructural observations made on sand samples subjected to either two stage creep under dry and subsequent flooded conditions *or* to single stage creep under flooded conditions (refer section 5.4 for sample numbers), compaction creep of all samples is inferred to have involved particle fragmentation (crushing) caused by time-dependent transgranular and divergent cone cracking under dry and flooded conditions. Accordingly, the observed dramatic enhancement of creep, acoustic emission (AE) activity and microcracking by an added aqueous pore fluid, implies that such fluids significantly promote creep via chemically related brittle deformation of the sand grains / contacts such as crack growth by stress corrosion, or some other mechanism.

The observed effect of pore fluid salinity on creep suggests, in a purely phenomenological sense, that increasing NaCl concentration in solution promotes one or other of the mechanisms for particle deformation mentioned above, e.g. by lowering the activation energy for subcritical crack growth and therefore speeding up its kinetics. This is a plausible suggestion, since aqueous NaCl is known to increase the dissolution rate of quartz in water around pH 7 by promoting the accessibility of water molecules to the siloxane (Si-O) bonds at the quartz-water

interface. In this process, the weakening and attack of the Si-O bonds is thought to be due to the formation of  $\equiv\text{Si-O}^-\text{Na}^+$  "ion pair" surface complexes (Wirth & Gieskes, 1979; Miller & Dunning, 1985; Brady & Walther, 1990; Dove, 1994). In detail, molecular orbital calculations suggest that the  $\equiv\text{Si-O}^-\text{Na}^+$  bond angle is increased while the Si-O bond is stretched (hence weakened) in comparison to optimized silanol (Si-O-H) surface complexes (Dove & Crerar, 1990; Lasaga & Gibbs, 1990). Furthermore, the  $\text{Na}^+$  ions are considered to enhance the local dissociation of water, providing  $\text{OH}^-$  ions for attack of the Si atoms and leading to rupture of the adjacent Si-O bonds (Dove & Elston, 1992; Gratz & Bird, 1993a,b; Dove, 1994). In addition, aqueous NaCl has been reported to promote crack growth by stress corrosion around pH 7, in soda-lime-silica glass and silica optical fibers, by a similar, inferred mechanism (Takeda *et al.*, 1991; Inniss *et al.*, 1992).

The unsystematic effect of grain size observed during the flooded phase of the two stage creep tests performed on sands from the three different size fractions (refer Figures 5.4b&d) is inferred to be due to the larger amount of volumetric strain (i.e. brittle damage) accumulated by the largest grain size fraction during the "dry vacuum" creep phase, leading to a relatively larger grain size reduction than other, smaller, size fractions, and hence giving rise to slower creep during the flooded phase.

As reported in chapter 4, no acoustic emission (AE) activity was detected during loading of a steel dummy sample used for stiffness calibrations of the compaction apparatus. Moreover, it is unlikely that any AE activity would have been detected during long-term loading of the dummy sample at constant stress. Consequently, the AE events observed on the oscilloscope and counted during sand compaction creep under both dry and flooded conditions are inferred to be caused by the sample, i.e. by time-dependent grain crushing involving transgranular and divergent cone cracking and by sliding-induced rearrangement of grains and grain fragments.

The near-linear relation between cumulative AE event count and volumetric strain ( $e_v$ ), obtained during two stage and single stage creep tests, under dry and flooded conditions, suggests that each grain failure / crushing event contributed to a more or less constant amount of  $e_v$ . The larger number of AE events counted per unit  $e_v$  during the flooded phase of a two stage creep test using distilled water saturated with silica as pore fluid, in comparison with such data obtained during the "dry vacuum" stage or during the final phase with samples drained in *n*-decane, may be explained by the larger number of cracks per grain observed in the microstructure.

The clear effect of grain size ( $d$ ) on the number of AE events ( $n_{\text{AE}}$ ) counted per unit  $e_v$  may be explained with a simple model in which failure of a sand grain is considered to contribute to an incremental volume change equal to  $\alpha d^3$  where  $\alpha$  is a dimensionless constant ( $0 \leq \alpha \leq \pi/6$ ). Accordingly, the "brittle" volumetric strain ( $e_{v(\text{br})}$ ) accumulated due to failure of a cumulative number  $n_N$  of grains is defined by the relation  $e_{v(\text{br})} = (n_N \alpha d^3) / V_0$  where  $V_0$  is the initial (external) volume of the sand

sample. It is further assumed that (i)  $n_{AE}$  and  $n_N$  are linearly related through the relation  $n_{AE} = B(\sigma_a, d) n_N$ , (ii)  $B(\sigma_a, d)$ , being the number of AE events per failing grain, is equal to the number of incremental crack surface steps and hence proportional to the total crack surface created (e.g. Lysak, 1994), and (iii) the crack surface created scales with  $d^2$ , so that  $B(\sigma_a, d) = C(\sigma_a) d^2$ . Notice that these assumptions imply that the AE wave energy associated with a single AE event ( $e_{AE}$ ) is given by the relation  $e_{AE} = D(\sigma_a) A_{AE}$  where  $A_{AE}$  is the characteristic crack surface created per AE event, (notably) independent of grain size. Accordingly, it is easily shown that the number of AE events counted per unit  $e_{v(br)}$  is expressed as  $dn_{AE} / de_{v(br)} = C(\sigma_a) V_0 / (\alpha d)$ . In accordance with this model, the cumulative AE event counts depicted in Figure 5.11a were used to construct the log-log plot of AE event counts per unit  $e_v$  versus grain size displayed in Figure 5.13a. The data clearly show that the number of AE events counted per unit  $e_v$  is roughly proportional to  $d^{-0.9}$  which is in close agreement with the model.

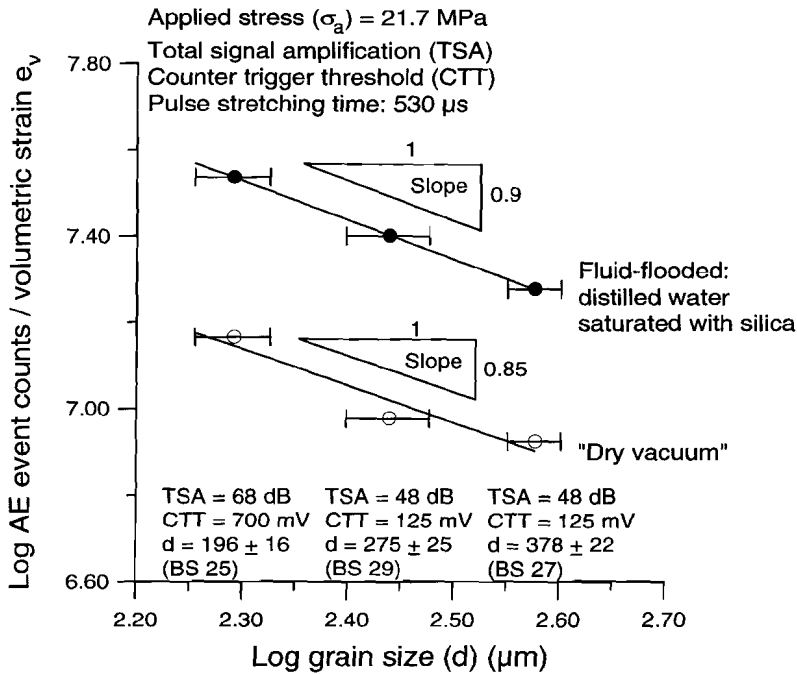


**Figure 5.13a.** Log-log plot of the number of AE events counted per unit volumetric strain ( $e_v$ ) versus grain size ( $d$ ) constructed using the cumulative AE event count data presented in Figure 5.11a (two stage creep tests, room T). The data show that the number of AE events counted per unit  $e_v$  is roughly proportional to  $d^{-0.9}$ .

Moreover, the cumulative AE event counts depicted in Figure 5.12a, from samples flooded with aqueous pore fluid, were used to construct the log-log plot of AE event counts per unit  $e_v$  versus applied stress ( $\sigma_a$ ) presented in Figure 5.13b. The data show that the number of AE events counted per unit  $e_v$  is roughly proportional to  $\sigma_a^{0.9}$ . In the light of the above model, the stress dependence of  $dn_{AE} / de_{v(br)}$  suggests that  $C(\sigma_a)/\alpha$  is some function of  $\sigma_a$ . However, as shown in chapter 4 (section 4.7.3),  $\alpha$  is likely to be independent of  $\sigma_a$ . Consequently, a possible explanation for the stress dependence of the AE data presented in Figure 5.13b might be that  $C(\sigma_a)$  is a linear function of  $\sigma_a$ . This may be a reasonable suggestion, since the microstructural observations have shown that the number of cracks per failed grain increases with increasing  $\sigma_a$ .

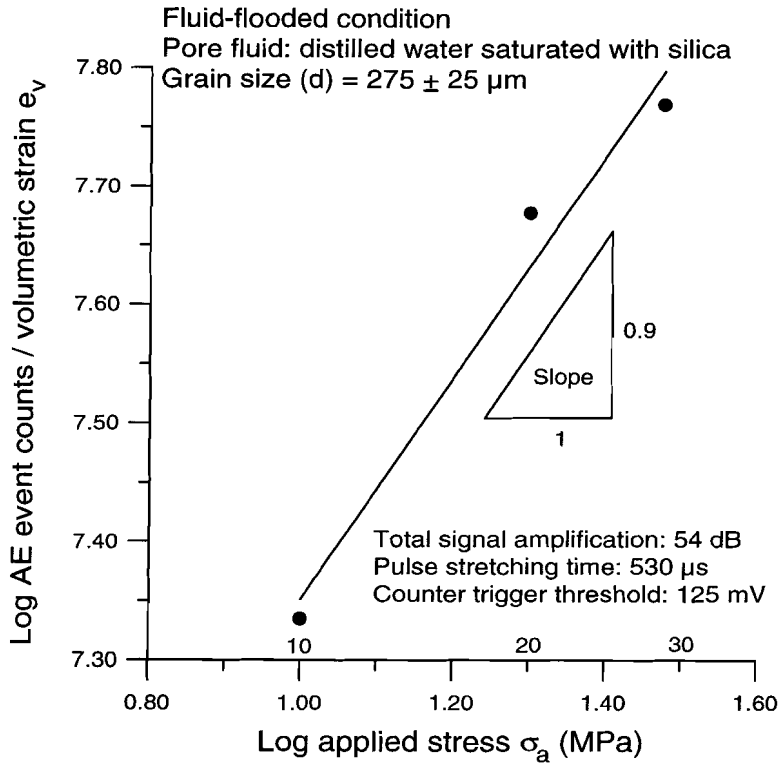


**Figure 5.13b.** Log-log plot of the number of AE events counted per unit volumetric strain ( $e_v$ ) versus applied stress ( $\sigma_a$ ) constructed using the cumulative AE event count data presented in Figure 5.12a, obtained from sand samples subjected to single stage creep and flooded with distilled water saturated with silica (room T). The data show that the number of AE events counted per unit  $e_v$  is roughly proportional to  $\sigma_a^{0.9}$ .

In summary, combining the interpretations of the mechanical, microstructural and AE data discussed above, it is inferred that the compaction creep behaviour of the present sand aggregates under both dry and flooded conditions is primarily controlled by time-dependent contact cracking leading to crushing of grains. This time-dependent grain failure process is clearly promoted by a chemically active pore fluid, by a higher pore fluid salinity, by a larger grain size and by a higher applied stress. Although the detailed time-dependent cracking mechanisms are unknown, it is likely that crack growth by stress corrosion is predominantly operative in the presence of aqueous solutions.

## 5.7 MICROPHYSICAL MODELLING CONSIDERATIONS

Having gained insight into the active microphysical mechanisms, the development of a micromechanical model for time-dependent compaction creep of sands under wet conditions has been attempted (see Appendix). In accordance with the conclusions drawn from the experiments and the time-independent behaviour reported in chapter 4, compaction creep at constant applied stress is modelled as "brittle" strain due to time-dependent failure of individual grains caused by subcritical growth of grain surface flaws by stress corrosion. Grain failure is envisaged to contribute to an incremental volume change due to subsequent, sliding-induced rearrangement of grains and grain fragments.

The model employs the failure criterion for an individual grain formulated in chapter 4, section 4.6.4. Extending this earlier treatment, the model addresses a population of grains. At a given initial applied stress (at a fixed remote load  $F$ ), a certain fraction of the population of grains satisfies this criterion and fails. Consequently, surface flaws in the surviving grain population are of subcritical initial dimension  $c_0$ , i.e. smaller than the crack size at failure  $(c_f)_c$ , for the fixed load  $F$ . While the applied stress remains constant, these subcritical cracks are considered then to grow with a velocity  $v_c$ , under the action of the Hertzian maximum tensile radial stress, until grain failure occurs when the "critical" crack dimension  $(c_f)_c$  is reached after a time  $t_{life}$ , representing the *life time of the individual grain*. The grain life time is defined as  $t_{life} = \int 1/v_c dc$  and is a function of the initial flaw dimension  $c_0$ , the relative radius of curvature  $R_r$  of grain-to-grain contacts (defined in chapter 4) and various material parameters.

This approach implies that if all grains in the model pack were identical and contained identical surface flaws, the model would predict simultaneous failure of all grains after a characteristic  $t_{life}$ , at a fixed load. This is clearly unrealistic. In reality,  $t_{life}$  will be a distributed quantity due to the distributed nature of  $c_0$  and  $R_r$  at the grain-to-grain level. Bearing this in mind, the model has been applied for a *population of grains having distributed  $t_{life}$*  by considering two extreme cases: (i) *spherical* grains with constant radius of curvature plus a grain-to-grain distribution of  $c_0$  (assumed constant per grain) or (ii) *non-spherical* grains with constant  $c_0$ , plus

a grain-to-grain, distribution of "effective" radius of curvature  $r_g$ , characterising contact asperity amplitude. The model can thus be considered as a time-dependent version of that presented in chapter 4 for the time-independent case.

In order to compare the experimental sand compaction creep data, reported in this chapter, with the compaction creep behaviour predicted by cases (i) and (ii) of the above microphysical model, the model has been used as a basis for numerical simulations focusing on wet creep and the effect of applied stress ( $\sigma_a$ ). These simulations showed creep behaviour which is qualitatively similar to that observed in aqueous solution flooded samples, particularly regarding the extreme sensitivity of the compaction creep rate ( $\dot{\beta}$ ) to  $\sigma_a$ . However, the predicted creep rates obtained typically varied from three orders of magnitude faster to three orders of magnitude slower than those observed, depending on the choice of values of crack growth rate law and crack growth limit parameters from the literature (Atkinson, 1979; Atkinson & Meredith, 1981; Darot & Gueguen, 1986; Gueguen *et al.*, 1990; Dunning *et al.*, 1993; McDonald, 1994). Indeed, the model results were found to be so sensitive to these parameters, that the uncertainty in their values apparent in the literature renders comparison between the present model and experimental results meaningless. Comparison is further exacerbated by a lack of data on crack growth rate law parameters for sand grains rather than synthetic quartz single crystals, an insufficient amount of experimental datapoints per time interval at the early stage of tests, and a lack of microstructural constraint on the fraction of grains broken during the initial stages of creep. Suggestions for further experimental research to tackle these problems will be formulated in the following chapter. Nonetheless, it is believed that the basic microphysical processes embodied in the model are a reasonable approximation of the actual processes operative in the experiments.

## 5.8 CONCLUSIONS

Uniaxial compaction creep experiments performed on sands at room temperature, applied stresses in the range 14.5 to 30 MPa and under dry and fluid-flooded conditions, for periods up to 24 days, have shown time-dependent deformation behaviour predominated by subcritical transgranular cracking leading to grain failure accompanied presumably by intergranular sliding rearrangements. The time-dependent grain crushing process is clearly promoted by a chemically active pore fluid, by a higher pore fluid salinity, by a larger grain size ( $d$ ) and by a higher applied stress ( $\sigma_a$ ). In terms of a crude empirical power law formulation, the sensitivity of the compaction rate ( $\dot{\beta}$ ) of the sands to  $\sigma_a$  and  $d$  can be expressed as  $\dot{\beta} \propto d^i \sigma_a^j$  where  $i \approx 6$  and  $j \approx 21$  under dry conditions, and  $i \approx 9$  and  $j \approx 15$  under wet conditions. The detailed cracking mechanism, in the presence of aqueous solutions, is inferred to be crack growth by stress corrosion probably involving cone crack growth under the action of Hertzian contact stresses until a critical crack size is reached. Acoustic emission (AE) monitored during creep of the sands exhibited a

near-linear relation between cumulative AE event counts and strain, suggesting a direct relation between progressive grain failure and strain. Moreover, the number of AE events counted per unit strain were found to be proportional to  $1/d$  and  $\sigma_a$ . This behaviour has been explained in terms of a simple model in which whole grain failure events contribute to a strain increment proportional to  $d^3$ , the number of AE events per failed grain is a direct function of  $\sigma_a$ , and crack surface area scales with  $d^2$ . In addition, the development of a microphysical model for compaction creep of sands by the inferred mechanism has been attempted but could not be meaningfully compared with the experimental results due to excessive sensitivity to input parameter values.

## APPENDIX: MICROPHYSICAL MODEL FOR COMPACTION CREEP OF SANDS BY STRESS CORROSION CRACKING

### A.1 Starting point and principal assumptions

In this model, sand aggregate compaction creep, at constant applied stress, is modelled as "brittle" strain due to time-dependent failure of individual grains caused by subcritical growth of grain surface flaws by stress corrosion. Grain failure is envisaged to contribute to an incremental volume change due to subsequent, sliding-induced rearrangement of grains and grain fragments. The sand aggregate is treated as an ordered packing of monosized grains. Identical assumptions apply as for the time-independent sand compaction model developed in chapter 4, section 4.6.1. These include that no interaction occurs between grain failure events, and that, after grain failure and subsequent rearrangement, the aggregate spatial structure can still be approximated by the ordered packing initially imposed. Furthermore, the grains and/or contact regions are considered to be Hertzian solids of revolution, the remote state of applied stress ( $\sigma_a$ ) is regarded as hydrostatic, and the grain contact force distribution is assumed uniform.

### A.2 Grain contact force and properties of an ordered pack

According to Hertzian theory, the total normal load  $F$  exerted between two grains across a circular planar contact area with radius  $a$  is given by the relation  $F = (2\pi\sigma_0 a^2) / 3 = \pi a^2 \sigma_n$  where  $\sigma_0$  and  $\sigma_n$  are the normal stress at the centre of the contact and the mean normal contact stress. The contact radius  $a$  is described by the relation  $a^3 = 3FR_t / (4E^*)$  where  $R_t$  is the relative radius of curvature and  $E^*$  is the effective Young's modulus (defined in chapter 4, section 4.6.2). In any ordered packing of grains with size  $d$ , the force balance condition prescribes the applied stress ( $\sigma_a$ ) to be equal to  $\zeta_\sigma \pi a^2 \sigma_n / d^2$ , while the initial (external) volume  $V_0$  of the aggregate is given by the relation  $V_0 = \eta N_0 d^3$  with  $N_0$ ,  $\zeta_\sigma$  and  $\eta$  being respectively the initial number of (intact) grains and packing dependent scaling factors of magnitude  $\sim 0.7 - 2.8$  (cf. chapter 4).

### A.3 Contact force enhancement during compaction

After failure and local rearrangement, a grain in the aggregate spatial structure can, as extremes, be envisaged (i) to remain load supporting, (ii) to vanish leaving no empty site or (iii) to no longer support load and hence to increase the load on surrounding grains without significantly changing the packing structure (as previously assumed). For situations (i) and (ii), the grain contact normal load ( $F$ ) remains as given in above. For situation (iii), load enhancement at a given applied stress ( $\sigma_a$ ) can be incorporated following the relation

$$F = \frac{\sigma_a d^2}{\zeta_\sigma} \frac{N_0}{N_0 - n_N} \quad (1)$$

where  $n_N$  is the cumulative number of failed grains.

### A.4 Subcritical crack growth by stress corrosion

A large body of experimental and observational evidence exists that in brittle materials including glass, ceramics and rocks, cracks can propagate in a stable, quasi-static manner at values of the mode I stress intensity factor ( $K_I$ ) substantially below its critical value ( $K_{Ic}$ ). A number of micromechanisms have been suggested to account for this phenomenon of "subcritical crack growth": e.g. atomic diffusion, dissolution, stress corrosion (Atkinson & Meredith, 1989a). At low homologous temperatures, the extension of pre-existing flaws and cracks is clearly enhanced by a chemically reactive, aqueous fluid implying "stress corrosion" to be the dominant mechanism (Atkinson & Meredith, 1989a). Crack growth by stress corrosion proceeds by the preferential weakening of strained bonds at crack tips through reactions with chemical species in the environment (Michalske & Bunker, 1984, 1993; Lindsay *et al.*, 1994). Numerous rate descriptions have been formulated. Many of these express the crack growth velocity ( $v_c$ ) *empirically* in power law form as  $v_c = A^* K_I^n$ , where  $A^*$  is a temperature dependent term and  $n$  is the subcritical crack growth index. Others have developed *phenomenological* models, employing reaction rate or transition state theory, and expressing growth velocity in exponential form as  $v_c = B^* \exp[C^* G_I]$ , where  $G_I$  is the mode I strain energy release rate while  $B^*$  and  $C^*$  are temperature dependent terms (Rice, 1978; Darot & Gueguen, 1986; Cook, 1989; Chuang & Fuller, 1992; Lawn, 1993; Cook & Liniger, 1993; cf. Meredith, 1990 and Gueguen *et al.*, 1990). Here, the growth rate law of Darot & Gueguen (1986) is chosen because of its theoretical basis. Following Darot and Gueguen (1986), the subcritical crack growth velocity ( $v_c$ ) (in quartz), in aqueous environment, is given



$$v_c = v_0 \left( \frac{a^*}{a_0^*} bl \Gamma_0 \right) \exp \left[ - \frac{E_{act} + bl\gamma_0}{k_B T} \right] \exp \left[ \frac{blG_I}{2k_B T} \right] = v_0^* \exp \left[ \frac{blG_I}{2k_B T} \right] \quad (2)$$

where  $v_0$  is the crack velocity with respect to the reference state  $G_I = 0$ ,  $a_0^*$  is a reference activity of the reactive species,  $a^*$  is the relative activity of the reactive species,  $b$  is the (elementary) crack advancement or jump distance,  $l$  is the crack front length,  $\Gamma_0$  is the surface concentration of the adsorbed species,  $E_{act}$  is the activation energy for crack growth,  $\gamma_0$  is the surface energy in vacuum,  $k_B$  is Boltzmann's constant,  $T$  is absolute temperature and  $G_I$  is the mode I strain energy release rate defined in plane strain and for identical bodies in contact by the relation  $G_I = K_I^2 (1-\nu^2) / E = K_I^2 / 2E^*$  with  $\nu$  being the Poisson's ratio (Lawn, 1993, § 2.4). In principle, the constraints  $G_{lim} < G_I < G_{Ic}$  and  $v_c < v_{Rayleigh}$  apply to eqn. 2, where  $G_{lim}$  and  $G_{Ic}$  are the strain energy release rates at the stress corrosion limit (for  $G_I < G_{lim}$ ,  $v_c = 0$ ) and at the critical point (for  $G_I = G_{Ic}$ ,  $v_c = v_{Rayleigh}$ ), and where  $v_{Rayleigh}$  is the (limiting) Rayleigh surface wave velocity.

#### A.5 Grain failure criterion and grain life time

The present model employs the failure criterion for an individual grain formulated in chapter 4 (section 4.6.4) as

$$F_c = \frac{9\pi\sqrt{\pi} K_{Ic}^3 R_r^2}{2c_f\sqrt{c_f} (m^*)^3 (1-2\nu)^3 (E^*)^2} \quad (3)$$

where  $F_c$  and  $c_f$  are the critical force and crack dimension at failure respectively while  $m^* \approx 1.12$  is an edge correction factor. Upon application of a fixed stress (at a fixed load  $F$ ), a certain fraction of the population of grains satisfies this criterion and fails. Consequently, surface flaws at grain contact margins (modelled as edge cracks, cf. chapter 4) in the surviving grain population are initially of subcritical initial dimension  $c_0 < (c_f)_c$  where  $(c_f)_c$  is the crack size at failure, at the fixed load  $F$ . These subcritical cracks are considered then to grow, under the action of the Hertzian maximum tensile radial stress at contact margins ( $\sigma_T = (1-2\nu)\sigma_0/3$ , cf. chapter 4). Crack growth continues in individual grains until grain failure occurs when reaching the critical crack dimension  $(c_f)_c$  after a time  $t_{life}$ . This time quantity represents the life time of an individual grain. It is further assumed that  $\sigma_T$  is uniform and constant along the (short) crack growth path. Since  $v_c = dc / dt$ , the lifetime ( $t_{life}$ ) of an individual grain can be written (e.g. Costin, 1989; Meredith, 1990; Cook, 1993)

$$t_{life} = \int_{c_0}^{(c_f)_c} \frac{1}{v_c} dc = \frac{1}{v_0^*} \int_{c_0}^{(c_f)_c} \exp \left[ -\frac{blG_I}{2k_B T} \right] dc \quad (4)$$

Making use of the relations for  $a$ ,  $\sigma_0$ ,  $\sigma_T$  and  $G_I$  given above, and for the mode I stress intensity factor  $K_I$  defined in chapter 4 (section 4.6.4) as  $K_I = \sigma_T m^* \sqrt{\pi c_0}$ ,  $t_{life}$  is given

$$t_{life} = \frac{1}{v_0^*} \left| -\frac{1}{A} \exp [-Ac] + Z \right|_{c_0}^{(c_f)_c} = \frac{1}{Av_0^*} \left( \exp [-Ac_0] - \exp [-A(c_f)_c] \right) \quad (5)$$

where  $Z$  is the constant of integration and  $A$  is expressed as

$$A = \frac{bl(m^*)^2(1-2\nu)^2}{12\pi k_B T} \sqrt[3]{\frac{4E^*F^2}{3R_r^4}} \quad (6)$$

Substitution for  $A$  and  $(c_f)_c$ , defined from the grain failure criterion as (cf. chapter 4)

$$(c_f)_c = 3\pi \left( \frac{K_{Ic}}{m^*(1-2\nu)} \right)^2 \sqrt[3]{\frac{3}{4F^2} \left( \frac{R_r}{E^*} \right)^4} \quad (7)$$

leads to

$$t_{life} = \frac{1}{Bv_0^*} \sqrt[3]{\frac{3R_r^4}{4E^*F^2}} \left( \exp \left[ -B \sqrt[3]{\frac{4E^*F^2}{3R_r^4}} c_0 \right] - \exp \left[ -\frac{blK_{Ic}^2}{4k_B T E^*} \right] \right) \quad (8)$$

where  $B$  is expressed as

$$B = \frac{bl(m^*)^2(1-2\nu)^2}{12\pi k_B T} \quad (9)$$

If all grains in the model pack were identical and contained identical surface flaws, eqn. 6 would predict simultaneous failure of all grains after a certain  $t_{life}$ , at a fixed load. This is clearly unrealistic. In reality,  $t_{life}$  will be a distributed quantity due to the distributed nature of  $c_0$  and  $R_r$  at the grain-to-grain level. Bearing this in mind, the model can be extended to a population of grains having distributed  $t_{life}$  by considering two extreme cases: (i) *spherical* grains with constant radius of curvature  $R$  ( $R_r = d/4$ ) plus a grain-to-grain distribution of initial flaw sizes ( $c_0$ ) (assumed constant per grain) written in terms of  $t_{life}$  as

$$c_0(t_{life}) = -\frac{1}{B} \sqrt[3]{\frac{3R_r^4}{4E^*F^2}} \ln \left( B v_0^* \sqrt[3]{\frac{4E^*F^2}{3R_r^4}} t_{life} + \exp \left[ -\frac{bIK_{lc}^2}{4k_bTE^*} \right] \right) \quad (10)$$

or (ii) *non-spherical* grains with constant initial flaw size  $c_0$ , plus a grain-to-grain, distribution of "effective" radius of curvature  $r_g$ , characterising contact asperity amplitude. Note that an expression for  $r_g(t_{life})$  cannot be written in explicit form. Implicit in case (ii) of the model is the assumption that, despite the non-spherical nature of the grains, the aggregate spatial structure can be treated as an ordered packing with an equivalent-sphere mean grain size  $d_{eq}$ . Furthermore, an asperity with effective radius of curvature  $r_g$ , on a specific grain, is considered to be always in contact with that side of a neighbouring grain whose radius of curvature  $R$  ( $\neq r_g$ ) is described by the relation  $d_{eq} = 2R$  (cf. chapter 4).

#### A.6 Brittle strain

Grain failure is considered to contribute to an incremental volume change equal to  $\alpha d^3$  or  $\alpha d_{eq}^3$  where  $\alpha$  is a dimensionless constant ( $0 \leq \alpha \leq \pi/6$ ). Employing the grain life time concept introduced above, at a certain point in time  $t$ , a cumulative number  $n_N(t)$  of grains with a lifetime  $t_{life} \leq t$  will have failed contributing to a "brittle volumetric strain"  $e_{v(br)}(t) = n_N(t) (\alpha d_{eq}^3)/V_0 = (\alpha/\eta) (n_N(t)/N_0)$ . Now, the ratio  $n_N(t)/N_0$  ( $\lim N_0 \rightarrow \infty$ ) represents the cumulative probability of failure of grains with a life time  $t_{life} \leq t$  (i.e.  $\Pr[t_{life} \leq t]$ ) and is therefore expressible using a suitable cumulative distribution function. Furthermore, for case (i) of the model, it follows from eqn. 8 that the probability  $\Pr[t_{life} \leq t]$  coincides with the probability of existence of grains with cracks grown to a size  $c_t \geq (c_f)_c$  (i.e.  $\Pr[c_t \geq (c_f)_c]$ ). Besides, it follows from eqn. 10 that a particular  $t_{life} = t$  corresponds to a certain initial crack size  $c_0(t_{life})$ , which has grown to a size  $(c_f)_c$  in the time  $t$ . Accordingly, at time  $t$ , a cumulative number of grains  $n_N$  with initial crack size greater than or equal to  $c_0(t_{life})$  have failed (i.e.  $n_N(c_0 \geq c_0(t_{life}))$ ).

Similarly, for case (ii) of the model, it follows from eqn. 6 that the probability  $\Pr[t_{life} \leq t]$  coincides with the probability of existence of a grain with an effective radius of curvature of size  $r_g \leq (r_g)_c$  where  $(r_g)_c$  is the effective radius of curvature

at failure defined

$$(r_g)_c = \frac{4RE^*a^3}{3RF - 4E^*a^3} = \left( \frac{3}{E^*} \sqrt{\frac{1}{2F} \left( \frac{K_{Ic}}{m^*(1-2\nu)} \right)^3 \frac{\pi\sqrt{\pi}}{c_f\sqrt{c_f}}} - \frac{1}{R} \right)^{-1} \quad (11)$$

It follows from eqn. 8 that a particular  $t_{life} = t$  corresponds to a certain (grain with an) effective radius of curvature  $r_g(t_{life})$  whose initial crack has grown to a size  $c_f$  in the time  $t$ . Thus, at time  $t$ , a cumulative number of grains  $n_N$  with an effective radius of curvature smaller than or equal to  $r_g(t_{life})$  have failed (i.e.  $n_N(r_g \leq r_g(t_{life}))$ ).

Assuming a Weibull distribution of  $c_0$ , the "brittle volumetric strain"  $e_{v(br)}$  for case (i) of the model can accordingly be written as ( $\lim N \rightarrow \infty$ )

$$e_{v(br)(i)}(t_{life}) = \frac{\alpha}{\eta} \frac{n_N(c_0 \geq c_0(t_{life}))}{N} \approx \frac{\alpha}{\eta} \left( 1 - W(c_0(t_{life})) \right) = \frac{\alpha}{\eta} \exp \left[ - \left( \frac{c_0(t_{life})}{k} \right)^m \right] \quad (12)$$

where  $W(c_0(t_{life}))$  is the Weibull cumulative distribution function,  $k$  and  $m$  being the scale and shape parameters of this distribution. The expression can be rewritten as

$$c_0(t_{life}) \approx k \left[ \ln \left( \frac{\alpha}{\eta e_{v(br)(i)}(t_{life})} \right) \right]^{\frac{1}{m}} \quad (\lim N \rightarrow \infty) \quad (13)$$

Likewise, assuming a Weibull distribution of  $r_g$ , the "brittle strain" for case (ii) of the model can be expressed as ( $\lim N \rightarrow \infty$ )

$$e_{v(br)(ii)}(t_{life}) = \frac{\alpha}{\eta} \frac{n_N(r_g \leq r_g(t_{life}))}{N} \approx \frac{\alpha}{\eta} W(r_g(t_{life})) = \frac{\alpha}{\eta} \left( 1 - \exp \left[ - \left( \frac{r_g(t_{life})}{k} \right)^m \right] \right) \quad (14)$$

This expression can be rewritten as

$$r_g(t_{life}) \approx k \left[ \ln \left( \frac{\alpha}{\alpha - \eta e_{v(br)(ii)}(t_{life})} \right) \right]^{\frac{1}{m}} \quad (\lim N \rightarrow \infty) \quad (15)$$

## A.7 Final model

Final expressions for time as a function of the "brittle volumetric strain"  $e_{v(br)}$ , at a point of time  $t$  equal to a certain  $t_{life}$  (taken from the  $t_{life}$ - distribution), can now be obtained by substitution of either eqn. 13 or 15 into eqn. 8.

For case (i) of the model, substitution of eqn. 1 and the relation  $R_r = d/4$  into eqn. 8 demonstrates  $t_{life}$  (and therefore  $t(e_{v(br)})$ ) to be grain size independent. The relation  $t(e_{v(br)})$  for case (i) of the model only exhibits a grain size dependence if the Weibull parameters  $m$  and  $k$  (in eqns. 12 or 13) are grain size dependent. For case (ii) of the model, substitution of eqn. 1 (taking  $d$  equal to  $d_{eq}$ ) and the relation  $2R = d_{eq}$  into eqn. 8 illustrates  $t_{life}$  (and therefore  $t(e_{v(br)})$ ) to be grain size dependent.

Simulations of the model produced creep curves of similar shape but with a condensed or expanded time scale, in comparison to curves obtained during single stage creep tests on sands flooded with distilled water saturated with silica. The predicted timescales obtained typically varied  $\pm$  three orders of magnitude dependent on the choice of values of crack growth rate law and crack growth limit parameters in the literature (cf. section 5.7). In addition, the simulated creep curves showed extreme sensitivity to  $\sigma_a$ ; a factor of three change in  $\sigma_a$  caused time scale changes of four orders of magnitude (refer eqn. 8 where  $F$  is proportional to  $\sigma_a$ ).

## CHAPTER 6 GENERAL CONCLUSIONS AND SUGGESTIONS FOR FURTHER RESEARCH

This thesis has investigated the failure behaviour of single quartz sand grains, and the compaction and creep behaviour of quartz sand aggregates (Heksenberg Sand, Heerlen, The Netherlands). The purpose of the present final chapter is to summarize the principal conclusions following from the findings presented in the preceding chapters. In addition, questions which remain unanswered are identified and suggestions are made for further research.

### 6.1 FAILURE BEHAVIOUR OF SINGLE SAND GRAINS

The review and synthesis, presented in Chapter 2, of all available theoretical solutions to the elastic stress distribution in a sphere subjected to diametric surface loading has shown that near-field (contact) stresses can be satisfactorily described with the classical Hertz-Huber solution (Hertz, 1896; Huber 1904), whereas far-field (internal) stresses can be described adopting the solution after Sternberg & Rosenthal (1952) for a sphere under concentrated loads. Furthermore, a comparison between microstructural observations, reported in the literature, and the various theoretical solutions demonstrated that sphere failure is expected to initiate at surface flaws which develop into ring cracks at the edge of the loaded contact area. Under the action of the local maximum radial tensile stress, these propagate as (transgranular) convergent cone cracks leading to whole-grain failure. In addition, a comparison of the magnitudes of (local) maximum tensile stresses predicted by the stress distribution models has shown that the Hertzian radial stress at the edge of the contact circle is the maximum tensile stress occurring anywhere within or on the surface of a quartz grain. Combining the expression for the Hertzian maximum tensile stress ( $\sigma_T$ ) with linear elastic fracture mechanics (LEFM) considerations, the following failure criterion for a brittle quartz grain was obtained

$$K_{Ic} = 1.12 \sigma_T \sqrt{\pi c_f} \quad (1)$$

where  $K_{Ic}$  is the fracture toughness, for quartz equal to 1 MPa  $\sqrt{m}$  (Atkinson & Meredith, 1989b), and  $c_f$  is the flaw dimension at failure.

Making use of this grain failure criterion, micromechanical models for grain crushing under conditions of (diametric) compression between flat platens have been developed (Chapter 3). Applying the Hertzian/LEFM model for grain failure, which predicts that the load at failure ( $F_c$ ) is a function of  $c_f$  and of the radius of curvature ( $R_g$ ) of the unloaded grain contact surface,  $F_c$  data obtained from crushing tests carried out on selected, well-rounded single sand grains (i.e. with measurable  $R_g$ ) have been translated into an accurate estimate of  $c_f$  equal to  $0.115 \pm 0.065 \mu m$ . Likewise, the distributed  $F_c$  data obtained from crushing tests, performed on grains sampled from different grain size batches, have been translated into distributions of

failure stress ( $\sigma_f = \sigma_T$ ). Assuming spherical grains and a single flaw population causing grain failure, a statistical model for grain crushing based on Weibull weakest link theory is unable to account for an observed grain size dependence of  $\sigma_f$ . On the other hand, the Hertzian/LEFM model enables the translation of the distributed  $F_c$  data, considering two extreme cases, into distributions of (i)  $c_f$ , assuming a perfectly spherical grain geometry, or (ii) "effective" radius of curvature ( $r_g$ ), characterising surface asperity amplitude of non-spherical grains. The data imply  $c_f$  or  $r_g$  to be proportional to the grain size ( $d$ ) as  $d^f$  where  $f \approx 0.5-0.7$ . Since there is no clear physical basis for a grain size dependence of  $c_f$  and since sphericity and roundness data reported for dune sands exhibit a similar relation between  $r_g$  and  $d$ , it is inferred that the Hertzian/LEFM model assuming non-spherical grains with a distributed  $r_g$  is the most physically reasonable model for grain failure.

## 6.2 COMPACTION AND CREEP BEHAVIOUR OF SAND AGGREGATES

In Chapter 4, uniaxial compaction experiments were reported. These were performed on sand aggregates, at room temperature, stresses up to 30 MPa, with grain sizes of  $196 \pm 16$ ,  $275 \pm 25$  and  $378 \pm 22$   $\mu\text{m}$ , under dry and fluid-flooded conditions (using an aqueous or inert pore fluid), and applying constant loading rates in the range 3.90 to 5495 MPa/hour. They typically showed quasi-elastic loading behaviour and permanent deformation caused by grain contact distortion and grain failure. In particular, the stress-strain data obtained exhibited a systematic effect of grain size but no significant effect of loading history and chemical environment. On this basis, a microphysical model for the time-independent compaction of sands has been developed, considering aggregate densification to be the sum of "elastic" strain due to Hertzian grain contact distortion and "brittle" strain due to crushing (instantaneous failure) of individual grains, employing the Hertzian/LEFM model for grain failure referred to above. Again, two extreme cases have been considered: (i) spherical grains with distributed flaw size at failure ( $c_f$ ), and (ii) non-spherical grains with distributed effective surface radius of curvature, characterising contact asperity amplitude. Results produced by simulating case (ii) of the model offered the best agreement with the form and the grain size dependent trend of the experimental stress-strain curves, suggesting that a grain size dependent departure from sphericity of the grains is important in controlling the compaction behaviour of sands as well as the failure behaviour of single grains.

In addition, Chapter 5 reported uniaxial compaction *creep* experiments performed on sand samples at room temperature, (constant) applied stresses in the range 14.5 to 30 MPa, and under dry and fluid-flooded conditions (using an aqueous or inert pore fluid). The results showed time-dependent deformation behaviour predominated by subcritical transgranular cracking leading to grain failure. The time-dependent grain crushing process is clearly promoted by a chemically active pore fluid and by

a higher pore fluid salinity, and is strongly promoted by larger grain sizes ( $d$ ) and higher applied stresses ( $\sigma_a$ ). The detailed cracking mechanism, in the presence of aqueous solutions, is inferred to be growth of grain surface flaws by stress corrosion, at grain-to-grain contacts. Acoustic emission (AE) monitored during creep of the sands exhibited a near-linear relation between cumulative AE event counts and strain, suggesting a direct relation between progressive grain failure and strain. Moreover, the number of AE events counted per unit strain were found to be proportional to  $1/d$  and  $\sigma_a$ . This behaviour can be explained in terms of a simple model in which whole grain failure events contribute to a strain increment proportional to grain volume (i.e.  $d^3$ ), the number of AE events per failed grain is a direct function of  $\sigma_a$ , and crack surface area scales with  $d^2$ .

### 6.3 IMPLICATIONS OF RESULTS

The work presented in this thesis provides basic microphysical insight into sand grain failure and into the compaction behaviour of sands. It thus provides relevant micromechanical underpinning for studies of both natural and man-induced deformation of clastic sediments. Examples include the compaction of fault gouge materials, oil sands and poorly consolidated clastic hydrocarbon reservoirs in the (post-)production phase, the response of hydrocarbon-bearing reservoir rocks to cyclic steam stimulation and explosive perforation methods (techniques designed to improve hydrocarbon recovery rates from such formations). In this section, consideration will be given to the implications of the results presented in this thesis for the compaction of fault gouge materials and (poorly) consolidated clastic hydrocarbon reservoirs in the (post-)production phase.

Grain crushing alongside dissolution-precipitation processes are known to play an important role in controlling the time-dependent compaction behaviour of fault gouge materials such as quartz sands (Marone & Scholz, 1989; Morrow & Byerlee, 1989; Sleep & Blanpied, 1992; Blanpied *et al.*, 1992; Rutter & Maddock, 1992; Scott *et al.*, 1994). Consolidation (porosity loss) is not only considered to lead to increased strength of the gouge with time but also to elevate the pore fluid pressure within the fault, due to sealing, allowing frictional failure at relatively low shear stress (Sleep & Blanpied, 1992; Blanpied *et al.*, 1992). The resulting earthquake faulting is considered to restore porosity and to decrease the fluid pressure, thereby initiating a new compaction or earthquake cycle (Sleep & Blanpied, 1992; cf. Gratier *et al.*, 1994 and Knipe, 1994). The sand compaction creep data presented in this thesis provide insight into the brittle consolidation processes of the type found to operate in fault gouge materials and may eventually lead to an improved capacity to model the damage mechanics controlling crustal earthquakes, e.g. in accretionary wedges (cf. King & Sammis, 1992; Davis, 1994; Sibson, 1994).

Compaction of hydrocarbon-bearing clastic reservoir rocks during production is widely considered to lead to surface subsidence (e.g. Segall, 1992). For example, in-



situ (earth surface and well site) measurements of the compaction behaviour of the Groningen gas field (N-Netherlands) over the last decades have revealed that the amount of compaction is linearly related to the decrease in gas pressure (i.e. the increase in effective stress) (Doornhof, 1992; NAM status report, 1990, 1995). The apparently linear stress-strain behaviour of the *consolidated* reservoir rock could be interpreted as an effect of time-independent deformation occurring during each gas pressure reduction step or effective stress increment. However, the compaction experiments on *unconsolidated* sands, reported in this thesis, have shown that extensive, permanent and apparently time-independent densification is attained during loading to effective stresses comparable with reservoir conditions, and is followed by less important but nonetheless significant (i.e. on-going) time-dependent consolidation creep. Accordingly, the apparently time-independent compaction behaviour observed for reservoir rocks such as those in Groningen may originate from combined time-independent and time-dependent consolidation processes, the latter being so rapid in comparison with production rates that the overall behaviour appears to be instantaneous. Consequently, time-dependent compaction of the reservoir rock leading to continued surface subsidence may only become apparent when production ends. However, compaction creep of the reservoir rock will presumably decelerate quickly, giving rise to considerable consolidation only on very long-term scales. On the basis of the permanent deformation attained in the present tests, it is inferred that incomplete strain recovery will occur if unloading of the reservoir rock is attempted with the recoverable part corresponding to elastic unloading.

## 6.4 REMAINING PROBLEMS AND SUGGESTIONS FOR FURTHER RESEARCH

While the present study has addressed a substantial number of the *fundamental* questions posed in the introduction, it will be apparent that numerous questions remain unanswered or only partly answered, and that some new questions are raised. This prompts the following suggestions for further research.

### 6.4.1 Grain contact stress fields / grain failure criteria

On the basis of experimental observations carried out by the Karlsruhe-Freiburg group (Rumpf *et al.*, 1967; Rumpf & Schönert, 1972; see also Kienzler & Schmitt, 1990) on brittle spheres loaded diametrically to failure (refer chapter 2, section 2.4), ring cracks initiating due to the maximum Hertzian radial tensile stress ( $\sigma_{rr}$ ) at the contact circle edge of a quartz sphere *have been inferred in this thesis to lead to whole-grain failure*. Hence, the ring crack is considered to be subjected to a uniaxial stress field equal to  $\sigma_{rr}$  and to propagate in tensile mode I. This whole-grain failure criterion could be refined by clarifying / incorporating the three issues

formulated below. First, the ring crack is subjected to (at least) a biaxial stress field composed of  $\sigma_{rr}$  and the (compressive) tangential stress component  $\sigma_{\theta\theta}$  (if shear stresses just below the contact surface are disregarded). Clearly, it should be investigated in how far the ring crack is further affected (apart from  $\sigma_{rr}$ ) by  $\sigma_{\theta\theta}$  or shear stresses. In other words, the true nature of the equivalent stress ( $\sigma_{eq}$ ), representing the local state of stress (refer chapter 3, section 3.2.2), should be evaluated by conducting single grain failure tests designed to vary the  $\sigma_{rr}$  to  $\sigma_{\theta\theta}$  ratio. Secondly, it should be established, by conducting finite element (FE) computations for example, whether the ring crack is indeed *unstable* after its stress intensity factor attains a value equal to the fracture toughness, instead of (indirectly) assuming instability. Third, the FE computations could serve to predict the *exact* crack propagation path and to clarify in how far the crack indeed *remains unstable* along its advancement path.

In the micromechanical models developed in this thesis, sand grains are assumed to make *idealized Hertzian (i.e. frictionless) contact* with each other or with flat platens that load the grains diametrically (cf. chapter 2, section 2.2.4 and 2.2.5). However, under realistic loading conditions, the contact stress distribution may be modified due to *adhesion or friction*, the latter caused either by contact surface roughness or by mismatch of the elastic constants of the bodies in contact (Johnson, 1987, chapter 5). Recently, Tutuncu & Sharma (1992) have incorporated the effect of adhesive surface forces into Hertzian contact theory and have demonstrated that the surface forces only become important at extremely low loads ( $\sim 0.001$  N for glass spheres with a diameter of  $20\text{ }\mu\text{m}$ ) (cf. Johnson *et al.*, 1971; Barquins & Maugis, 1982; Derjaguin *et al.*, 1975, 1987; Johnson, 1987, § 5.5; Rimai *et al.*, 1995). With regard to the effect of elastic mismatch of smooth contacting elastic bodies, considerable controversy exists in literature about the detailed description of the stress components at the loaded contact (cf. Johnson *et al.*, 1973; Hills & Sackfield, 1987; Warren & Hills, 1994). However, if the contacting bodies possess the same elastic constants, friction-induced tangential tractions occurring at the contact surface do not disturb the Hertzian normal stress distribution (cf. Johnson, 1987, § 5.4 and 7.1). On the other hand, Dai *et al.* (1995) (cf. Warren *et al.*, 1994) have recently carried out a theoretical analysis of the mode I crack tip stress intensity factor  $K_I$  existing around the front of a surface flaw, when it is propelled by a Hertzian stress field at the frictionless contact between two similar bodies. They have shown that a surface flaw will "run around" in an unstable manner, to form a shallow ring crack just outside the contact radius (at the locus of maximum  $K_I$ ), before propagating inwards into the material. Consequently, expecting the asperity amplitudes of real surface roughness to be generally larger than the range of action of adhesive surface forces, and considering the effects of elastic mismatch to be of secondary importance, an attempt could be made to further elaborate the micromechanical models developed in this thesis by (i) incorporating the effect of surface roughness, following e.g. Yoshioka & Scholz (1989), Boitnott *et al.* (1992)

and Yoshioka (1994), and (ii) to consider the exact distribution of  $K_I$  at the grain-to-grain contact, e.g. following the analysis by Dai *et al.* (1995).

Finally, in order to further evaluate the role of grain non-sphericity / contact angularity on the time-independent compaction and compaction creep behaviour of sands, grain failure criteria should be developed based on *non-Hertzian contact stress fields*, and be tested by carrying out single grain crushing and compaction (creep) tests on sands of different roundness.

#### 6.4.2 Instantaneous failure behaviour of single sand grains

In chapter 3, flaw sizes at failure ( $c_f$ ) of individual sand grains have been estimated on the basis of results obtained from crushing tests carried out on selected well-rounded grains and employing the Hertzian/LEFM model for grain failure. In conjunction with this, fractography on single sand grains should be pursued to (possibly) independently evaluate the nature (i.e. dimension and shape) of the flaws associated with failure. Furthermore, a fracture toughness ( $K_{Ic}$ ) for sand grains equal to 1 MPa  $\sqrt{m}$  was employed in this thesis - a representative value based on double torsion tests on synthetic quartz single crystals at room temperature and under vacuum (0.1 Pa), ambient or water-immersed conditions. Clearly, it is desirable to determine the value of  $K_{Ic}$  for quartz sand grains and (if any) the effect of chemical environment on  $K_{Ic}$ .

#### 6.4.3 Time-dependent failure behaviour of single sand grains

During numerical simulations of the microphysical model for compaction creep of sands by stress corrosion cracking (chapter 5, section 5.7), crack growth law fit parameters and a representative value for the stress intensity factor at the lower crack growth limit ( $K_{lim}$ ) were used, based on double torsion tests carried out on synthetic quartz single crystals at room temperature and under water-immersed conditions. Since crack growth rate law fit parameters for quartz sand grains are unknown, a need exists to assess the effect of subcritical crack growth on the strength of individual sand grains. Therefore, single grain crushing tests should be carried out at orders of magnitude different loading rates and using different immersion fluids (distilled water vs. an inert fluid, e.g. *n*-decane). Accordingly, the crack growth rate law fit parameters obtained for the sand grains could be used to evaluate initial surface flaw dimensions (before growth) on the basis of the flaw sizes at failure acquired from the single grain crushing tests. In addition, improved (i.e. better constrained) crack growth rate law fit parameters and a representative value for  $K_{lim}$  are needed for natural and synthetic quartz single crystals.

It was shown in chapter 5, that compaction creep of sands by time-dependent transgranular cracking is promoted by a higher pore fluid salinity (NaCl content). In order to further elucidate the detailed cracking mechanism, creep tests should be carried out on quartz sands using aqueous pore fluids with different salts (e.g. LiCl,

NaCl, CsCl). Such an effort could lead to resolving questions such as: which ion (cat- or anion) controls the cracking mechanism (inferred to be the weakening and attack of siloxane bonds at the quartz-water interface, cf. section 5.6.1) and what is the effect of ion size.

#### 6.4.4 Experimental aspects

With regard to the acoustic emission (AE) signal conditioning system built in the HPT Laboratory at Utrecht, a need exists to develop the possibility to determine the energy content of individual AE waveforms ( $e_{AE}$ ), obtained during compaction creep experiments performed on sands at different applied stresses ( $\sigma_a$ ) and using different grain size ( $d$ ). This would enable, in the light of the model presented in chapter 5, to (a) evaluate the relation between  $e_{AE}$  and the characteristic crack surface area created per AE event ( $A_{AE}$ ) at different  $\sigma_a$ , and (b) to verify whether  $e_{AE}$ , and hence  $A_{AE}$ , is independent of  $d$  at constant  $\sigma_a$  (cf. chapter 5, section 5.6). In addition, logging of the time interval between consecutive AE events would enable the assessment of the importance of AE event clustering in time and hence of grain failure interaction effects (cf. chapter 4, section 4.5).

To enable the comparison of data obtained from sand compaction creep tests with the behaviour predicted by the microphysical model for compaction creep of sands by stress corrosion cracking developed in chapter 5, single stage creep tests (refer section 5.2.5) should be performed on sands at room temperature, stresses below 15 MPa and with different grain size. During initial stages of these tests, the data logging time interval should be  $\ll 1$  s. Furthermore, the creep tests should be interrupted after different periods of time in order to determine the amount of microstructural damage (fraction of broken grains) and, consequently, the point in time when the model is no longer valid due to expected global interactions between failing grains.

#### 6.4.5 Geotechnical applications

The compaction experiments on sands and microphysical models reported in this thesis are appropriate to describe the behaviour of clastic *unconsolidated* granular material found near the surface of the Earth's crust. Clearly, experiments should also be carried out to determine the compaction behaviour of *consolidated* sands, i.e. porous sandstones, found in hydrocarbon reservoirs situated at deeper levels of the upper crust. In the course of the present research programme, a series of long-term ( $\sim 500$  days duration) compaction creep experiments have been performed on samples of the Fontainebleau (France) and Heksenberg (Heerlen, The Netherlands) Sandstones with initial porosities ( $\phi_i$ ) in the range  $12 \leq \phi_i \leq 30$  %. The experiments involved rubber jacketed cylindrical samples loaded hydrostatically at room temperature, at effective pressures ( $P_e$ ) stepped in the range  $5 \leq P_e \leq 50$  MPa, and

under wet conditions (samples drained in distilled water saturated with silica). Compaction creep was monitored as a function of time by measuring the volume of pore fluid displaced from the samples into a burette system. The creep rates obtained increased non-linearly with increasing  $P_e$  and were in the order of  $10^{-8.5}$  -  $10^{-10} \text{ s}^{-1}$ . However, the experiments could not be reliably repeated due to temperature fluctuations in the laboratory and minor leakage of the jackets and the burette system. Evidently, experimental work of this kind needs to be conducted at controlled elevated temperatures and using saline pore fluids, corresponding to reservoir conditions. For this purpose, very special methods have to be developed to jacket the samples and to accurately determine sample volume changes by measuring the pore fluid volume displaced from the samples, inside the (heated) pressure vessel.

## REFERENCES

- Abramowitz, M. & Stegun, I.A., 1972. Handbook of mathematical functions - 10th edition. US NBS, Washington, DC.
- Adams, M.J. & Briscoe, B.J., 1994. Deterministic micromechanical modelling of failure and flow in discrete planes of densely packed particle assemblies: introductory principles. In: Mehta, A. (ed), Granular matter - an interdisciplinary approach. Springer, Berlin. pp 259-291.
- Antonellini, M.A., Aydin, A. & Pollard, D.D., 1994. Microstructure of deformation bands in porous sandstones at Arches National Park, Utah. *Journal of Structural Geology*, 16, 7, 941-959.
- Arbiter, N., Harris, C.C. & Stamboltzis, G.A., 1969. Single fracture of brittle spheres. *Society of Mining Engineers Transactions, American Institute of Mechanical Engineers*, 244, 118-133.
- Arzt, E., Ashby, M.F. & Easterling, K.E., 1983. Practical applications of hot-isostatic pressing diagrams: four case studies. *Metallurgical Transactions A*, 14, 211-221.
- Atkinson, B.K., 1979. A fracture mechanics study of subcritical tensile cracking of quartz in wet environments. *Pure and Applied Geophysics*, 117, 1011-1024.
- Atkinson, B.K. & Avidis, V., 1980. Fracture mechanics parameters of some rock-forming minerals determined using an indentation technique. *International Journal of Rock Mechanics and Mining Sciences & Geomechanics Abstracts*, 17, 383-386.
- Atkinson, B.K. & Meredith, P.G., 1981. Stress corrosion cracking of quartz: a note on the influence of chemical environment. *Tectonophysics*, 77, T1-T11.
- Atkinson, B.K. & Meredith, P.G., 1989a. The theory of subcritical crack growth with applications to minerals and rocks. In: Atkinson, B.K. (ed). *Fracture mechanics of rock*. Academic Press, London. pp 111-166.
- Atkinson, B.K. & Meredith, P.G., 1989b. Experimental fracture mechanics data for rocks and minerals. In: Atkinson, B.K. (ed), *Fracture mechanics of rock*. Academic Press, London. pp 477-525.
- Barker, G.C., 1994. Computer simulations of granular materials. In: Mehta, A. (ed), *Granular matter - an interdisciplinary approach*. Springer, Berlin. pp 35-83.
- Barquins, M. & Maugis, D., 1982. Adhesive contact of axisymmetric punches on an elastic half-space: the modified Hertz-Huber's stress tensor for contacting spheres. *Journal de Mécanique théorique et appliquée*, 1, 2, 331-357.
- Barrett, P.J., 1980. The shape of rock particles, a critical review. *Sedimentology*, 27, 291-303.
- Batdorf, S.B. & Crose, J.G., 1974. A statistical theory for the fracture of brittle structures subjected to nonuniform polyaxial stresses. *Journal of Applied Mechanics*, 41, 2, 459-464.
- Batdorf, S.B. & Heinisch, H.L., 1978. Weakest link theory reformulated for arbitrary fracture criterion. *Journal of the American Ceramic Society*, 61, 7-8, 355-358.
- Bathurst, R.J. & Rothenburg, L., 1990. Observations on stress-force-fabric relationships in idealized granular materials. *Mechanics of Materials*, 9, 65-80.
- Baudendistel, E., 1981. Numerische Beanspruchungsanalyse einer definiert belasteten Kugel. Final report to the German Science Foundation (DFG) (no. Schm 522/1). Internal Report W 4/81, Fraunhofer-Institut für Werkstoffmechanik, Freiburg, Germany.
- Bazant, Z.P., Xi, Y. & Reid, S.G., 1991. Statistical size effect in quasi-brittle structures: I. Is Weibull theory applicable? *Journal of Engineering Mechanics*, 117, 11, 2609-2622.

- Behringer, R.P. & Baxter, G.W., 1994. Pattern formation and complexity in granular flows. In: Mehta, A. (ed), *Granular matter - an interdisciplinary approach*. Springer, Berlin. pp 85-119.
- Bernabe, Y. & Brace, W.F., 1990. Deformation and fracture of Berea sandstone. In: Duba, A.G., Durham, W.B., Handin, J.W. & Wang, H.F. (eds). *The brittle-ductile transition in rocks. The Heard Volume. Geophysical Monograph Series, 56*. American Geophysical Union, Washington DC. pp. 91-102.
- Bideau, D. & Hansen, A. (eds), 1993. *Disorder and granular media*. North Holland, Amsterdam.
- Birch, F., 1966. Compressibility; elastic constants. In: Clark Jr., S.P. (ed). *Handbook of physical constants - revised edition*. The Geological Society of America Memoir, 97, 97-173.
- Blanpied, M.L., Lockner, D.A. & Byerlee, J.D., 1992. An earthquake mechanism based on rapid sealing of faults. *Nature*, 358, 574-252.
- Boitnott, G.N., Biegel, R.L., Scholz, C.H., Yoshioka, N. & Wang, W., 1992. Micromechanics of rock friction - 2. Quantitative modeling of initial friction with contact theory. *Journal of Geophysical Research*, 97, B6, 8965-8978.
- Borg, I., Friedman, M., Handin, J. & Higgs, D.V., 1960. Experimental deformation of St. Peter sand: a study of cataclastic flow. In: Griggs, D. & Handin, J. (eds), *Rock deformation - a symposium*. The Geological Society of America Memoir, 79, chapter 6, 133-191.
- Borodich, F.M., 1993. The Hertz frictional contact between nonlinear elastic bodies (the similarity approach). *International Journal of Solids and Structures*, 30, 11, 1513-1526.
- Boussinesq, J., 1885. *Application des potentiels a l'etude de l'équilibre et du mouvement des solides élastiques*. Gauthier-Villars, Paris.
- Brady, P.V. & Walther, J.V., 1990. Kinetics of quartz dissolution at low temperatures. *Chemical Geology*, 82, 253-264.
- Burley, S.D., 1986. The development and destruction of porosity within Upper Jurassic reservoir sandstones of the Piper and Tartan Fields, Outer Moray Firth, North Sea. *Clay Minerals*, 21, 649-694.
- Ceramic Source 1991•1992, Volume 7. L.M. Sheppard (ed.), Annual company directory and buyer's guide compiled by the American Ceramic Society, Inc., Westerville, OH.
- Chang, C.S., Chang, Y. & Kabir, M.G., 1992a. Micromechanics modeling for stress-strain behavior of granular soils. I: Theory. *Journal of Geotechnical Engineering*, 118, 12, 1959-1974.
- Chang, C.S., Kabir, M.G. & Chang, Y., 1992b. Micromechanics modeling for stress-strain behavior of granular soils. II: Evaluation. *Journal of Geotechnical Engineering*, 118, 12, 1975-1992.
- Chang, C.S., 1993. Micromechanical modeling of deformation and failure for granulates with frictional contacts. *Mechanics of Materials*, 16, 13-24.
- Chao, L-Y. & Shetty, D.K., 1990. Equivalence of physically based statistical fracture theories for reliability analysis of ceramics in multiaxial loading. *Journal of the American Ceramic Society*, 73, 7, 1917-1921.
- Chuang, T-j. & Fuller, E.R., 1992. Extended Charles-Hillig theory for stress corrosion cracking of glass. *Journal of the American Ceramic Society*, 75, 3, 540-545.
- Cook, R.F., 1989. Influence of crack velocity thresholds on stabilized non-equilibrium fracture. *Journal of Applied Physics*, 65, 5, 1902-1910.

- Cook, R.F., 1993. Theory of time-dependent failure for fractal porous aggregates. In: Boland, J.N. & Fitz Gerald, J.D. (eds). Defects and processes in the solid state: geoscience applications - the McLaren volume. Elsevier Science Publishers, Amsterdam. pp 229-242.
- Cook, R.F. & Liniger, E.G., 1993. Kinetics of indentation cracking. *Journal of the American Ceramic Society*, 76, 5, 1096-1105.
- Costin, L.S., 1989. Time-dependent deformation and failure. In: Atkinson, B.K. (ed). *Fracture mechanics of rock*. Academic Press, London. pp 167-215.
- Cox, S.J.D. & Meredith, P.G., 1993. Microcrack formation and material softening in rock measured by monitoring acoustic emissions. *International Journal of Rock Mechanics and Mining Sciences & Geomechanics Abstracts*, 30, 1, 11-24.
- Cundall, P.A. & Strack, O.D.L., 1979. A discrete numerical model for granular assemblies. *Géotechnique*, 29, 1, 47-65.
- Curtin, W.A. & Sher, H., 1992. Algebraic scaling of material strength. *Physical Review B*, 45, 6, 2620-2627.
- Dai, D.N., Hills, D.A., Warren, P.D. & Nowell, D., 1995. The propulsion of surface flaws by elastic indentation testing. *Acta Metallurgica et Materialia*, 43, 3, 985-991.
- Darot, M. & Gueguen, Y., 1986. Slow crack growth in minerals and rocks: theory and experiments. *Pure and Applied Geophysics*, 124, 4/5, 677-692.
- Davis, D.M., 1994. Porosity loss in the evolution of accretionary wedges: some mechanical and seismic implications. In: Hickman, S.H., Sibson, R.H. & Bruhn, R.L. (eds). *Proceedings of workshop LXIII - The mechanical involvement of fluids in faulting*. U.S. Geological Survey Open-file report 94-228. Menlo Park, CA. pp 460-465.
- Deresiewicz, H., 1958. Stress-strain relations for a simple model of a granular medium. *Journal of Applied Mechanics, Series E, Transactions of the American Society of Mechanical Engineers*, 25, 402-406.
- Derjaguin, B.V., Muller, V.M. & Toporov, Y.P., 1975. Effect of contact deformations on the adhesion of particles. *Journal of Colloid and Interface Science*, 53, 2, 314-326.
- Derjaguin, B.V., Churaev, N.V. & Muller, V.M., 1987. *Surface forces*. Consultants Bureau. New York.
- Dewers, T. & Hajash, A., 1994. Rate laws for water-assisted densification and stress-induced water-rock interaction in sandstones. In: Hickman, S.H., Sibson, R.H. & Bruhn, R.L. (eds). *Proceedings of workshop LXIII - The mechanical involvement of fluids in faulting*. U.S. Geological Survey Open-file report 94-228. Menlo Park, CA. pp 576-611.
- Dobkins, J.E. & Folk, R.L., 1970. Shape development on Tahiti-Nui. *Journal of Sedimentary Petrology*, 40, 4, 1167-1203.
- Donaldson, E.C., Chilingarian, G.V. & Yen, T.F., 1995a. Introduction to compaction/subsidence - introduction to tectonics and sedimentation. In: Chilingarian, G.V., Donaldson, E.C. & Yen, T.F. (eds). *Subsidence due to fluid withdrawal. Developments in Petroleum Science*, 41. Elsevier Science, Amsterdam. pp 1-46.
- Donaldson, E.C., Chilingarian, G.V. & Rieke, H.H., 1995b. Stresses in sediments. In: Chilingarian, G.V., Donaldson, E.C. & Yen, T.F. (eds). *Subsidence due to fluid withdrawal. Developments in Petroleum Science*, 41. Elsevier Science, Amsterdam. pp 165-192.
- Doornhof, D., 1992. Surface subsidence in The Netherlands: the Groningen gas field. *Geologie en Mijnbouw*, 71, 119-130.



- Dortmans, L.J.M.G. & de With, G., 1991. Noise sensitivity of fit procedures for Weibull parameter extraction. *Journal of the American Ceramic Society*, 74, 9, 2293-2294.
- Dove, P.M., 1994. The dissolution kinetics of quartz in sodium chloride solutions at 25° to 300°C. *American Journal of Science*, 294, 665-712.
- Dove, P.M. & Crerar, D.A., 1990. Kinetics of quartz dissolution in electrolyte solutions using a hydrothermal mixed flow reactor. *Geochimica et Cosmochimica Acta*, 54, 955-969.
- Dove, P.M. & Elston, S.F., 1992. Dissolution kinetics of quartz in sodium chloride solutions: analysis of existing data and a rate model for 25°C. *Geochimica et Cosmochimica Acta*, 56, 4147-4156.
- Duffy, J. & Mindlin, R.D., 1957. Stress-strain relations and vibrations of a granular medium. *Journal of Applied Mechanics, Series E, Transactions of the American Society of Mechanical Engineers*, 24, 585-593.
- Dunn, D.E., LaFountain, L.J. & Jackson, R.E., 1973. Porosity dependence and mechanism of brittle fracture in sandstones. *Journal of Geophysical Research*, 78, 14, 2403-2417.
- Dunning, J., McDonald, S.K., Douglas, B.J. & Dintaman, C., 1993. Measurement of the stress corrosion limit,  $K_0$ , in quartz and Na-lime glass. *International Journal of Rock Mechanics and Mining Sciences & Geomechanics Abstracts*, 30, 7, 687-690.
- Dvorkin, J., Mavko, G. & Nur, A., 1991. The effect of cementation on the elastic properties of granular material. *Mechanics of Materials*, 12, 207-217.
- Dvorkin, J., Nur, A. & Yin, H., 1994. Effective properties of cemented granular materials. *Mechanics of Materials*, 18, 351-366.
- Elias, B.P. & Hajash, A., 1992. Changes in quartz solubility and porosity due to effective stress: an experimental investigation of pressure solution. *Geology*, 20, 451-454.
- Ferguson, C.C., Lloyd, G.E. & Knipe, R.J., 1987. Fracture mechanics and deformation processes in natural quartz: a combined Vickers indentation, SEM, and TEM study. *Canadian Journal of Earth Sciences*, 24, 544-555.
- Fischmeister, H.F. & Arzt, E., 1983. Densification of powders by particle deformation. *Powder Metallurgy*, 26, 2, 82-88.
- Fjaer, E., Holt, R.M. & Horsrud, P., 1992. Petroleum related rock mechanics. *Developments in petroleum science*, 33. Elsevier, Amsterdam.
- Folk, R.L., 1955. Student operator error in determination of roundness, sphericity, and grain size. *Journal of Sedimentary Petrology*, 25, 4, 297-301.
- Folk, R.L., 1978. Angularity and silica coatings of Simpson desert sand grains, Northern Territory, Australia. *Journal of Sedimentary Petrology*, 48, 2, 611-624.
- Fuchs, S., 1913. Hauptspannungstrajektorien bei der Berührung einer Kugel mit einer Platte. *Physikalisches Zeitschrift*, 14, 1282-1285.
- Gallagher, J.J., Friedman, M., Handin, J. & Sowers, G.M., 1974. Experimental studies relating to microfracture in sandstone. *Tectonophysics*, 21, 203-247.
- Gallagher, J.J., 1976. Fracturing of quartz sand grains. In: Site characterisation, preprint-proceedings 17th Symposium on Rock Mechanics, 2 A4-1 - 2 A4-8.
- Gallagher, J.J., 1987. Fractography of sand grains broken by uniaxial compression. In: Marshall, J.R. (ed). *Clastic particles. Scanning electron microscopy and shape analysis of sedimentary and volcanic clasts*. Van Nostrand Reinhold Company, New York. pp 189-228.
- Gildemeister, H.H., 1976. Spannungszustand und Bruchphänomene in prallbeanspruchten Kugeln. Unpublished PhD thesis University of Karlsruhe, Germany.

- Gill, J.J., Miglionico, C. & Andrews, M., 1990. Measurement of the microstructural response of lightly-cemented granular soils under uniaxial strain conditions. In: Shah, S.P., Swartz, S.E. & Wang, M.L. (eds), *Micromechanics of failure of quasi-brittle materials*. Elsevier Applied Science, pp 206-213.
- Grasso, J.-R., 1992. Mechanics of seismic instabilities induced by the recovery of hydrocarbons. *Pure and Applied Geophysics*, 139, 3/4, 507-534.
- Gratier, J.P., Chen, T. & Hellmann, R., 1994. Pressure solution as a mechanism for crack sealing around faults. In: Hickman, S.H., Sibson, R.H. & Bruhn, R.L. (eds). *Proceedings of workshop LXIII - The mechanical involvement of fluids in faulting*. U.S. Geological Survey Open-file report 94-228. Menlo Park, CA. pp 279-300
- Gratz, A.J. & Bird, P., 1993a. Quartz dissolution: negative crystal experiments and a rate law. *Geochimica et Cosmochimica Acta*, 57, 965-976.
- Gratz, A.J. & Bird, P., 1993b. Quartz dissolution: theory of rough and smooth surfaces. *Geochimica et Cosmochimica Acta*, 57, 977-989.
- Griffith, A.A., 1920. The phenomena of rupture and flow in solids. *Philosophical Transactions of the Royal Society of London*, A 221, 163-198.
- Groshong, R.H., 1988. Low-temperature deformation mechanisms and their interpretation. *Geological Society of America Bulletin*, 100, 1329-1360.
- Gueguen, Y., Reuschlé, T. & Darot, M., 1990. Single crack behaviour and crack statistics. In: Barber, D.J. & Meredith, P.G. (eds), *Deformation processes in minerals, ceramics and rocks*. Unwin Hyman, London, pp 334-353.
- Guyon, E., Roux, S., Hansen, A., Bideau, D., Troadec, J-P. & Crapo, H., 1990. Non-local and non-linear problems in the mechanics of disordered systems: application to granular media and rigidity problems. *Reports on Progress in Physics*, 53, 373-419.
- Helle, A.S., Easterling, K.E. & Ashby, M.F., 1985. Hot-isostatic pressing diagrams. *Acta Metallurgica et Materialia*, 33, 12, 2163-2174.
- Hertz, H.R., 1882a. Ueber die Berührung fester elastischer Körper. *Journal für die reine und angewandte Mathematik*, 92, 156-171.
- Hertz, H.R., 1882b. Ueber die Berührung fester elastischer Körper und über die Härte. *Verhandlungen des Vereins zur Beförderung des Gewerbefleißes*, Berlin, Germany.
- Hertz, H.R., 1896. *Miscellaneous Papers by H. Hertz*. Eds. Jones & Schott, MacMillan, London (translation of: *Gesammelte Werke von Heinrich Hertz*. J.A. Barth, Leipzig, Germany, 1895).
- Hicks, B.D., 1989. Dissolution of experimentally compacted quartz sand. PhD thesis University of Missouri-Columbia.
- Hills, D.A. & Sackfield, A., 1987. The stress field induced by normal contact between dissimilar spheres. *Journal of Applied Mechanics*, 54, 8-14.
- Hills, D.A., Nowell, D. & Sackfield, A., 1993. *Mechanics of elastic contacts*. Butterworth Heineman.
- Hippler, S.J., 1993. Deformation microstructures and diagenesis in sandstone adjacent to an extensional fault: implications for the flow and entrapment of hydrocarbons. *The American Association of Petroleum Geologists Bulletin*, 77, 4, 625-637.
- Hiramatsu, Y. & Oka, Y., 1966. Determination of the tensile strength of rock by a compression test of an irregular test piece. *International Journal of Rock Mechanics and Mining Sciences & Geomechanics Abstracts*, 3, 89-99.
- Horne, M.R., 1965. The behaviour of an assembly of rotund, rigid, cohesionless particles - I and II. *Proceedings of the Royal Society of London, series A*, 286, 62-97.

- Horowitz, P. & Hill, W., 1989. The art of electronics - second edition. Cambridge University Press, Cambridge.
- Houseknecht, D.W., 1987. Assessing the relative importance of compaction processes and cementation to reduction of porosity in sandstones. *The American Association of Petroleum Geologists Bulletin*, 71, 6, 633-642.
- Huber, M.T., 1904. Zur Theorie der Berührung fester elastischer Körper. *Annalen der Physik*, 14, 153-163.
- Inniss, D., Brownlow, D.L. & Kurkjian, C.R., 1992. Effect of sodium chloride solutions on the strength and fatigue of bare optical fibers. *Journal of the American Ceramic Society*, 75, 2, 364-368.
- Isichenko, M.B., 1992. Percolation, statistical topography, and transport in random media. *Reviews of Modern Physics*, 64, 4, 961-1043.
- Issa, J.A. & Nelson, R.B., 1989. Numerical analysis of micromechanical behavior of granular materials. In: Mustoe, G.G.W., Henriksen, M. & Huttelmaier, H-P. 1st U.S conference on discrete element methods. CSM Press.
- Jaeger, J.C. & Cook, N.G.W., 1984. Fundamentals of rock mechanics - Third edition. Chapman and Hall, London.
- Jagota, A., Dawson, P.R. & Jenkins, J.T., 1988. An isotropic continuum model for the sintering and compaction of powder packings. *Mechanics of Materials*, 7, 255-269.
- Jayatilaka, A. de S. & Trustrum, K., 1977. Statistical approach to brittle fracture. *Journal of Materials Science*, 12, 1426-1430.
- Jenkins, J.T., Cundall, P.A. & Ishibashi, I., 1989. Micromechanical modeling of granular materials with the assistance of experiments and numerical simulations. In: Biarez, J. & Gourvès, R. (eds), *Powder and Grains*, Balkema, Rotterdam, pp 257-264.
- Johnson, N.L. & Kotz, S., 1970. Continuous univariate distributions - 1. John Wiley, New York.
- Johnson, K.L., Kendall, K. & Roberts, D.A., 1971. Surface energy and the contact of elastic solids. *Proceedings of the Royal Society of London A*, 324, 301-313.
- Johnson, K.L., O'Connor, J.J. & Woodward, A.C., 1973. The effect of the indenter elasticity on the Hertzian fracture of brittle materials. *Proceedings of the Royal Society of London A*, 334, 95-117.
- Johnson, K.L., 1987. Contact mechanics. Cambridge University Press, Cambridge.
- Karig, D.E. & Hou, G., 1992. High-stress consolidation experiments and their geologic implications. *Journal of Geophysical Research*, 97, B1, 289-300.
- Kemeny, J.M. & Cook, N.G.W., 1991. Micromechanics of deformation in rocks. In: Shah, S.P. (ed). *Toughening mechanisms in quasi-brittle materials*. Kluwer, Dordrecht, The Netherlands. pp. 155-188.
- Khalaf, F.I. & Gharib, I.M., 1985. Roundness parameters of quartz grains of recent aeolian sand deposits in Kuwait. *Sedimentary Geology*, 45, 147-158.
- Kienzler, R. & Baudendistel, E., 1985. Numerische Beanspruchungsanalyse einer definiert belasteten Kugel. Final report to the German Science Foundation (DFG) (no. Schm 522/2-4). Internal Report W 5/85, Fraunhofer-Institut für Werkstoffmechanik, Freiburg, Germany.
- Kienzler, R., 1985. Numerische Beanspruchungsanalyse einer definiert belasteten Kugel. Final report to the German Science Foundation (DFG) (no. Schm 522/3-3). Internal Report W 6/85, Fraunhofer-Institut für Werkstoffmechanik, Freiburg, Germany.
- Kienzler, R. & Schmitt, W., 1990. On single-particle comminution: numerical analysis of compressed spheres. *Powder Technology*, 61, 29-38.

- King, G.C.P. & Sammis, C.G., 1992. The mechanisms of finite brittle strain. *Pure and Applied Geophysics*, 138, 4, 611-640.
- Kittle, P. & Diaz, G., 1988. Weibull's fracture statistics, or probabilistic strength of materials: state of the art. *Res Mechanica*, 24, 99-207.
- Knipe, R.J., 1989. Deformation mechanisms - recognition from natural tectonites. *Journal of Structural Geology*, 11, 1/2, 127-146.
- Knipe, R.J., 1994. Micromechanisms of deformation and fluid behaviour during faulting. In: Hickman, S.H., Sibson, R.H. & Bruhn, R.L. (eds). *Proceedings of workshop LXIII - The mechanical involvement of fluids in faulting*. U.S. Geological Survey Open-file report 94-228. Menlo Park, CA. pp 301-310.
- Ko, H-Y. & Scott, R.F., 1967. Deformation of sand in hydrostatic compression. *Journal of the Soil Mechanics and Foundations Division, Proceedings of the American Society of Civil Engineers*, SM3, 137-156.
- Krumbein, W.C., 1941. Measurement and geological significance of shape and roundness of sedimentary particles. *Journal of Sedimentary Petrology*, 11, 2, 64-72.
- Kruyt, N.P., 1994. Aspects of constitutive relations for cohesionless granular materials. PhD thesis Technical University of Twente, Enschede, The Netherlands.
- Kschinka, B.A., Perrella, S., Nguyen, H. & Bradt, R.C., 1986. Strengths of glass spheres in compression. *Journal of the American Ceramic Society*, 69, 6, 467-472.
- Kuyl, O.S., 1975. Lithostratigraphy of Mio-Oligocene deposits in South-Limburg. In: Zagwijn, W.H. & van Staaldunin, C.J., *Explanatory notes to geological survey maps of The Netherlands (in Dutch)*. Dutch Geological Survey, Haarlem, The Netherlands. pp 56-63.
- Lambe, T.W. & Whitman, R.V., 1979. *Soil mechanics, SI version*. Series in soil engineering. Wiley, New York.
- Lamon, J., 1988. Statistical approaches to failure for ceramic reliability assessment. *Journal of the American Ceramic Society*, 71, 2, 106-112.
- Lasaga, A.C. & Gibbs, G.V., 1990. Ab-initio quantum mechanical calculations of water-rock interactions: adsorption and hydrolysis reactions. *American Journal of Science*, 290, 263-295.
- Lawn, B.R., 1968. Hertzian fracture in single crystals with the diamond structure. *Journal of Applied Physics*, 39, 10, 4828-4836.
- Lawn, B.R., 1993. *Fracture of brittle solids - Second edition*. Cambridge University Press, Cambridge.
- Lee, K.L. & Farhoomand, I., 1967. Compressibility and crushing of granular soil in anisotropic triaxial compression. *Canadian Geotechnical Journal*, 4, 1, 68-86.
- Lindsay, C.G., White, G.S., Freiman, S.W. & Wong-Ng, W., 1994. Molecular orbital study of an environmentally enhanced crack growth process in silica. *Journal of the American Ceramic Society*, 77, 8, 2179-2187.
- Liu, Z., Myer, L.R. & Cook, N.G.W., 1993. Micromechanics of granular materials - numerical simulation of the effects of heterogeneities. *International Journal of Rock Mechanics and Mining Sciences & Geomechanics Abstracts*, 30, 7, 1281-1284.
- Lockner, D., 1993. The role of acoustic emission in the study of rock fracture. *International Journal of Rock Mechanics and Mining Sciences & Geomechanics Abstracts*, 30, 7, 883-899.
- Love, A.E.H., 1929. The stress produced in a semi-infinite solid by pressure on part of the boundary. *Philosophical Transactions Royal Society of London, A*, 228, 377-420.

- Lloyd, G.E. & Knipe, R.J., 1992. Deformation mechanisms accommodating faulting of quartzite under upper crustal conditions. *Journal of Structural Geology*, 14, 2, 127-143.
- Lundberg, G. & Sjövall, H., 1958. Stress and deformation in elastic solids. Publikation nr. 4, The Institution of theory of elasticity and strength of materials, Chalmers University of Technology, Gothenburg, Sweden.
- Lurje, A.L., 1963. Räumliche Probleme der Elastizitätstheorie. Akademie-Verlag, Berlin, Germany.
- Lysak, M.V., 1994. Acoustic emission during jumps in subcritical growth of cracks in three-dimensional bodies. *Engineering Fracture Mechanics*, 47, 6, 873-879.
- Mai, Y-W. & Lawn, B.R., 1986. Crack stability and toughness characteristics in brittle materials. *Annual Review of Materials Science*, 16, 415-439.
- Marone, C. & Scholz, C.H., 1989. Particle-size distribution and microstructures within simulated fault gouge. *Journal of Structural Geology*, 11, 7, 799-814.
- Matthews, J.R., McClintock, F.A. & Shack, W.J., 1976. Statistical determination of surface flaw density in brittle materials. *Journal of the American Ceramic Society*, 59, 7-8, 304-308.
- Maxwell, J.C., 1960. Experiments on compaction and cementation of sand. In: Griggs, D. & Handin, J. (eds), *Rock deformation - a symposium*. The Geological Society of America Memoir, 79, chapter 5, 105-132.
- McBride, E.F., Diggs, T.N. & Wilson, J.C., 1991. Compaction of Wilcox and Carrizo sandstones (Paleocene-Eocene) to 4420 m, Texas Gulf coast. *Journal of Sedimentary Petrology*, 61, 1, 73-85.
- McDonald, S.K., 1994. Subcritical fracture propagation and its application to compound earthquakes. PhD thesis Indiana University, Bloomington, IN.
- Mehrabadi, M.M., Loret, B. & Nemat-Nasser, S., 1992. A constitutive model for granular materials based on micromechanics. In: Shen, H.H., Satake, M. & Mehrabadi, M. (eds). *Advances in micromechanics of granular materials*, Proceedings of the 2nd US/Japan seminar, Potsdam, NY, USA, 5-9 August 1991. Elsevier, Amsterdam, pp 81-90.
- Mehrabadi, M.M., Loret, B. & Nemat-Nasser, S., 1993. Incremental constitutive relations for granular materials based on micromechanics. *Proceedings of the Royal Society of London, series A*, 441, 433-463.
- Mehta, A. (ed), 1994. *Granular matter - an interdisciplinary approach*. Springer, Berlin.
- Meredith, P.G. & Atkinson, B.K., 1982. High-temperature tensile crack propagation in quartz: experimental results and application to time-dependent earthquake rupture. *Earthquake Prediction Research*, 1, 377-391.
- Meredith, P.G., 1990. Fracture and failure of brittle polycrystals: an overview. In: Barber, D.J. & Meredith, P.G. (eds). *Deformation processes in minerals, ceramics and rocks*. Unwin Hyman, London. pp 5-47.
- Michalske, T.A. & Bunker, B.C., 1984. Slow fracture model based on strained silicate structures. *Journal of Applied Physics*, 56, 10, 2686-2693.
- Michalske, T.A. & Bunker, B.C., 1993. A chemical kinetics model for glass fracture. *Journal of the American Ceramic Society*, 76, 10, 2613-2618.
- Miller, M.E. & Dunning, J.D., 1985. Evidence for a coordinated attack of H, OH in water weakening of quartz. *Eos, Transactions of the American Geophysical Union*, 66, 46, 1065.

- Milliken, K.L., 1994. The widespread occurrence of healed microfractures in siliciclastic rocks: evidence from scanned cathodoluminescence imaging. In: Nelson, P.P. & Laubach, S.E., 1994. Rock mechanics models and measurements, challenges from industry, 825-832. Balkema, Rotterdam.
- Mindlin, R.D., 1954. Mechanics of granular media. Proceedings of the 2nd US National Congress on Applied Mechanics, American Society of Mechanical Engineers, pp 13-20.
- Morey, G.W., Fournier, R.O. & Rowe, J.J., 1962. The solubility of quartz in water in the temperature interval from 25° to 300° C. *Geochimica et Cosmochimica Acta*, 26, 1029-1043.
- Morrow, C.A. & Byerlee, J.D., 1989. Experimental studies of compaction and dilatancy during frictional sliding on faults containing gouge. *Journal of Structural Geology*, 11, 7, 815-825.
- Morton, W.B. & Close, L.J., 1922. Notes on Hertz's theory of the contact of elastic bodies. *Philosophical Magazine*, 43, 6, 321-329.
- Mouginot, R. & Maugis, D., 1985. Fracture indentation beneath flat and spherical punches. *Journal of Materials Science*, 20, 4354-4376.
- Myer, L.R., Kemeny, J.M., Zheng, Z., Suarez, R., Ewy, R.T. & Cook, N.G.W., 1992. Extensile cracking in porous rock under differential compressive stress. In: Li, V.C. (ed). *Micromechanical modeling of quasi-brittle materials behavior*. *Applied Mechanics Review*, 45, 8, 263-280.
- NAM status report, 1990 (in Dutch). Bodemdaling door aardgaswinning. Groningen veld en randvelden - Status rapport 1990 - Prognose tot het jaar 2050. Rapportnr. 17.527. Nederlandse Aardolie Maatschappij B.V. (NAM), Assen, The Netherlands.
- NAM status report, 1995 (in Dutch). Bodemdaling door aardgaswinning. Groningen veld en randvelden in Groningen, Noord Drenthe en het Oosten van Friesland - Status rapport 1995 en prognose tot het jaar 2050. Rapport nr.: 27600. Nederlandse Aardolie Maatschappij B.V. (NAM), Assen, The Netherlands.
- Nishizawa, O. & Noro, H., 1990. A self-exciting process of acoustic emission occurrence in steady creep of granite under uniaxial stress. *Geophysical Research Letters*, 17, 10, 1521-1524.
- Oda, H., Koami, H. & Seya, K., 1989. Effect of occurrence rate of acoustic emissions on their statistical behavior. *Pure and Applied Geophysics*, 130, 1, 5-29.
- Oka, Y. & Majima, H., 1970. A theory of size reduction involving fracture mechanics. *Canadian Metallurgical Quarterly*, 9, 2, 429-439.
- Onasch, C.M., 1994. Assessing brittle volume-gain and pressure solution volume-loss processes in quartz arenite. *Journal of Structural Geology*, 16, 4, 519-530.
- Ouwerkerk, C.E.D., 1991. A micro-mechanical connection between single-particle strength and the bulk strength of random packings of spherical particles. *Powder Technology*, 65, 125-138.
- Owen, G., 1987. Deformation processes in unconsolidated sands. In: Jones, M.E. & Preston, R.M.F. (eds), *Deformation of sediments and sedimentary rocks*. Geological Society Special Publication, 29, 11-24.
- Panayiotopoulos, K.P. & Mullins, C.E., 1985. Packing of sands. *Journal of Soil Science*, 36, 129-139.
- Papamichos, E., Vardoulakis, I. & Ouadfel, H., 1993. Permeability reduction due to grain crushing around a perforation. *International Journal of Rock Mechanics and Mining Sciences & Geomechanics Abstracts*, 30, 7, 1223-1229.

- Pittmann, E.D., 1981. Effect of fault-related granulation on porosity and permeability of quartz sandstones, Simpson Group (Ordovician), Oklahoma. *The American Association of Petroleum Geologists Bulletin*, 65, 11, 2381-2387.
- Pittmann, E.D. & Larese, R.E., 1991. Compaction of lithic sands: experimental results and applications. *The American Association of Petroleum Geologists Bulletin*, 75, 8, 1279-1299.
- Press, W.H., Flannery, B.P., Teukolsky, S.A. & Vetterling, W.T., 1988. *Numerical recipes* in C. Cambridge University Press, Cambridge.
- Quinn, G.D. & Morell, R., 1991. Design data for engineering ceramics: a review of the flexure test. *Journal of the American Ceramic Society*, 74, 9, 2037-2066.
- Ramez, M.R.H. & Mosalamy, F.H., 1969. The deformed nature of various size fractions in some clastic sands. *Journal of Sedimentary Petrology*, 39, 3, 1182-1187.
- Reuschlé, T., 1989. Les fluides et l'évolution des propriétés mécaniques des roches. PhD thesis Université Louis Pasteur de Strasbourg, France.
- Reuschlé, T., Darot, M. & Gueguen, Y., 1989. Mechanical and transport properties of crustal rocks: from single cracks to crack statistics. *Physics of the Earth and Planetary Interiors*, 55, 353-360.
- Rice, J.A., 1988. *Mathematical statistics and data analysis*. Wadsworth & Brooks, Pacific Grove, California.
- Rice, J.R., 1978. Thermodynamics of the quasi-static growth of Griffith cracks. *Journal of the Mechanics and Physics of Solids*, 26, 61-78.
- Rice, J.R., 1992. Fault stress states, pore pressure distributions, and the weakness of the San Andreas fault. In: Evans, B. & Wong, T.-f. (eds), *Fault mechanics and transport properties of rocks - A festschrift in honor of W.F. Brace*. Academic Press. pp 475-503.
- Riley, N.A., 1941. Projection sphericity. *Journal of Sedimentary Petrology*, 11, 2, 94-97.
- Rimai, D.S., DeMejo, L.P., Bowen, R. & Morris, J.D., 1995. Particles on surfaces: adhesion induced deformations. In: Mittal, K.L. (ed), *Particles on surfaces - detection, adhesion, and removal*. Marcel Dekker, New York.
- Rimstidt, J.D. & Barnes, H.L., 1980. The kinetics of silica-water reactions. *Geochimica et Cosmochimica Acta*, 44, 1683-1699.
- Roberts, J.E. & de Souza, J.M., 1958. The compressibility of sands. *Proceedings of the American Society for Testing and Materials (ASTM)*, 58, 1269-1277.
- Robie, R.A., Hemingway, B.S. & Fisher, J.R., 1979. Thermodynamic properties of minerals and related substances at 298.15 K and 1 bar ( $10^5$  Pa) pressure and at higher temperatures. *US Geological Survey Bulletin*, 1452.
- Rothenburg, L. & Bathurst, 1993. Influence of particle eccentricity on micromechanical behavior of granular materials. *Mechanics of Materials*, 16, 141-152.
- Roux, S., Bideau, D. & Hansen, A., 1993. Properties of the grain space of packings: effects of heterogeneities. In: Bideau, D. & Hansen, A. (eds), *Disorder and granular media*. North Holland, Amsterdam.
- Rowe, P.W., 1962. The stress-dilatancy relation for static equilibrium of an assembly of particles in contact. *Proceedings of the Royal Society of London, series A*, 269, 500-527.
- Rumpf, H., Faulhaber, F., Schönert, K. & Umhauer, H., 1967. Analyse der Brucherscheinungen in Glaskugeln und kreisrunden Glasscheiben. In: Rumpf, H. & Pietsch, W. (eds.), *Zerkleinern, DECHEMA Monographien*, Band 57, no. 993-1026, A3, 85-126. Verlag Chemie GmbH, Weinheim/Bergstraße.

- Rumpf, H. & Schönert, K., 1972. Die Brucherscheinungen in Kugeln bei elastischen sowie plastischen Verformungen durch Druckbeanspruchung. In: Rumpf, H.C.H. & Schönert, K. (eds.), *Zerkleinern*, DECHEMA Monographien, Band 69, no. 1292-1326, Teil 1, I-2, 51-80. Verlag Chemie GmbH, Weinheim/Bergstraße.
- Rutter, E.H. & Maddock, R.H., 1992. On the mechanical properties of synthetic kaolinite-quartz fault gouge. *Terra Nova*, 4, 489-500.
- Scholten, H.F., 1993. Evaluation of multiaxial fracture models for technical ceramics. PhD thesis Technical University Eindhoven, The Netherlands.
- Schutjens, P.M.T.M., 1991a. Intergranular pressure solution in halite aggregates and quartz sands: an experimental investigation. *Geologica Ultraiectina*, 76. PhD thesis Utrecht University, The Netherlands.
- Schutjens, P.M.T.M., 1991b. Experimental compaction of quartz sand at low effective stress and temperature conditions. *Journal of the Geological Society of London*, 148, 527-539.
- Schutjens, P.M.T.M., de Ruig, H. & van Munster, J.G., 1994. Compressibility measurement and acoustic characterisation of quartz-rich consolidated reservoir rock (Brent Field, North Sea). In: *Eurock '94 - Rock mechanics in petroleum engineering*. Proceedings of the SPE/ISRM International Conference, Delft, The Netherlands, 29-31 August 1994. A.A. Balkema, Rotterdam. pp 557-571.
- Schutjens, P.M.T.M., Fens, T.W. & Smits, R.M.M., 1995. Experimental observations of the uniaxial compaction of quartz-rich reservoir rock at stresses up to 80 MPa. Paper presented at the 5th International Symposium on land subsidence, The Hague, The Netherlands, 16-20 October 1995. To be published in: *Conference proceedings of the International Association of Hydrological Sciences (IAHS)*. IAHS Press, Institute of Hydrology, Wallingford, U.K..
- Scott, D.R., Marone, C.J. & Sammis, C.G., 1994. The apparent friction of granular fault gouge in sheared layers. *Journal of Geophysical Research*, 99, B4, 7231-7246.
- Segall, P., 1989. Earthquakes triggered by fluid extraction. *Geology*, 17, 942-946.
- Segall, P., 1992. Induced stresses due to fluid extraction from axisymmetric reservoirs. *Pure and Applied Geophysics*, 139, 3/4, 535-560.
- Segall, P., Grasso, J-R. & Mossop, A., 1994. Poroelastic stressing and induced seismicity near the Lacq gas field, southwestern France. *Journal of Geophysical Research*, 99, B8, 15423-15438.
- Shipway, P.H. & Hutchings, I.M., 1993a. Fracture of brittle spheres under compression and impact loading I. Elastic stress distributions. *Philosophical Magazine A*, 67, 6, 1389-1404.
- Shipway, P.H. & Hutchings, I.M., 1993b. Fracture of brittle spheres under compression and impact loading II. Results for lead-glass and sapphire spheres. *Philosophical Magazine A*, 67, 6, 1405-1421.
- Shen, H.H., Satake, M. & Mehrabadi, M. (eds), 1992. *Advances in micromechanics of granular materials*. Elsevier Science Publishers, Amsterdam.
- Sibson, R.H., 1994. Geological evidence for fluid involvement in the rupture processes of crustal earthquakes. In: Hickman, S.H., Sibson, R.H. & Bruhn, R.L. (eds). *Proceedings of workshop LXIII - The mechanical involvement of fluids in faulting*. U.S. Geological Survey Open-file report 94-228. Menlo Park, CA. pp 31-38.
- Simmons, G. & Wang, H., 1971. *Single crystal constants and calculated aggregate properties*. MIT Press, Cambridge.
- Sleep, N.H. & Blanpied, M.L., 1992. Creep, compaction and the weak rheology of major faults. *Nature*, 359, 687-692.



- Sneed, E.D. & Folk, R.L., 1958. Pebbles in the lower Colorado river, Texas. A study in particle morphogenesis. *Journal of Geology*, 66, 114-150.
- Spiers, C.J. & Brzesowsky, R.H., 1993. Densification behaviour of wet granular salt: theory versus experiment. In: Kakehana, H., Hardy, H.R., Hoshi, T. & Toyokura, K. (eds). *Seventh symposium on salt*, I, 83-92. Elsevier Science Publishers, Amsterdam.
- Stauffer, D. & Aharony, A., 1992. *Introduction to percolation theory - second edition*. Taylor & Francis, London.
- Sternberg, E., Eubanks, R.A. & Sadowsky, M.A., 1952. On the axisymmetric problem of elasticity theory for a region bounded by two concentric spheres. *Proceedings First US National Congress of Applied Mechanics*, 209-215.
- Sternberg, E. & Sadowsky, M.A., 1952. On the axisymmetric problem of the theory of elasticity for an infinite region containing two spherical cavities. *Journal of Applied Mechanics*, E, 74, 19-27.
- Sternberg, E. & Rosenthal, F., 1952. The elastic sphere under concentrated loads. *Journal of Applied Mechanics*, 19, 4, 413-421.
- Stieß, M. & Schönert, K., 1974. Dehnungen und Spannungen in der Oberfläche gedrückter PMMA-Kugeln. *Colloid & Polymer Science*, 252, 743-748.
- Stieß, M., 1976. Die Druckbeanspruchung von elastischen und inelastischen Kugeln bis zum Bruch. Unpublished PhD thesis University of Karlsruhe, Germany.
- Subhash, G., Nemat-Nasser, S., Mehrabadi, M.M. & Shodja, H.M., 1991. Experimental investigation of fabric-stress relations in granular materials. *Mechanics of Materials*, 11, 87-106.
- Sumino, Y. & Anderson, O.L., 1984. Elastic constants of minerals. In: Carmichael, R.S., *Handbook of physical properties of rocks*, Volume III, CRC Press, New York, pp 39-138.
- Suresh, S., 1992. *Fatigue of materials*. Cambridge University Press, Cambridge.
- Swinkels, F.B., Wilkinson, D.S., Arzt, E. & Ashby, M.F., 1983. Mechanisms of hot-isostatic pressing. *Acta Metallurgica et Materialia*, 31, 11, 1829-1840.
- Takeda, S.-i., Nakada, S. & Tari, I., 1991. Surface-chemical study on stress corrosion of glass in aqueous solutions (part 2) - influence of alkali metal ions. *Journal of the Ceramic Society of Japan, International Edition*, 99, 137-141.
- Thiemeier, T., Brückner-Foit, A. & Kölker, H., 1991. Influence of the fracture criterion on the failure prediction of ceramics loaded in biaxial flexure. *Journal of the American Ceramic Society*, 74, 1, 48-52.
- Thoman, D.R., Bain, L.J. & Antle, C.E., 1969. Inferences on the parameters of the Weibull distribution. *Technometrics*, 11, 3, 445-460.
- Thomas, D.S.G., 1987. The roundness of aeolian quartz sand grains. *Sedimentary Geology*, 52, 149-153.
- Thornton, C., 1993. *Powders & Grains 93*. Proceedings of the second international conference of granular media, Birmingham, UK, 12-16 July 1993. Balkema, Rotterdam.
- Timoshenko, S.P. & Goodier, J.N., 1970. *Theory of elasticity*, Int. 3rd ed.. McGraw-Hill Int. Ed., Engineering Mechanics Series, London.
- Tompkins, W.J. & Webster, J.G., 1988. *Interfacing sensors to the IBM® PC*. Prentice Hall, Englewood Cliffs, NJ.
- Troadec, J.P. & Dodds, J.A., 1993. Global geometrical description of homogeneous hard sphere packings. In: Bideau, D. & Hansen, A. (eds), *Disorder and granular media*. North Holland, Amsterdam.

- Trustrum, K. & Jayatilaka, A. de S., 1979. On estimating the Weibull modulus for a brittle material. *Journal of Materials Science*, 14, 1080-1084.
- Tutuncu, A.N. & Sharma, M.M., 1992. The influence of fluids on grain contact stiffness and frame moduli in sedimentary rocks. *Geophysics*, 57, 12, 1571-1582.
- Vepraskas, M.J. & Cassel, D.K., 1987. Sphericity and roundness of sand in coastal plain soils and relationships with soil physical properties. *Soil Science Society of America Journal*, 51, 1108-1112.
- Vesić, A.S. & Clough, G.W., 1968. Behaviour of granular materials under high stresses. *Journal of the soil mechanics and foundations division, Proceedings of the American Society of Civil Engineers*, SM3, 661-687.
- de Waal, J.A., 1986. On the rate type compaction behaviour of sandstone reservoir rock. PhD thesis Technical University Delft, The Netherlands.
- Wadell, H., 1932. Volume, shape, and roundness of rock particles. *Journal of Geology*, 40, 443-451.
- Wadell, H., 1935. Volume, shape, and roundness of quartz particles. *Journal of Geology*, 43, 250-280.
- Wallner, H., 1939. Linienstrukturen an Bruchflächen. *Zeitschrift für Physik*, 114, 368-378.
- Walther, J.V. & Helgeson, H.C., 1977. Calculation of the thermodynamic properties of aqueous silica and the solubility of quartz and its polymorphs at high pressures and temperatures. *American Journal of Science*, 277, 1315-1351.
- Warren, P.D. & Hills, D.A., 1994. The influence of elastic mismatch between indenter and substrate on Hertzian fracture. *Journal of Materials Science*, 29, 2860-2866.
- Warren, P.D., Hills, D.A. & Roberts, S.G., 1994. Surface flaw distributions in brittle materials and Hertzian fracture. *Journal of Materials Research*, 9, 12, 3194-3202.
- Weibull, W., 1939. A statistical theory of the strength of materials. *Proceedings of the Royal Swedish Institute of Engineering Research*, 151.
- Weibull, W., 1951. A statistical distribution function of wide applicability. *Journal of Applied Mechanics*, 18, 293-297.
- Weibull, W., 1952. A survey of "statistical effects" in the field of material failure. *Applied Mechanics Reviews*, 5, 11, 449-451.
- Wijk, G., 1978. Some new theoretical aspects of indirect measurements of the tensile strength of rocks. *International Journal of Rock Mechanics and Mining Sciences & Geomechanics Abstracts*, 15, 149-160.
- Wilson, J.C. & McBride, E.F., 1988. Compaction and porosity evolution of Pliocene sandstones, Ventura Basin, California. *The American Association of Petroleum Geologists Bulletin*, 72, 6, 664-681.
- Wirth, G.S. & Gieskes, J.M., 1979. The initial kinetics of the dissolution of vitreous silica in aqueous media. *Journal of Colloid and Interface Science*, 68, 3, 492-500.
- Wissler, T.M. & Simmons, G., 1985. The physical properties of a set of sandstones - part II. permanent and elastic strains during hydrostatic compression to 200 MPa. *International Journal of Rock Mechanics and Mining Sciences & Geomechanics Abstracts*, 22, 6, 393-406.
- Wong, R.C.K., Barr, W.E. & Kry, P.R., 1993. Stress-strain response of Cold Lake oil sands. *Canadian Geotechnical Journal*, 30, 220-235.
- Wong, T-f., 1990. Mechanical compaction and the brittle transition in porous sandstones. In: Knipe, R.J. and Rutter, E.H. (Eds), *Deformation mechanisms, rheology and tectonics*. Geological Society Special Publication, 54, 111-122.

- Wu, S. & Groshong, R.H., 1991. Low-temperature deformation of sandstone, southern Appalachian fold-thrust belt. *Geological Society of America Bulletin*, 103, 861-875.
- Yoffe, E.H., 1982. Elastic stress fields caused by indenting brittle materials. *Philosophical Magazine A*, 46, 4, 617-628.
- Yoffe, E.H., 1984. Modified Hertz theory for spherical indentation. *Philosophical Magazine A*, 50, 6, 813-828.
- Yoshioka, N. & Scholz, C.H., 1989. Elastic properties of contacting surfaces under normal and shear loads - 1. Theory. *Journal of Geophysical Research*, 94, B12, 17681-17690.
- Yoshioka, N., 1994. Elastic behavior of contacting surfaces under normal loads: a computer simulation using three-dimensional surface topographies. *Journal of Geophysical Research*, 99, B8, 15549-15560.
- Zallen, R., 1983. *The physics of amorphous solids*. John Wiley, New York.
- Zang, A. & Wong, T-f., 1995. Elastic stiffness and stress concentration in cemented granular material. *International Journal of Rock Mechanics and Mining Sciences & Geomechanics Abstracts*, 32, 6, 563-574.
- Zeng, K., Breder, K. & Rowcliffe, D.J., 1992. The Hertzian stress field and formation of cone cracks - I. theoretical approach. *Acta Metallurgica et Materialia*, 40, 10, 2595-2600.
- Zhang, J., Wong, T-f. & Davis, D.M., 1990a. Micromechanics of pressure-induced grain crushing in porous rocks. *Journal of Geophysical Research*, 95, B1, 314-352.
- Zhang, J., Wong, T-f., Yanagidani, T. & Davis, D.M., 1990b. Pressure-induced microcracking and grain crushing in Berea and Boise sandstones: acoustic emission and quantitative microscopy measurements. *Mechanics of Materials*, 9, 1-15.
- Zoback, M.D. & Byerlee, J.D., 1976. Effect of high-pressure deformation on permeability of Ottawa sand. *The American Association of Petroleum Geologists Bulletin*, 60, 9, 1531-1542.

## NEDERLANDSE SAMENVATTING

In de bovenkorst van de Aarde treden vervormingen op zowel door natuurlijke processen, zoals breukbewegingen, als door, door de mens teweeggebrachte, veranderingen, zoals het wegpompen van olie of gas. De compactie van zand en zandsteen kan een belangrijke rol spelen bij deze vervormingen.

Veel theoretisch en experimenteel werk is verricht naar de instantane compactie en het compactiekruipgedrag van zanden. Onder druk- en temperatuurcondities die dicht onder het aardoppervlak en in de bovenkorst van de Aarde heersen, en waar brosse vervormingsprocessen een belangrijke rol spelen bij de compactie en het compactiekruipgedrag van zanden, blijft een aantal belangrijke vragen onbeantwoord. In het bijzonder is er nog weinig inzicht in de (micro)fysica die het breukgedrag van een enkele zandkorrel bepaald. Bovendien is in voorgaande experimentele studies verricht op zandaggregaten, geen systematisch onderzoek gedaan naar het effect van de opgelegde belasting, de korrelgrootte en de chemie van een tussen de zandkorrels (in de poriënruimte) aanwezige vloeistof, op de instantane compactie en het compactiekruipgedrag. Verder missen theoretische modellen voor de compactie van zanden als gevolg van het instantane breken van korrels een fundamentele basis van het vervormingsmechanisme op microschaal. Tenslotte zijn er geen microfysische modellen ontwikkeld voor de compactie van zanden als gevolg van (tijdsafhankelijke) scheurgroei op korrelschaal.

Het onderzoek beschreven in dit proefschrift richt zich op het verkrijgen van een fundamenteel begrip van de (micro)mechanische processen die het compactie (kruip)gedrag van zanden bepalen, met name onder condities waar bros en elastisch materiaalgedrag overheersen. De gebruikte aanpak bestaat uit theoretisch en experimenteel onderzoek naar het breukgedrag van zandkorrels en naar het compactiegedrag van zandaggregaten. Het onderzoek richt zich op zowel tijdsafhankelijke als instantane (tijdsafhankelijke) processen. De verkregen resultaten verschaffen inzicht in de fundamentele processen die optreden tijdens het breken van zandkorrels en tijdens de compactie van zanden. Dit inzicht is nodig om vooruitgang te boeken bij het opstellen van constitutieve, micromechanisch gefundeerde relaties, die kunnen gebruikt worden bij het modelleren van zowel door de natuur als door de mens veroorzaakte, vervorming van zandaggregaten en zandstenen.

**Hoofdstuk 1** van dit proefschrift introduceert de probleemstelling en definieert het doel van het onderzoek.

**Hoofdstuk 2** geeft een overzicht van alle beschikbare theoretische oplossingen met betrekking tot de spanningsverdeling op het oppervlak en in het inwendige van een bolvormige korrel, die onderworpen wordt aan een diametrale belasting van het oppervlak. Hieruit blijkt dat de Hertziaanse radiale trekspanning aan de rand van het belaste contactoppervlak de maximale trekspanning is die optreedt op het oppervlak

van of in het inwendige van de korrel. Daarnaast is er een vergelijking gemaakt tussen de resultaten van dit overzicht en microstructurele waarnemingen gericht op de wijze waarop samengedrukte bollen breken. Deze vergelijking bevestigt dat, in een bolvormige kwartskorrel onder realistische belastingscondities, breuk van de korrel begint bij oppervlakte-barstjes die zich ontwikkelen tot ringscheurtjes aan de rand van het belaste contactoppervlak. Deze ringscheurtjes ontwikkelen zich onder invloed van de Hertziaanse radiale trekspanning die optreedt aan de rand van het contact en planten zich voort als convergerende kegelvormige scheurtjes, die uiteindelijk leiden tot het breken van de gehele korrel. De combinatie van deze resultaten met breukmechanische overwegingen, resulteert in een breukcriterium voor een brosse kwartskorrel.

**Hoofdstuk 3** beschrijft breuktesten, uitgevoerd bij constante verplaatsingssnelheid, enerzijds op geselecteerde, goed afgeronde, enkelvoudige zandkorrels, en anderzijds op korrels die willekeurig uit hoeveelheden puur kwartszand met verschillende korrelgrootten ( $d$ ) zijn getrokken. De verdeling van de breukkrachten ( $F_c$ ), verkregen voor elk willekeurig getrokken monster, toont aan dat  $F_c$  evenredig is met  $d^f$  waarbij  $f$  ongeveer gelijk is aan 1.3. Gebruikmakend van het breukcriterium voor de gehele korrel zoals omschreven in hoofdstuk 2, zijn vervolgens micromechanische modellen ontwikkeld voor het breken van afzonderlijke korrels die samengeperst worden tussen vlakke platen. Door toepassing van een Hertziaans-breukmechanisch model op de  $F_c$  gegevens van de geselecteerde korrels, is een nauwkeurige schatting verkregen van de grootte ( $c_f$ ) van de oppervlakte-barstjes die worden geassocieerd met breuk van de zandkorrels. Op grond van de  $F_c$  gegevens van de willekeurig getrokken monsters zijn met behulp van dit model ook verdelingen van korrelbreukspanning ( $\sigma_f$ ) bepaald ( $\sigma_f$  is de Hertziaanse radiale trekspanning die optreedt aan de rand van het contact). Een statistisch model voor het breken van korrels, gebaseerd op de theorie van Weibull, is echter niet in staat om de waargenomen korrelgrootte-afhankelijkheid van  $\sigma_f$  te verklaren. Daarnaast zijn, door toepassing van het Hertziaans-breukmechanisch model op de  $F_c$  gegevens van de willekeurig getrokken monsters, verdelingen bepaald van  $c_f$  (onder aanname van bolvormige korrels) óf van de effectieve kromtestraal ( $r_g$ ), die de mate van kromming van het contactoppervlak tussen korrels weergeeft (in het geval van niet-bolvormige korrels). De verkregen verdelingen van  $c_f$  en  $r_g$  laten zien dat  $c_f$  óf  $r_g$  evenredig is met de korrelgrootte ( $d$ ) volgens de relatie  $d^g$  waarbij  $g$  ongeveer gelijk is aan 0.5 tot 0.7. Er bestaat echter geen duidelijke, fysische verklaring voor een verband tussen de grootte van de oppervlaktebarstjes ( $c_f$ ) en de korrelgrootte. Bovendien laten gegevens over de rondheid van duinzanden een soortgelijke relatie tussen  $r_g$  en  $d$  zien, zoals die is gevonden bij de breuktesten op de enkelvoudige zandkorrels. Daarom is het Hertziaans-breukmechanisch model voor het breken van korrels, dat niet-bolvormige korrels met een verdeling van  $r_g$  aanneemt, in fysisch opzicht het meest aanneemelijk.

**Hoofdstuk 4** handelt over experimentele en theoretische aspecten van het korte termijn compactiegedrag van kwartszanden. Zandaggregaten bestaande uit zandkorrels met een geringe spreiding in korrelgrootte ( $196 \pm 16$ ,  $275 \pm 25$  en  $378 \pm 22$   $\mu\text{m}$ ) zijn onderworpen aan éénassige compactie-experimenten. Deze experimenten zijn uitgevoerd bij kamertemperatuur, opgelegde belastingen tot 30 MPa, constante belastingssnelheden tussen 3.90 en 5495 MPa/uur, en onder zowel droge als "natte" omstandigheden (waarbij in het laatste geval de poriënruimte volledig gevuld is met een waterige oplossing of een inerte vloeistof). De resultaten tonen quasi-elastisch belastingsgedrag in combinatie met permanente vervorming, veroorzaakt door het breken en het herrangschikken van zandkorrels. In het bijzonder laten de resultaten zien dat met toenemende korrelgrootte meer permanente vervorming optreedt.

Op grond van de uit de resultaten afgeleide mechanismen van vervorming is een microfysisch model ontwikkeld voor de tijdsafhankelijke compactie van zandaggregaten. Dit model beschrijft de verdichting van een aggregaat als de som van "elastische" vervorming als gevolg van de (elastische) inééndrukking van korrelcontacten en "brosse" vervorming als gevolg van het breken en het herrangschikken van afzonderlijke korrels. Verdere uitwerking van het Hertziaans-breukmechanisch model voor het breken van korrels (zie hoofdstuk 3) resulteert in het formuleren van twee uiterste gevallen van het compactiemodel: (i) bolvormige korrels met oppervlaktebarstjes, waarvan de grootte ( $c_f$ ) is verdeeld en die leiden tot breuk van de korrels, en (ii) niet-bolvormige korrels met een effectieve kromtestraal van het contactoppervlak tussen korrels, waarvan de grootte ( $r_g$ ) verdeeld is. In overeenstemming met de conclusies uit hoofdstuk 3, geven numerieke simulaties, uitgaande van geval (ii) van het model, een bevredigende beschrijving van het korrelgrootte-effect zoals dat is waargenomen tijdens de zandcompactie-experimenten.

In **hoofdstuk 5** wordt het (tijdsafhankelijke) compactiekruipgedrag van zanden systematisch onderzocht. Hierbij staat het effect van de chemie van de vloeistof in de poriënruimte, de opgelegde belasting, en de korrelgrootte centraal. Eénassige kruiptesten worden beschreven die zijn uitgevoerd op zandaggregaten bij kamertemperatuur, constante opgelegde belastingen tussen 14.5 en 30 MPa, en onder zowel droge als "natte" omstandigheden (waarbij in het laatste geval de poriënruimte volledig gevuld is met een waterige oplossing of een inerte vloeistof). De verkregen resultaten vertonen tijdsafhankelijk vervormingsgedrag, dat voornamelijk wordt bepaald door (subkritische) groei van scheurtjes door de korrel heen, hetgeen leidt tot het breken van de korrel. Tijdens de kruiptesten op de zandaggregaten zijn geluidspulsen (acoustische emissie) gemeten, die worden veroorzaakt door het breken van korrels. Deze acoustische emissie metingen vertonen een bijna rechtlijnige relatie tussen het cumulatief aantal getelde pulsen en de mate van vervorming van het zandaggregaat. Dit wijst op een directe relatie tussen de mate van vervorming en het toenemende aantal gebroken korrels. Het kruipproces wordt duidelijk versneld door een chemisch actieve vloeistof (een waterige oplossing) in de

poriënruimte, en bovendien door een hoger zoutgehalte van deze vloeistof. De versnelling van het krimpproces wordt groter naarmate de korrels groter en de opgelegde belastingen hoger zijn. Op grond van de resultaten wordt ervan uitgegaan dat het gedetailleerde breukmechanisme van de korrels het groeien van oppervlaktebarstjes is als gevolg van spanningscorrosie op contacten tussen korrels. Tenslotte is gepoogd een microfysisch model op te stellen voor het compactiekrimpgedrag van zandaggregaten als gevolg van dit mechanisme. Het model kan echter niet zinvol worden vergeleken met de experimentele resultaten, omdat het zeer gevoelig is voor de waarden van de invoerparameters.

**Hoofdstuk 6** bestaat uit een samenvatting en een generalisatie van de belangrijkste conclusies uit de voorgaande hoofdstukken. Dit wordt gevolgd door een discussie over de implicaties van de verkregen resultaten voor het compactie- en krimpgedrag van poedermaterialen in seismisch actieve breuken in de bovenkorst van de Aarde, en voor de krimp-effecten die verwacht worden in olie of gas bevattende klastische reservoirgesteenten, nadat de productie gestopt is. Het proefschrift wordt afgesloten met een beschouwing van gerelateerde, niet opgeloste problemen en suggesties voor verder onderzoek.

## NAWOORD

Er zijn een aantal mensen die een belangrijke bijdrage hebben geleverd aan mijn promotieonderzoek. Het is nu een lang verwacht, maar prachtig moment hen hier kort te noemen.

Allereerst zou ik graag mijn promotor, Chris Spiers, willen danken voor het feit dat hij mij in staat heeft gesteld mijn promotieonderzoek in het HPT lab in Utrecht te verrichten. Hij is een onuitputtelijke inspiratiebron geweest en heeft mij steeds tot het uiterste gedreven. Zijn drang naar ongekend detail en daadwerkelijke, exacte oplossingen hebben mij gevormd en mij overtuigd van het motto "Science is fun".

Mijn copromotor, Florian Lehner, was altijd bereid om met mij in discussie te gaan over mijn talloze theorieën. Hij was de eerste die met champagne toastte op het gereedkomen van dit proefschrift.

Colin Peach was onmisbaar in zijn inzicht in de vaak complexe apparatuur in het HPT lab. Met groot, niet aflatend enthousiasme heeft hij mij ingewijd in de electronica, de binnenzijde van de PC en het programmeren. Zijn onverwachte inbreng van onbetreden, fysische paden heeft het onderzoek verrijkt.

De technici van het HPT lab zijn voor mij van onschatbare waarde geweest. Gert Kastelein heeft met grote kundigheid en precisie drukvat na drukvat gebouwd. Eimert de Graaff ontwikkelde een prachtig acoustisch emissie systeem. Peter van Krieken gaf vele praktische adviezen bij het uitvoeren van de experimenten.

Op het KSEPL in Rijswijk heb ik veel genoeg beleefd aan de discussies met en de adviezen van Wolfgang Heidug en Yves Leroy.

Op het Natuurkundig Laboratorium van Philips in Eindhoven, heeft Bert de With, tijdens het laatste stadium, een zeer belangrijke rol gespeeld als discussie-partner en als coach voor de laatste meters.

Tenslotte, mijn paranimfen, Peter Schutjens en Bas den Brok. Reeds tijdens het Zoutproject gaf Peter mij steeds het goede voorbeeld, terwijl Bas mij met zijn onuitputtelijke opgewektheid altijd heeft weten te inspireren.



## CURRICULUM VITAE

Rolf Brzesowsky was born on 5 October 1963 in Ede, The Netherlands. He passed his final examination in June 1982 at Gymnasium Sorghvliet in The Hague. In this year, he started to study Geology at the University of Utrecht, The Netherlands. The Dutch "Doctoraal" ( $\approx$  M.Sc.) degree was conferred to him on 27 February 1989 (cum laude). His principal subject was structural geology with specialisation materials science.

During his M.Sc. studies, he was employed as a research assistant in the High Pressure/Temperature (HPT) Laboratory, Faculty of Earth Sciences, University of Utrecht, in the framework of research on the disposal of radioactive waste in salt rock sponsored by the European Community and the Dutch Ministry of Economic Affairs under supervision of Prof. Dr. C.J. Spiers and Prof. Dr. H.J. Zwart. He performed experimental research into and micromechanical modelling of the compaction creep behaviour of wet granular salt with emphasis on plasticity induced solution transfer processes.

From 1989 till 1994, he was employed as a research assistant (PhD student) in the HPT Laboratory. The position was funded by Shell Research Rijswijk (Royal Dutch Shell Exploration and Production Laboratory) and supervised by Prof. Dr. C.J. Spiers (University of Utrecht) and Dr. F.K. Lehner (Shell Research). During this period, he conducted the research described in this thesis.

From 1994 till present, he is employed as a postdoctoral researcher at Philips Research Laboratories Eindhoven, The Netherlands.